UNIVERSITY OF
LIVERPOOL

Department of Engineering

PhD Thesis

Laser Assisted Ink Consolidation for Direct Write Component Fabrication

Thesis submitted in accordance with the requirements of The University of Liverpool for the degree of Doctor in Philosophy

By

Taku Sato

October 2010

Laser Group
Department of Engineering
The University of Liverpool
Brownlow Street
Liverpool
L69 3GH
UK

Declaration

I hereby declare that all of the work contained within this dissertation has not been submitted for any other qualification.

Signed: _____

Date: _____

Abstract

The work presented here, within this thesis is concerned with the fabrication of antenna using a syringe based additive manufacturing technique along with a novel post laser curing process that eliminates the need for an oven curing step of silver based polymer inks. The process falls under the umbrella term known as direct write (DW).

A novel CO_2 laser process developed at the University of Liverpool is investigated that eliminates the need for conventional oven curing of silver based screen printable inks. The results of the laser curing trials are given along with an in depth analysis and comparison of both laser cured and oven cured inks before and after processing using FTIR and TGA/DSC analysis, helping to explain how the laser curing process works and demonstrating that the cured products are the same regardless of the processing method. The results of a novel experiment are also shown where the resistance of the inks as a function of temperature during hotplate and laser cure are shown and compared.

It is put forward that laser curing is a viable alternative to oven curing, with faster processing times; dependent on geometry/quantity as it is a vector patterning process as opposed to a batch process, and competitive sheet resistance. It also allows for the fabrication of components directly on to heat sensitive substrates that could not be placed in an oven such as glass re-enforced plastic (GRP) or carbon fibre composite (CFC), which are widely used in the aerospace industry along with no associated thermal damage.

The laser curing process is combined with a syringe deposition process that allows for conformal deposition directly on to any curved or doubly curved surface enabling in-situ fabrication and curing of a functional component. This ability is demonstrated by the fabrication of a working microwave genetic algorithm antenna with a frequency of 2.4 GHz on a fibre glass re-enforced foam wing that has a maximum operating temperature of 120^0C, made as part of the Towards a Wireless Aircraft project.

A life size demonstrator is also shown as part of the ASTRAEA project which created an antenna array directly on to a GRP. This demonstrator incorporated DW of a dielectric as well as a silver ink.

List of Publications to Date by the Author

Laser Assisted Direct Write for aerospace applications

Sato T, Fearon E, Curran C, Watkins KG, Dearden G, Eckford D.

Proc. IMechE, Vol.223, Part G: J. Aerospace Engineering

The Opportunities and challenges associated with wireless interconnects in aircraft

Panitz M, Christopoulos C, Sewell P, Hope DC, Dawson, JF, Marvin AC, Sato T, Fearon E, Watkins KG, Dearden G, Harley CD, Crowther WJ.

Proc. IMechE vol. 223, Part G: J. Aerospace Engineering, 2009.

The Effects of Multiple Passes of a Gaussian Laser Beam to Cure Silver Loaded Polymeric inks

Sato T, Fearon E, Wellburn D, Watkins K, Dearden G.

ICALEO 2008, M505

Thermal Effects of Substrate Materials Used in the Laser Curing of Particulate Silver Inks.

Fearon E, Sato T, Wellburn D, Watkins KG, Dearden G.

LANE 5, 2007, Germany

Output Beam Stability in a Large Mode Area Fibre delivery System

Sato T, Lewis S, Naeem M, Watkins K, Dearden G.

Proc. 4th International WLT-Conference, LIM 2007

Acknowledgements

I would like to thank all the people who have supported me during my PhD and contributed to this final submission through advice, help, and general idea thrashing. In particular I would like to pay special attention to the following people.

Firstly, I would like to thank my supervisors Prof. Ken Watkins and Dr. Geoff Dearden for their unwavering support and help during my studies and for accepting me for the studentship in the first place. Without their support and input this publication would never have come about. Thank you both.

I would also like to thank Dr. Amonn Mcfurlong and Doug Eckford, they have both been an inspiration to me during my studies and I have enjoyed the countless hours spent postulating, idea bashing, and generally putting the world to rights and also for their support in making the logistics of the experiments possible. I would like to add that the support I have received in developing the UET may produce fruits yet. Dr. Andrew Fogg has been invaluable in the help and support he has given me, and has gone above and beyond what I had hoped for when I first approached him for help.

My fellow colleagues have been a constant source of support throughout my studies. Dr. Dan I am in awe at the work you have done and thank you for the advice given to me. To Dr. Kenneth Robert Jedward, Craig, Joe and Lee, fellow laser patrons and grazers thank you for the fun times we have had and for putting up with my erratic playing skills.

I would also like to thank my fellow colleagues on the Towards a Wireless Aircraft Project, I have thoroughly enjoyed this project and our time working collaboratively on creating something truly new, unique and state of the art. I wish you all the best in the future.

Finally I would like to thank my family. Mum Shirley for constant support and unwavering faith in her son, my dad Motoshi. For whom without a series of events many years ago, things would be very different today.

I would also like to thank BAE Systems and EPSRC for sponsoring my studentship and Gwent Group for supplying and helping out with resources.

Contents

List of Figures

List of Tables

List of Symbols

A	Adjacent side (trigonometry, only in chapter 3)
A	Area
A_R	Reference amplitude
A_S	Sample amplitude
B(k)	Spectral power density
C	Specific heat capacity
c	Heat capacity
c	Speed of light (chapter 5 only)
C_P	Specific heat capacity at constant pressure
C_{PR}	Specific heat capacity of reference at constant pressure
C_{PS}	Specific heat capacity of sample at constant pressure
C_{XD58}	Specific heat capacity of D58 at cross linking phase
C_{BD58}	Specific heat capacity of D58 at B-stage cure
C_{XD1}	Specific heat capacity of D1 at cross linking phase
C_{BD1}	Specific heat capacity of D1 at B-stage cure phase
C_{XD15}	Specific heat capacity of D15 at cross linking phase
C_{BD15}	Specific heat capacity of D15 at B-stage cure phase
Ch	Channel number for input into the data logger
d	Thickness of material
E	Energy
f	Force constant
H	Enthalpy
H_e	Enthalpy of the empty pan
H_S	Enthalpy of the sample
H_Z	Enthalpy of zinc
h	Planck`s constant
I	Measured Intensity
I_0	Initial Intensity
I(δ)	Intensity falling on detector
K	Calibration factor
k	Extinction Coefficient
k	Wavenumber (chapter 5 only)
k_T	Thermal conductivity
L	Length
m	Mass
m_R	Reference mass
m_S	Sample mass
m_1	Mass of atom 1
m_2	Mass of atom 2
O	Opposite side
P	Pressure
Q	Energy flow
R	Resistance
R_S	Sheet resistance
S11	reflection Coefficient
S21	Efficiency coefficient
T	Temperature
T_i	Initial temperature
T_f	Final temperature

T_P	Programmed temperature
T_S	Sample Temperature
T_T	Transition Temperature
t	Time
U	Internal energy
V	Volume
W	Width
α	Thermal diffusivity
α_λ	Absorption coefficient
θ	Angle
λ	Wavelength
μ	Reduced mass
ν	Frequency
ρ	Resistivity
ρ_D	Density
ϕ	Angle

Thesis Introduction

The following thesis is the formal documentation of the experimental work carried out. The nature of the experimental work conducted requires the reader to understand different areas of science. Because of this, the thesis has been laid out in a specific way so as to make it easier for the reader to follow and inform them as they go along.

The thesis starts with a state of the art literature review, giving a background to the current state of the art in the area of direct fabrication of functional materials and puts in to context the work that has been carried out but the author and has been broadly speaking, broken up in to two classes: laser based and non-laser based techniques. Following on from the literature review, the experimental work has been introduced and divided up in to four main sections: Oven curing of polymeric inks, laser curing of polymeric Inks, thermal analysis of polymeric inks, FTIR spectroscopy analysis. Within each section, there is a brief introduction followed by the equipment used and the method employed for each experiment followed by the results section. The conclusions for the experiments are in section 7 so that the reader can see how the results relate to each other.

For sections 4 and 5, in addition to the above, there is also an introduction to the analytical techniques used. This has been included to help the reader understand the results, method of analysis along with the reasoning behind using these two techniques within the investigation.

It is hoped that by formatting the thesis in this way, it makes it easier and more enjoyable for the reader to navigate through and understand the concepts and arguments that are being introduced along with the experimental methods used.

1 Literature Review of Direct Write Technologies.

This chapter presents a literature review and is intended to inform the reader of the current state of the art of technology used under the umbrella term "Direct Write". It is broken up into two main parts. The first being laser based additive manufacturing technologies and the second being non-laser based technologies.

The term direct write (DW) is a general umbrella term for a range of flexible multi-scale, CAD/CAM controlled fabrication technologies, largely involving 'point of process' deposition which can be used to produce 2D and/or 3D structures on pre-existing substrates with a wide range of materials. They can be used to form simple 2D components or complex 3D architectures on curved and doubly-curved surfaces. Within this definition of additive manufacturing lie several techniques. They can be broadly placed into four categories:

- Energy Beam
- Drop on demand
- Filamentary Flow
- Tip Based

Within these categories are several sub-categories of technologies that can deposit materials from the nm scale to mm. For ease of reading and assessment of these technologies they have been classified into the four main groups (where possible) as stated above, for the purposes of this review. With energy beam relating to laser or electron based processes. Each sub-section contains a brief introduction to the methodology of the technology and its capabilities along with the types of architectures that are currently being presented by proponents of that technology.

Though there are many technologies encompassed within Direct Write an effort has been made to restrict the scope of this review to those which can be seen as being of direct benefit to the task at hand, viz. the generation of electrically significant components on 3D CFC laminates with no damage to the CFC laminate itself. A further task may be that of

generating sensor or electrical components in metallic parts. Therefore some of the better known technologies such as laser sintering which would have been considered to be outside the scope of this review due to excessive heat input into the laminate material are also included. Those techniques that are considered not suitable for conformal deposition or fabrication upon a thermally sensitive substrate such as laser cladding and selective laser melting (which relies on a roller or scraper to produce a flat powder bed for deposition purposes) has not been included in the review even if it may satisfy the primary phases of the project, but would face difficulties when the task altered to that of producing sensors on curved surfaces. Some technologies are included which may be of use in relatively large scale (>1mm^2) deposition of a desired set of materials even though they may require some finishing processes. These are included due to higher deposition rates which may be useful in conjunction with the more accurate systems and for completeness.

1.1 Background

The laser since its inception in the 60`s has been very important for materials processing bringing a new form of processable energy. It has the ability to direct high amounts of energy in a controllable way at precisely where it is needed on very small scales. There are many ways of manipulating a laser beam through optics once the raw beam has left the laser output, through pulsing of the beam or a continuous wave depending on cavity design or ancillary equipment and polarisation of the beam. Since the first ruby laser, many different types have been developed with new types constantly being introduced. The most recent and significant development in laser technology being the advent of the fibre laser, where the fibre is used as the cavity producing high quality high power beams with the ease of a fibre optic for integration.

The most common types of laser are CO_2, solid state or excimer. The use of these lasers in industry range from bio-medical applications to surface modification and materials processing such as welding, cutting and drilling. They all rely on the coherent and monochromatic nature of a laser. When lasers are used in direct write (DW), they are generally used to remove material from one surface which is then deposited on to another surface. For this a short pulse laser of the order of nanoseconds or picoseconds is used in a process that is termed ablation or spallation depending on the exact mechanism involved.

A constant stream of pulses of a specific wavelength and at a set frequency are incidented upon the material to be removed/deposited.

For the purposes of this research and development of a laser assisted DW process a continuous wave CO_2 laser has been employed and to a lesser extent a pulsed fibre laser. The motivation for using a laser is to utilise its accurate and direct ability in placing thermal energy exactly where it is required. The process is a thermal one and depends on the thermal association of the absorption of photons by the material. In this manner a continuous wave laser is the primary candidate with an IR output.

1.1.1 Introduction

With the advent and growth of DW, there is a desire within industry for the development of these processes to be used to fabricate functional components for real world solutions. With many technologies out there each with their own merit, no single technology has become a single solution for microfabrication needs.

The research conducted within this thesis was industry led with a solution desired to the problem of fabricating functional electrical components on heat sensitive materials on large and small scales for the aerospace industry. Techniques exist with some of these capabilities but not all.

The work conducted within this thesis and presented here details the development of a laser curing low thermal process used in conjunction with a COTS syringe deposition system and COTS inks, creating a low cost manufacturing process for conformal directly written components. The emphasis of which has been on the fabrication of antenna for UAV applications with analysis of the inks to gain a better understanding of what occurs during the thermal cure process.

As technology progresses, there is a tendency and requirement for electronics to become smaller, cheaper and more reliable. Further to this, in an energy conscious environment the desire for more efficient ways of manufacturing components with less material waste and shorter life cycles. Additive manufacturing for which DW is a sub-category, is a well suited manufacturing tool. In general it allows for low material wastage and ease of modification,

due to its computer controlled nature different designs can be easily made with just a change in programming and no requirement for hard tooling. Due to it encompassing several technologies (of which the more common and appropriate ones for electronics manufacture are mentioned here) it is able to fabricate components of differing geometries and materials, from tissue scaffolds and cells to ceramics and piezoelectric materials. There is extensive growth in the area of DW research with several commercially available systems and systems already in industrial usage. Over the years inkjet and screen printing (a modern twist on an ancient technique) have become common in the industrial workplace being used in electronics manufacture today. DW is proving to be a competitive, disruptive technology that is still at an early stage of maturity, with no single dominant process it is likely that several will emerge as the process of choice for any single component manufacturing.

1.2 Laser Based DW Technologies

Lasers can be used to create small features on a suitable substrate by using additive, ablative or reactive chemical methods. For fine (<100 micron) features, the shorter wavelength lasers are most commonly used. These include excimer (193 and 248nm), frequency doubled or frequency tripled Nd:YAG and high beam quality short-pulse lasers (nanosecond pulsed or lower). With additive processes, lasers can be used to generate 2 and 3-D structures at resolutions of a few tens of microns whereas laser machining or ablative processes can remove pre-placed materials in defined patterns to a feature resolution of less than half a micron. With some processes, laser machining is used as a final step to remove unwanted material which has been deposited in order to refine the deposited feature to the required resolution/dimensions.

The following processes are representative of those currently available which could satisfy the requirements for NAC research. In most cases, to implement these processes at the University of Liverpool Laser Group would require some modification of existing equipment and procurement of new equipment depending on the manufacturing method.

1.2.1 Pulsed Laser Deposition (PLD)

PLD is a process that uses an off axis pulsed laser to vaporise areas of a sacrificial rotating target such that the resultant plume of evaporated material is deposited upon a facing pre-placed substrate. PLD has usually been used to deposit ceramics, (especially the high temperature superconducting oxygen-defect perovskite materials of the late 1980s/ early 1990s [1]) and semiconductors [2]. It is not suitable for depositing organic or polymeric materials due to the high temperatures and violent mechanism of deposition. Typically it employs UV lasers (usually excimer) and takes place within a hard vacuum. Factors affecting the amount of material deposited include pulse energy, pulse length, spot size, pulse repetition rate and the degree of vacuum within the chamber (typical values are a laser fluence of 3 to 4 J/cm^2, a spot size of 2 to 3mm^2, a repetition rate of approx. 20 Hz and a target to substrate distance of a few tens of mm). PLD is used almost exclusively for the generation of thin films with area coverage, and as a result any component desired would need to be fabricated by post laser-machining or etching of some sort in order to be of use as a functional component. In addition the need for a vacuum chamber would raise problems for the generation of components on sections of an unmanned air vehicle (UAV) and would not be suitable for 3D conformal deposition, unless area coverage was desired. However, the process can be of used in the generation of ribbons for use with the LIFT (section 1.2.4) or MAPLE-DW (section 1.2.3) processes. A schematic of the PLD process can be seen in Figure 1.1.

PLD is a popular technique, where thin films are required T. Miller et al [3] describe the fabrication of micro-scale ITO (Indium Tin Oxide) thin film strain sensors using a combination of PLD and focussed ion beam (FIB) machining. The ITO layer deposited was 100~246 nm thick with feature sizes down to 20μm, whilst E. W. Kreutz et al as far back as 1997, were looking at using PLD for large area coverage of alumina on stainless steel [4] using an excimer laser at 248nm for the generation of the plume. J. Gottmann along with E. W. Kreutz used PLD for the deposition of alumina and zirconia thin films on polymers and glass as optical and protective coatings. Again an excimer laser was used at 248nm to create the plume on the target with thin film thicknesses of 94nm and 144nm for the alumina and zirconia respectively on milled cylindrical lenses in PMMA (poly methyl methacrylate) [5]. U Singh et al investigate the deposition of palladium thin films on glass using PLD [6], whilst Y-W Ju et al have reported using the technique to create Ni-Fe bimetallic anodes in the fabrication of solid oxide fuel cells in conjunction with the Mitsubishi Materials corporation [7].

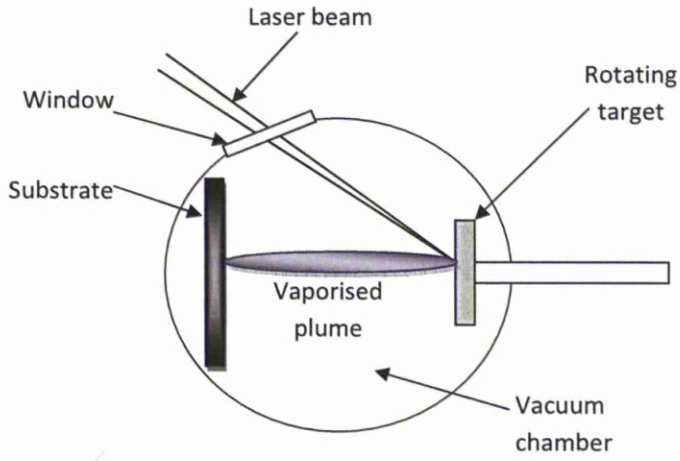

Figure1.1: Schematic of the pulsed laser deposition arrangement.

Work carried out by Miller et al [8] indicates that indium-tin-oxide (ITO) can also be used to generate thin film sensors by depositing an ITO layer with a pulsed laser ablation method and post machining it with an ion-beam apparatus. This simple configuration for the strain sensor, Figure 1.2, appears to be in the form of an interdigitive capacitive track but other configurations can be manufactured. The basic premise behind these strain gauges relies upon a change in resistance of the material as a function of the strain it is put under. They can be drawn conformally and can be placed directly onto a desired surface.

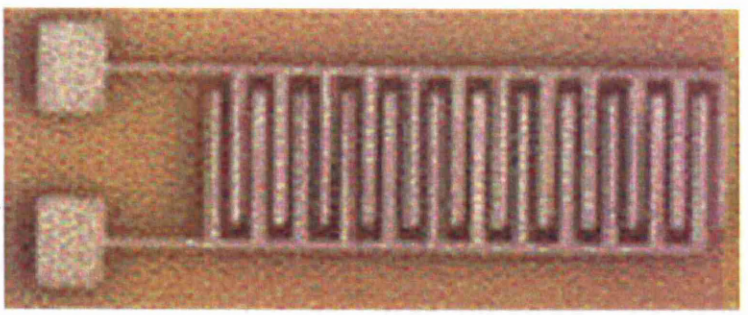

Figure 1.2: Photograph of a simple strain gauge fabricated using PLD [10].

Though resistive strain gauges can be simple in design and simple to manufacture they are not generally suitable for application in situations where high temperatures or large variations in temperature may occur due to the physical limitations of the materials from which they are fabricated. Li et al [10] demonstrate the fabrication of an interdigital capacitive strain gauge for harsh robust environments manufactured using DW thermal

spray followed by laser micro machining of the deposited material. This process would not be suitable for direct deposition onto a large structural surface, but more suited to depositing on a flat substrate usually alumina. The specific design, Figure 1.2, allows measurements to be taken in two perpendicular planes, reducing the number of sensors that maybe required. The strain gauge shows good linear change with strain.

1.2.2 Matrix Assisted Pulsed Laser Evaporation (MAPLE)

MAPLE was developed at the United States Naval Research Laboratory in the late 1990s, and is a hybrid technique of PLD for the soft deposition of polymers and organic material, but is not suitable for the deposition of biological materials as they must be frozen within a matrix. Like PLD it is thin film deposition or coating method for whole areas, and is not suitable for conformal deposition or the coating of large objects due to the requirement of a vacuum. In this technique an ultraviolet (excimer) laser pulse is directed at a sacrificial target which consists of a dilute matrix of a specifically chosen solvent and the organic material (solute) to be deposited. The solvent is chosen so that it has a near zero sticking coefficient on the substrate and preferentially absorbs the laser radiation over the organic molecules to be deposited. The matrix is frozen along with the target being rotated in order to reduce the effects of localised heating by successive laser pulses striking the same area and hence reducing the effect of decomposition of the organic molecules. The thermal effects are generally large compared with the melting point of the solvent, but low compared with the decomposition temperature of the solute. When the laser beam irradiates the target, the solvent is evaporated, imparting kinetic energy to the released polymer molecules. This effect appears as a plume being ejected from the frozen target. If a substrate is placed in the path of this plume it will be coated with a thin layer of polymer molecules. The gaseous solvent, which has a very low sticking coefficient, is evacuated from the chamber by means of a pump. This process is carried out using a pulsed laser beam of typically 193nm and a fluence of 0.01 to 0.5 J/cm^2 and has been used to successfully deposit a variety of polymers and organic materials [9, 11, 12].

In order to create any functional geometric components, post processing of the thin film would be required as with PLD. This could be done using a laser or some other subtractive technique. A schematic of the MAPLE setup can be seen in Figure 1.3

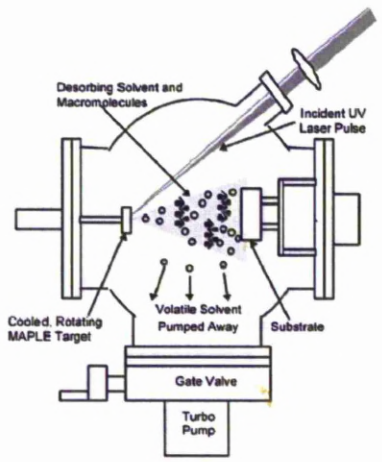

Figure 1.3: A schematic of the MAPLE system [14].

The benefit of MAPLE over PLD is its ability to deposit organic and piezoelectric material without any adverse side effects. This is done by the addition of a preparation step in terms of the frozen matrix that is created with the desired material to be deposited. In all other respects it is similar to PLD and has the same deposition limitations. Due to this MAPLE has evolved in to another technique called MAPLE-DW which is introduced in the next section.

1.2.3 MAPLE-DW

MAPLW-DW is a combination of the MAPLE and LIFT (section 1.2.4) processes and has given rise to MAPLE direct-write, otherwise known as MAPLE-DW [15, 16]. It was first demonstrated by Pique et al [16] in the late 90`s. This process was originally designed to allow the deposition of electrical components on the mesoscopic scales, 10 μm to 5 mm, and can deliver metallic, phosphors, dielectric and resistive materials, along with polymers, organic material and living cells [17].

MAPLE-DW is accomplished by coating a UV transparent ribbon with an 'ink' consisting of the material to be deposited and a strong UV absorbent solvent (as in MAPLE). As in LIFT, a focussed laser beam is directed at the back of the ribbon, evaporating the solvent and causing the forward transfer of the material to be deposited onto the substrate, whilst the solvent is removed. Both the ribbon and the substrate are mounted on computer-controlled stages in order to generate complex 3D geometries. However it is not suitable for conformal deposition. Unlike LIFT, the process does not involve the vaporization of the

solute material and is therefore a form of soft deposition. It has a resolution comparable to the LIFT process of about 10 μm with each pass depositing typically, less than 1 μm thick layer with scan speeds up to 500 mm/s [18] at ambient temperature and pressure. MAPLE-DW can be carried out using either excimer or frequency tripled Nd:YAG lasers and is a sufficiently gentle that the deposited material is not vaporised in the process of being depsoited. This method has also been used to deposit a wide variety materials and components such as micro capacitors, interconnects, phosphor displays, coplanar resistors [16, 19], laminated band pass filters, and more recently lithium-ion microbatteries [20], inductors, and fractal antennas on honeybees which resonate at 25 GHz [17]. Since MAPLE-DW utilises a laser for the deposition of the material it is capable of micromachining as well. The same laser can be used to modify the deposited material increasing the effective resolution of the process when the ribbon is removed from the processing area.

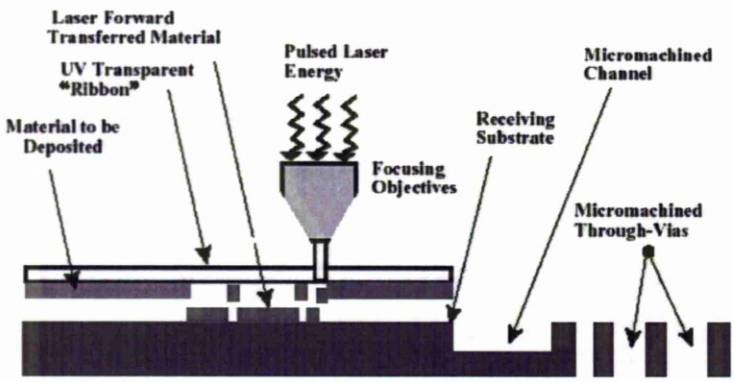

Figure 1.4: A schematic of the MAPLE-DW process setup [16]

Though MAPLE-DW is an effective way of depositing a wide range of materials and creating functional mesoscale components, in some cases, in particular metallics, it requires a post annealing process to achieve the desired properties of the deposited material. A laser curing process or convection oven maybe used to achieve the desired properties. Currently the process is a serial process and so is limited by the speed of one traversing beam, making the process relatively slow in industrial terms. A way round serial processing has been developed at the University of Liverpool where a spatial light modulator (SLM) has been demonstrated to be able to create up to 32 micron sized holes simultaneously by splitting a single beam into 32 using a computer generated hologram, with each beam addressable independently [21]. This technique has the potential to drastically increase the fabrication process of MAPLE-DW and LIFT.

Examples of components fabricated using MAPLE-DW are parallel plate capacitors [16, 19], a chemoresistor [16, 20], temperature sensor [20], and micro batteries [20]. It has also been used to demonstrate the fabrication of conformal mesoscopic electronic devices [22] for capacitors, interconnects, coplanar resistors and inductors.

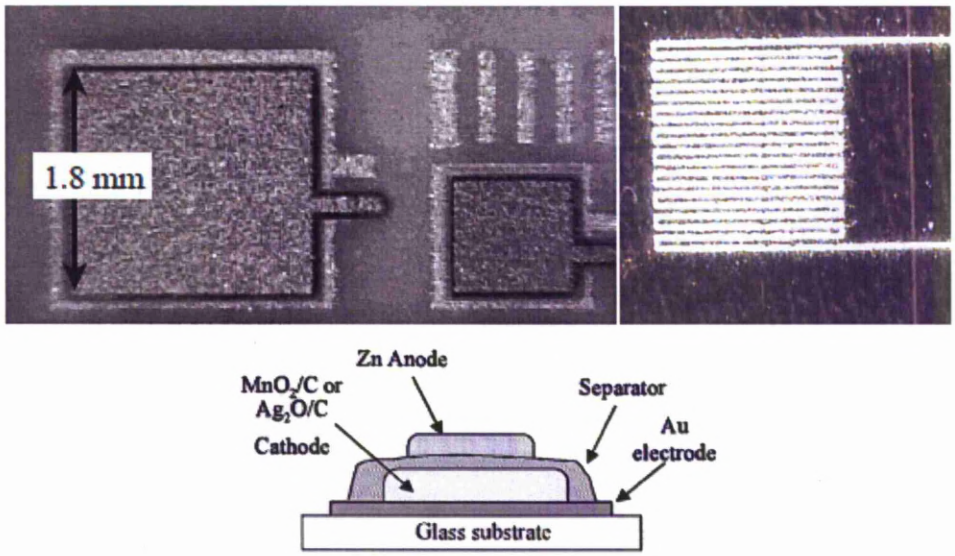

Figure 1.5: Top left shows an image of a parallel plate capacitor [16], the top right is an image of a serpentine temperature sensor on polyimide [20], and the schematic cross-section of a stacked alkaline battery [20].

Other research being conducted by Arnold et al [23] also demonstrates the possibility of using a Laser based DW method for the fabrication of planar alkaline micro-batteries figure 1.6. Here the MAPLE-DW technique is used to deposit Zn-Ag_2O alkaline batteries in a micro configuration and then subsequent laser machining is required to suitably pattern the deposited material. The resultant micro-battery has an electrode thickness of between 10 and 20 μm and exhibit the expected flat discharge behaviour under constant current. The open circuit potential witnessed was 1.55 V and typical load values of 270 $\mu Ahcm^{-2}$ and 450 $\mu Ahcm^{-2}$.

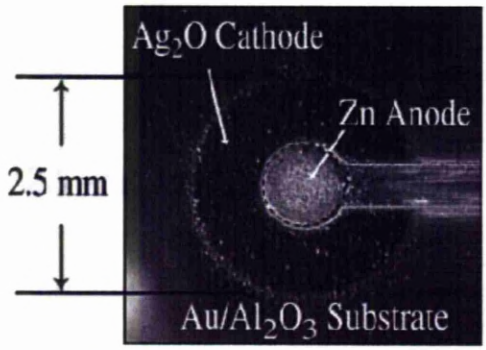

Figure 1.6: Picture of a planar alkali micro battery made using MAPLE-DW [23].

With the advancement of DW as a manufacturing technology, new avenues are being opened up for traditional components. A lot of research into DW is being aimed at the fabrication of traditional and new antennas designs. The desire to be able to fabricate antennas directly on to a structural surface without the need for an intermediary substrate is driving this research. Conformal antennas are now possible through DW and finding wide applications from packaging to aerospace. In addition to this, they can be fabricated along with other components making a wireless network of sensor arrays with the versatility of rapid prototyping. There are many different types of antenna design and many different applications. Pique et al [24, 25] have demonstrated the use of MAPLE-DW for the fabrication of a spiral antenna with a resonant frequency of 4.7 GHz for a half wave antenna. In this method channels are micro machined and then a conductive line is deposited with the machined channel. The substrate acts as the dielectric, Figure 1.7.

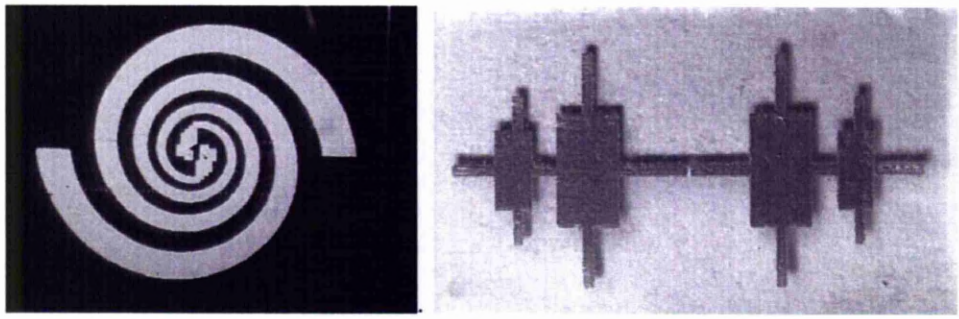

Figure 1.7: An image of a planar antenna made by DW (left), and a loaded half wave dipole antenna (right). Image reproduced from [24].

1.2.4 Laser Induced Forward Transfer (LIFT)

LIFT is a relatively cheap and simple DW manufacturing technique that relies on a disparity between the optical, thermophysical and mechanical properties of the materials involved. It has been shown to work over a range of laser wavelengths, pulsed and continuous wave (CW), and in a vacuum, inert and air atmospheres and the deposition of metals, oxide compounds and diamond particles have been demonstrated on a variety of substrates [17] along with the capability of fabricating precise 3D structures. The process is not currently suitable for conformal deposition and cannot be easily modified to create this capability.

The process was first demonstrated by Bohandy et al [32]. in the 1980s where it was shown that deposition of Cu and Ag lines of ~50 μm in width could be achieved. It is a process which uses a focussed laser to vaporise a thin film which has been placed on a laser-transparent medium which acts as a supporting plate; usually quartz but specific to the wavelength used. The laser passes through the transparent medium and impinges upon the film at the thin film/supporting plate interface, where it is absorbed and causes a small portion of the film to vaporise. The vaporised material is expelled away from the supporting plate due to the high pressures that occur during vaporisation, and re-condenses upon the substrate. In general the material deposited is the same as the target material.

Though the amount of material deposited and the achievable resolution is related to the film thickness, laser intensity, wavelength and optical extinction coefficient of the target, the substrate must be held in close proximity to the target so that the vaporised material does not diverge during propagation to the substrate and hence have a spatial resolution of the order of the material ablated. Typically the substrate will be between 25 μm to 100 μm from the target material [18] and directly proportional to the width of the track deposited as well as the laser fluence employed [26].

As indicated in the previous paragraph, the heating regime employed in the LIFT process also has a direct effect upon the spatial resolution of the pattern. High fluences result in excessive heating rates and an associated turbulent transfer of molten material, causing poor resolution. An approach which has led to smaller track widths is the reduction of power coupled with longer pulse lengths. This causes some of the film to be transferred in the solid phase and allows for more homogenous heating, improving the deposited

resolution. Because LIFT causes the vaporisation of the transfer material, it is not generally considered to be appropriate for the transfer of polymers, though they

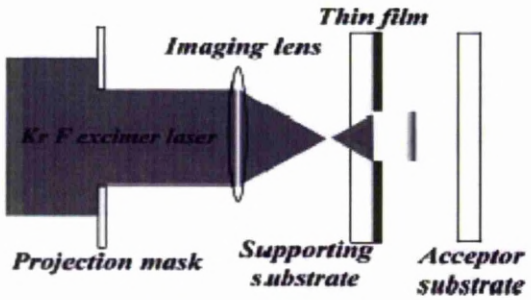

Figure 1.8: Schematic of a typical LIFT setup using a KrF laser at 248nm.

may be used as a sacrificial binder in certain applications [18]. It has also been demonstrated that successful deposition of bio molecules such as DNA from salmon sperm [27], proteins, prokaryotic and eukaryotic cells [28] has been achieved.

An area of LIFT that has been further investigated recently and that may have more direct applications for UAVs in sensor applications is the direct manufacture and micro deposition of oxide compounds such as YBaCuO and BiSrCaCuO [29-31]. With post thermal annealing at 850-900^{0}C they were successfully turned into superconductors with a critical temperature of ~90 K and zero resistance at 80 K. Feature sizes between 1 μm for Cr, Pt, Mo, In and In_2O_3 [27] and 200 μm for Al [32] wide have been demonstrated and typical thicknesses of between 100 nm for W [33] and 800 nm for Al [32] for single layer deposition have been achieved leading to high aspect ratios. LIFT has been successfully used to fabricate conductive lines, micro resistors, capacitors, superconductors and complex 3D holograms, and has the potential to grow miniature amorphous and crystalline structures [17]. Au lines of 30 μm widths (with post laser machining) have been achieved with a resistivity of ~ x30 of bulk Au [34], whilst parallel plate capacitors have been fabricated with a capacitance ranging between 2 to 40 pF [17].

Pique et al [35] have reported the successful fabrication of both Zn-Ag_2O and Li-ion micro-batteries with the planar zinc-silver oxide alkaline cell configuration, Figure 1.9, showing an open circuit potential of 1.5-1.55 V. The battery is 10 mm^2 and shows a flat discharge under constant current loads with a capacity of ~100 μAhcm^{-2}. The stacked rechargeable Li-ion

battery with a footprint of 9 mm^2, has a 3.80 V open circuit potential with a capacity of up to 110 $\mu Ahcm^{-2}$ and has continued to work with up to 50 charge/discharge cycles.

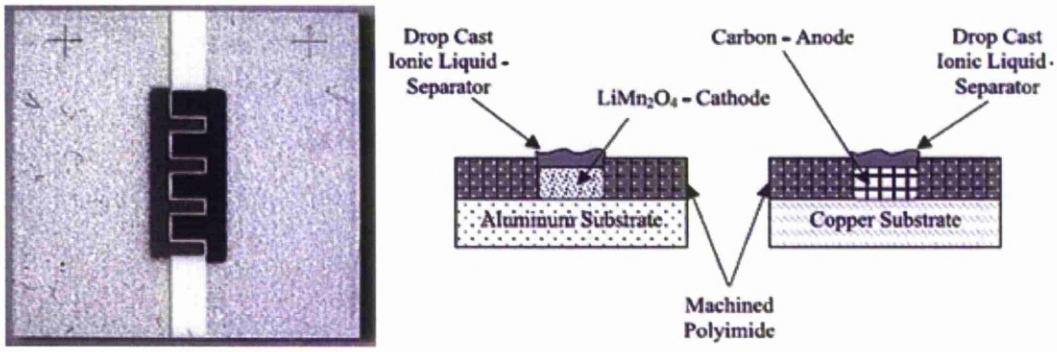

Fig 1.9: The image on the left shows an optical micrograph of the Zn-Ag_2O alkaline battery and on the right a cross-sectional schematic of the Li-ion battery. Image reproduced from Pique et al [35].

1.2.5 Direct Write Laser Lithography

Direct Write Laser Lithography (DWL) is a lithography process based around localised surface modification of a substrate surface. This modification can include annealing of thin metal films, etching and deposition. In many DWL systems the laser (UV or near UV visible) is used to selectively remove portions of a bi-layer resist, allowing the generation of an undercut trench in the resist which can be filled with thermally deposited metal [37]. The remains of the resist are then removed chemically to leave a standalone metallic track, Figure 1.10.

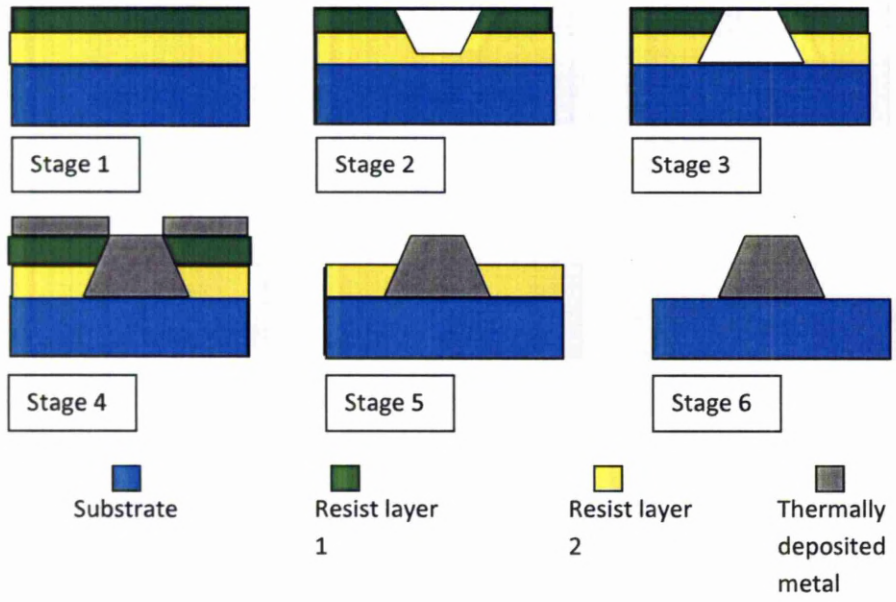

Figure 1.10: Stage 1, Deposition of 2 layer resist. Stage 2, Laser removal of resist layer 1 and partially into resist layer 2. Stage 3, use of resist layer 2 etchant creates undercut profile. Stage 4, thermal deposition of Al or Cr. Stage 5, Chemical removal of resist layer 1. Stage 6, Chemical removal of resist layer 2, leaving metallic feature alone on substrate.

This method can be used to generate extremely small conducting features of the order of a few tens of nanometres thick but may be unsuitable for the generation of sensors on CFCs due to the need for chemicals as well as heat input into the substrate when the metal is thermally deposited.

1.2.6 Laser-Induced Chemical Vapour Deposition (LCVD)

Laser-Induced Chemical Vapour Deposition (LCVD) is a method of depositing metals, semiconductors, ceramics and insulating materials by causing reactions to occur between a gas and a solid. This process has been investigated for the possible deposition of sensors since the mid-1980s [38]. The process consists of using a laser to excite gas molecules at or just above the surface of a solid, causing a reaction to take place and depositing the required material in an area defined by the laser path over the surface of the substrate. It is a well established process which has been used to deposit optoelectronic devices using GaAs [39], pressure sensors in silicon [40], to deposit metals for conduction paths [41] and

for the deposition of ceramic coatings [42]. Typically the lasers used are in the visible range (ie Argon ion or frequency multiplied Nd:YAG) with powers of approximately 1W and a spot size of less than 10 microns. Other required equipment consists of a gas chamber for the reactant gas and a suitable X-Y table for writing.

Features deposited in this manner can be as small as a few microns in width but must be written at quite low speeds (of the order of 50 microns/sec) to allow the pyrolytic reaction of the gas with the substrate to be initiated.

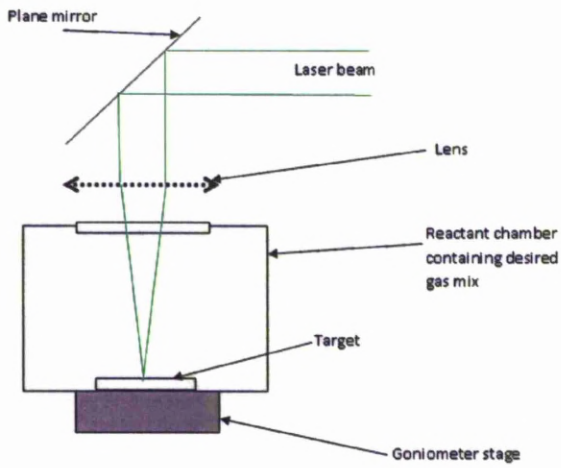

Figure 1.11: Schematic diagram of LCVD.

1.2.7 Laser and Electron Beam Deposition

Laser Deposition is an extension of the laser cladding process in that it allows three-dimensional parts to be built by cladding successive layers on top of one another in pre-determined vector paths (work began on the process in Liverpool in 1990 with the first paper published in 1993.)[43]. The process utilises a laser beam to create a shallow melt pool on a substrate into which powder is incorporated and subsequently melted. By moving the laser and powder feed relative to the substrate a track of solidified material can thus be created. Utilising CNC tables and/or goniometer stages this track can be laid down in a particular vector pattern, forming a layer. By repeating the process on top of this generated layer a 3-dimensional part can be made in a layered manufacturing form. Since the layers are fusion bonded to each other, a fully dense metallic part can thus be made

using 'soft tooling' (i.e. in order to make a different part only the program used to control the CNC equipment needs to be changed rather than needing to change tools or make new moulds). At present, most laser deposited parts need some post-process machining to finish them to required tolerances [44].

When a clad bead is laid onto a previously produced layer, a number of extra considerations in addition to the utilised process parameters affect its generation. One of the most important of these is the effect of whether an elevated temperature persists in this previous layer due to insufficient cooling time or heat retention in the bulk of the part. Therefore, unless steps are taken to control the layer height during a build, the retained heat in the part from previous layers will result in a cumulative increase in the height of the deposited layer. At dwell areas such as corners this will be magnified [45], causing a significant and progressive build-up beyond the parameters of constant velocity areas of the clad structure.

One of the most common uses for laser deposition processes is in the repair and/or modification of existing parts. Uneven surface profiles on these parts may necessitate rapid alteration of the height of the deposited layer in order to compensate. This would normally require extensive modelling of the surface or extremely responsive feedback systems. Research carried out at the University of Liverpool has resulted in a method of controlling the deposited layer height by abruptly limiting the availability of powder in the vertical plane at a fixed point relative to the powder feed nozzle [46]. This method employs a four port powder feed nozzle and is dependent upon the configuration of the powder feed tubes as well as on the nozzle usage parameters.

Electron beam deposition is fundamentally the same process but uses an electron beam rather than a laser to create the initial melt pool. One major difference between electron beam deposition processes and is that for electron beam the process must be carried out in a vacuum chamber.

1.2.8 Selective Laser Sintering

Selective Laser Sintering is a process by which a carbon dioxide or Nd:YAG laser is used to bind together defined areas of pre-placed powders. The first patent applicable to the

system of SLS was filed in 1977 by private inventor called Ross Housholder [47], and the process was later commercialised from experimental work carried out at the University of Texas in the mid 1980s by Desk Top Manufacturing (DTM) Corp. A roller or scraper is used to deposit a thin layer of powder over a piston, and then a laser (or electron beam) is used to scan over defined areas, sintering or fusing the powder together. The piston is then lowered and a new layer of powder deposited to allow the generation of successive layers. An advantage of this process is that overhanging structures can be built, as the unsintered powder acts as a support layer. Any powder capable of being melted can be used in this process and multimode powders can be used to allow high densities to be achieved. Commercial systems are available including the DTM Sinterstation and the EOSINT.

Though this process may not be of use in the production of sensor layers directly onto parts for the UAV, it may still be useful in the deposition of sensor layers onto transparent substrates for subsequent transfer to CFC laminates. Work has been carried out using SLS in conjunction with gelcasting to produce complex piezoelectric parts from lead zirconate titanate (PZT)[48].

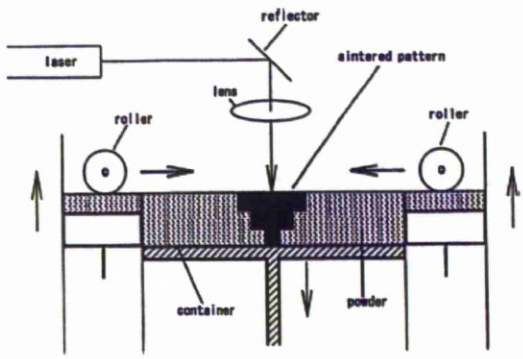

Figure1.12: Schematic of the Selective Laser Sintering process [49].

1.2.9 Laser Guided Direct Write (LGDW) and Flow Guided Direct Write (FGDW)

LGDW and FGDW are both laser based deposition techniques for liquids and colloidal materials and can be deposited and processed on most substrates, with no special

atmospheric requirements. The liquid or colloidal suspension is fed into an atomiser which turns the liquid into an aerosol. The aerosol containing the particles is then fed into the laser beam and is either flow guided or laser guided depending on the technique. Stream of particles is then focussed by the hydrodynamic and optical forces into a narrow beam. The laser guided system focuses the aerosol through momentum transfer in a similar mechanism to that of optical tweezers. This is fed into a hollow optical fibre, similar to that used for the propagation of mid-infrared laser systems, to help maintain the narrow focussed beam. The substrate is then placed beneath the optical fibre. In this manner the particles can be guided through the fibre over a distance of several centimetres and the rate of particle deposition can be changed from 1 – 10000/s [17]. Using this method it is also possible to bundle several fibres together to get simultaneous material deposition. This may be advantageous if a higher deposition rate is required or multiple material types are desired at the same time.

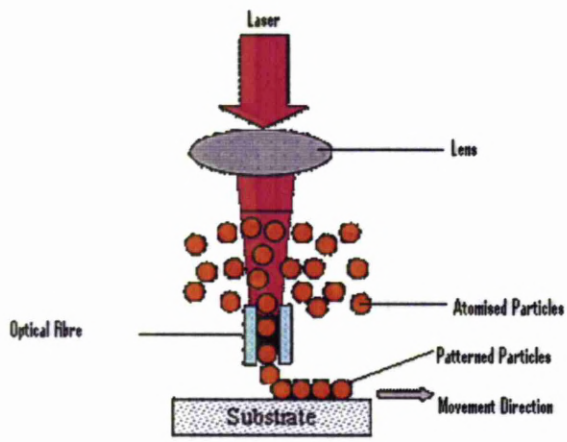

Figure 1.13: Diagram of LGDW [38]

Another way of increasing deposition rate is to use FGDW, where the particles involved are accelerated from ~1 cm/s to 10 m/s by utilising an aerosol assist method. Here the atomised particles are fed into a sealed chamber that is transparent to the laser beam with a millimetre sized orifice in the direction of the substrate. The particles are forced through the orifice and enter into the centre or core of an aerosol assist gas, which surrounds the stream in the form of a cylindrical sheath. This combined stream is then forced through another orifice that is of the order of sub-millimetres and is focussed down to the desired width. The stream can travel several millimetres without any significant divergence due to

the focussing effect of the assist gas. The assist gas controls the width of the particle stream, whilst the rate of atomisation of the liquid or colloidal suspension determines the mass flow rate.

With optimum parameter settings it is possible to create line widths as small as 1 μm. Normally however line widths are greater than that due to several factors. Factors include particle size, viscosity, mass flow rate, beam width and laser power. After deposition, the material usually needs to be consolidated in some way to get the desired physical and/or electrical properties. This can be done either chemically or thermally or with the laser that is being used to deposit the material. For electronic applications, several metallic precursors have been developed based on simple organic or inorganic salts that are easily atomised that when suitably treated reduce down to the composite material. Successful examples include Pt, Au, Cu, Ag and Pd, with quoted resistivities 2.4 $x10^{-8}$ Ωm on Teflon and 3.1 $x10^{-8}$ Ωm on glass [17]. Alloys have also been deposited and have been shown to demonstrate thermocouple like behaviour [17].

1.3 Non-Laser DW Technologies

1.3.1 Syringe or Nozzle based Technologies

nScrypt is one of the main manufacturers of syringe based DW machines. They are generally filamentary based, Figure 1.14, though it is possible to deposit drops of ~75μm in diameter generally on a larger scale than that of other techniques such as inkjet, nano litres rather than pico litres [50]. The advantage of syringe deposition is the ability to conformally deposit a desired ink over a surface and it`s capability of depositing a wider range of materials than that of ink jet with a greater range of visocosities. Flow-based DW requires high precision micro-dispensing technology which could be in the form of a precision pneumatic pump as is with the case of nScrypt or an extrusion process that is used in MicroPen deposition. The material is delivered is through a very small orifice or a needle restricting the size of the particles that can populate a composite ink. In practice for syringe deposition the particles are of the order tens of microns as a maximum and recently more common inks employ nano particulates. This kind of DW system is able to cope with materials over a wide range of viscosities from 0.5 to 1,000,000 cps. Unlike inkjet where the

ink is discretized as individual droplets, the delivery of material for flow-based DW is continuous.

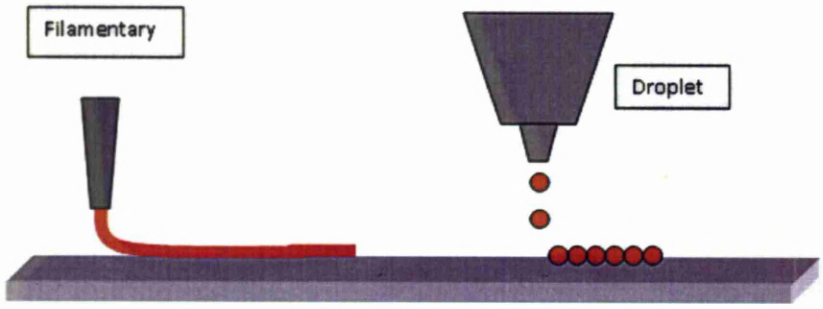

Figure1.14: Illustration of the difference between syringe deposition (filamentary) and droplet (ink jet).

Common components that are fabricated using this type of technology include conductive lines, resistors, antenna, and 3D polymeric structures, figure 1.15, [50]. Line widths down to 25μm have been demonstrated and recent systems can include a laser for curing and/or machining of the deposited part. In general post curing in an oven is required.

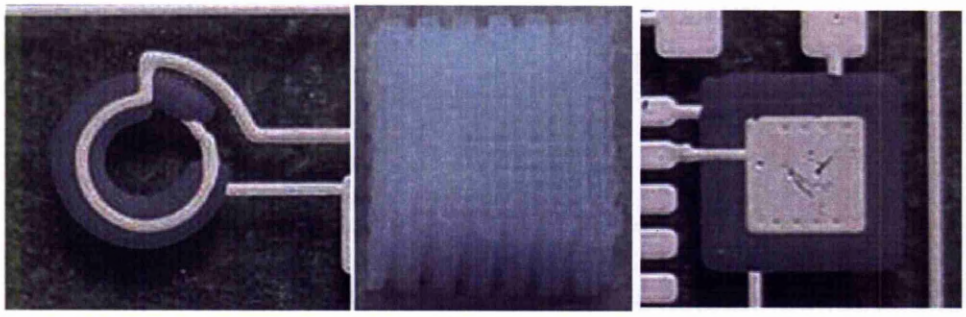

Figure 1.15: The right image is of passive circuitry, the middle is a 3D scaffold, and the right image is an RF bypass capacitor [50].

Apart from nScrypyt another technique using syringe based deposition is the Micropen technique as developed by OhmCraft. In the same way as nScrypt it can be fully automated using a computer controlled gantry system and the components drawn out form a CAD file. The force applied to the tip of the deposition system is via screw feed, allowing for consistent very accurate volume pumping and has a force feedback system from the pen tip allowing for conformal deposition. However it is a contact process and so if multiple layers are desired, the underlying material needs to be cured first.

1.3.2 Ink jet Technologies

Inkjet technologies for the deposition of sensors have evolved from printing technologies and can create multilayer systems by the deposition of inks containing colloids, nanoparticles or organic compounds (including viable cells). Inkjet technologies can be separated into two broad classes based on how the ink is delivered, whether it is delivered in a continuous stream (filamentary approach) or in a series of discrete droplets (the more common technique). As can be surmised, one of the most important considerations is the properties of the ink itself, which must have the required viscosity, shear stress and viscoelastic properties for the relevant process – especially in the case of self-supporting structures. An extra consideration when printing on hard (i.e. non-absorbent) surfaces is that the drying of the ink relies entirely on solvent evaporation, however, the emergence of UV-curable inks has obviated this problem to an extent.

Discrete droplet systems rely upon low-dilution (<5% solids by volume), low-viscosity inks (typically 2cp but can be up to 100cp) which will form consistent droplet sizes [51]. A feature of these low-viscosity inks is their propensity to spread on contact with the substrate, forming tracks with a very high ratio of height to width. Filamentary systems can utilise inks with much higher concentrations of solute and higher viscoelastic properties, allowing the generation of high-aspect ratio 3-D structures. This is because they do not require the formation of a drop to occur which is dependent on the surface tension and viscosity of the fluid, and so can tolerate a larger range of ink properties compared to drop on demand. Drop on demand has very specific property requirements as the viscoelastic nature of the fluid determines the snap off of the ligament that is formed during drop formation. This ligament needs to break away from the droplet and re-coalesce in to the nozzle so that satellite droplets are not formed.

Metallic paths can be printed by using a metal precursor which can be subsequently treated to convert it to the pure metal. Silver and copper electrodes have been printed using this technique. Ceramics can also be inkjet printed, either directly with particles in solution (to be subsequently sintered) or by printing a binder on pre-placed ceramic particles. The latter method is more commonly used to make ceramic moulds for casting.

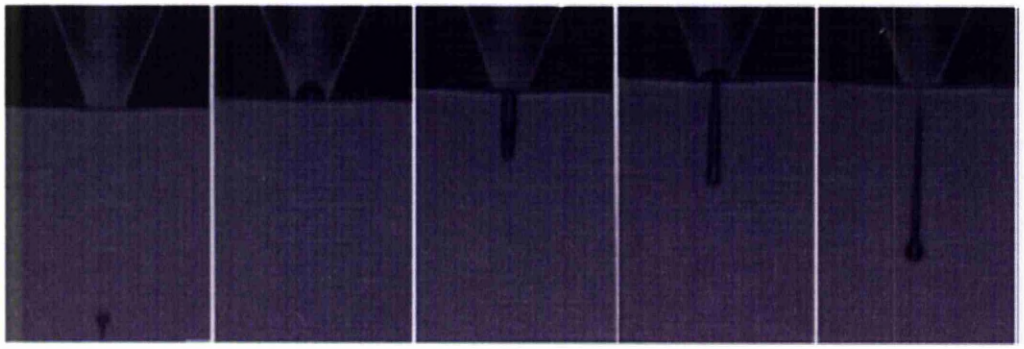

Figure 1.16: Sequential photograph of a inkjet nozzle jetting, using drop on demand technique. Generating 60μm droplets at 2kHz. Image set spans 130μs [52]

In general for the fabrication of electrical components the inkjet heads use a piezoelectric orifice that squeezes or jets the ink out. A discrete droplet is formed in this manner. Another technique is to thermally heat the ink (no piezoelectric orifice) creating a bubble at the end. This bubble then bursts in a controlled manner and is directed towards the substrate. Thermal ink jet printing has been superseded by piezoelectric ink jets due to the inability of thermal inkjet heads to deposit volatile solvents placing limitations upon the types of materials that they are able to deposit.

In general inkjet printing can create very high aspect ratio lines, with drop sizes on the substrate about 80μm across with a 30μm diameter orifice and tens of nanometres thick. Several overlaps are required to create a solid line and though speeds of 500mm/s have been achieved. Another benefit of inkjet printing is the use of multiple heads on anyone system to increase deposition rates with hundreds of nozzles jetting at any one time. Inkjet is generally limited to flat substrates or feature or 2D patterning on 3D substrates due to the nature of the inkjet head. Another limitation is the requirement of a bitmap for the deposition process. Patterning abnormalities can arise when converting a DXF file to bitmap and so care needs to be taken when converting files. This can be overcome using the appropriate software and so is only a minor limitation. This technique has been used for the fabrication of flexible electronics [53], organic transistors [54], deposition of TCO`s (transparent conductive oxides) and ceramics [55-57], OLED`s (organic LED`s) [51], and for soldering droplets [51].

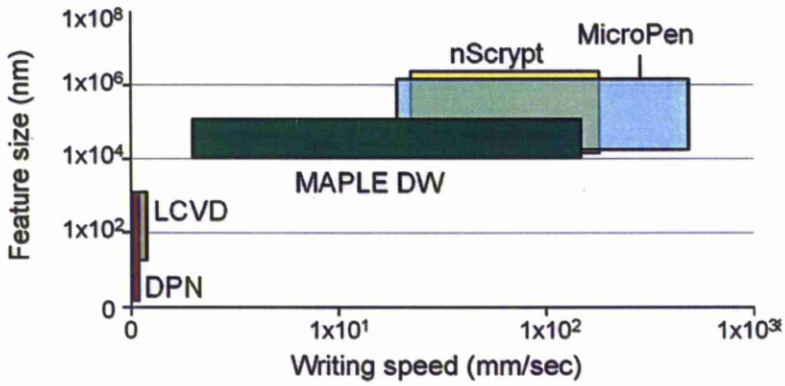

Figure 1.17: Representative DW technology capabilities [18].

Inkjet has also been successfully used to create coplanar waveguides (CPW) in the microwave frequency [58], photovoltaics [59-61], micro fluidic devices [62], and metallic lines and crossovers [63].

Figure 1.18: On the left is an optical image of CPW [58], the middle picture is a micro fluidic device [62], and the right image is of a dielectric and silver conductive track [63].

1.3.3 Screen Printing

Screen printing of films with required electrical properties is an outgrowth of the printing techniques used commercially for cloth and paper. The basic process is to use a mesh screen (originally silk), parts of which are treated to make it impermeable to an ink. This screen is then placed over the part to be printed and ink drawn across it. The ink passes through the permeable parts of the screen and is thus deposited on the substrate. This method has been in use to produce thick conductive films and circuits since the 1960's [64]. Today the use of conductive inks and colloidal suspensions allows the deposition of electrical components including piezoelectric ceramics [65], metals, semiconductors and the generation of batteries [66]. Though the thickness of screen printed layers can be controlled to a couple of microns, the width of deposited features is only accurate to a resolution of approx 100 microns and may need to be post-processed by laser machining or photoresist methods.

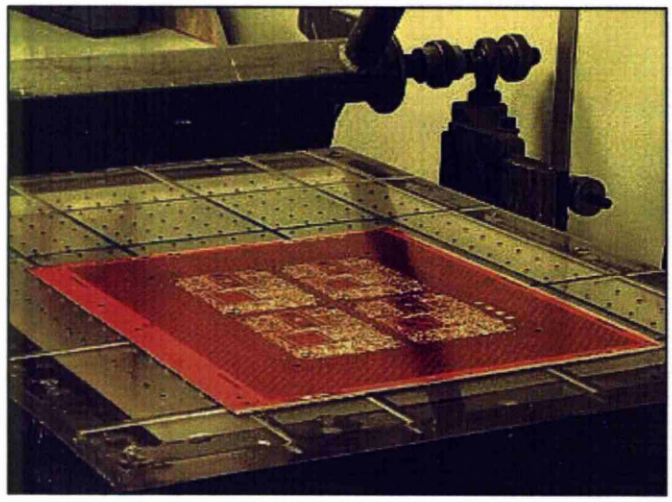

Figure 1.19: A fast set-up manual screen printer used for making printed circuit boards [65].

Screen printing is a very fast way of producing large batches of similar items on flat thin substrates. It is limited by the mesh that is used and any new design requires a new mesh to be fabricated, making it unsuitable for small batch runs. The component once deposited will also require some form of post treatment to functionalise the ink that was deposited. It is also a wasteful process in that the whole mesh needs to be sufficiently flooded for the ink to permeate through it, meaning more ink is required to make a component then what is actually used. The ink used to flood the mesh cannot be used subsequently due to possibilities of contamination. It is analogous to doctor blading in terms of the process.

1.3.4 Maskless Mesoscale Materials Deposition

M^3D, or Maskless Mesoscale Materials Deposition is a droplet deposition system developed by Optomec Corporation of Alberquerque (Optomec is more well known for Laser Engineered Net Shaping (LENS)).Within the M3D system, a liquid or colloidal suspension is atomised and the resultant aerosol mist is directed at the substrate surface through a focusing nozzle which utilises a gas sheath to collimate the aerosol stream. Either the substrate or the nozzle can be moved to generate the desired pattern and the resultant deposit can be cured by using a low power visible laser or oven. Deposition rates are up to 100mm/s and deposited paths can be less than 10 microns in width, though path widths of 25 micron are more commonly quoted. The M^3D system has been tested with a variety of materials including metals, ceramics, polymers and organic cells and also incorporates the

ability to use the curing laser in post-deposition machining of the deposited feature as required. Unlike the MAPLE-DW and related systems, the nozzle has a fairly large (~5mm) standoff from the substrate and therefore can be used to write tracks over uneven surfaces or for the generation of 'vias' between layers. M3D has been used to produce high-resolution organic thin film transistors (TFTs), light emitting diodes and high density interconnect backplanes on flexible low-temperature substrates [67].

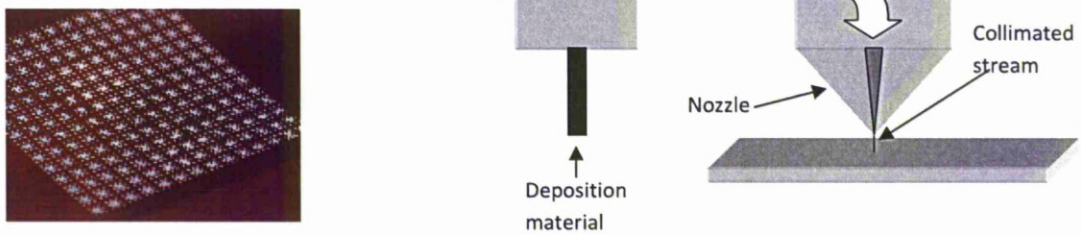

Figure 1.20: The left image shows a Ruthinate resistor and the right image is a schematic diagram of the M^3D setup[68].

Writing speeds up to 200mm/s with a single nozzle have been quoted [68]. Aerosols DW has been used in a wide range of applications including the microelectronics industry for conformal interconnects, fabrication of ceramic components, resistors, inductor coils (figure 1.21), flat panel displays. There is further investigation in to the process being used for biological applications and solar cell printing [69].

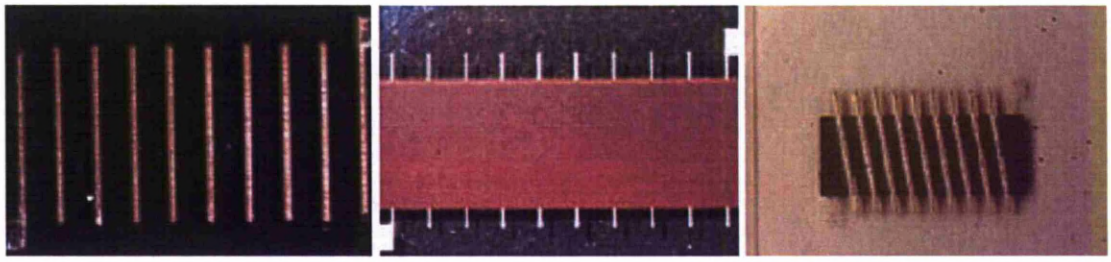

Figure 1.21: various stages of Inductor fabrication using M^3D [68].

1.3.5 Direct Write Thermal Spray

Thermal spray is a process which melts wire, rod or powder feedstock using a flame or plasma arc to produce molten droplets which are then accelerated onto a substrate to form a coating which has been demonstrated to be capable of resolutions of the order of 50 microns thick with minimum 150 micron line widths. It can be used to deposit metallic, polymeric or ceramic materials and is currently being investigated for the DARPA Mesoscale Integrated Conformal Electronics (MICE) project by researchers at the State University of New York. SUNY researchers have built several sensors using this technology including humidity sensors [70], strain gauges, thermocouples and thermistors on both flat and curved surfaces [71]. The thermally sprayed films can be laser machined to required tolerances [72] due to the difficulty in achieving line widths of less than 500 microns for direct spray [73] or 200 microns for masked spray techniques [74].

This technology can be used on a wide variety of surfaces and has minimal heat input into the substrate due to the small size of the droplets and their subsequent quenching by the bulk material. It is capable of high throughput and high speed writing with deposited materials being used functional as deposited or requiring a post treatment such as thermal or UV cure. Another advantage is that it can be fully automated and used in conjunction with robotics increasing the areas in which it can be used, also meaning that it is good for small batch quantities and rapid prototyping.

1.3.6 Cold Gas Deposition

Cold gas deposition is an emerging technology whereby particles are accelerated within a supersonic gas stream (typically helium) to impact upon a substrate. Upon impact, their high kinetic energy results in deformation of the particle and bonding with the substrate. This process has been demonstrated for ductile materials including aluminium [75] and other metals [76] and to a lesser extent with WC-Co cermets[42] and has the potential to deposit metallic paths on substrates with no heat input and therefore no associated thermal damage to the substrate but has concentrated upon high deposition rates rather than fine accuracy. The process may produce residual stresses within the deposited material but has oxygen concentrations similar to that of the original powder. Due to the fact that it is not a melting process, reactions between dissimilar materials do not occur

and mixed powders can be sprayed to undergo controlled reaction later by heating processes. It is not apparent in the literature whether it has been possible to produce the thin films required as a prerequisite of thin film sensor generation.

Thermal spray is a process which melts wire, rod or powder feedstock using a flame or plasma arc to produce molten droplets which are then accelerated onto a substrate to form a coating which has been demonstrated to be capable of resolutions of the order of 50 microns thick with minimum 150 micron line widths. It can be used to deposit metallic, polymeric or ceramic materials and is currently being investigated for the DARPA Mesoscale Integrated Conformal Electronics (MICE) project by researchers at the State University of New York. SUNY researchers have built several sensors using this technology including humidity sensors [70], strain gauges, thermocouples and thermistors on both flat and curved surfaces [71]. The thermally sprayed films can be laser machined to required tolerances [72] due to the difficulty in achieving line widths of less than 500 microns for direct spray [70] or 200 microns for masked spray techniques [73].

This technology can be used on a wide variety of surfaces and has minimal heat input into the substrate due to the small size of the droplets and their subsequent quenching by the bulk material.

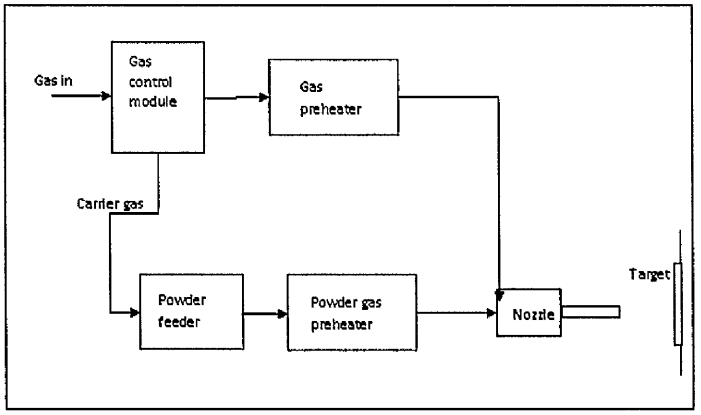

Figure 1.22: A schematic of the cold gas process

1.3.7 Sol Gel

The sol-gel process used for making ceramic and glass materials involving a change from a typically colloidal liquid solution "sol" to a solid "gel" phase. Using this method, it is possible to make ultra-fine or spherical shaped powders, thin film coatings, ceramic fibers, microporous inorganic membranes, monolithic ceramics and glasses, or extremely porous aerogel materials. Inorganic or organic metal compounds are made into a colloidal solution which is then spread over a surface to produce thin films or put into a mould to form a gel. Drying or evaporation then results in a dense ceramic in the required form. If the liquid in a wet "gel" is removed, a porous, low density material is formed ("aerogel"). Altering the viscosity of a "sol" allows ceramic fibers to be drawn from the "sol". Ultra-fine and uniform ceramic powders are formed by precipitation, spray pyrolysis, or emulsion techniques. In addition to chemical and biosensors, thin film sensors of interest that have been produced in this manner include strain sensors and actuators from PZT [72] in addition to trace moisture sensors made from alumina [70].

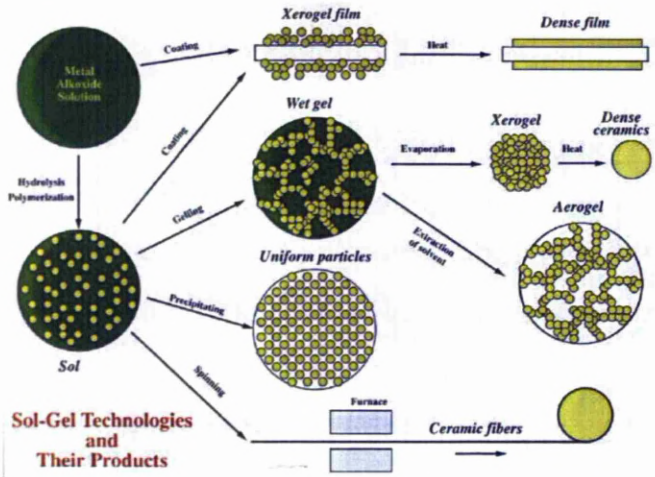

Figure 1.23: A flow diagram of the Sol Gel process [77].

1.4 Materials Used in DW

In DW as with any manufacturing process, the quality of the materials used is paramount when producing high cost, high quality components. The form that the starting material will take, very much depends on what process is being used to fabricate a certain

component. In general, the starting point is a slurry or paste for syringe/MicroPen or screen printing techniques, a sacrificial solid layer for PLD, a complex organic matrix for MAPLE (-DW), solvent or aerosol as those used for M^3D or colloidal suspension as used in many different processes. Some techniques are better able then others for depositing a wider range of materials. The LIFT and MAPLE processes require the material to be prepared in a very specific way prior to deposition and in the case of the LIFT process, wavelength sensitive substrates are required. Inorganic, semiconductor and ceramic materials are primarily deposited using these techniques. Organic materials are not so suitable due to the explosive nature of the process. The syringe deposition process is rather more versatile, with the ability to deal with materials that have a wide range of physical properties with the main limiting factor being particle size. Screen printing is similar in this fashion, but with the desire to get to smaller and smaller feature sizes, the particles making up any ink or slurry are heading towards nano sizes. Inkjet is also capable of printing a wide range of materials due to its simple premise of liquid being forced out of an orifice. Materials for inkjet deposition include metals, ceramics, polymers and living cells. The deposition of ceramics and metals is usually via a carrier system where the desired material is held either in suspension or as a colloid and requires post treatment for fictionalisation. The main parameter that affects whether a material can be printed via inkjet is the materials viscosity with the requirement that they are generally below 100cps. For M^3D and aerosol based processes a liquid precursor is required that then needs to be atomised creating droplet sizes of around 1-5μm. The atomisation process can be either ultrasonic pneumatic. In either case nano particles in a solvent suspension is the norm.

References

1 Chrisey DB, Grabowski KS, Osofsky MS, *"Pulsed laser deposition of $YBa_2Cu_3O_{7-\delta}$ in an oxygen background and discharge"*. Physica C: Superconductivity, vol. 162-164, Part 1, 1989, pp. 129-130.

2 Hakola A, Heczko O, Jaakkola A, Kajava T, Ullakko K, *"Ni–Mn–Ga films on Si, GaAs and Ni–Mn–Ga single crystals by pulsed laser deposition"*. Applied Surface Science 238, 2004, pp. 155-158.

3 Miller TM, Fang H, Magruder RH III, Weller RA, *"Fabrication of a micro-scale, indium tin oxide thin film strain-sensor by pulsed laser deposition and focussed ion beam machining"*. Sensors and Actuators A: Physical, vol. 104, Issue 2, 2003, pp. 162-170.

4 Kreutz EW, Backes G, Mertin M, *"Large area pulsed laser deposition of ceramic films". Surface and Coatings Technology 97, (1997), pp. 435-441.*

5 *Gottman J, Kreutz EW, "Pulsed laser deposition of alumina and zirconia thin films on polymers and glass as optical protective coatings"*. Surface and Coatings Technology, 116-119 (1999) pp. 1189-1194.

6 Singh U, Jha N, Prakash Singh T, Kapoor A, Perrone A, *"Investigation of transmittance property of palladium thin films fabricated by pulsed laser deposition with polarisation using single layer model"*. Optics and Laser Technology, 42 (7), pp. 1128-1133 (2010).

7 Ju Y-W, Eto H, Inagaki T, Ida S, Ishihara T, *"Preparation of Ni-Fe bimetallic porous anode support for solid oxide fuel cells using LaGaO based electrolyte film with high power density"*. Journal of Power Sources, 195 (19), pp. 6294-6300 (2010).

8 Miller TM, Fang H, Magruder III RH, Weller RA, *"Fabrication of a micro-scale, Indium-Tin-Oxide thin film strain-sensor by pulsed laser deposition and focused ion-beam machining"*. Sensors and Actuators A: Physical, vol. 104, issue 2, 2003, pp. 162-170.

9 Pique A, *"Growth of organic thin films by the matrix-assisted pulsed laser evaporation (MAPLE) technique"*. Thin Solid Films, vol. 355-356, issue 1, 1999, pp. 536-541.

10 Li J, Longtin JP, Tankiewicz S, Gouldstone A, Sampath S, *"Interdigital capacitive strain gauges fabricated by direct write thermal spray and ultrafast laser micromachining"*. Sensors and Actuators A: Physical, vol.133, issue 1, 2007, pp. 1-8.

11 Pique A, Wu P, Ringeisen BR, Bubb DM, Melinger JS, McGill RA, Chrisey DB, *"Processing of functional polymers and organic thin films by the matrix-assisted pulsed laser evaporation (MAPLE) technique"*. Applied Surface Science, vol. 186, 2002, pp. 408-415.

12 Pique A, Auyeung RCY, Stepnowski JL, Weir DW, Arnold CB, McGill RA, Chrisey DB, *"Laser processing of polymer thin films for chemical sensor applications. Surface and Coatings Technology"*, vol. 163-164, 2003, pp. 293-299.

13 Pique A, Auyeung RCY, Stepnowski JL, Weir DW, Arnold CB, McGill RA, Chrisey DB, *"Laser processing of polymer thin films for chemical sensor applications. Surface and Coatings Technology"*, 163-164, pp. 293-299 (2003).

14 Pique A, Auyeung RCY, Lakeou S, Nguyen V, Chung R, Duignan, *"Direct writing of electronic and sensor materials using a laser transfer technique"*. Journal of Material Resources, vol. 15, No. 9 (2000).

15 Chrisey DB, Pique A, Fitz-Gerald J, Auyeung RCY, McGill RA, Wu HD, Duignan M, *"New approach to laser direct writing active and passive mesoscopic circuit elements"*. Applied Surface Science, vol. 153-155, 2000, pp. 593-600.

16 A Pique, Chrisey DB, Auyeung RCY, Fitz-Gerald J, Wu HD, McGill RA, Lakeous S, Wu PK, Nguyen V, Duigan M, *"A novel laser transfer process for direct writing of electronic and sensor materials"*. Applied Physics A: Materials Science and Processing, vol. 69, 1999, pp. S279-S284

17 Pique A, Chrisey DB, *"Direct Write Technologies for Rapid Prototyping Applications"*. Academic Press, San Diego, Calif., USA, 2002.

18 Hon KKB, Li L, Hutchings IM, *"Direct Writing Technology-Advances and developments"*. CIRP Annals, Manufacturing Technology 57 (2008) 601-620.

19 Pique A, Arnold CB, Wartena RC, Pratrap B, Shasshishekar B, Swider-Lyons KE, Weir DW, Kant RA, *"Laser direct write of miniature sensor and microbattery systems"*. Riken Review No. 50 (2003), Focused on Laser Precision Micrfabrication (LPM 2002).

20 Wartena R, Curtright AE, Arnold CB, Pique A, Swider-Lyons KE, *"Lithium-ion microbatteries generated by a laser direct-write method"*. Journal of Power Sources, vol. 126, 2004,pp. 193-202.

21 Kuang Z, Perrie W, Leach J, Sharp M, Edwardson SP, Padgett M, Dearden G, Watkins KG, *"High throughput diffractive multi-beam femtosecond laser*

processing using a spatial light modulator". Applied Surface Science vol. 254, 2008, pp 2284–2289.

22 Chrisey DB, Pique A, Modi R, Wu HD, Auyeung RY, Young HD, "***Direct Writing of conformal mesoscopic electronic devices by MAPLE DW***". Applied Surface Science, vol. 168, 2000, pp. 345-352.

23 Arnold CB, Kim H, Pique A, "***Laser Direct Write of Planar Alkaline Microbatteries***". Applied Physics A: Materials Science and Processing, vol. 79, 2004, pp. 417-420.

24 Pique A, Arnold CB, Pratrap B, Auyeung RCY, Kim H, "***Laser Direct Write of Metal Pattern Interconnects and Antennas***". Photon Processing in Microelectronics and Photonics II, SPIE, vol. 4977, 2003, pp. 602-608.

25 Bohandy J, Kim BF, Adrian FJ, "***Metal deposition form a supported metal film using an excimer laser***". Journal of Applied Physics, vol. 60, 1986, pp.1538-1539.

26 Yamada H, Sano T, Nakayama T, Miyamoto I, "***Optimisation of laser-induced forward transfer process of metal thin films***". Applied Surface Science, vol. 197-198, 2002, pp. 411-415.

27 Zerigioti I, Mailis S, Vainos NA, Papakonstantinou P, Kalpouzos C, Grigoropoulos CP, Fotakis C, "***Microdeposition of metal oxide structures using ultrashort laser pulses***". Applied Physics A: Materials Science and Processing, vol. 66, 1998, pp. 579-582.

28 Baron JA, Wu P, Ladouceur HD, Ringeisen BR, "***Biological Laser Printing: A novel technique for creating Hetrogeneous 3-Dimensional Cell Patterns***". Biomedical Microdevices, vol. 6, 2004, pp. 139-147.

29 Fogarassy E, Fuchs C, Kerherve F, Hauchecorne G, perriere J," ***Laser induced forward transfer: A new approach for the deposition of High T_C super conducting thin films***". Journal of Materials Research, vol. 4, pp.1082-1086.

30 Mashburn DN, Geohegan DB, Eres D, Lowndes DH, Boatner LA, "***Deposition of high T_C superconductor thin films by pulsed laser ablation***". Materials Research Society, 1998, pp. 699-702 "High T_C super conducting thin film deposition by laser induced forward transfer" Mater. Manufac. Process.

31 Fogarassy E, Fuchs C, Kerherve F, Hauchecorne G, Perriere J, "***Laser Induced forward transfer of high T_C YBaCuO and BiSrCaCuO superconducting thin films***". Journal of Applied Physics, vol. 66, 1989, pp. 457-459.

32 Schultze V, Wagner M, *"Laser induced forward transfer of Aluminium"*. Applied Surface Science, vol. 52, issue 4, 1991, pp. 303-309.

33 Toth Z, Szorenyi, Toth AL, *"Ar^{+} laser induced forward transfer (LIFT): A novel method for micrometre size surface patterning"*. Applied Surface Science, vol. 69, issue 1-4, 1993, pp. 317-320.

34 Chrisey DB, pique A, McGill RA, Horwitz JS, Ringeisen BR, *"Laser deposition of polymer and biomaterial films"*. Chemical reviews, vol. 103, 2003, pp. 553-576

35 Pique A, Arnold CB, Kim H, Ollinger M, Sutto TE, *"Rapid Prototyping of micropower sources by laser direct write"*. Applied Physics A: Materials Science and Processing, vol. 79, pp. 783-786.

36 Chrisey DB, Pique A, Modi R, Wu HD, Auyeung RY, Young HD, *"Direct Writing of conformal mesoscopic electronic devices by MAPLE DW"*. Applied Surface Science, vol. 168, 2000, pp. 345-352.

37 Forsen E, Carlberg P, Montelius L, Boisen A, *"Laser lithography on resist bi-layer for nanoelectromechanical systems prototyping"*. Microelectronic Engineering, vol. 73-74, 2004, pp. 491-495.

38 Karam NH, Liu H, Yoshida I, Jiang BL, Bedair SM, *"Low temperature selective epitaxy of III–V compounds by laser assisted chemical vapor deposition"*. Journal of crystal growth, vol. 93, issues 1-4, 1988, pp.254-258.

39 Liu H, Roberts JC, Ramdani J, Bedair SM, Farari J, Vilcot JP, Decoster D, *"A new approach for the integration of optoelectronic devices using laser selective area epitaxy"*. Journal of Crystal Growth, vol. 107, issues 1-4, 1991, pp. 878-882.

40 Moilanen H, Leppávuori S, Uusimaki A, *"Laser-induced chemical vapour deposition in piezoresistive pressure sensor fabrication"*. Sensors and Actuators A: Physical, vol. 41, issues 1-3, 1994, pp. 150-155.

41 Metzger D, Reichl H, *"Laser direct writing of gold to repair defective lines in thin-film metallizations"*. Applied Surface Science, vol. 8, 1993, pp. 69-74.

42 Pou J, Gonzalez P, Garcia E, Fernandez D, Serra J, Leon B, *"Ceramic coating for high-temperature corrosion protection by laser-CVD processes"*. Applied Surface Science, vol. 79-80, 1994, pp. 338-343.

43 Murphy M, Lee C, Steen WM, *"Studies in Rapid Prototyping by Laser Surface Cladding"*. Proceedings of International Congress on Applications of Lasers and Electro-Optics (ICALEO), 1993, Laser Institute of America, vol. 77, pp. 882-891.

44 Choi J, Sundaram R, *"A process planning for 5-axis laser-aided DMD process"*. Proceedings of International Conference on Metal Powder Deposition for Rapid Manufacturing, San Antonio, 2002, pp. 112-120.

45 McLean M, Shannon G, Steen WM, *"Laser Direct Casting High Nickel Alloy Components"*. PM^{2}TEC conference, Chicago, 1997, Advances in Powder Metallurgy and Particulate Materials, pp. 3-17.

46 E Fearon, *"Laser Free Form Fabrication applied to the manufacture of metallic components"*. PhD thesis, University of Liverpool, 2003.

47 R Housholder, *"Moulding process"*, US patent application 4247508 filed Dec 3, 1979

48 Guo D, Cai K, Nan C, Li L, Gui ZI, *"Gelcasting based solid freeform fabrication of piezoelectric ceramic objects"*. Scripta Materialia, vol. 47, issue 6, 2002, pp. 383-387.

49 Kathuria YP, *"Microstructuring by selective laser sintering of metallic powder"*. Surface and Coatings Technology, 116/119, 1999, pp. 643-647.

50 Li B, Church KH, Active mixing and depositing/patterning of materials, nScrypt presentation.

51 Calvert P, *"Inkjet printing for materials and devices"*, Chemical Materials, vol. 13, 2001, pp. 3299-3305.

52 Shah VG, Hayes DJ, Wallace DB, *"Inkjet as direct write technology for fuel cell packaging and manufacturing"*, Microfab Technology Inc.

53 Seung HK, Pan H, Grigoropoulos CP, Luscombe CK, Frechet JMJ, Poulikakos D, *"All inkjet printed flexible electronics fabrication on a polymer substrate by low temperature high resolution selective laser sintering of metal nanoparticles"*. Nanotehnology 18 (2007) 345202.

54 Seung HK, Pan H, Grigoropoulos CP, Luscombe CK, Frechet JMJ, Poulikakos D, *"All stable high resolution organic transistors by selective laser sintering of inkjet printed metal nanoparticles"*. Appl. Phys. Lets., 90 141103 (2007).

55 Song JH, Edirisinghe MJ, Evans JRG, *"Formulation and multilayer jet printing of ceramic inks"*. J. Am. Ceram Soc., 82 (12) 3374-80 (1999).

56 Seerden KAM, Reis N, Evans JRG, Grant PS, Halloran JW, Derby B, *"Inkjet printing of wax based alumina suspensions"*. Journal of American Ceramic Society, 84 (11) 2514-20 (2001).

57 Lewis JA, *"Direct write assembly of ceramics from colloidal inks"*. Current Opinion in Solid State and Materials Science, 6 (2002) 245-250.

58 Azucena O, Kubby J, Scarbrough D, Goldsmith C, *"Inkjet printing of passive microwave circuitry"*. IEEE 978-1-4244-1780 (2008), pp. 1075-1078.

59 Fthenakis V, *"Sustainability of photovoltaics: The case for thin film solar cells"*. Renewable and Sustainable Energy Reviews, 13 (2009), pp. 2746-2750.

60 Microfab, Photonics Bulletin, p. 7, November 2003.

61 Irvine SJC, BArrioz V, Stafford A, Durose K, *"Materials issues in very thin film CdTe for photovoltaics"*. Thin Solid Films, 480-481 (2005), 76-81.

62 Noia B, *"Fabrication of a polymeric microfluidic device with inkjet printed silver electrodesfor electrokinetic bioparticle characterisation"*. Biological Applications, national Nanostructure Infrastructure Technology, REU Research Accomplishments (2007).

63 Sanchez-Romaguera V, Madec BM, Yeates SG, *"Inkjet printing of 3D metal-insulator-metal crossovers"*. Reactive and Functional Polymers 68 (2008), pp. 1052-1058.

64 R G Finch, *"Thick film materials"*. Thin Solid Films, vol. 3 issue 3, 1969, pp. 189-199.

65 Yao K, He X, Xu Y, Chen M, *"Screen-printed piezoelectric ceramic thick films with sintering additives introduced through a liquid-phase approach"*. Sensors and Actuators A, vol. 118, 2005, pp. 342-348.

66 Do JS, Yu SH, Cheng SF, *"Thick-film nickel–metal-hydride battery based on porous ceramic substrates"*. Journal of Power Sources, vol. 117, 2003, pp. 203-211.

67 B King, *"Maskless Mesoscale Materials Deposition"* Article, EP & P magazine February 2003

68 Carter M, Amundson T, Colvin J, Sears J, *"Characterisation of soft magnetic nano material deposited with M^3D technology"*. J. Mater. Sci., (2007) 42, 1828-1832.

69 Horteis M, Mette A, Richter PL, Fidorra F, Glunz SW, *"Further progress in metal aerosol jet printing for front side metallisation of silicon solar cells"*. Proc. 22nd European Photovoltaic Solar Energy Conference (2007).

70 Ahn K, Wessels BW, *"Spinel humidity sensors prepared by thermal spray direct writing"*. Sensors and Actuators B-Chemical, vol. 107, issue 1, 2005, pp. 342-346.

71 Longtin J, Sampath S, Tankiewicz S, Gambino RJ, Greenlaw RJ, *"Sensors for harsh environments by direct-write thermal spray"*. Sensors Journal IEEE, vol. 4, issue 1, 2004, pp. 118-121.

72 Tong T, Li J, chen Q, longtin JP, Tankiewicz S, Sampath S, *"Ultrafast laser micromachining of thermal sprayed coatings for microheaters: design, fabrication and characterization"*. Sensors and Actuators A: Physical, vol. 114, issue 1, 2004, pp. 102-111.

73 Bustillo JM, Howe RT, Muller RS, *"Surface Micromachining for microelectromechanical systems"*. Proceedings IEEE, vol. 86, issue 8, 1998, pp. 1552-1574.

74 Herman H, Sampath S, McCune R, *"Thermal spray: current status and future trends"*. MRS Bulletin, vol. 25, 2000, pp. 17-25.

75 Morgan R, Fox P, Pattison J, Sutcliffe C, O`Neill W, *"Analysis of cold gas dynamically sprayed aluminium deposits"*. Materials Letters, vol. 58, issues 7-8, 2004, pp. 1317-1320.

76 Novoselova T, Fox P, Morgan R, O`Neill W, *"Experimental study of titanium/aluminium deposits produced by cold gas dynamic spray"*. Surface Coating Technology, vol. 200, 2006, pp. 2775-2783.

77 http://sariyusriati.wordpress.com

2 Oven Curing of Polymeric Inks

The following chapter introduces the concept of curing polymeric inks through oven cure. The inks used throughout this investigation are designed for screen printing and once deposited oven curing. The inks are cured by placing in an oven at elevated temperatures for a specified period of time.

2.1 Introduction

The aim of this Chapter is to fully investigate how the polymeric inks behave under different thermal curing regimes. This work concentrates on the conventional method of oven curing. Though there are different techniques available to a manufacturer for curing inks, the inks in this work have specifically been designed to be oven cured. A thorough investigation has been undertaken, to study the effects of thermal changes on ink consolidation and resistivity. Optical and scanning electron microscopy along with interferometry have been used to investigate the physical and visual side of the materials, whilst a four-point probe, designed and built within the Laser Group, specifically for the testing of polymeric inks has been used to investigate the electrical properties.

2.2 Inks Used

The inks used during these experiments were provided by The Gwent Group [5]. Due to IP rights very little is known about the inks. The content is approximately 45 to 55% (wt) silver, 10-40% (wt) solvent which is diethylene glycol butyl ether, $C_4H_9(OCH_2CH_2)_2OH$, it is a clear hydroscopic liquid with a melting point of -68°C and boiling point of 231°C [6], with the remainder being made up by the resin. There are three types of inks being used within this investigation. The solvent is used to reduce the viscosity of the inks so that it can be easily deposited through a screen printer mesh or syringe. The first is the D58 ink: C2050712D58, batch #209.0813.03. The D58 ink is the base of the other two inks and is available off the shelf from Gwent Group, and is a screen printable flexible conductive ink. The second is the D1 ink: C2061130D1, batch #2090220.09, and is the D58 ink but doped with 1% (wt) carbon. The third is the D15 ink: C2070801D15 batch #2090224.11, which also used the D58 ink as a base but contains 1% (wt) graphite powder. The D1 and D15 inks

have been specially developed for this project. The idea behind the dopants was to help increase coupling of the laser in to the inks due to the absorptive nature of the dopants, see section 5.3.1 to see the FTIR analysis (CO_2=943.4 cm^{-1}). An investigation into the inks in chapters 4 and 5 gives some information on what the resin maybe made of using FTIR and TGA/DSC analysis. However an exact chemical composition was outside the scope of this research and was not required.

2.2.1 Ink Constituents

SEM images were taken of the carbon, graphite and silver flakes used within the inks. In Figure 2.1 SEM images can be seen of the three constituents. The carbon powder is spherical in nature and appears to have feature sizes of about 7 μm, whilst the graphite is very much more flake like in that it appears to be very thin and jagged. There is a larger distribution in size with the graphite flakes compared to the carbon particles with feature sizes from a couple of microns to tens of microns. The silver flakes are similar to the graphite flakes in that they are flat and jagged. Also the size distribution is similar as well. For details on the size distribution of the silver please refer to section 5.2.1.1 in the FTIR chapter.

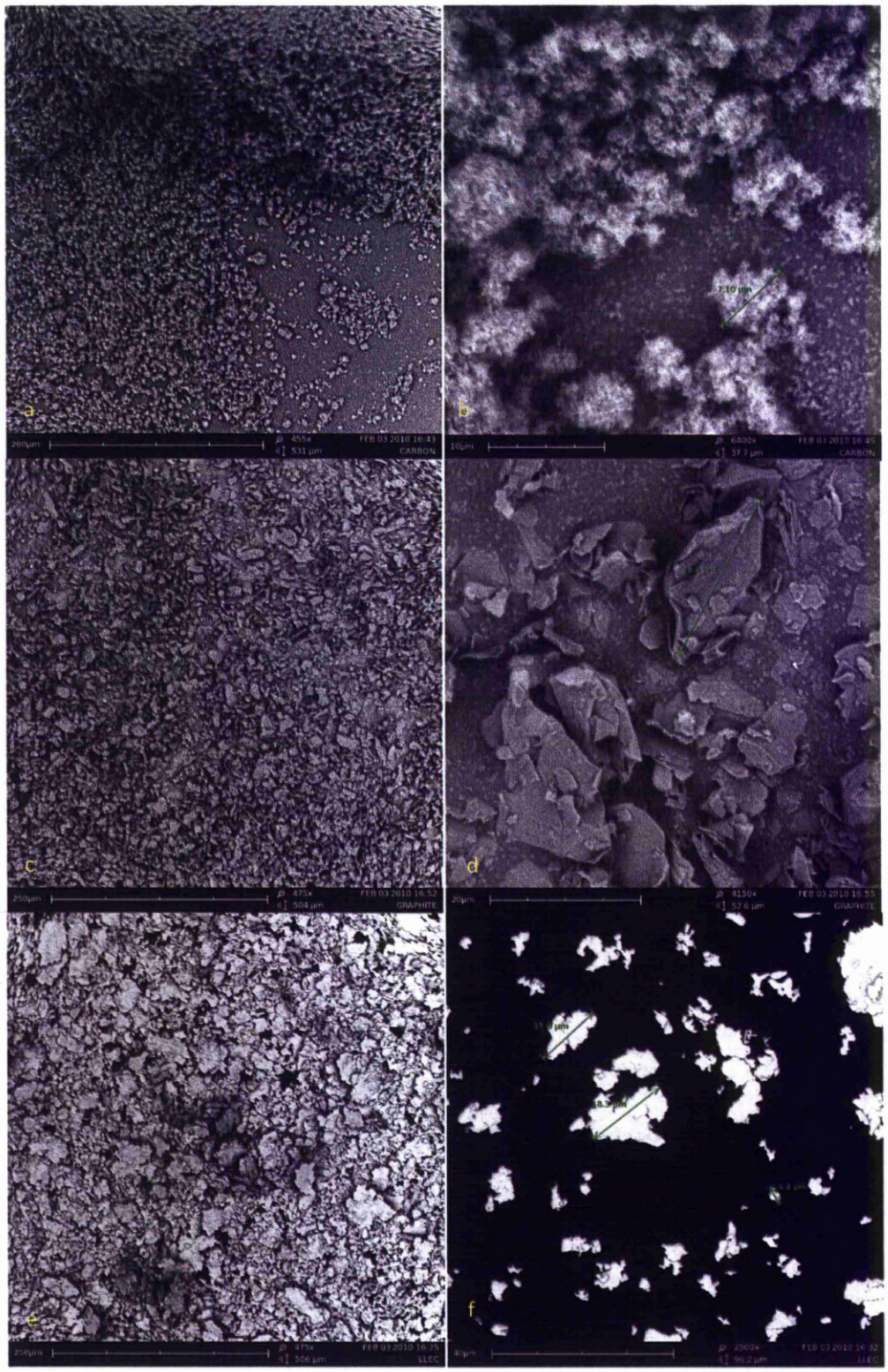

Figure 2.1: Images a-f are SEM images of the constituents that make up the inks. a-b is the carbon powder, c-d is the graphite powder and e-f is the silver flakes used. Carbon is used in D1, graphite in D15 whilst the silver flakes are used in all three inks. Note difference in magnifications between the two adjacent images.

2.3 Equipment Used

The following section details all the equipment used for the following experiments, comprising:

Memmert Oven, Fischer Scientific Hot Plate, Type-K Thermocouples, four point probe, Agilent Data logger, Kehr Scales, deposition stencil, Tamiya modelling tape.

2.3.1 Memmert Oven

For the oven curing trials, a 600W Mememrt oven was used with a maximum operating temperature of 220°C. This oven is specially designed to have thermal stability at a specified temperature from 30°C and at least 5°C above room temperature [1]. Figure 2.2 illustrates the main features of the oven used. The oven relied on convection for even heat treatment, with heating coils on two side walls and on the bottom of the oven.

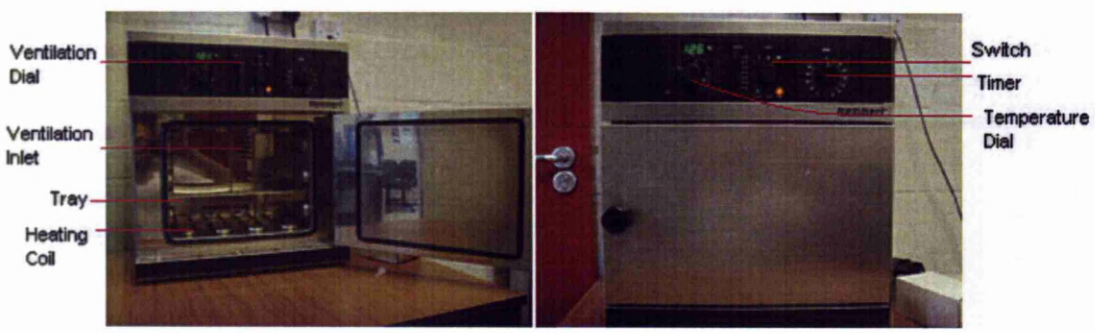

Figure 2.2: Two images of the oven used with the main features labelled. The digital display shows the temperature readout of the oven.

The oven was calibrated using Type-K thermo couples attached (section 2.2.1.3) to a data logger (section 2.2.1.5) at varying temperature intervals between 60°C and 220°C. Figure 2.3, shows the temperature of the oven as measured by the thermocouples when set at a specified temperature. Three thermocouples were placed inside the oven to calibrate it. They were placed in such as manner so that they were not touching each other, but were all as close to the centre of the oven where the samples would be placed during cure. The thermocouples were not touching any of the sides, and so were measuring the temperature of the air only. The desired temperature was set, and once the oven

registered the desired temperature, the thermocouples were placed within the oven and measurements taken for 5 minutes.

Overall the temperature set was close to the temperature registered with the exceptions of the 60°C and 100°C tests. In both cases the average standard deviation as measured by the thermocouples, was high, 3.46°C and 3.33°C respectively. The next highest was the 170°C run with a high of 1.94°C over the whole 5 minutes. The remaining tests all had a deviation lower than 2°C for the whole 5 minutes from the set temperature. This is shown in Figure 2.4. The results indicate, that over the course of the curing process temperature variation does occur, but within reasonable approximations the set temperature can be taken to be the temperature achieved. Consistency is the main issue with regards to temperature, and that is achieved by using this specific oven for each test run.

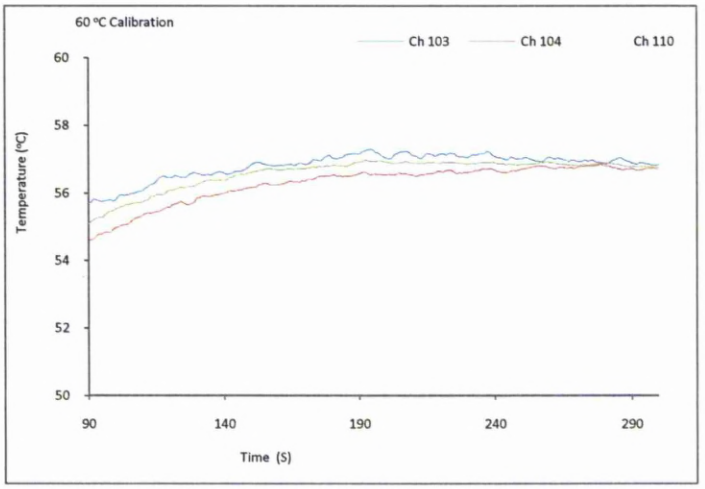

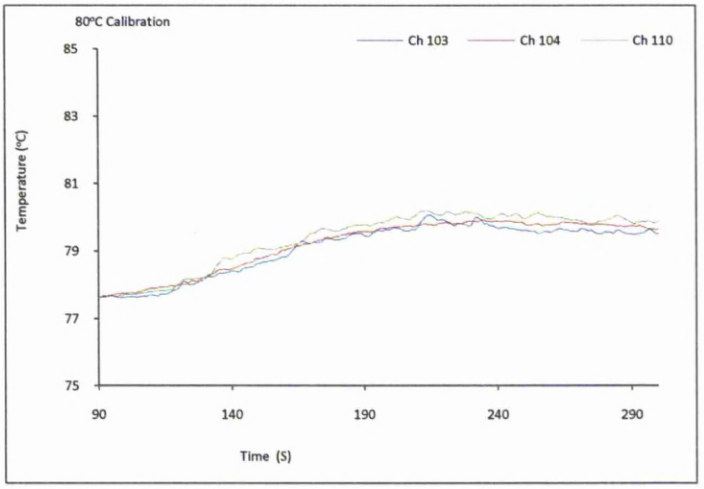

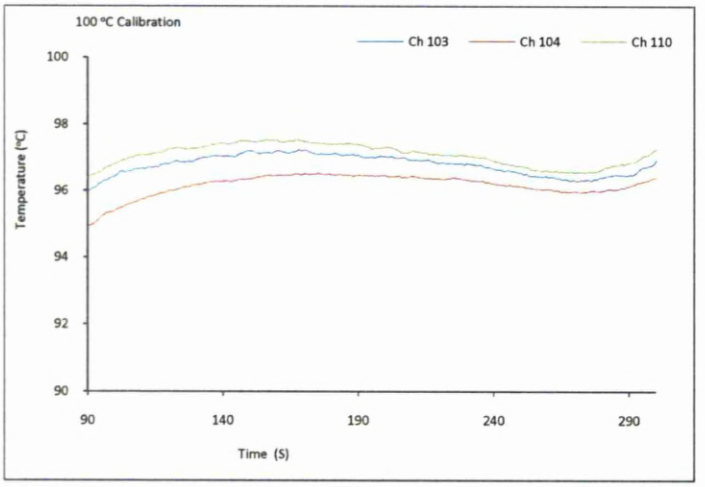
100 °C Calibration
Ch 103
Ch 104
Ch 110
Temperature (°C)
100
98
96
94
92
90
90
140
190
240
290
Time (S)

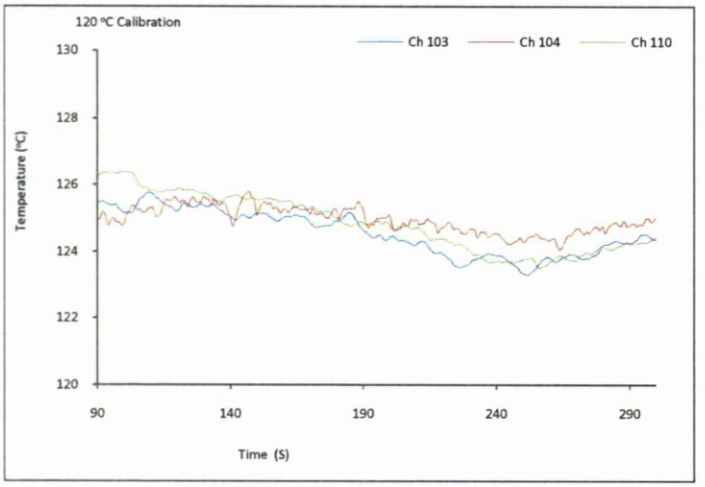
120 °C Calibration
Ch 103
Ch 104
Ch 110
Temperature (°C)
130
128
126
124
122
120
90
140
190
240
290
Time (S)

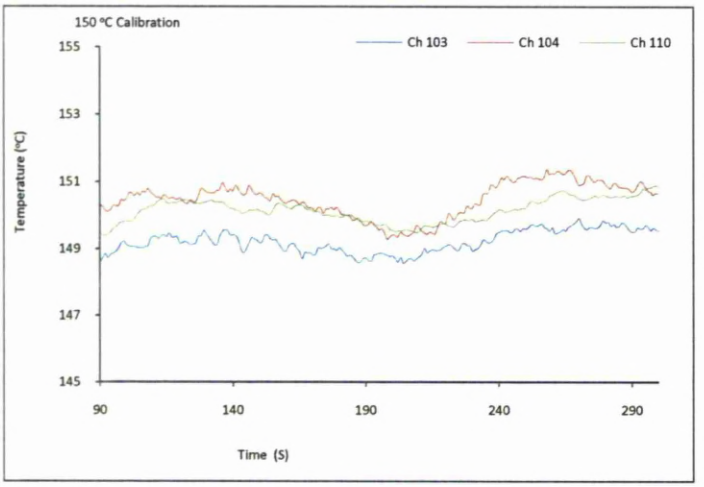
150 °C Calibration
Ch 103
Ch 104
Ch 110
Temperature (°C)
155
153
151
149
147
145
90
140
190
240
290
Time (S)

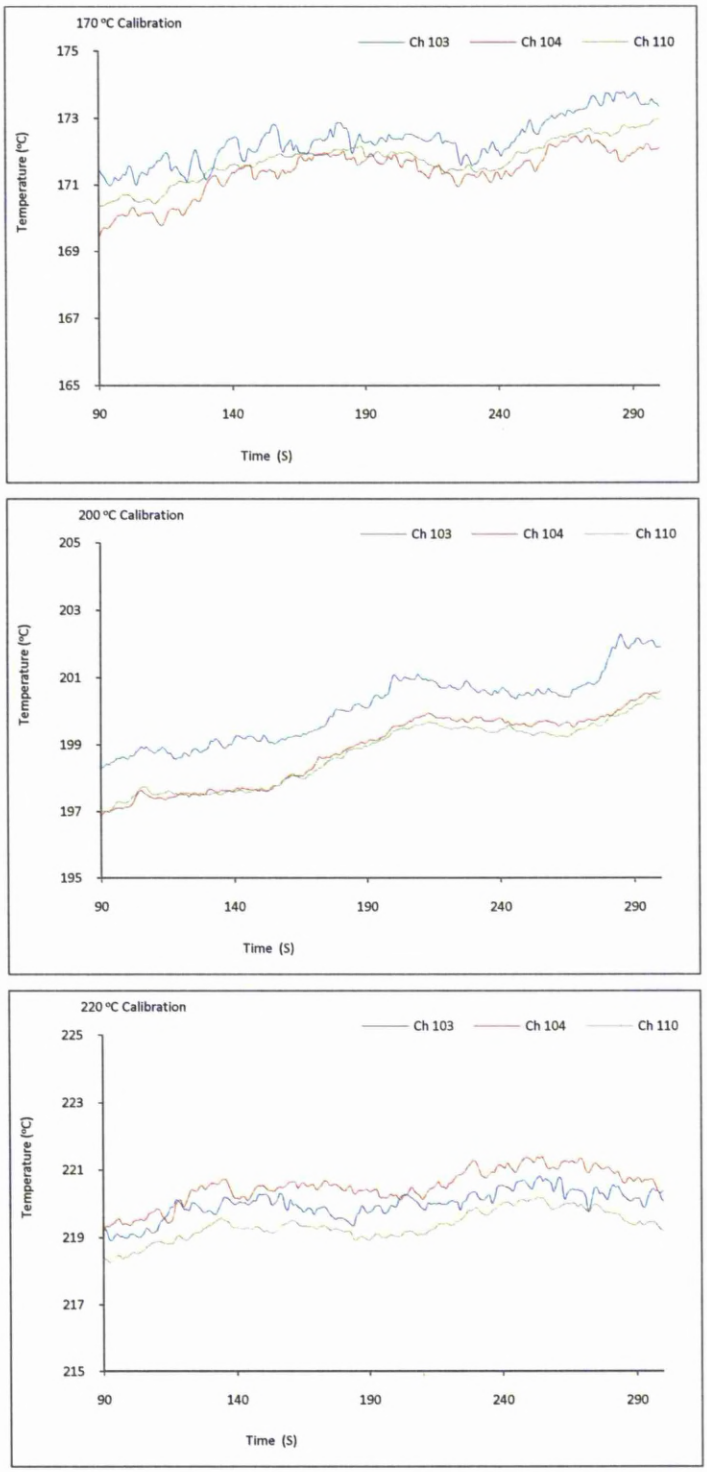

Figure 2.3: Graphs showing the temperature profile of the Memmert oven at set temperature stages: 60, 80, 100, 120, 150, 170, 200 and 220°C. Plots are shown 90 seconds in, once the environment had equilibrated after placement of the thermocouples in to the oven.

Each thermocouple records a slightly different temperature. However this temperature difference has a standard deviation of less than 1°C for all the readings except the 200°C run which has a deviation of 1.19°C over the 5 minute test, as shown in Figure 2.3.

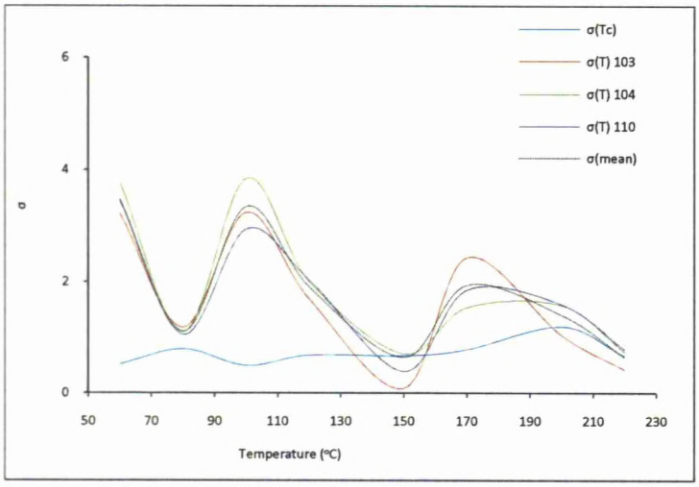

Figure 2.4: The graph illustrates the standard deviation, σ, of the thermocouples during the various temperature cycles. σ(Tc) is the standard deviation with respect to each of the thermocouples, whilst σ(T)103,104 and110 is the standard deviation between the temperature set and the temperature recorded for each thermocouple, and σ(mean) is the average deviation from the temperature.

2.3.2 Hot plate

Due to the nature of the oven and the logistics of carrying out temperature-resistance measurements (the four point probe could not be placed inside the oven), a Fischer Scientific FB15001 hot plate was employed, with a power rating of 630W and a max operating temperature of 370°C [2], to conduct the dynamic temperature Vs resistance curing trials. A picture of the hot plate can be seen in Figure 2.5.

Figure 2.5: Image showing the hot plate used for the dynamic resistance Vs temperature measurements. The hotplate as shown is setup for an experiment with a four point probe and thermocouples in place.

2.3.3 Type-K Thermocouples

To measure the temperature of the sample during specific experiments and to calibrate the oven, type-K thermocouples were employed. These thermocouples were chosen because they are very accurate and have a reliable linear temperature range between 270°C and 1372°C. The theory behind the thermocouple relies upon a voltage drop across two dissimilar metals when they are in contact with each other. The difference in voltage is directly proportional to temperature. The output is only a function of the potential difference between the dissimilar metals and so no further input is required. Therefore the thermocouples are considered to be passive sensors.

The thermocouples used throughout this investigation were welded tip fast response type-K. The junction is made up of nickel-chromium (positive side) and nickel-aluminium (negative side) and was welded in an inert atmosphere to create a small bead at the end of the sensor wire.

2.3.4 Four Point Probe

To measure the resistance of the inks during and after curing a four point probe was used. No suitable commercially available probes were found so a probe was specifically designed for use in the application of testing thick films. The probe was designed in-house and the manufacture was outsourced. The probe was then calibrated against copper tape. An image of the four point probe can be seen in Figure 2.6 above the hot plate.

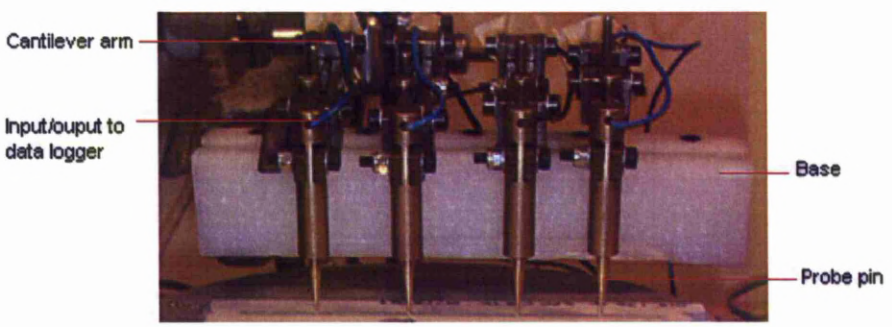

Figure 2.6: An image of the four point probe on a sample (enlarged from Figure 2.5). The wires coming out of each probe pin are leading to the data logger which converts the analogue signal.

A four point probe is an accurate way of measuring the resistance of a sample so long as the contacts are small compared to the sample and that each probe pin applies the same

amount of pressure. The probe was designed so that the pressure applied is the weight of the probe pin itself and the cantilevered arm to which it is attached. This arm moves freely under its own weight. With each arm and probe pin manufactured to the same designs, they each apply the same amount of pressure to sample. The probe pins themselves are 1mm in diameter and with the smallest track width ~2mm, they are sufficiently small to give an accurate reading. The nature of the probe eliminates contact resistance as the resistance is calculated from a relative change in the potential difference between the probe pins when a current is passed through the material, Figure 2.7. The two outer probes pass a known current through the sample whilst the two inner probes measure the potential difference. From this the resistance is then calculated.

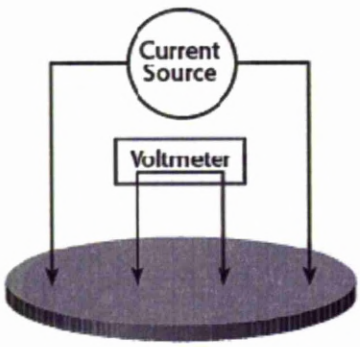

Figure 2.7: Schematic drawing of a four point probe [3].

2.3.5 Agilent Data Logger

When using the four point probe and thermocouples, a data logger is required. For this an Agilent 34970A data logger was used. Channels 102 and 112 were designated for the four point probe, with channel 102 being the output channel, whilst channels 103, 104 and 110 were used for the thermocouples. In this manner, readings of the resistance and temperature in different areas of the sample could be taken simultaneously for any single experiment with a wide range of time intervals.

Figure 2.8: A photo of the Agilent data logger used throughout the experiment in scanning mode.

2.3.6 Kern Scales

The scales used to measure the mass of the samples before and after processing was the Kern 770-60 microbalance. These scales are highly sensitive with micron accuracy, 10μg. It also has a glass incubator in which to place the samples with two sliding side panels and a sliding top. This helps to reduce the effect of any atmospheric changes whilst the sample is inside being weighed and reduces contamination from dust particles or debris within the ambient atmosphere. Figure 2.9 shows two photographs of the microbalance as set up during its use.

Figure 2.9: Picture of the Kern 770-60 microbalance and the user interface.

2.3.7 Substrate Properties

The substrates used during the oven curing trials was commercially available off the shelf aluminium oxide, alumina. The alumina was used due to the consistency of manufacture, high operating temperature +1000°C, its ease of use and relative inexpensiveness. The

alumina used was 96% alumina with dimensions of 114.3 x 114.3 x 0.635 mm^3. It is white and has a density of 3.7 g/cm^3 and a thermal conductivity of 25 W/m/K [4].

2.3.8 WYKO NT1100 Interferometer

The WYKO white light interferometer is an analytical piece of equipment that allows the user to create 3D images of a specimen. The optical profiling system can be used to gain greater in depth information then what can be obtained through conventional optical microscopy. Using the this system resolutions of microns in the X-Y axis and nanometres in the Z axis can be achieved along with information on surface roughness and topology, volumetric analysis, and statistical analysis. An image of the WYKO system used along with a screen shot of the GUI can be seen in Figure 2.10.

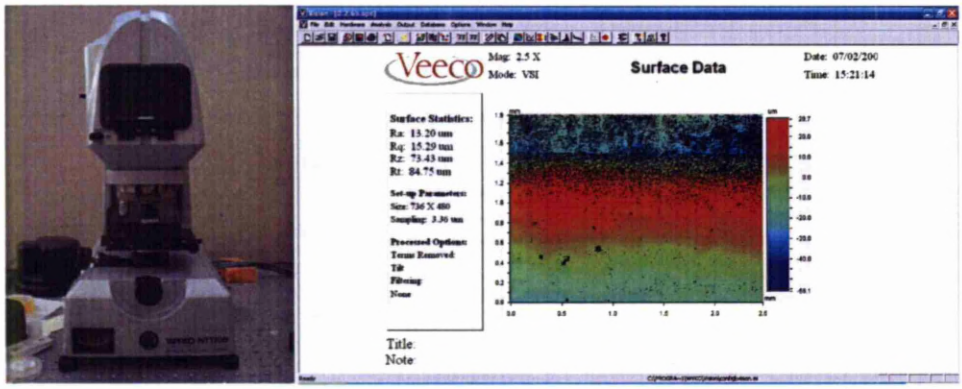

Figure 2.10: Wyko NT1100 Optical profiling system and the Graphical user interface (GUI).

2.4 The Effect of Temperature on Cure

This section investigates how the temperature at which the ink is treated at, affects the resultant properties of the ink track. It will specifically look at the mass lost during cure and the densification of the ink that makes it conductive, along with the resultant resistivity that the cured track has. The final stage will be to investigate how the resistance of the track changes during the curing process.

2.4.1 Method

Since oven curing is the standard method of processing these polymeric inks, the investigation was undertaken so as to create a benchmark by which the laser curing process could be compared. Also there is no information on how a change in the curing regime affects the resultant properties of the track. The guidelines are to cure these inks at 120°C for a period of 30 minutes.

2.4.1.1 Deposition Method

For this investigation the samples were deposited on the alumina substrates using the doctor blade method. The doctor blade method is a common technique and is similar to that of manual screen printing. A stencil is created which acts as a negative of the image/dimensions desired. The stencil is then flooded with ink and a scraper drawn across the surface of the stencil flooding the negative (gaps) with ink. Once it has been properly flooded and scraped with excess ink removed, the stencil is peeled of the substrate leaving a positive image of ink, Figure 2.11. It is only suitable for simple geometries and in this case it was used to create single lines.

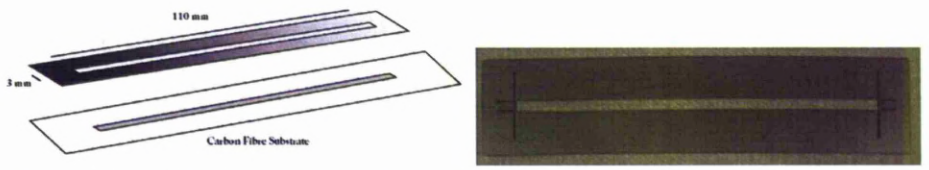

Figure 2.11: Illustration of the stencil and the resultant track on a substrate, and a picture of one of the stencils used.

The stencil in this case was used as a template to cut out the actual stencil that would be flooded. Tamiya modelling tape was used to create the stencil which was used in the deposition of the ink. The stencil shown in Figure 2.11 was placed over the tape once the tape had been placed on the alumina substrate. A scalpel or surgical knife was used to trace the outline of the metallic stencil over the tape, than the central portion of the tape was removed creating a clean negative stencil made from tape on the substrate. Tamiya modelling tape was used because it had consistent thickness and it was easy to cut. It was also low tack meaning no residue would be left upon the substrate once the tape was peeled off. If a thicker sample was required the tape could be doubled up or layered

depending on what thickness was required. Figure 2.12 shows a white light interferometer image that profiles the tape and was used to measure its thickness. The tape was placed on to a Perspex substrate and a scan conducted. Two layers were then placed, one on top of the other upon the Perspex and a scan conducted. The single tape layer had an average thickness of 89.67 µm, whilst the double layer thickness had an average thickness of 181.79 µm, with an average surface roughness of 4.26 µm.

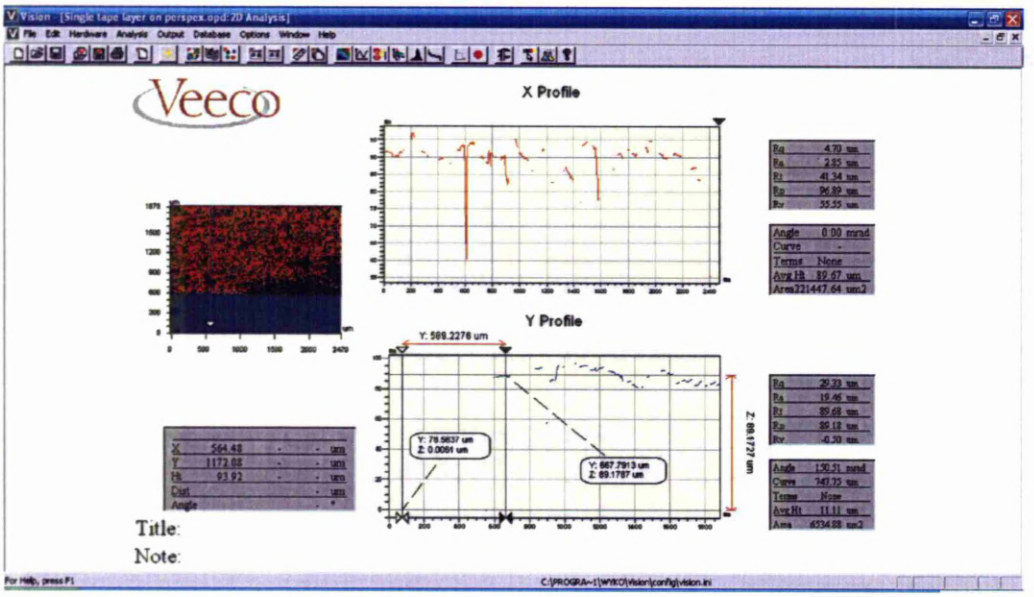

Figure 2.12: A screen grab image of the GUI of the WYKO software in graphical mode. This mode was used to analyse the samples by measuring various points. In this case the distance from substrate to the top of the tape.

The geometry of the lines produced was 2 x 110 x 0.09mm^3. A double layer of tape was used as it was found that using a single layer produced very thin lines that were not comparable to syringe deposition which would be used to fabricate components and so would be harder to test. By using a double tape layer with a measured thickness of ~181 µm, this produced a line thickness on average of 90 µm before cure. Six lines were deposited on each piece of alumina with a spacing of approximately a 1.5 cm spacing between each of them. The samples once prepared were placed in the pre-heated oven at the desired temperature. Tests were conducted at temperatures in the range 60°C and 220°C, at 10°C intervals. They were placed in the oven for 20 minutes at a time. The experiment was conducted for the D58, D1, and D15 inks.

Once the inks have been in the oven for 20 minutes and cured at the allotted temperature they were removed and placed on a work bench to cool. Once they had cooled to room

temperature each track was tested to find its resistance. To do this each pin of the four point probe, as shown in Figure 2.6, was placed in the centre of the track. The two inner pins are spaced 2.5 cm apart, whilst the outer pins are 2 cm from the adjacent central pin. The distance between the inner pins is the distance over which the resistance is measured and this distance is also the distance used to calculate the resistivity ρ, $\rho = \frac{RA}{L}$, where R is the resistance, whilst A is the area. This is calculated by multiplying the height of the track by the width of the track. Because these values vary slightly along the length of the track an average value is calculated using from multiple WYKO measurements and this value is used. The L is the length of the track, which in this case is 2.5 cm.

For thin films that are thought of as being uniformly thick and with a resistance that is measured using a four point probe, it may also be useful to use the terminology of sheet resistance. Sheet resistance is applicable to two dimensional systems as long as the film is deemed to be uniformly thick. It is used when measuring with a four point probe because the current flows along the plane of the film and not perpendicular to it. It is calculated by dividing the resistivity by the thickness of the sheet, or multiplying the resistance by the width over the length, $R_s = \frac{\rho}{d} = R\frac{W}{L}$. Where R_s is the sheet resistance and is usually measured in units of Ω/Sq or mΩ/Sq. The symbol Sq denoting square. R is the resistance as in equation 2.1 whilst W and L and d are the width, length and thickness respectively. Though the tracks are not completely uniform in thickness, the mean height is taken and uniformity is assumed as the variation is negligible.

2.4.1.2 Mass loss and Densification

For the mass loss experiments, the deposition of the inks were conducted in the same way as that for the resistivity measurements. However prior to deposition the alumina substrate was weighed on the Kern scales to an accuracy of 10 µg. Necessary precautions to reduce any contamination as fingerprints and dust fall within the µg bracket were undertaken. These included prior cleaning of the substrates using laboratory grade isopropanol and any areas that may come in to contact with the samples and use of dust free gloves at all times. Once the substrate had been weighed, it was placed on a clean surface and deposition of the inks was carried out. The substrate with the six tracks on it was then weighed and placed in to the oven at the required temperature, 60°C to 220°C,

thereafter. The tracks were then cured for 20 minutes. After the 20 minutes the sample was removed and placed on another clean surface that had previously been cleaned and then subsequently covered. They were allowed to cool to room temperature and then weighed. From this, the total mass loss for all six tracks for that particular curing regime was calculated, and hence the average mass reduction per track found. An average figure is used due to the small scale changes involved and it was felt that this would be a more accurate way of measuring the mass change, by reducing the effect of any contaminations on the measured quantities.

2.4.1.3 Temporally Dynamic Resistance and Temperature

The final experiment for the oven cured inks was to investigate how the resistance changed in real time as a function of temperature. For this a Fischer Scientific FB15001 hot plate was employed as mentioned in section 2.2.1.2. This was required because the four point probe could not be placed within the oven. Therefore the circumstances in which these measurements took place were not identical to the other tests which were carried out using the Memmert oven. Hence the results cannot be directly compared to the other samples in terms of end resistance and hence resistivity, but can be used to demonstrate how the resistance changes dynamically with temperature. Another point that sets the hot plate apart from the oven is that it is not enclosed, therefore the surface of the ink will be at a different temperature to the substrate-ink interface as it is being heated almost completely by conduction from the hotplate and through the alumina substrate. This means that the substrate goes through a larger temperature range, since it would cool quicker, compared to that experienced when calibrating the oven. This scenario is consistent for all the inks tested and so can be ignored when comparing the results for this test. Also the thickness of the inks being of the order of 90 μm means that they are very thin, so the temperature variation through the thickness of the ink during the experiment should only be small.

The samples were deposited in a similar way to that mentioned Section 2.4.1.1; however, this time a smaller dimensioned substrate was used. The alumina substrate was 30 x 114.3 x 0.635 mm^3. This was because only one sample was being tested at any single moment. Once the sample had been prepared, it was placed directly on to the hot plate. It was held in position using high temperature foil tape that is available off the shelf, at each end. The

four point probe was then moved in to position and carefully placed on the ink track. All three thermocouples were used to measure the temperature profile of the sample. Ch 110 was placed directly on to the alumina substrate and held in place with tape. This made sure that it was in contact with the substrate during the experiment and would measure the substrate temperature profile. Ch 103 and 104 were placed on the alumina substrate, but they were not in contact with it. Once in place a small amount of ink was placed over the two thermocouples so that it was completely covering both end points. Here the thermocouples would measure the temperature profile of the ink during the thermal cycle. The track itself could not be tested directly due to the thin nature of the track. The thermocouples are about 1.5 mm thick at the tip and so an accurate reading could not be gained in that way. The test was conducted for 20 minutes with the hotplate starting off cold (room temperature) in the off position. Measurements were taken every 0.7 s. An image of the setup can be seen in Figure 2.13. The inks tested were the D58, D1 and D15.

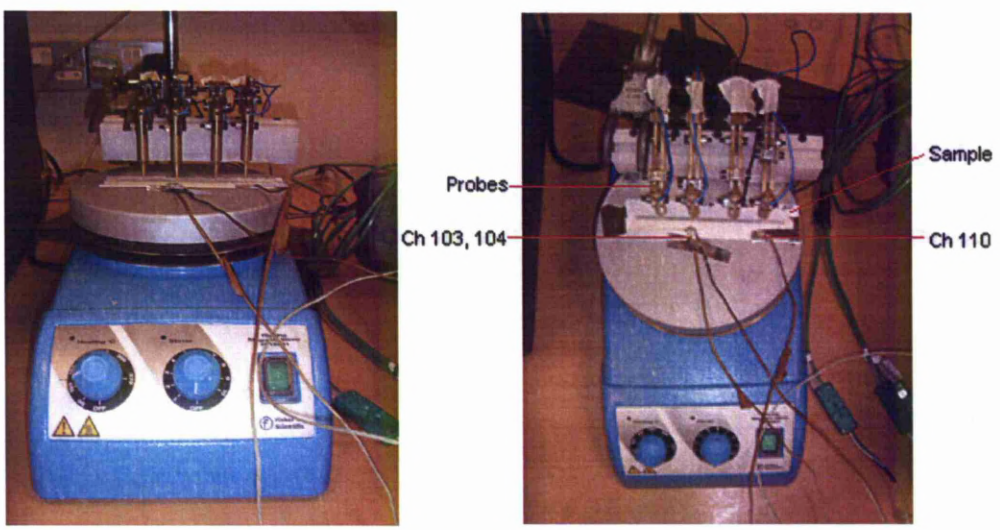

Figure 2.13: Two images of the experimental setup of the T Vs R dynamic experiment.

2.5 Results

The results of all three experiments will be presented in this section. The resistivity of the processed samples will be introduced first, followed by the mass loss results. Finally the results of the dynamic temperature measurements will be presented.

2.5.1 Resistivity

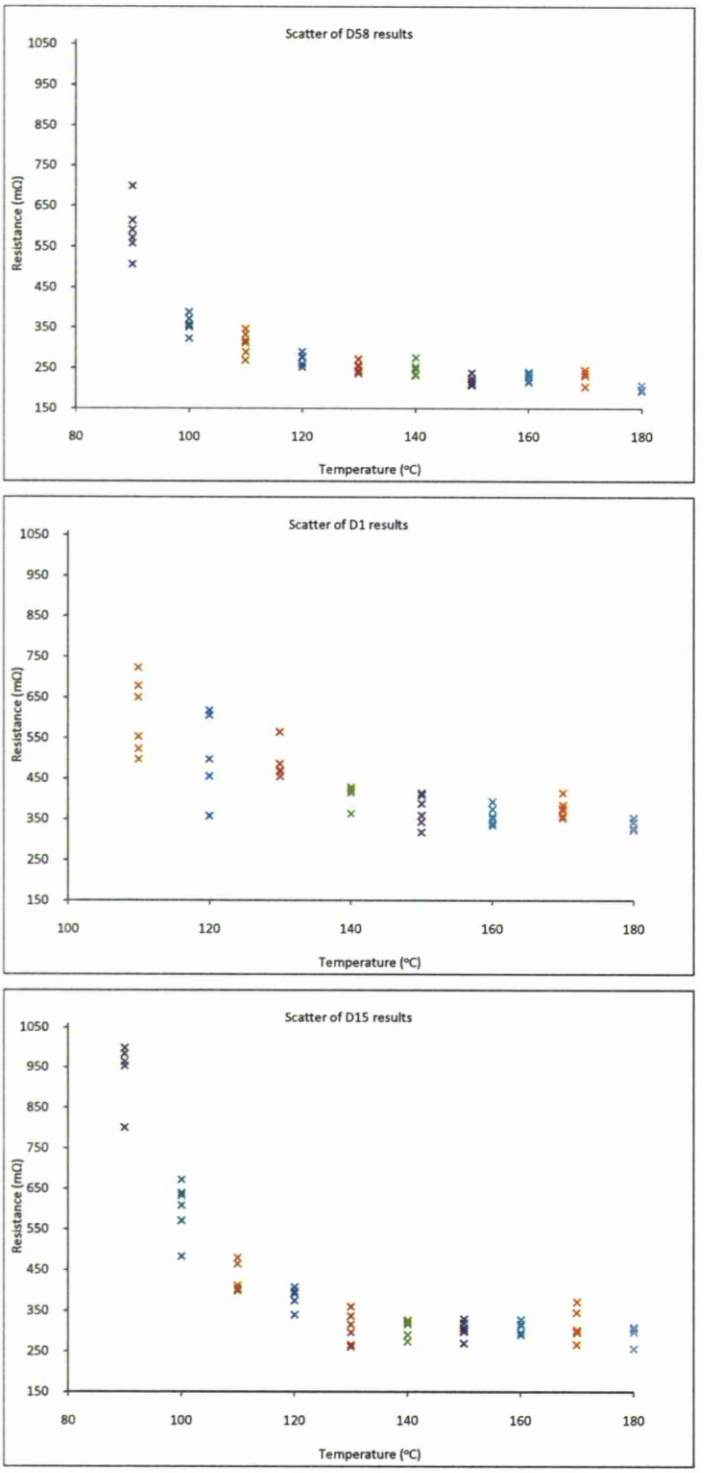

Figure 2.14: The top graph shows the resistance of the six tracks for each curing regime of the D58 ink. The middle one is the D1, whilst the bottom is the results of the D15 ink.

The resistance of the three inks as measured by the four point probe is shown in Figure 2.14. The graphs have been shown to illustrate the variation between any two tracks that are deposited and cured in the same way. The graphs start at the point where the cured tracks measure a resistance of less than 1 Ω. For the D58 and D15 inks this occurs at 90°C, where as the D1 ink requires a higher temperature to reach this threshold. It has a resistance of less than 1 Ω when cured at 110°C. The D58 has a low of 192 mΩ at 180°C, whilst the D15 has a low of 252 mΩ at 200°C. The D1 has a low of 265 mΩ at 220°C. The carbon and graphite dopants increase the resistance of the inks with the carbon acting slightly worse compared to the graphite, when looking at resistance alone. With the D58 ink there is a clear tendency for resistance to increase after 180°C whilst the addition of the graphite or carbon seems to negate this effect. The D1 ink (carbon doped) seems to decrease in resistance as the cure temperature increases, whilst the D15 ink (graphite doped) levels out after 130°C.

There is a large scatter between the points for any given cure regime with this decreasing as a function of temperature. The D58 ink upon cure at 60°C has a measured resistance range of 3.6 to 8.3 Ω, which equates to all values measured being at least 57% of the largest value. This figure increases to 86% when curing at 220°C where the range is 250.9 to 292.3 mΩ. The D1 ink has a range of between 16.5 to 66.1 Ω, so all values are at least 25% of the highest. At 200°C this value increases to 77% with a range of 266 to 345 mΩ. The D15 ink has a range of 15.7 to 44.4 Ω at 60°C which equates to 35% of the maximum value, and 81% at 220°C with a range of 280.7 to 344.5°C. The consistency of the electrical properties increase with cure temperature, and the effect of the dopants also reduces with increased temperature. The increased consistency is due to the cross-linking process bringing the silver flakes together and so there being an increased amount of contact (and hence lower resistance) as the polymer binder cross-links. As the temperature increases, the degree of cross-linking also increases creating more uniformity within the ink track. The carbon and graphite samples have a very high resistance at 60°C whilst the D58 ink is relatively small with a high of 8.3 Ω. This however, is not the whole picture as track volume will affect the resistance. By taking this into account the results are independent of the size of the track and so are directly comparable. In Figure 2.15 the resistivities of the same tracks are shown. There is still some variation within the tracks, now that the volume has been taken into account, indicating that consistency is an issue, especially if it is required for a certain application such as fabrication of a resistor where repeatability is desirable, however it does become more consistent with temperature as shown more clearly in Figure 2.16. The

spread of results is not however reduced by taking the volume into account. It seems to increase the spread, but the trend witnessed for the resistance curve does occur, in that the consistency of resistance values increases with increasing temperature. The D58 ink has the lowest percentage of the maximum value, with the tracks being within 48% of the maximum value at 60°C (resistivity values $1.76x10^{-5}$-$3.63x10^{-5}$ Ωm), whilst this increases to 63.4% at 220°C (resistivity values $9.95x10^{-7}$-$1.57x10^{-6}$ Ωm). The D15 shows a larger disparity between the two curing regimes. At 60°C the range is $1.13x10^{-5}$-$5.65x10^{-5}$ Ωm which equates to all values being at least 20% of the maximum measured. This increases to 76% at 220°C with a range of $8.29x10^{-7}$-$1.09x10^{-6}$ Ωm. The D1 is in between both the D58 and D15 inks with a low of 20% at 60°C with a spread of $5.08x10^{-5}$-$2.5x10^{-4}$ Ωm. This increases to 67% at 220°C (resistivity values $1.06x10^{-6}$-$1.59x10^{-6}$ Ωm). The results show that overall the D58 is more consistent due to its higher consistency at lower temperatures, but the D15 has a higher consistency at the higher temperatures, whilst the D1 has a low consistency to start like the D15, but has a slightly higher consistency than the D58 at 220°C. As a whole the samples are less consistent than that of the resistance measurements. The resistivity reduces significantly as the temperature increases almost halving for every 10°C increase in temperature until 90°C for the D58, 110°C for the D1 and 90°C for the D15 where after it plateaus. In terms of resistivity the values of the D15 is similar to that of the D58 ink, as compared to resistances mentioned previously. The D15 hovers around the $1x10^{-6}$ Ωm mark, Figure 2.14, which is equal to 63 x bulk silver, from 100°C onwards. Silver has a resistivity of 1.59×10^{-8} Ωm [7].

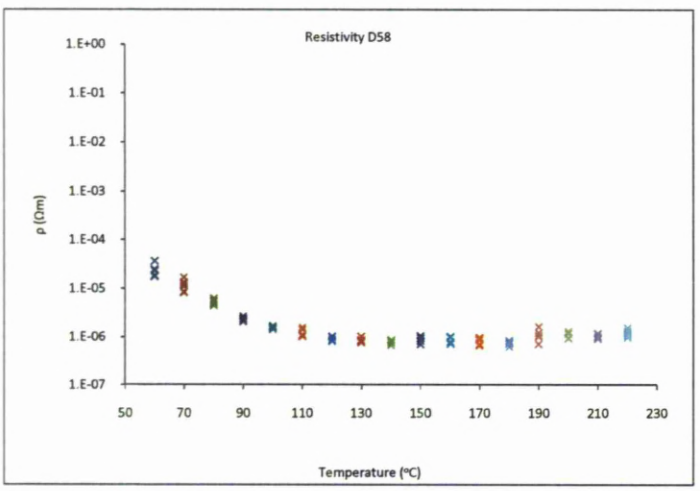

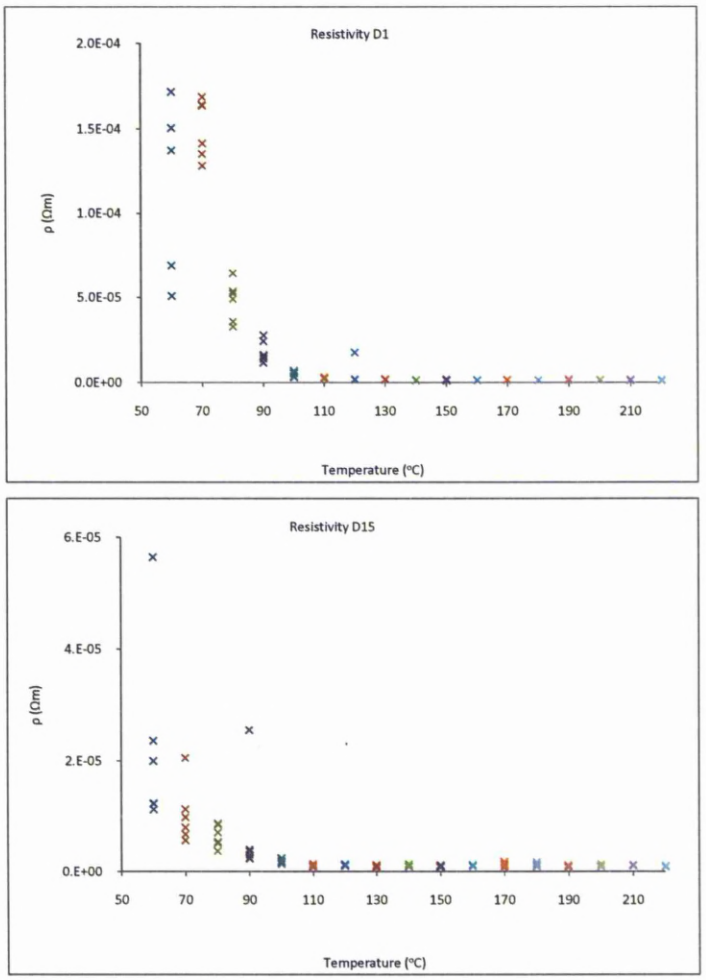

Figure 2.15: Graphs for the three inks showing the range of resistivities calculated from the resistances measured.

The D58 ink has a resistivity that is slightly less than $1x10^{-6}\Omega m$ consistently for temperatures in the range 120-180°C. At $7x10^{-7}$ Ωm, the resistivity is x44 that of bulk silver. The D58 ink is between 44 and 63 x bulk silver between 120°C and 180°C, but after 180°C as the ink goes through its B-cure stage the resistivity increases again, Figure 2.15, showing that curing of the inks is not simply higher temperatures equates to lower resistivity, but there is an optimum curing regime, even before thermal degradation. To get optimum results, it is undesirable to reach the B-curing process. The B-curing stage is a secondary phase in which the ink goes through an alternative cross-linking phase. This generally occurs at about 180^0C and is undesirable as it is not as effective at bringing the silver flakes in to contact and hence reducing resistance. For the D1 ink some samples, they reach the $1x10^{-6}$ Ωm line, but this is at higher temperatures, unlike the D58 which at this time has already started increasing in resistivity. The sample tracks which do reach this lower threshold appear to be more of a statistical anomaly rather than the norm, and shows that

unlike the D58, the D1 and D15 do not increase in resistivity with onset of the B-cure stage. The dopants have an unexpected side effect on the B-stage cure where increased resistivity is not witnessed. This is advantageous for the laser curing process as it increases the tolerances of the inks for producing the best possible resistivity and allows for a higher power density during cure.

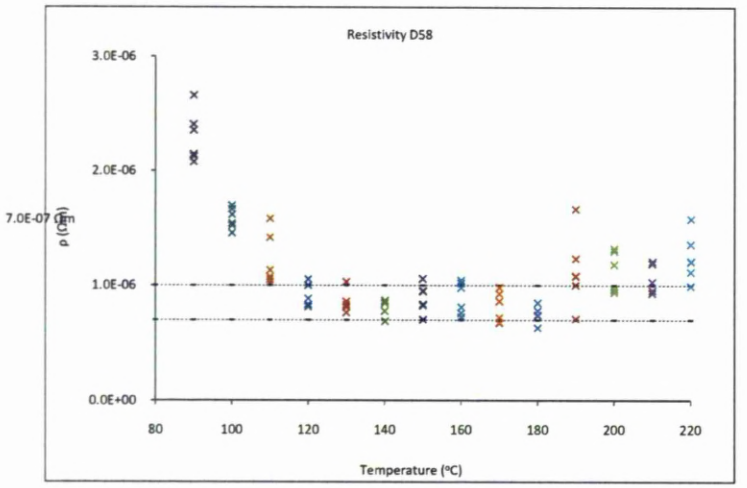

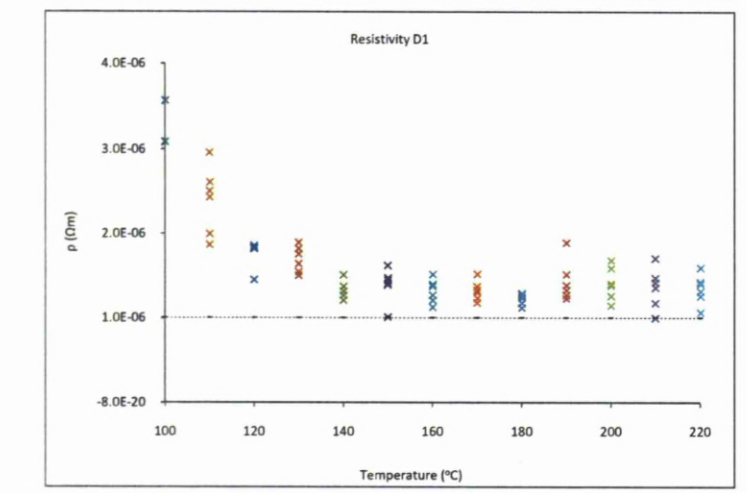

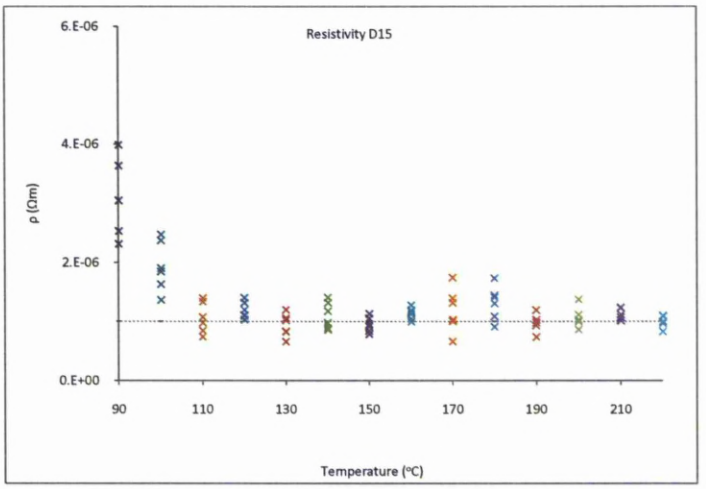

Figure 2.16: The three graphs show the resistivity of the inks at higher temperatures. The dashed line represents the $1x10^{-6}$ Ωm and this is equivalent to 63 x bulk silver which is $1.59x10^{-8}$ Ωm, whilst the second dashed line on the D58 graph represents $7x10^{-7}$ Ωm which is x44 of bulk silver.

In Figure 2.17 the mean resistivity of the tracks has been plotted. To calculate the mean, the largest and smallest values were removed and the mean calculated. This was so that the statistically anomalous results did not skew the average and hence a better representation of the results is presented. BY looking at the mean, it can be seen that the D15 is very similar in behaviour to the D58. Whereas the D1 is consistently higher than the D15 and D1 inks, and takes longer to make that transition to lower resistivities.

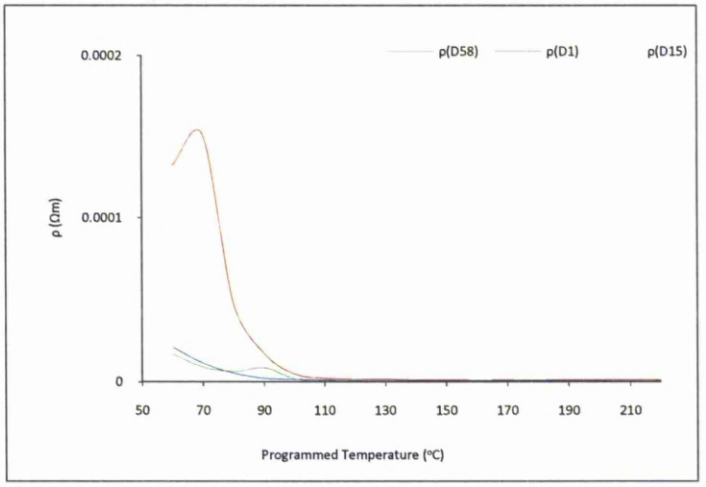

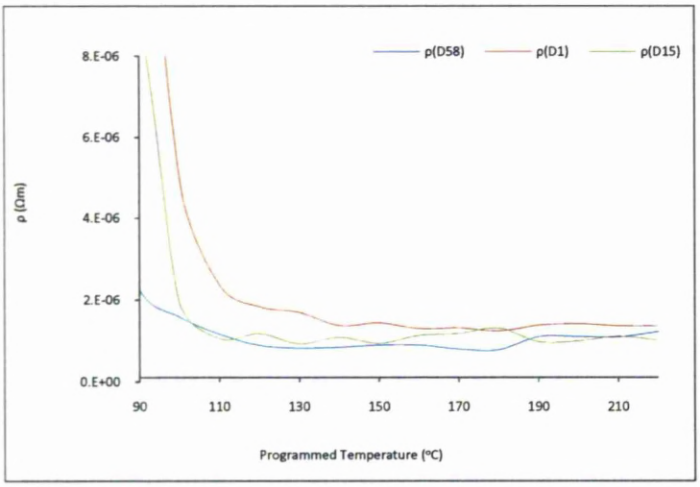

Figure 2.17: The left graph shows the variation in the average resistivity of the three inks as a function of temperature. There is a large variation in values, several orders of magnitude. The right graph is the same graph as the left, but starts at 90°C.

By dividing the resistivity by the thickness of the track, equation 2.2, the sheet resistance can be found. As stated previously, the sheet resistance is an industrially accepted measure of thin and thick films. In Figure 2.18 the results of the average sheet resistance can be seen. Once again the D1 acts in a dissimilar way to the other two inks, with higher average resistivities. This would be expected as the sheet resistance is a function of the resistivity. However unlike the resistivity results, the graphs illustrate that as a function of temperature the R_S of the three inks becomes more aligned due to the increase of the D58 B-cure stage, and only has a slightly lower R_S value than the D58 at 220°C. Conventionally created plasma sprayed copper lines have an R_S =6.5-8.5 mΩ/Sq [8], about ten times less than that achieved through oven curing of these inks.

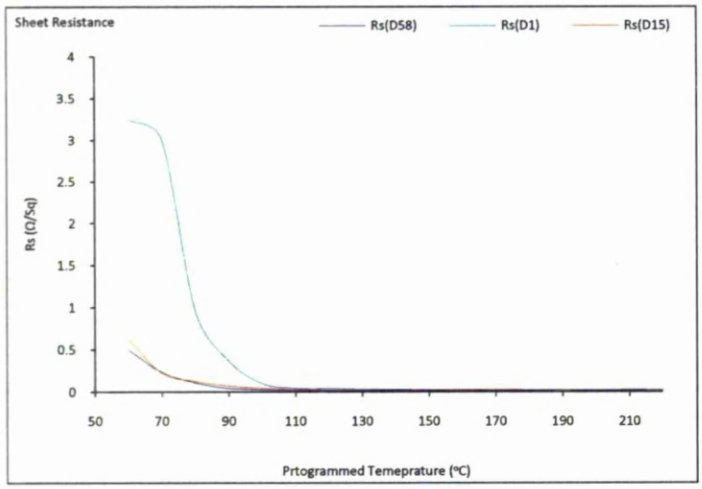

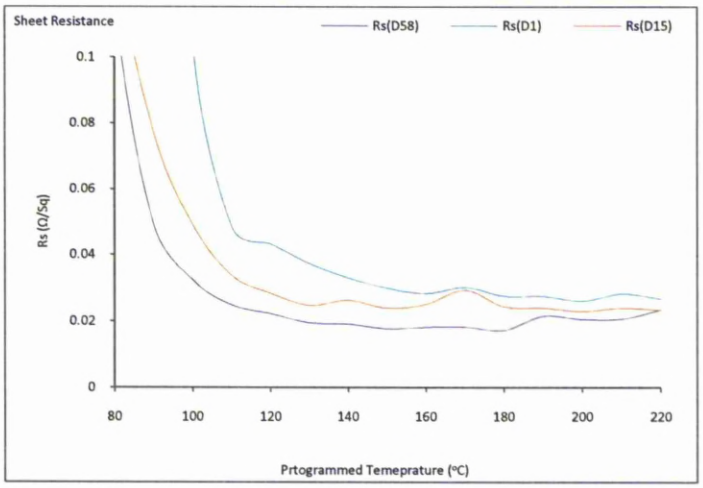

Figure 2.18: The left graph is the average sheet resistance of the inks as calculated from the resistivity. The right graph is an expanded view of the left, concentrating on the large change that occurs at 90°C.

2.5.2 Mass Loss and Densification

The mass lost in any curing process should be a guide as to the degree of cure that has occurred. This is because during the curing and cross-linking process the mass reduces along with the volume of the ink. As this volume reduction occurs the silver flakes are brought in to contact with each other. The volume reduction is related to mass loss and so it should be possible to gauge the degree of cure as a function of mass loss of the in track. During the curing process the ink cross-links and in doing so loss of functional groups occurs. This mass loss would be noticeable but slight compared to the other loss which is mainly from solvent evaporation. As stated previously the solvent is used to reduce the viscosity of the inks so that they are malleable and easy to use to create the desired pattern. Removal of the solvent increases the viscosity, in combination with the cross-linking phase; this hardens the ink and makes it functional. As in section 2.2 the solvent is anywhere between 40% and 10% by mass of the ink. The solvent is constantly evaporating so the mass of the ink is generally dynamic. The percentage of the solvent present will depend on the age of the ink. To try and negate this, new inks were used for the experiment, meaning that the solvent content was as close to the manufactured content as possible.

The mass loss was calculated as an average per track. Figure 2.19 shows the percentage of mass lost per track for each curing regime. The results, though wildly varying do show a

trend towards increased mass loss as a function of cure temperature. Similar to the resistivity results, a sharp increase in mass loss can be seen for all the inks after each 10°C rise, peaking at 100°C for the D58 and D15 inks, whilst the D1 ink peaks at 80°C. Therefore the D1 ink behaves in a different way to the other two. It also has a shallower gradient of mass loss when compared to the D58 and D15 inks which have the same gradient of mass loss when looking at the linear interpolation trend line.

The other noticeable thing about the graph is that the mass lost during the curing regime is a maximum of 23%. This corresponds to 7.6 mg at 190°C for the D15 ink per track. This is substantially lower than what would be expected. Comparing these results to the TGA analysis conducted in chapter 4, it can be seen that the percentage loss agrees with what was witnessed using the TGA, a maximum of 18% at 220°C. Further to this the TGA was conducted over a slightly longer time scale, about 40 minutes for a 220°C run, therefore it can be assumed that almost all of the solvent has been removed after 20 minutes and cross-linking has occurred to the extent that it will occur at any given temperature when curing within a pre-heated oven.

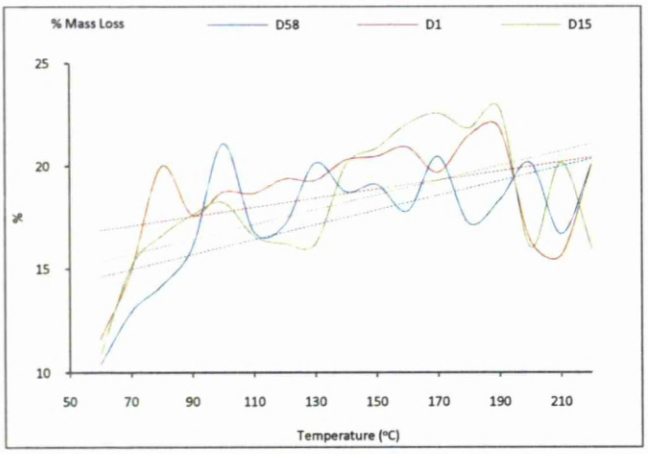

Figure 2.19: The graph illustrates the variation in mass lost by the ink tracks as a function of cure. The values vary a lot, but do follow an overall trend as illustrated by the dashed trend lines. The results and trend line colours match.

For the TGA experiment, after 20 minutes a temperature of 123°C was reached. This corresponded to a mass loss of 3.5%. This is substantially less than that of the 17%, 19% and 16% seen for the D58, D1 and D15 inks respectively. However that sample is only above 80°C for 10 minutes. When looking at the TGA/DSC of the uncured resin only sample, section 4.3.3, this is sufficient time and energy for cross-linking to occur. By this time substantial mass loss has occurred and the associated change in heat flow when cross-

linking occurs is witnessed. These results taken together would imply that the gradual increase in temperature associated with the TGA process slightly inhibits mass loss in the first instance when compared to oven curing where the sample is placed in to a pre-heated oven at a given temperature.

To find the density of the inks before and after cure, the volume of the track is measured before and after cure using the WYKO interferometer and then the necessary calculations conducted. Table 2.1 shows a table of the values for before cure and Table 2.2 after cure. For the uncured ink average measurements were taken of the track after deposition. The values did not vary that much showing a consistency in the repeatability of the deposition process. For the oven cured samples an average of the height and width was also taken for all the samples as used for the resistivity calculation. As the inks lose solvent through evaporation and cross-link they reduce in volume. The mass loss is less per unit volume than the density of the track so the track also increases in density even though it loses a large percentage of its weight.

Table 2.1: Values of the density of the inks before cure. The volume was taken to be 90 µm x 2 mm x 110 mm.

D58	D1	D15
2.08 g/cm^3	1.76 g/cm^3	1.71 g/cm^3

The D58 is the densest prior to cure and this would be expected as the carbon and graphite are less dense than the other constituents, and graphite is even more less dense than carbon and so the results show a trend which would be expected. After cure the same can be said again, which demonstrates that the carbon and graphite is still present within then solidified track after cure. There does not appear to be a trend towards increased density with increased temperature, Figure 2.20, even though there was a general trend of increased mass with an increase of temperature. This implies that there is a change in the volume and hence porosity of the ink as a function of cure temperature

Table 2.2: The values of the densities of the inks after cure at the stated temperature. Values in g/cm^3.

T (°C)	D58	D1	D15
60	3.24	3.07	5.47
70	2.97	2.82	3.03
80	3.02	2.62	2.46
90	2.98	2.66	2.34
100	2.93	2.76	3.26
110	3.30	2.57	4.23
120	3.70	2.76	3.19
130	3.59	2.63	3.31
140	3.58	2.83	2.92

150	3.16	2.64	3.26
160	3.20	2.59	2.61
170	3.31	2.73	2.51
180	3.26	2.66	2.24
190	2.59	2.27	2.92
200	2.66	2.54	2.80
210	2.78	2.75	2.38
220	2.55	2.57	2.92

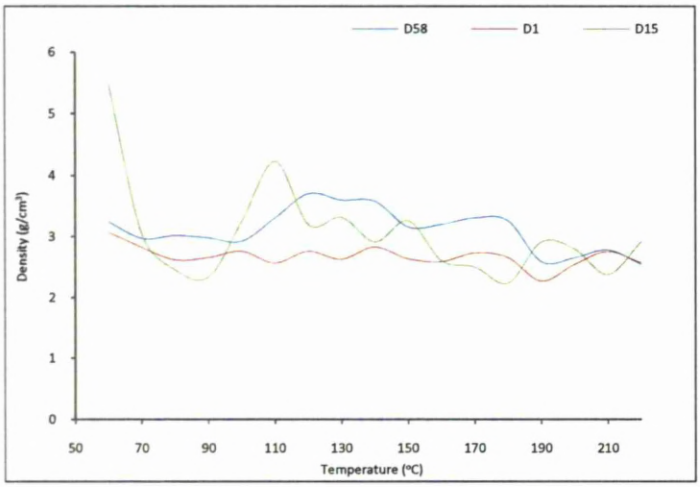

Figure 2.20: Graphical interpretation of table 2.2.

2.5.3 Temporally Dynamic Resistance and Temperature

The dynamic resistance and temperature profiles help give an insight in to the time and temperature function of cure that could not be gained by carrying out the static oven tests alone. Though the hot plate was set at 100°C and 200°C for the two runs conducted per ink, the temperature oscillated around this temperature and the resulting temperature profile produced was a saw wave. This temperature profile exists because the system works on an internal thermostat that measures the temperature of the hotplate directly. The sample being on the surface of the hotplate and of a thin nature would cool more rapidly than that of the thick metallic hotplate, exaggerating any cooling that occurs as the hot plate tries to regulate the temperature. Table 2.3 is a table of the maximum and minimum values of the temperature recorded for each run. The minimum value is quoted as the lowest value recorded after the hotplate has got up to temperature. That is after the initial peak, as measured by Ch 110. Ch 110 measures the temperature of the substrate directly, whilst Ch 103 and 104 measures the temperature of the ink.

Table 2.3: Table of the maximum and minimum temperatures of the alumina substrate during each ink run and the time in to the experiment that it occurred. Values taken from Ch 110 thermocouple

	100°C				200°C			
	Time (mins)	Max (°C)	Time (mins)	Min (°C)	Time (mins)	Max (°C)	Time (mins)	Min (°C)
D58	2:20	152	13:57	77	3:42	263	14:17	194
D1	2:17	148	12.29	82	3:50	266	14:29	197
D15	2:04	162	18:57	90	3:54	230	14:44	171

For the 100°C run, the maximum and minimum values are similar, but show a large variation during the heating cycle. From table 2.1-2.3, it can be seen that during one run of the 100°C setting the hotplate goes through about 1.5 heating cycles, with generally two maximums. The initial peak is the maximum whilst the following maximums are slightly lower. This means that when the hotplate heats up initially, it over shoots its target temperature. This is probably due to the speed that it heats up. From table 2.3 it can be seen that the hotplate reaches its maximum temperature in just over two minutes for the 100°C setting and just under four minutes for the 200°C setting. The difference between the maxima and minima of the two different runs is approximately equal making the 100°C run have a greater variation in temperature as a percentage of average temperature achieved. These variations are not a concern as they are consistent across all six test runs, and the absolute values are not of interest. What is of interest is how the resistance changed and at what point. This information can clearly be seen from Figures 2.21-2.23.

Looking at table 2.2 for the D58 100°C run, it can immediately be seen that the temperature profile is a saw like wave function as for all the graphs and mentioned previously. The other striking feature is the resistance curve. The resistance is very high to start off with, 10,000,000 Ω +. There appears to be a steady increase in the resistance as the hot plate heats up. This is probably due to the ink heating up, but not cross-linking. It is the cross-linking that reduces the resistance, so prior to that where the sample is just heating up, it is increasing in resistance as it becomes a viscous liquid due to solvent evaporation.

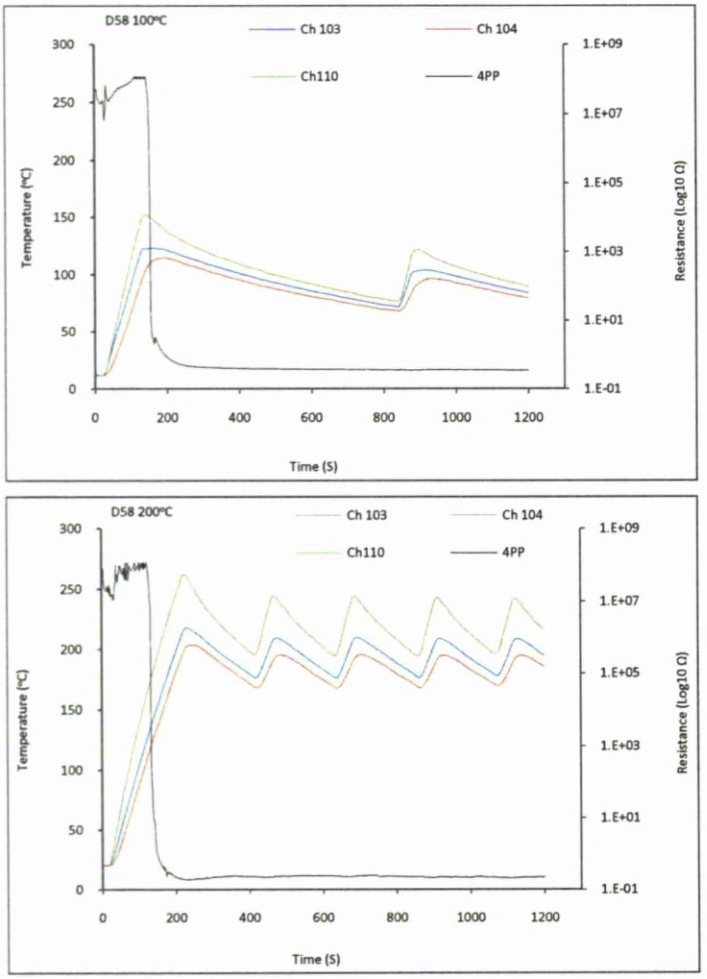

Figure 2.21: Dynamic temperature and resistance profiles of the D58 ink during cure. Hot plate set to 100°C and 200°C. Resistance plotted in $\log_{10}$ scale. Ch 110 is measuring the substrate whilst Ch 103 and 104 are measuring ink temperature.

This increase is common to most of the results, to varying degrees. There is then a sudden drop in resistance that is almost instantaneous just after the substrate hits maximum temperature at 152°C after 140 s. The transition from a poor conductor (5399081 Ω) to a good conductor (8 Ω) takes place in 6 seconds. When measuring the results of the oven cured samples, section 2.5.1, lower resistances were seen at lower temperatures seemingly to contradict the results witnessed here. However when looking at Ch 103 and 104 which were encapsulated with ink, there is a lag in temperature when comparing that to the substrate. The presence of the ink acts to dampen the cyclic process of heating and cooling and so when the ink starts to reduce significantly in resistance, the actual temperature of the ink and not the substrate is between 109°C and 123°C after 148 s. This corresponds more with the results witnessed in section 2.5.1 and the sudden change in resistance seen as a function of temperature. The same can be said for the 200°C run in Figure 2.20, with a

slight change at which the resistance of the track changes suddenly. Here it is between a sample temperature of 122°C and 138°C however the timing is consistent with this occurring at 134 s in to the heating cycle. The 200°C run for all samples seems to go through approximately 4.5 cycles of heating and cooling during one run as the hotplate tries to maintain temperature.

The D1 and D15 samples act in a very similar way to that of the D58 ink. The D1 ink, in a similar manner to the other results takes slightly longer to make that transition compared to the D15 and D58, from a poor conductor to a good conductor. The D1 sample during the 100°C run starts to make that transition 202s in to the test, with a temperature of 102°C. Significantly later on than either the D58 or D15 which makes its transition about 194 s into the test with a temperature of 112°C-114°C. For the 200°C run, the D1 ink again takes longer with the transition occurring at 176 s, with a temperature between 136°C-141°C. For the D15 ink this transition occurs at about 173 s in, similar to that of the D1 ink, but with a lower temperature of 120°C-122°C.

It should be noted that the samples take longer to make the transition from a poor conductor to a low conductor when being tested under the 200°C run. It would appear that there is a minimum amount of time required for the sample to cross-link during oven/hotplate curing, but this threshold is clearly seen in the 100°C run at a little over 2 minutes. As to why there is a difference between the 100°C and 200°C runs, it is not fully understood though it will probably have something to do with the thermal properties of the polymer binder and the onset of the B-Curing stage. This is an unexpected observation that has arisen from the experiments and one that would be of interests for someone to study as future work. Though it was unexpected, these results do not affect any of the following experiments or results described within this thesis.

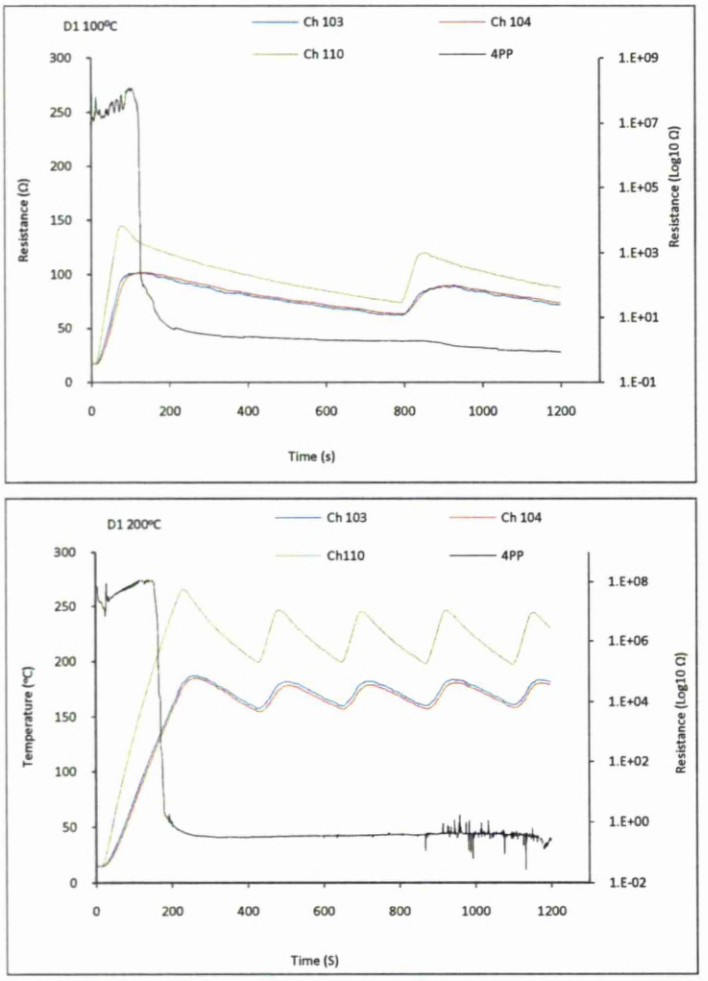

Figure 2.22: Dynamic temperature and resistance profiles for the D1 ink during cure.

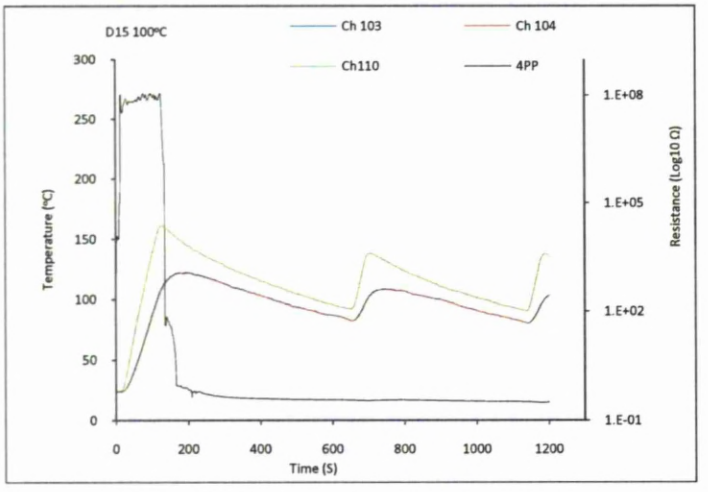

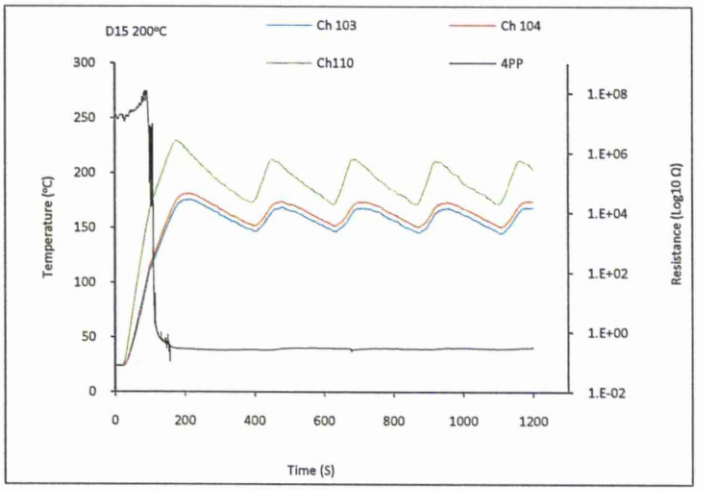

Figure 2.23: Dynamic temperature and resistance profiles for the D15 ink during cure.

References

1 http://www.memmert.com/en/products/universal-oven/universal-ovens-models/models/UNB-100/.

2 https://extranet.fisher.co.uk/webfiles/uk/web-docs/1309_LC.pdf.

3 *"Determining resistivity and conductivity type using a four point collinear probe and the model 6221 current source",* Number 2615, Keithley Application note series.

4 www.ceramic-substrates .co.uk/ceramic_products/properties_alumina.

5 www. gwent.org

6 www.chemicalland21.com

7 Halliday D, Resnick R, Walker J, Fundamentals of Physics, John Wiley & Sons, 6th ed. 2001. ISBN 0471332364.

8 Pique A, Chrisey DB. Direct Write Technologies for Rapid Prototyping Applications Academic Press, 2002. ISBN 01217432318.

3 Laser Curing of Polymeric Inks

This chapter introduces the concept of laser curing of polymeric inks as a new technique that negates the use of an oven curing stage, in the application of composite polymer inks. The work presented here solely looks at the process from first principles and analyses the results using the results obtained in chapter 2 for the oven cured inks, as a bench mark. The applications of this work in creating functional microwave antenna will be introduced and discussed in chapter 6. This includes the research carried out for the ASTRAEA project and the TaWA (Towards a Wireless Aircraft) demonstrator. It has been left out of this section for ease of reading and creating a coherent research story.

3.1 Introduction

The aim of this chapter is to introduce the concept of using IR lasers as a means of curing conventional polymeric inks that are normally thermally cured. Currently there are several systems that employ lasers for additive manufacturing and deposition of thin and thick films. When it comes to curing of inks, the more conventional method is UV cure. This poses restrictions on the environment in which it can be used and the materials that the inks can be made out of. By employing an IR laser, many more ink architectures can be cured as the resin carrier needs only be a thermo or thermosetting polymer and as shown within this chapter does not necessarily need to be designed for laser use. A brief description of a laser in is given next.

3.2 Equipment Used

The following section describes the equipment used in carrying out the laser curing investigation. Any equipment overlap with the oven curing experiments will be omitted here.

The laser used for the experiments conducted within this investigation was a 25 W Synrad sealed CO_2 laser. It had a lasing wavelength of 10.6 μm and a Gaussian beam profile. A

beam print can be seen in Figure 3.3. The setup of the laser system and workbench can be seen in Figure 3.1.

Figure 3.1: Photograph of the setup used to conduct the laser curing investigation.

The laser system due to its low power nature could be plugged straight in to the mains. It also uses convection to cool itself and so had internal fans for this purpose, Figure 3.2. The computer interface was used to control the laser system using WinMark software provided with the laser. The laser was attached to a galvo head Figure 3.2, 3.2 manufactured by Synrad. The galvo head used an F-theta flat field lens with a focal length of 242 mm. At focus the spot size was measured to be 150 µm Figure 3.4.

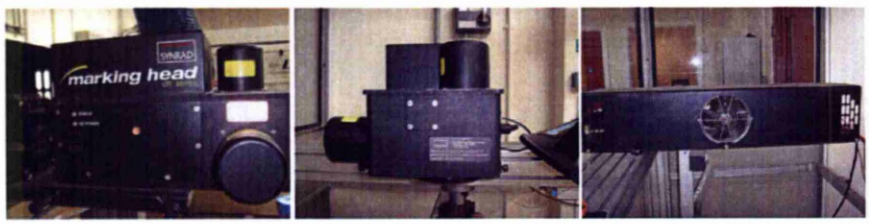

Figure 3.2: Close up images of the galvo head (left, middle) and the laser with a side fan showing. The laser is connected to the galvo head via a hollow tube, which can be seen in the left image.

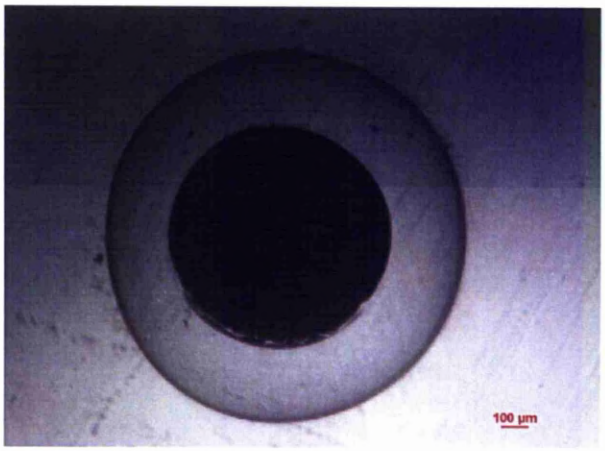

Figure 3.3: A photograph of a beam print conducted using the Synrad CO_2 laser.

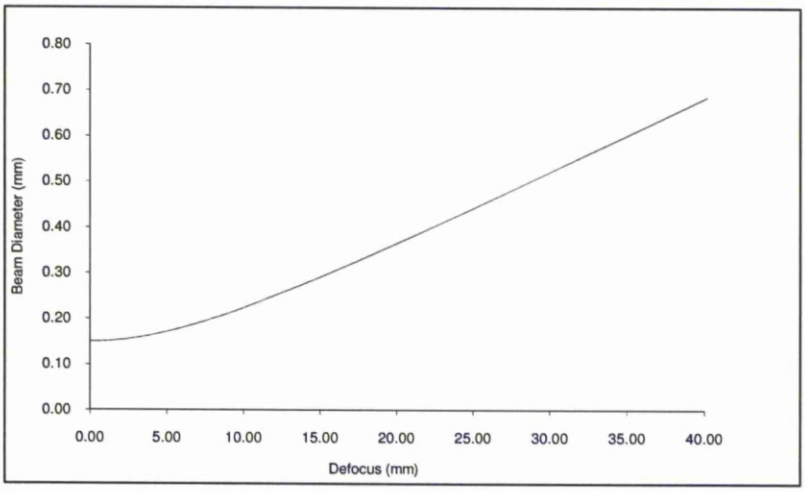

Figure 3.4: Graph showing the variation of spot size with beam position

To calibrate the laser and so an accurate power rating was known, several power measurements were taken during the curing trials. This was conducted by placing a power metre at a defocused position beneath the beam. A defocused position was used so that the laser did not burn the metre. Using the WinMArk programme to control the power, the settings are in percentages, going from 1-100% of the power in integer increments.

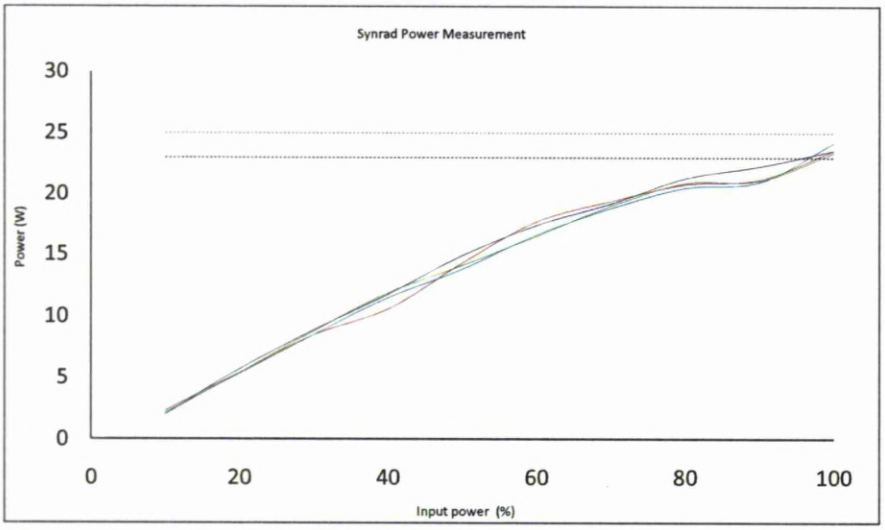

Figure 3.5: Power readings over the experimental period. The dashed lines represent a power of 23 W and 25 W.

Though the system is rated as a 25 W laser it does not actually reach 25 W at 100%. The average power at 100% is 23.7 W, Figure 3.5. It shows good consistency up to 30% power, than the values slightly deviate. Overall the consistency is good and an average value can be used to for any calculations.

3.3 Method

Within this section the methodology of investigating the laser cure process will be presented. The same three inks will be investigated as those used in Chapter 2 for the oven curing experiments. The D58, D1 and D15 inks. The D1 and D15 were designed to help enhance coupling of the laser in to the ink specifically for these investigations. The experiments looked at the affect of power, traverse speed and the number of passes on the resultant resistivity of the cured tracks.

3.3.1 Experimental Setup

The laser used has a focal length of 242 mm and a spot size of 150 µm, however the focus was not used for these experiments. A focussed spot would have a too high energy density and would burn the polymer and with such a small spot size multiple scans would have to be conducted to create a cured patch. By using a defocused spot size it was possible to

match the width of the tracks deposited and modulate the power setting accordingly to achieve the right energy density. The appropriate energy density was found through experiments. Since the track sizes used were 2 mm in width and a thickness of 90 μm, it was desirable that the spot size would match this. It was found that if the sample was placed 350 mm form the lens the spot size would be approximately 2 mm. Using this width the beam would irradiate the whole width of the track in one pass, removing the requirement for rastering. Because a different position was being used, in this case further away from the lens, Figure 3.6, this means that the input speeds would no longer correspond to the actual speeds as seen by the sample. The speeds would now be faster as the sample is further away from the focus. Conversely if it was closer the speeds would be slower.

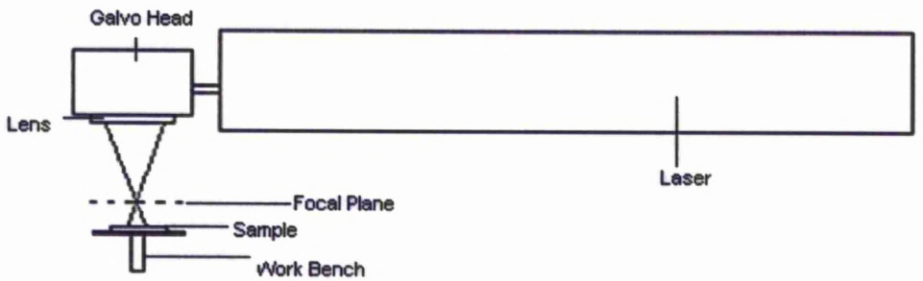

Figure 3.6: A schematic of the setup of the laser with respect to the work bench and sample. The focal plane has been indicated with a dashed line, the sample is 108 mm lower than the focus.

To calculate the actual velocities as seen on the sample triangulation is required. By creating a series of triangles, Figure 3.7, that represent the distance between the work piece and the lens and the focal plane and the lens, it is possible to calculate what the actual velocity is on the sample for a given input velocity.

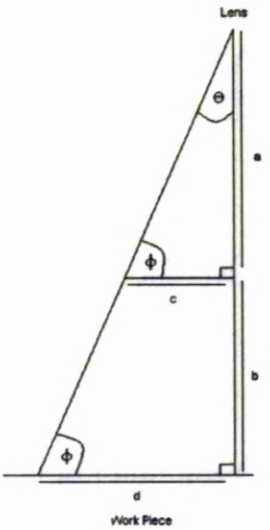

Figure 3.7: Triangulation of the laser setup between the work piece, focal plane and the lens. The focal plane is length c. Drawing is not to scale.

If we treat Figure 3.7 as the setup of the laser, focal plane and the work piece then lengths *a* and *b* are known. Length *a*=242 mm, the focal length, length *b*=108 mm, the distance the work piece is below the focal plane. If it is said that length *c* is 100 mm and the velocity input through the computer interface is set at 100 mm/s, then length c and length d will be traversed in 1 second. To find length *d*, ϑ needs to be found. Using simple trigonometry, equation 3.1 where O=opposite and *A*= Adjacent, it is found to be ϑ= 22.45°.

$$tan\theta = \frac{O}{A} = \frac{c}{a} \tag{3.1}$$

Now that ϑ is known and rearranging equation 3.1, *d* can be found using ϑ=22.45° and *A*=*a*+*b*. Using these values *d*=144.62 mm. This means that the actual speed as measured by the sample is 1.45 times the input velocity.

3.3.2 Laser Curing Trials

For the laser curing trials it was desirable to find the optimum curing parameters that would yield the best results. The best results would be interpreted as the parameters that created a cured track with the lowest resistivity whilst limiting energy input so that the substrate was not damaged.

The method for doing this was to start off by conducting the trials initially as a function of power and traverse speed. The power would be set and a single pass would be traversed over the track at a speed of 1.45 mm/s, the minimum power requirement was found for cure to occur with a single pass. The power was incremented by 10% up to the maximum or till damage would occur to the substrate, whichever came first. The traverse speed would then be incremented to 3 mm/s which would yield an actual velocity of 4.35 mm/s. The power would be reset starting from the minimum value previously found to create a cured track with one pass. If cure did not occur after one pass, then subsequent passes would be traversed over the track till cure had occurred, to a maximum of ten passes for any single track. As before the power would be increased and a new test conducted finding the number of passes required to cure with that specific power setting and traverse speed. The same was done for a velocity of 5 mm/s which yielded an actual velocity of 7.25 mm/s.

By using this technique of investigation it was possible to find the minimum energy threshold for cure to occur at a specific speed and the effect of multiple passes.

The track was deposited on to an alumina substrate using the doctor blade method as described in the oven curing chapter, section 2.4.1. The sample was aligned beneath the laser using markers on the work piece so that the sample was in the same place every time and the start of the track situated at the start of the scan so that no initial heating of the substrate would occur. The resistance of the track once cured was tested using the four point probe as mentioned in the section 2.4.1. Alumina was used for the laser curing trials as it is highly thermally conductive meaning that it is one of the hardest materials to get a good cure with as it acts as a heat sink removing energy from the ink track. This creates a scenario in which the surface maybe cured, but the track/substrate interface is still uncured. Alumina is also a relatively cheap material to work with, commercially available and is very consistent from batch to batch in terms of its thermal and physical properties.

3.3.3 Temporally Dynamic Resistance and Temperature

As with the oven curing experiments, it is of interest to find out how the resistance profile changes with time as the laser is traversing over the ink track. The thermocouples were also used to try and gauge the temperature the ink was achieving before during and after the laser passes over any single point. Two were at each end of the ink track and one was placed directly on to the substrate to measure its temperature. The thermocouples used

and the four point probe is the same as that in chapter 2. For the purposes of this experiment it was necessary to modify the four point probe so that it could measure the resistance of the track whilst it was being cured. The laser works on a line of sight principle and the pins would have either reduced the effectiveness of the laser, at best or inhibited it completely.

To modify the four point probe, thin wire of 200 µm diameter was used. The wire was used to be a replacement for the pins. The wire was cut to equal lengths of 20 cm. At one end 2 cm of the insulator clad was removed and the wire wound round the pin at the top creating a good electrical connection. This was done for each of the four pins. At the other end of the wire approximately 3 cm of insulator clad was removed. The pins were placed on to an alumina substrate so that they would not affect the results. Once the sample was in place, each wire was placed perpendicularly on the track. The central two wires (pins) were placed 2.8 cm apart and the outer two wires were 2.3 cm form them. For the thermocouples, Ch 103 was placed at the start of the ink track, whilst Ch 104 was placed at the end, before and after respectively of the wires from the four point probe so as not to interfere with the readings. Ch 110 was placed about two thirds of the way up and 0.5 cm from the track upon the alumina substrate. Though the thermocouples will not give an accurate reading of the temperature of the ink as it cures, it will be a good guide of the types of temperatures due to the laser and an accurate temperature of the substrate. In Figure 3.8 pictures of the setup are shown. Ch 103 and 104 were placed directly in to the ink track so that the laser would traverse over it and the temperature of the ink during cure could be measured. Ch 110 was attached to the substrate so the temperature profile of the substrate could be measured. The thermocouples were attached using masking tape to hold them in place as well as the wires from the four point probe.

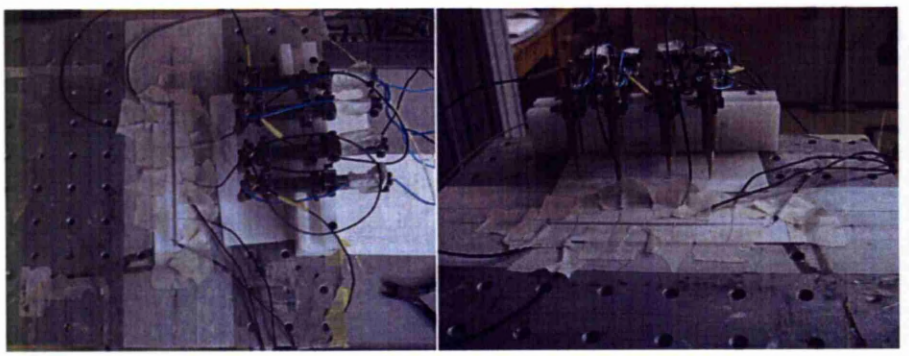

Figure 3.8: Over head and side view of the setup for the dynamic temperature and resistance measurements for the laser curing process.

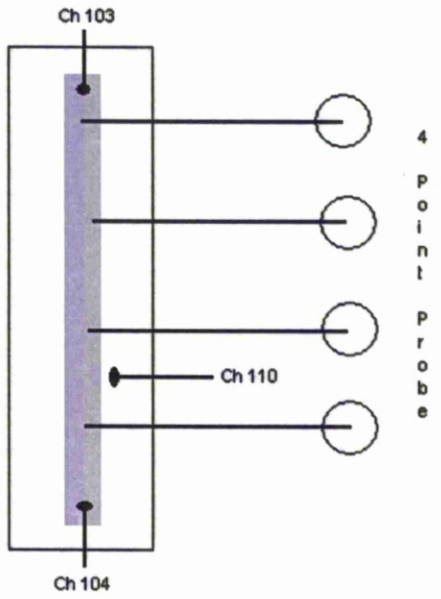

Figure 3.9: A schematic of the setup used for the dynamic temperature and resistance measurements for the laser curing process.

3.3.4 Resin Absorption Test

It is well known that silver is highly reflective to 10.6 μm radiation. Therefore the absorption of the laser into the ink is primarily through the resin and dopents, if the latter is present. An investigation was conducted to find the absorption or extinction coefficient of the resin when irradiated with a CO_2 laser. To do this a sodium chloride polished glass widow was used, Figure 3.10. The window had dimensions a 25 mm diameter and thickness of 5 mm. First an accurate reading of the laser power was taken using the power metre, the power output was found to be 3 W. The glass window was then placed upon the power metre and on the work bench where a new power reading could be taken so as to ascertain the absorption of the window to the laser, as shown in Figure 3.11.

Figure 3.10: A photograph of the sodium chloride window used for this experiment.

Once the absorption rate of the lens was found the resin was spin coated on to the lens. To be able to measure the height of the resin deposited on to the lens, one edge of the lens was covered in tape so as to stop any resin getting on to the window. This gave an edge from which to conduct the height measurement. Once the resin had been spin coated on to the window the tape was removed and a Wyko measurement was taken to measure the thickness of the resin deposit. The window was then placed on to the power metre below the laser and a new measurement taken.

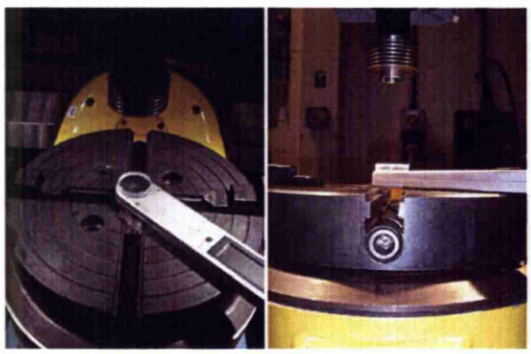

Figure 3.11: Images of the setup used for testing the absorption coefficient of the resin.

3.4 Results

3.4.1 Laser Curing Trials

The experiment for the laser curing trials started off by looking for cure as a function of power and keeping the speed constant at effective velocity of 1.45 mm/s. It was found, with one pass, cure could not be achieved below 50% power, 14.28W. The laser has a fixed energy density for a specific power rating and spot size. In the case of these experiments the spot size was kept at 2mm in the defocused position 350mm from the lens. As the power increase the energy density or intensity will also increase. This fine for a static beam or pulsed operation, but if the beam is traversing over a sample then the energy imparted to the track per unit area will not only depend on the power and spot size, but will also be a function of the velocity, as a unit area is swept out. If the velocity is greater than the spot size per second, then the energy imparted will be a fraction of the power rating. Conversely if the velocity is slower than the spot size per second, the energy imparted to the sample will be some multiple of the power rating. Figure 3.12 illustrates this point. The parameters for the graph have been chosen as these parameters were successful for cure with varying number of passes.

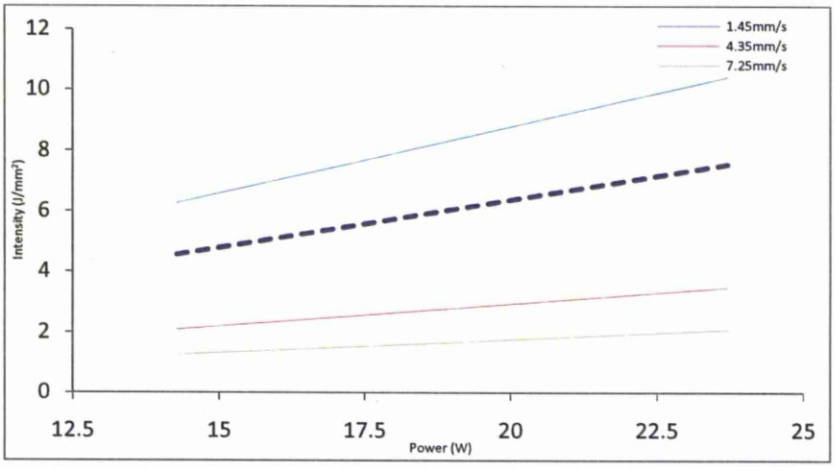

Figure 3.12: Graph illustrating the linear change in intensity of the energy imparted to the track as velocity and power increases. The dashed line is the static intensity profile of the laser.

For cure to occur with the D58, D1 and D15 inks in a single pass at 1.45 mm/s, the energy density must be 6.27 J/mm^2. It was not possible to cure the inks at higher velocities in a single pass. Table 3.1 is a table of the successful curing regimes of the inks on alumina.

Table 3.1: A table of the results of the curing experiment. The gaps for the D1 and D15 inks indicates where either the substrate was broke due to thermal input (shattered) or cure could not be achieved after 10 passes.

Power	Speed	D58			D1			D15		
(W)	(mm/s)	Pass #	Resistivity (Ωm)	Rs (Ω/Sq)	Pass #	Resistivity (Ωm)	Rs (ΩSq)	Pass #	Resistivity (Ωm)	Rs (Ω/Sq)
14.28	1.45	1	$6.11x10^{-6}$	0.046	1	$9.84x10^{-6}$	0.057	1	$1.25x10^{-5}$	0.068
17.05	1.45	1	$4.05x10^{-6}$	0.031	1	$8.8x10^{-6}$	0.048	1	$8.95x10^{-6}$	0.050
19.1	1.45	1	$5.35x10^{-6}$	0.029	1	$8.68x10^{-6}$	0.041	1	$6.81x10^{-6}$	0.041
20.88	1.45	1	$5.28x10^{-6}$	0.029				1	$5.93x10^{-6}$	0.033
21.4	1.45	1	$4.19x10^{-6}$	0.027						
14.28	4.35	4	$1.12x10^{-5}$	0.062						
17.05	4.35	4	$1.03x10^{-5}$	0.058						
19.1	4.35	4	$8.86x10^{-6}$	0.049						
20.88	4.35	4	$8.57x10^{-6}$	0.048	10	6.7x10 6	0.047	7	$8.52x10^{-6}$	0.048
21.4	4.35	3	$8.47x10^{-6}$	0.047	4	$9.08x10^{-6}$	0.050	4	$8.29x10^{-6}$	0.046
23.7	4.35	2	$9.21x10^{-6}$	0.051	3	$9.19x10^{-6}$	0.051	4	$9.73x10^{-6}$	0.054
21.4	7.25	10	$8.93x10^{-6}$	0.050						
23.7	7.25	10	$7.22x10^{-6}$	0.040						

For the curing trials with the D1 ink, good cure was achieved with a single pass at 1.45 mm/s until a power rating of 20.88 W was tried. At this point, the laser with a dynamic intensity of 9.17 J/mm^2 caused the substrate to crack due to thermal overload. The same occurred with the D15 ink with a dynamic intensity of 9.40 J/mm^2. The D58 ink failed with at the limit of the laser with a dynamic intensity of 10.41 J/mm^2. The reason for the substrate cracking is due to thermal stresses being induced within the alumina. It is able to handle temperatures greater than 100°C but as it is a ceramic, it is very brittle. The localised temperature gradient caused by the laser traversing the ink, causes these stresses and hence the crack. The reason for the disparities between the inks is due to the dopents. From the FTIR analysis in chapter 5, there appears to be little difference between the absorption of the D58, D1 and D15 inks within the finger print region where the 10 μm radiation sits, with a wavenumber of 943.4 cm^{-1}. The dopents are causing this disparity by increasing theheat flow to the substrate, due to the D1 and D15 inks having a higher thermal diffusivity and creating a higher temperature gradient between the ink and the substrate, inducing thermal stresses causing the substrate to crack. This idea is backed up by the heat capacity calculations made in the results section of chapter 4 and the density calculations from chapter 2 and the fact that they required more passes and hence a greater amount of energy to cure when compared to the D%8 with respect to power and traverse speed.

The thermal diffusivity of a sample, equation 3.2[1], dictates how the material will react to a thermal gradient within it and its surroundings. A material with a high thermal diffusivity will adjust quickly to be in thermal equilibrium with that of the surroundings. This is because it is able to conduct heat quickly in comparison to its volumetric heat capacity.

$$\alpha = \frac{k_T}{\rho_D C_p} \tag{3.2}$$

The volumetric heat capacity is the denominator in equation 3.2 and has units of J/m^{3}K. A is the thermal diffusivity, ρ_D is the density, k the thermal conductivity and C_p the specific heat capacity. The thermal conductivity of the inks is not known, whilst the density and the specific heat capacity have been calculated in chapters 2 and 4 respectively. Treating α as inversely proportional to the volumetric heat capacity it can be seen from Table 3.2 that

[1] The suffix D has been added to the density symbol to try and remove confusion with resistivity.

the thermal diffusivity is proportionally the largest with the D15 ink whilst the smallest with the D58 ink.

Table 3.2: Table showing the calculations illustrating the differences in volumetric heat capacity and hence thermal diffusivity.

Ink	C_p (J/KgK)	P_D (Kg/m^3)	$\rho_D C_p$ (J/m^{3}K)
D58	144.75	2080	301800
D1	149.99	1760	263982
D15	153.30	1710	261630

This implies that the thermal diffusivity is going to be the smallest of the three for the D58 ink: reduced heat flow, lower thermal stresses in the substrate, and the largest of the three for the D15 ink: increased heat flow as the ink tries to equilibrate, leading to greater energy imparted and higher thermal stresses. The results in Table 3.2, do not exactly match the results of the curing trials, since the D15 was able to tolerate a higher dynamic intensity than the D1 ink. The trend is still apparent as the D58 has a significantly larger volumetric heat capacity compared to the D1 and D15 which differ by less than 1%, whilst the difference with the D58 is over 10%. The differences witnessed between the carbon and graphite can be explained by the different physical geometries. The carbon powder is generally more spherical than that of the graphite (as shown in the SEM images) and so has a lower surface area. The graphite on the other hand is flat and shard like with a large surface to volume ratio meaning it is able to dissipate heat more readily to its surroundings.

The results of the curing trials as shown in Table 3.1 are shown in graphical form in figure 3.13. Looking at the graph, there is a trend towards lower resistivities with increased power. The D1 and D15 inks buck this trend when processed at 4.35 mm/s. However, since the D1 and D15 inks did not create a cured track at lower powers, the "higher" resisitivites have not been plotted. The D1 and D15 when processed at 4.35 mm/s with 20.88, 21.4 and 23.7 W show a similar trend to the D58 which shows an increase in resistivity at this point. The lowest resistivity achieved for the D58 ink was 4.05×10^{-6} Ωm with 17.05 W and a traverse speed of 1.45 mm/s with 1 pass. The D1 however had a resistivity low of 6.7×10^{-6} Ωm with a power rating of 20.88, 10 passes and a traverse speed of 4.35 mm/s. The D 15 was similar to the D58 in that it had its lowest resistivity measured at a traverse speed of 1 mm/s and 1 pass. A power rating of 20.88 W and a resistivity low of 5.93×10^{-6} Ωm. They are 255, 421 and 373 times that of bulk silver respectively. This is very high and substantially more than that of the oven cured samples.

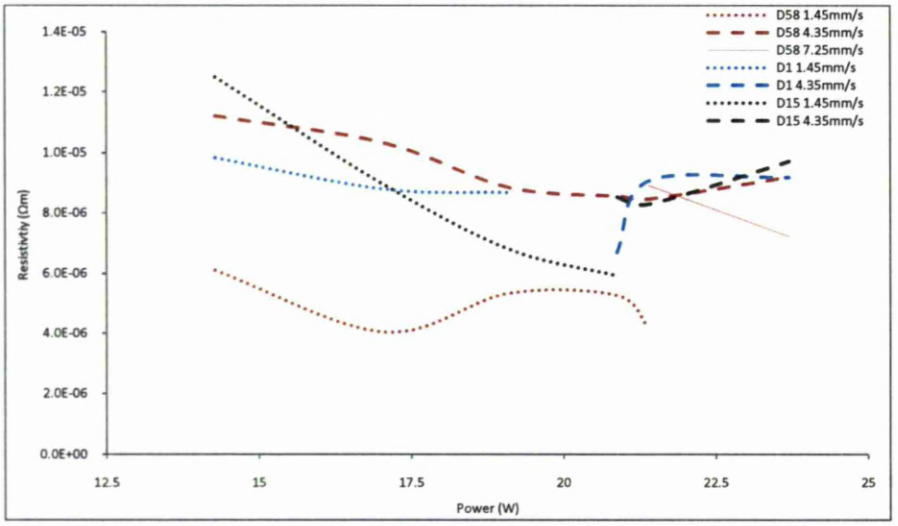

Figure 3.13: Graph showing the variation of resistivity with power, results of the curing trials as listed in Table 3.1.

By taking the height of the samples in to account, Figure 3.14, the sheet resistance of the tracks can be obtained. From Figure 3.14 it can be seen that the ink tracks follow a much clearer relationship to power and cure speed. As the power increases the sheet resistance decreases with the D1 and D15 having very similar results to that of the D58 for higher velocities and powers. The results of the sheet resistance go some way to indicating why the resistivities of the ink tracks when laser cured are so high. The thickness of the track is generally four to five times greater than that of the oven cured tracks, with average heights in the region of 170 µm, compared with 47 µm. Note that the height of the laser cured track is greater than that of the starting track, pre-cure. During the process, no material is added and so the laser creates a less dense ink track. This means that it is more porous than that of the oven cured tracks. The sheet resistance is similar to that of the oven cured tracks with a low of 0.026 Ω/Sq compared to the oven cured low of 0.012 Ω/Sq when cured at 180°C for the D58 ink. By taking into account the different heights, the sheet resistance demonstrates that the actual resistivity of the laser cured track is similar, but greater, to that of the oven cured.

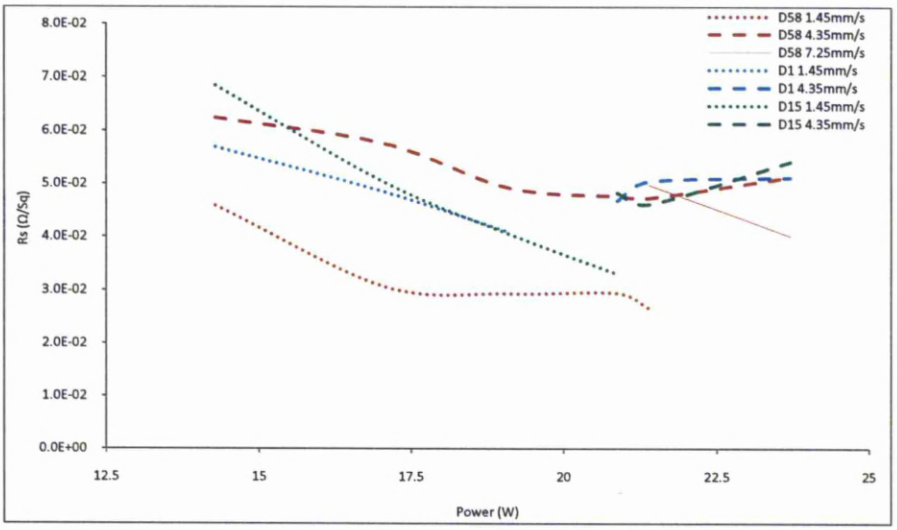

Figure 3.14: The Sheet resistance of the ink tracks. It is the resistivity divided by the track height.

Each ink acts slightly differently in the way it behaves whilst it is being irradiated with a laser. The D1 and D15, inks with the dopents, cannot be cured at 5 mm/s within the power rating of this Synrad laser. The results put upper and some lower limits on the curing parameters of the inks. The upper limit is governed by the substrate since that breaks before the ink appears to burn. Other substrates such as paper and CFC will have different values. The D58, d1 and D15 inks were able to be cured with a dynamic energy intensity of 6.27 J/mm^2 at 1 mm/s. The D1 failed at 9.17 J/mm^2 where as the D15 failed at 9.4 J/mm^2 and the D58 failed at 10.41 J/mm^2. Increasing the velocity to 4.35 mm/s extra passes were required to cure the tracks. Successful cure of the D58 ink occurred after a minimum of three passes at 14.28 W giving a dynamic energy of 2.09 J/mm^2. For the D1 ink 10 passes were required at 20.88 W and only 7 passes for the D15, a dynamic energy density of 3.06 J/mm^2. An upper limit was not achieved for the D58, D1 or D15 ink. At a velocity of 7.25 mm/s it was only the D58 which was able to be cured and this required a pass number of ten and a minimum dynamic energy intensity of 1.88 J/mm^2.

3.4.2 Temporally Dynamic Resistance and Temperature

The temporally dynamic measurements were taken using the results of the laser curing trials. Two different curing regimes were tested for each ink. The D58 ink was tested using the parameters of 17.05 W, 1.45 mm/s, 2 passes and 20.88 W 3.35 mm/s and 4 passes. Two passes were used for the D58 to see what the affect of the second pass would be on

the resistance. The D1 was tested using 17.05 W, 1.45 mm/s, 1 pass and 20.88 W, 4.35 mm/s and 10 passes. The D15 ink was tested using 17.05 W, 1.45 mm/s, 1 pass and 20.88 W, 4.35 mm/s and 7 passes. The results of the experiment can be seen in Figure 3.15.

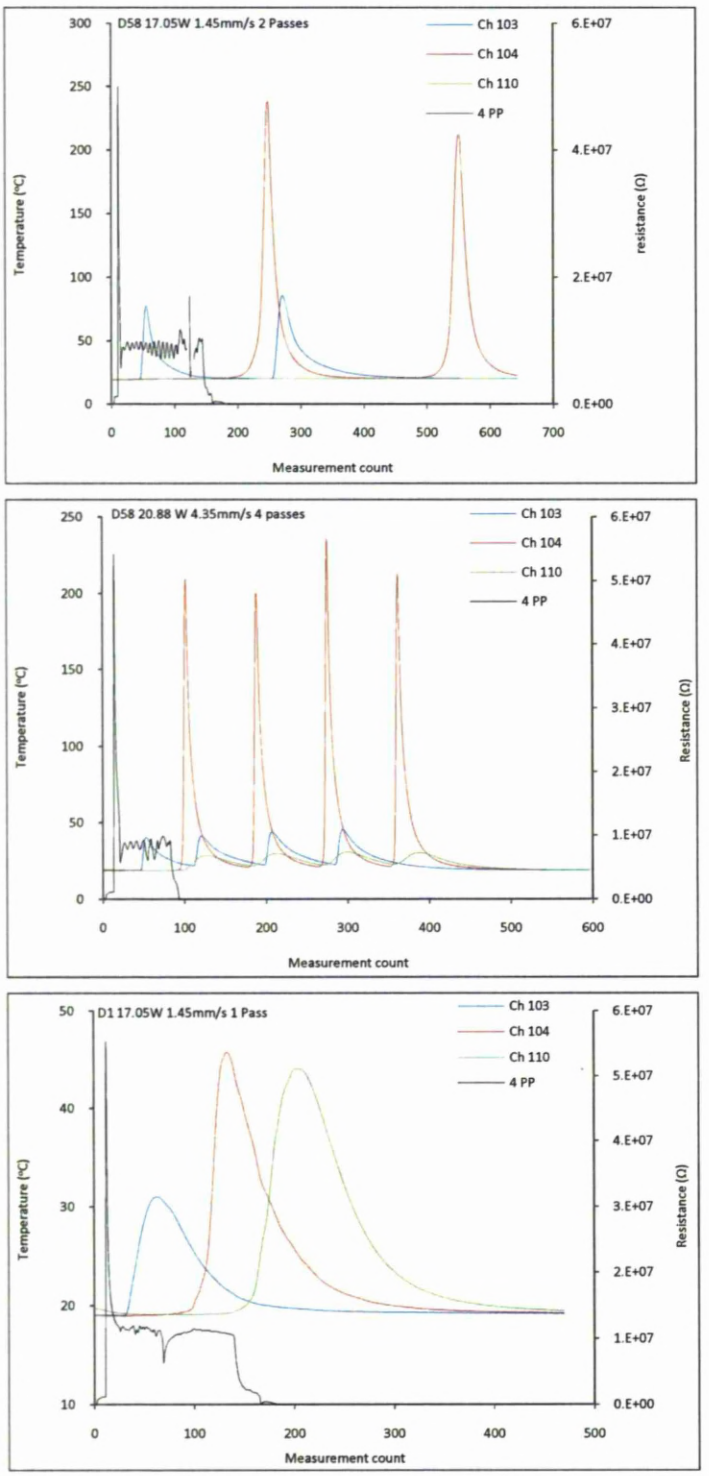

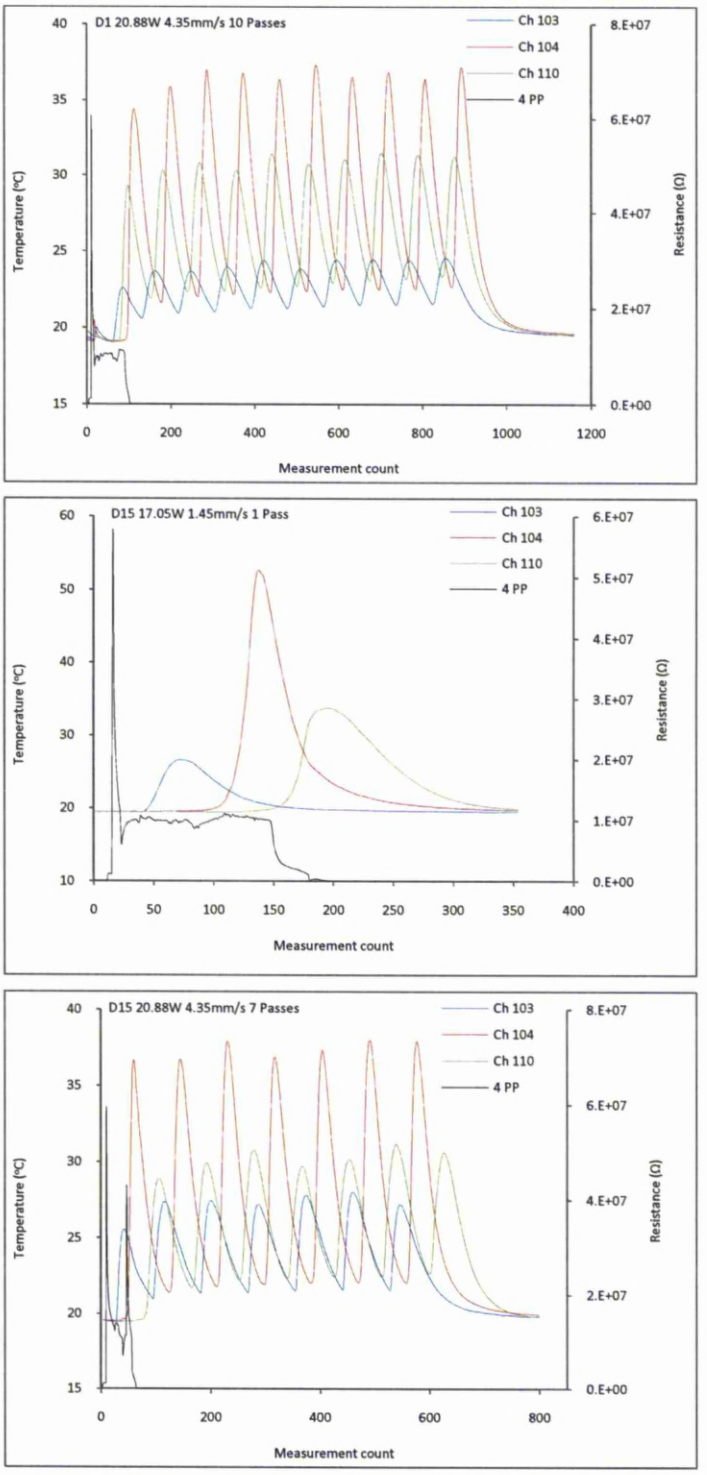

Figure 3.15: Results of the dynamic R and T measurements for the three different inks. The horizontal axis is measured in counts. A single count is one measurement.

Looking at the results, it is immediately apparent that there are significant differences between the D58 ink and the D1 inks. The temperature of the D58 ink hits a high at 238°C for the 1 mm/s run and 235°C for the 3 mm/s run. This is in stark contrast to the D1 and

D15 inks which hit a high of 46°C and 52°C respectively for the 1mm/s run and 37°C and 38°C for the 3mm/s run. The D58 is reaching a substantially higher temperature. The substrate is not heating up as much however, where the substrate temperature of the D58, D1 and D15 inks for the 1 mm/s run is 20°C, 44°C and 34°C respectively. For the 3mm/s run it is 31°C, 31°C and 31°C. These results back up the assertion stated earlier in section 3.4.1 that the differences in the volumetric heat capacity, and hence the thermal diffusivity, is causing the substrate to crack. Here the substrates for the D1 and D15 inks a significantly hotter than that of the D58, at least for the 1 mm/s run. In doing so it seems the inks are not heating up as much, as would be expected as the energy is being transferred to the substrate. It should be noted that no cross-linking should occur at the temperatures witnessed here, however there is an associated resistance drop that can only occur with cross-linking. Further to this the D58 ink actually increases in temperature with and increased power and processing speed where as the D1 and D15 inks see a drop in the maximum temperature obtained. Again this would back up the assertion about thermal diffusivity as it means the D58 is retaining the heat the laser generates more efficiently.

The resistance is high at the start of the runs for all three inks, after the laser has traversed all four points of the four point probe, the measured resistance is dropping almost instantaneously. This means that the resistance of the ink is low as soon as a single pass occurs of the laser and that the subsequent passes are required to consolidate the ink further on the higher velocity runs: curing the ink throughout its depth. A thin surface layer is being created that is cured, but beneath it, the ink is still not cured. This has been seen on many samples where it appears to be cured, but the surface layer slides off. This effect is more readily seen the greater the thermal conductivity of the substrate, as was investigated by E.Fearon et al [5].

From Figure 3.15 it can be seen that the first pass of a laser cures the whole track or just the surface layer creating a low resistance path as measured by the four point probe. In Figure 3.16 this area has been expanded and clearly shows that the track goes through an increased resistance phase as the laser heats it up[2], due to hotter objects in general displaying higher resistance. As the track cools it then has a new resistance low. Therefore the extra passes not only help to increase consolidation, but also reduce the resistance as it does so, decreasing the overall resistivity of the track.

[2] Note that the thermocouple Ch 104 is placed in the ink after the fourth wire of the four point probe.

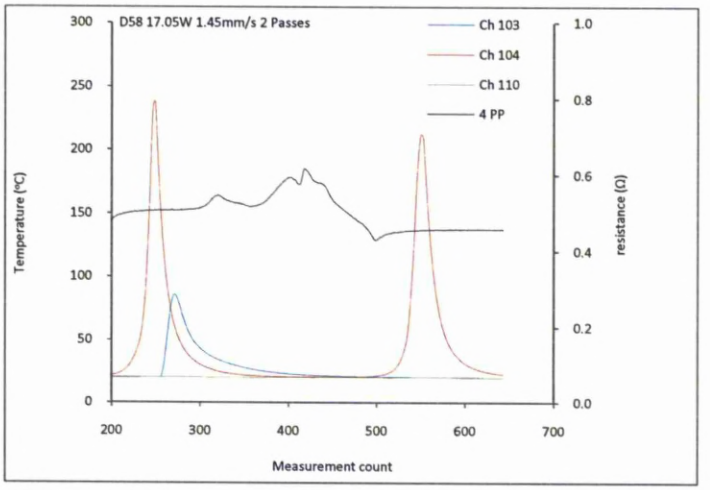
D58 17.05W 1.45mm/s 2 Passes
Ch 103
Ch 104
Ch 110
4 PP
Temperature (°C)
resistance (Ω)
Measurement count

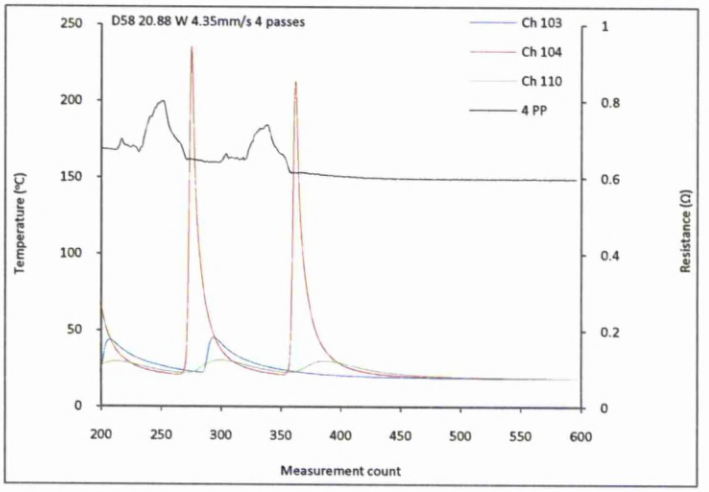
D58 20.88 W 4.35mm/s 4 passes
Ch 103
Ch 104
Ch 110
4 PP
Temperature (°C)
Resistance (Ω)
Measurement count

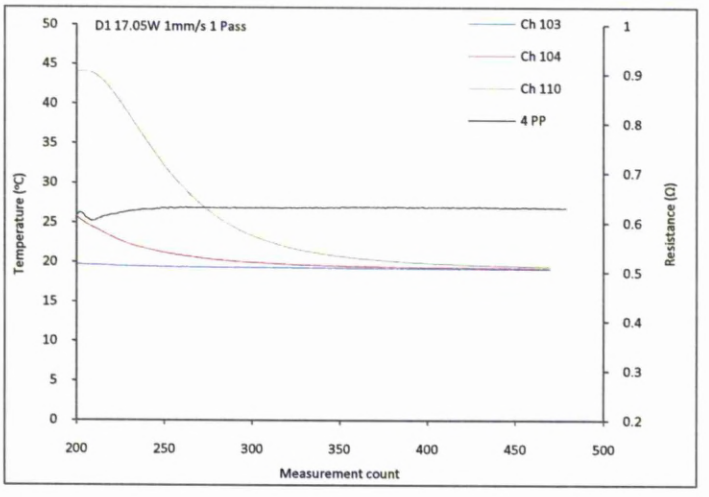
D1 17.05W 1mm/s 1 Pass
Ch 103
Ch 104
Ch 110
4 PP
Temperature (°C)
Resistance (Ω)
Measurement count

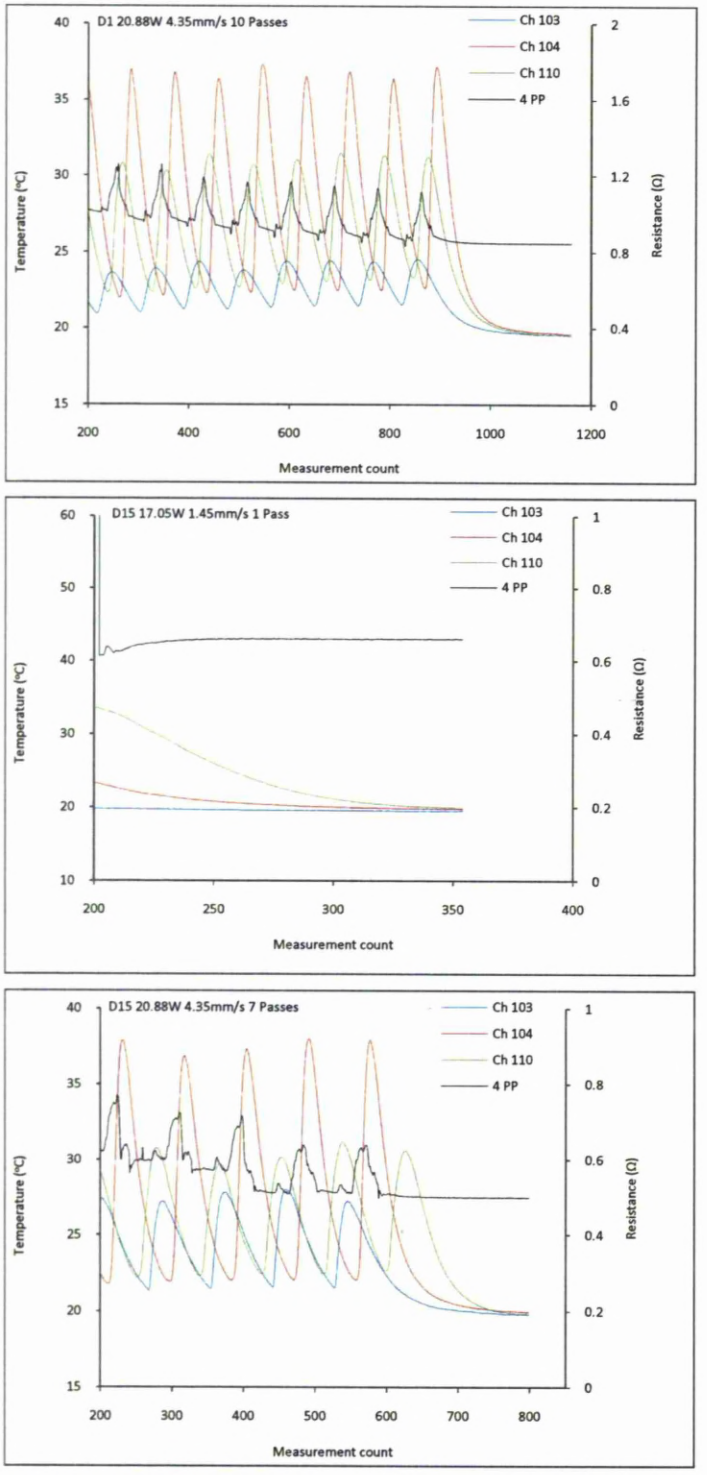

Figure 3.16: Graphs of the results shown in Figure 3.15, concentrating on measurements after the first pass of a laser.

3.4.3 Resin absorption

Table 3.3: Table of the power measurements found when conducting the resin absorption test.

Power	3
Power (Lens)	2.6
Power (Lens + Resin)	1.2

The height of the resin deposited on the window had an average height of 40.62 μm. To calculate the absorption coefficient of the resin the Beer-Lambert law is used, equation 3.3, where the absorption coefficient is α, equation 3.4.

$$I = I_0 e^{-(\frac{4\pi kd}{\lambda})} \quad 3.3$$

$$\alpha_\lambda = \frac{4\pi kd}{\lambda} \quad 3.4$$

I= the received intensity, I_0=the starting intensity, k = the extinction coefficient, d = the thickness of the material the beam is travelling through and λ=the wavelength of the radiation. Rearranging the equation to make α the subject, and using the quoted values gives an absorption coefficient α=0.78 m^{-1}, with an extinction coefficient k=1.61x10^{-2}.

References

1 Einstein, A., *"On the Quantum Theory of Radiation" - English Translation.* Physikalische Zeitschrift, 1917. 18: p. 121-128.

2 R. Ladenburg, H. Kopfermann, *"Research on the Anomalous Dispersion of Gases" - English Translation.* Physikalische Zeitschrift, 1928. 48: p. 26-57.

3 Maiman, T.H., *"Stimulated Optical Radiation in Ruby".* Nature, 1960. 187: p. 493-494.

4 *"Laser Materials Processing"*, W. M. Steen, 3rd Ed., Springer-Verlag, London, 2003. ISBN 1852336986.

5 E.Fearon, T. Sato, D. Wellburn, K. G. Watkins, G. Dearden. "Thermal effects of substrate materials use in the laser curing of particulate silver inks". Proc. LANE 2007, University of Liverpool.

4 Thermal Analysis of Polymers

This Chapter introduces the idea of using thermal analysis techniques to investigate the properties of polymeric materials and the experimental method employed for this investigation. It is split in to three main sections. The first introduces some common techniques used and how to interpret the results and the analytical tools that will be used in this investigation. The second section introduces the equipment and methodology utilised throughout this investigation, and the third section presents the results, analysis and discussion from these experiments.

4.1 Introduction

The Definition of *Thermal Analysis*, by the *International Confederation of Thermal Analysis and Calorimetry* (ICTAC) [1,2] is "a group of techniques in which a property of a sample is monitored against time or temperature while the temperature of the sample, in a specified atmosphere, is programmed."
It should be noted that though the programmed temperature for a given instrument maybe very accurate, the sample temperature may vary by as much as a few degrees due to exothermic or endothermic reactions and phase transitions induced by the programmed temperature. As it can be seen from the ICTAC definition, thermal analysis is a broad term that covers many analysis techniques, Table 4.1.

Table 4.1, is a list of the more common thermal analysis tools used. Though it lists the individual techniques, it is possible to run concurrent analytical techniques which share the same atmosphere and oven and hence the same sample. A common example is the combination of TGA and DTA, which was used in this research.
Within the context of the research carried out, TGA was used to look at the effect of temperature on mass loss; solvent evaporation, cross-linking and then thermal degradation and combustion of the polymer matrix. Along with this mass loss, heat flow changes were also measured, simultaneously combining TGA, DSC and DTA analysis for a single sample. For this reason, explanations of how the thermal analysis tools work will be limited to TGA, DSC and DTA.

Table 4.1: List of some more common thermoanalytical methods [1].

a) Change induced by an imposed magnetic field gradient
b) Power-compensated DSC
c) Heat Flux DSC
d) Absorption, fluorescence, Raman, etc. Non-optical forms[1] of spectroscopy, eg, NMR, ESR, Mössbauer, etc, are also applicable.

Property	Technique	Acronym
Mass	Thermogravimetry	TGA,TG
Apparent Mass[a]	Thermomagnetometry	TM
Volatiles	Evolved gas detection Evolved gas analysis Thermal desorption	EGD EGA
Radioactive decay	Emanation thermal analysis	ETA
Temperature	Differential thermal analysis	DTA
Heat[b] or heat flux[c]	Differential scanning calorimetry	DSC
Dimensions	Thermodilatometry	TD
Mechanical properties	Thermomechanical analysis Dynamic mechanical analysis	TMA DMA, DMTA
Acoustical properties	Thermosonimetry (emission) Thermoacoustimetry	TS
Electrical Properties	Thermoelectometry (resistance) (voltage) (current) (dielectric)	DETA, DEA
Optical properties	Thermooptometry (spectroscopy)[d] Thermoluminescence (emission) Thermomicroscopy (structure) Thermoparticulate analysis	TPA

4.1.1 Differential Thermal Analysis (DTA)

"A technique in which the difference in temperature between the sample and a reference material is monitored against time or temperature while the temperature of the sample, in a specified atmosphere, is programmed." [2]

DTA was first developed by Roberts-Austen over a hundred years ago [3], a reference sample and a test sample are held in two separate pans that are symmetrically situated within the oven; minimising any convection differences or thermal gradients. As the programmed thermal cycle is started, there will be no difference between the two samples until the test sample goes through a chemical or physical change. When the sample goes through a transition point, the temperature will depart from the baseline set by the reference sample and then return to the baseline once the transition has been completed. There will either be an endothermic reaction; where the temperature decreases with respect to the reference sample or an exothermic reaction; where the temperature increases with respect to the reference sample. There may also be a change in the specific

heat capacity of the test sample, and this would be shown as a change in the gradient of the ΔT verses time or temperature plot.
Modern systems generally use matched thermocouples that are in contact with the sample or the sample container, and one is placed in each of the reference and test samples. The output of the differential signal is amplified and then sent to a data logger system.

4.1.2 Differential Scanning Calorimetry (DSC)

"A technique in which the heat flow rate (power) to the sample is monitored against time or temperature while the temperature of the sample, in a specified atmosphere, is programmed" [2]

DSC was first developed in 1964 by E S Watson et al at Perkin-Elmer [1,3] and was a major development in thermal analytical tools. Soon after two main types of DSC came on to the market. The first being a power compensation DSC made by Perkin-Elmer. The Perkin-Elmer 1020 series thermal analyser was tested by C.Y. Zahara et al [4] and they describe calibration methods for this early DSC system along with methods for working out the heat capacities of unknown samples.

The concept of operation of the power compensation DSC, is to keep the temperatures of the reference sample and the test sample the same. This is achieved by having the thermometers (typically platinum resistance thermometers) in a bridge circuit so that any change in temperature of the sample is compensated through a corresponding change in current flow to drive the heating coil to keep them at the same temperature. This means that, depending on whether an exothermic or endothermic reaction had occurred in the test sample, current will be given to either the test or reference sample heater. This technique is useful for calculating the change in enthalpy, ΔH, and hence working out the energy absorbed or emitted by the system. It can be found through the integral of the power required to bring the samples up to the same temperature [1] from the fact that the amplitude of a transition denotes the power at each point in the transition, hence the integral of that amplitude will give you the total energy required to make that transition [3].

The second type of DSC machine, works on the principle of heat flux. This system is similar to that of a DTA machine, but the change in temperature that is found, is converted to a

change in heat flow when plotted as a graph. This is conducted internally through software and component calibration and is system specific. Both systems are accurate, with enthalpy data having an accuracy of around ± 1-2%. The heat flux DSC instruments can operate up to 1500°C, whilst the power compensated DSC can generally operate up to 750°C.

When analysing data from a DTA/DSC experiment, it is important to remember that the sample history will affect the enthalpy change witnessed from a material and possibly the end product. In the case here, three samples are being investigated. A comparison is being made between the uncured, oven cured and laser cured inks. For the uncured ink, the enthalpy change witnessed will be directly due to solvent evaporation, cross-linking and thermal degradation stages. As the sample is taken to higher temperatures past the polymer thermal degradation stage, any further changes in enthalpy witnessed will be due to a change in phase or change of state of the silver particulates within the inks. For the oven cured and laser cured samples, the solvent evaporation and cross-linking stages should not be witnessed as these stages have already occurred during the curing process.
With oven curing, both the curing (heating up) and cooling times are far greater than that of the laser curing process. The ink will cure gradually as the sample temperature rises uniformly and then cool uniformly as it is removed from the oven. This is in contrast to the laser curing process where the interaction time maybe less than a second. Here the ink is rapidly heated up, cured and then cooled in an anisotropic manner as the beam traverses along the track, and hence it may induce greater stresses within the ink as it cures and cools. These stresses would be visible through different enthalpy changes, whether in magnitude or position with respect to temperature, within the respective samples as they go through the thermal analysis heating cycle.
It should be noted here that Watson et al state the DSC has an analytical freedom from effects of sample geometry when conducting analysis, and this is demonstrated in their paper [3]. A change in the enthalpy graph may occur due to geometry, but the total energy input/output (area under the graph) will be equal for two materials of the same composition, but different geometries. As tested by Watson et al. Also they go on to say that the DSC takes results that is of the fundamental energy value undistorted by other sample properties such as thermal conductivity.

4.1.2.1 Heat capacity at constant pressure from first principles

As an unknown composite material is being tested, exact figures of the heat capacity cannot be found or referenced or the change in heat capacity as the material cross-links and cures. C.Y.Zahara et al [4] discusses two methods of calculating the heat capacity of unknown material using a Perkin-Elmer DSC system. The first technique is the dynamic or scanning method and the second is the integration or enthalpy method. It is better to use the integration or enthalpy method to remove any uncertainties of thermal lag within the sample and experimental setup, as it is a relative calculation [3,4]. Before going in to the detail of calculating the heat capacity from the DSC results using the enthalpy or scanning method, the required thermodynamic relationships will be introduced.

In thermodynamics, the state of a simple thermodynamic with a specific mass can be described in terms of three thermodynamic properties, temperature T, pressure P, and volume V. Therefore any system is a function of the three, $f(T,P,V)$. From the first law of thermodynamics, *"If a thermally isolated system is brought from one equilibrium state to another, the work necessary to achieve this change is independent of the process used"* **[5]**, we get

$$đQ = dU + PdV \qquad (1)$$

If a substance is then taken from an initial temperature T_i, to a final temperature T_f, resulting in a temperature difference ΔT with a change in energy flow Q, and change in internal energy U at constant pressure P, a resultant volume change will occur, ΔV. Equation 1 then becomes

$$\left(\frac{đQ}{dT}\right)_P = \left(\frac{\partial U + P\partial V}{\partial T}\right)_P \qquad (2)$$

The quantity, $đQ/dT$ is known as the heat capacity, *"The heat capacity C of a system is defined as the limiting ratio of the heat introduced reversibly into the system divided by the temperature rise"*, equation 3, [5]. From this definition the heat capacity can be interpreted as the amount of energy required to raise a substance by 1K, or the amount of energy that a substance will absorb before a change in temperature is witnessed. It has units of J/K.

$$C = \lim_{\Delta t \to 0} \left(\frac{Q}{\Delta T}\right) = \frac{đQ}{dT} \quad (3)$$

The heat capacity, as shown in equation 3 does not take into account the mass of the material, and in this sense is dimensionless. Therefore, we need to introduce the specific heat capacity, c, that takes in to account the mass of a substance, equation 4,

$$c = \frac{1}{m}\left(\frac{đQ}{dT}\right) \quad (4)$$

with units J/KgK. From equation 4 it can be seen that the heat capacity can be found by multiplying the specific heat capacity by the mass of the sample that has been tested.

A new state function will now be introduced, the enthalpy *H*, of a system. The enthalpy is the total energy of a system in a specific state, *PV*. When the system changes from one state to another there is a change in the energy of the system. This change is described as a change in enthalpy and is similar to that of the heat flow *Q*, however the enthalpy contains the heat flow term within it and unlike heat flow (which is not a state function) it is path independent. The enthalpy is thus

$$H = U + PV \quad (5)$$

$$dH = dU + PdV + VdP \quad (6)$$

As $\Delta P \to 0$, $VdP \to 0$ and hence the VdP term disappears for the DSC scenario since we are talking about an isobaric change of state, equation 6 becomes

$$dH = dU + PdV \qquad (dH \to đQ, as\ \Delta P \to 0) \quad (7)$$

If we substitute for enthalpy in equation 2, we get

$$\left(\frac{đQ}{dT}\right)_P = \left(\frac{\partial H}{\partial T}\right)_P \quad (8)$$

Therefore

$$C_P = \left(\frac{\partial H}{\partial T}\right) \quad (9)$$

and

$$c = \frac{1}{m}\left(\frac{\partial H}{\partial T}\right) \quad (10)$$

Now that we have the heat capacity C_P and the specific heat capacity c in terms of enthalpy, it is now possible to calculate the heat capacity of the sample from the data set given by the DSC using the enthalpy or dynamic method.

4.1.2.2 Dynamic/scanning method

As stated before, the dynamic or scanning method for calculating the thermal capacity a material from DSC data is one method. This is a well known technique that can be accurate to ±5% and as low as 1% when proper experimental procedures are followed. Figure 4.1 illustrates this technique.

An empty sample pan is heated at a constant rate of temperature change between two isothermal temperatures. The same cycle is carried out with a sample of known thermal capacity in the sample pan, such as zinc or tin, two DSC standards [2]. Then the same procedure is carried out with the sample of interest. The specific heat capacity can then be calculated using equation 11 [10].

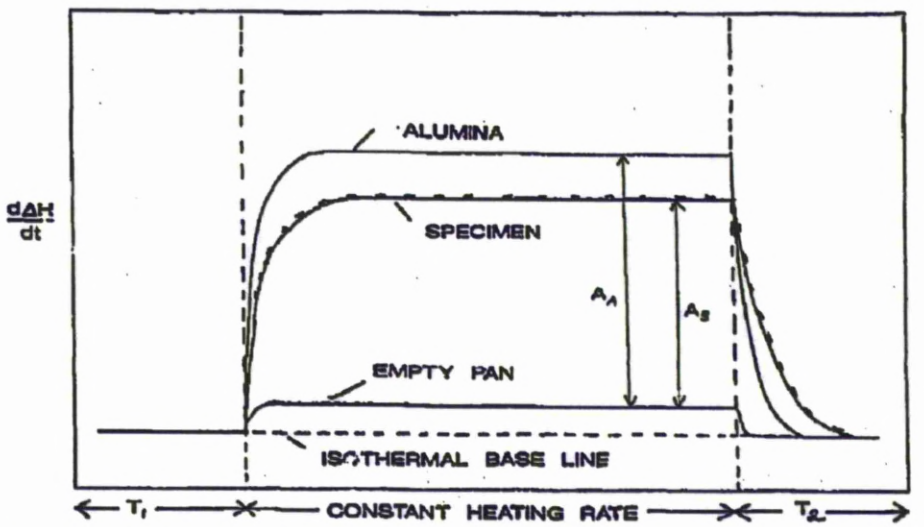

Figure 4.1: The dynamic method for specific heat capacity determination by DSC, power v temperature. In this illustration the author has used alumina as the reference sample.

$$C_P = C_{P,R} \times \left(\frac{m_R}{m_s}\right) \times \left(\frac{A_s}{A_R}\right) \tag{11}$$

Where A_R and A_s are the amplitudes of the reference sample and sample respectively, and $C_{P,R}$ is the reference sample thermal capacity at constant pressure and m_R and m_s are the respective masses of the two samples.

Errors in this method can occur due to vibration or movement from the purge gas, a change in the thermal resistance between pan and sample or between the calorimeter and sample pan.

4.1.2.3 The integration/enthalpy method.

The problems and uncertainties associated with the scanning method can be overcome by using the integration or enthalpy method [4, 6], and negates any issues that may arise due to mass loss (when conducted along with TGA) and their associated change in heat capacity [6]. In this method, the DSC is used as a calorimeter and the energy required to compensate for the constant rate of temperature change measured. In this method the sample is taken between two isothermal points, as in the scanning method, and the same is done for an empty pan. The graphs are plotted and the two curves are integrated with respect to their isothermal baselines, adjusted for the temperature change that occurred during this period. From this the mean specific heat capacity of a sample (and hence the heat capacity when using a DSC simultaneously with a TGA) can be found between two temperature points.

$$C_{P,s}(T_i, T_f) = K\frac{\int_{t_i}^{t_f}\left(\frac{dQ}{dt}\right)_s dt - \int_{t_i}^{t_f}\left(\frac{dQ}{dt}\right)_e dt}{(T_f - T_i)} \tag{12}$$

$$= \frac{\Delta H_s - \Delta H_e}{(T_f - T_i)} \tag{13}$$

Where t_i and t_f are the respective initial and final times where the heat capacity is being calculated for, and the s and e subscripts denote sample and empty pan respectively. K is the calibration factor which is calculated by using a calibration sample with known enthalpy change at a certain temperature [4, 7, 8]. The value of the known sample recorder is then compared to actual values found in literature and then normalised to give a ratio.

$$K = \frac{C_{p(lit)}}{C_{p(meas)}} \tag{14}$$

Where ΔH_{lit} is the value found in literature, and ΔH_{meas} is the measured value from the system.

From equation 13 the mean specific heat capacity of the sample can then be found using equation 15 [4], from the calculated enthalpy change.

$$C_{P,s} = \frac{K\Delta H}{m_s(T_f - T_i)} \tag{15}$$

If required a calibration test should also be conducted with a known sample of known purity (usually 99.999%) so that a temperature calibration can be conducted on the equipment to be used, Cammenga et al [9] recommend a set procedure and suitable samples.

4.1.2.4 First order transition measurement

A first order transition is one in which the first derivative of the free energy of a phase change is discontinuous with respect to a thermodynamic variable. In a first order transition, there is an associated enthalpy change to the system as it goes through the phase transition, i.e. from a liquid to a gas. They are associated with mix phase systems due to the nature of finite energy transfer to a system. Therefore the system as a whole does not heat up instantaneously or uniformly. There are two types of first order transitions as stated by J H. Flynn [6].

The first is a transition in which a sharp change in the enthalpy is seen, such as that witnessed for melting or boiling of a pure sample with a high thermal conductivity. This type of transition is said to be heat flow limited, when measured by a DSC. This is because the increment in temperature that it takes for the heat flow between the system and the sample to match the energy change of the transition, is greater than the increment in temperature to cause the transition.

The second type of first order transition is a diffuse transition and hence the DSC peak is limited by the kinematics of the sample. This is because the sample will have a larger temperature range over which the transition occurs and so the energy flow, equivalent to the transition energy, between the system and sample can occur within this temperature

range. Examples of this are composite materials that have an overlapping phase transition, long chained polymers or chemical reactions such as cross-linking.

The relevant enthalpy changes will be calculated using the step function technique as stated by Guttman and Flynn [10] this technique is used as the isothermal baseline is dynamic and significantly different before and after a transition occurs.

4.1.2.5 Isothermal baseline

In the previous discussions, the isothermal baseline has been mentioned. This is something of a misnomer when talking about DSC as the measurement is taken over a dynamic temperature range. There are two isothermal baselines. The first is the baseline that is measured when an empty pan run is conducted over the same dynamic temperature range as that for the sample, and needs to be taken into account when trying to calculate the correct enthalpy change-calibration factor. The second is the thermal baseline that is measured before and after a transition occurs, and hence a non-arbitrary one needs to be placed in during this transition so that the correct area can be calculated and hence the heat capacity deduced. How this baseline is calculated is often up to the author's discretion. For the purposes of this investigation, the analytical technique as described by Charles M Guttman and Joseph H Flynn [10] will be used in determining the baseline and heat of a transition [6]. Figure 4.2 illustrates a scenario in which a dynamic baseline is present during an endothermic first order transition.

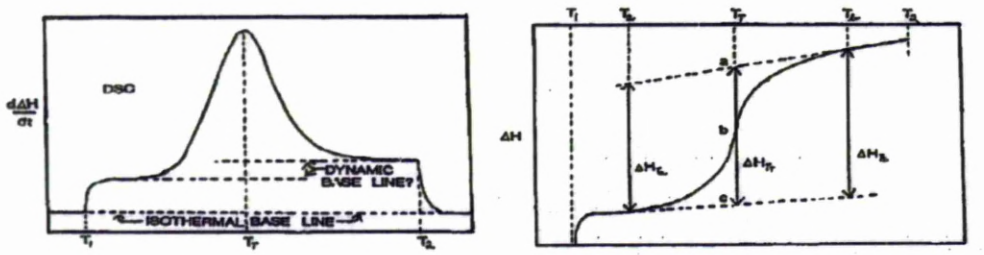

Figure 4.2: Schematic of a DSC trace in which there is a dynamic base line, and the integrated enthalpy change as a function of time. Both plots are against temperature (constant heating rate).

If the integrated value of the enthalpy change between the baseline and the curve is plotted against temperature as in Figure 4.2, then it is easy to work out the enthalpy change (and hence the heat capacity using the "integration" method) of a first order transition. Further to this, using the "lever rule" it is possible to calculate the fractional conversion of the transition at any stage along the integrated curve [10]. In this example the fractional

conversion of this transition at T_T is bc/ac, and the reaction enthalpy is obtained from the vertical line ac.

To create the correct baseline and hence calculate the correct ΔH from the scenario above, where there is a significant change in the heat capacity during the first order transition, Guttman and Flynn [10] put forward a step function approach. As the heat capacity is derived from the enthalpy change during the transition, and in turn the enthalpy is found through the integration of the DSC curve (using the integration method), therefore the accuracy of the result will be dependent on the accuracy of the calculated area (assuming that the correct baseline has been chosen). The step function approach can be used to calculate this area once the appropriate baseline has been chosen.

4.1.3 Thermogravimetry/Thermogravimetric Analysis (TG/TGA)

"A technique in which the mass of a sample is monitored against time or temperature while the temperature of the sample, in s specified atmosphere, is programmed." [2]

TG and TGA are two terms for the same process and both are accepted by ICTAC [2]. The process concerns itself with measuring the mass of a sample as it is heated up. The typical setup of a TGA contains a microbalance, a furnace, the programmer controller and a computer or data acquisition system [1]. In general the sensitivity of the micro balance is 1μg, and the heating cycle within the furnace can reach temperatures of up to 1200-1700°C. The former is generally sufficient for most polymer applications. TGA has become a good way of analysing polymers and their thermal stability, showing temperatures at which volatile solvents are removed or when it thermally degrades. Some compositional analysis can also be conducted, though it cannot tell you about cross-linking or chemical change.

When analysing TGA data it is common practice to plot mass loss (%) against temperature or time depending on what is trying to be conveyed. It is also good practice to do a derivative TGA graph (DTGA) as this enhances resolution and gives a so called "fingerprint" of the decomposition process and displays the rate of degradation [1].

4.1.4 Simultaneous Techniques

As thermal analysis techniques have evolved. More and more sophisticated instruments have been developed. Many instruments now offer parallel analysis- where two separate samples are treated at the same time and go through an individual thermal process; concurrent/combined analysis- where two separate samples are used, but the analysis is conducted in a common atmosphere or thermal environment, and simultaneous analysis- where a single sample is used in a defined thermal and atmospheric environment. Some of the simultaneous analytical instruments available currently are: TGA/DTA/DSC, TGA/DTA/FTIR, DTA (DSC)/EGA (EGD). Conducting simultaneous experiments helps to increase the information about the sample being tested and allows for a greater understanding. For example correlating mass loss to a change in thermal conductivity/heat capacity and when an endothermic or exothermic reaction occurs if mass loss also occurs.

4.2 Experimental Setup

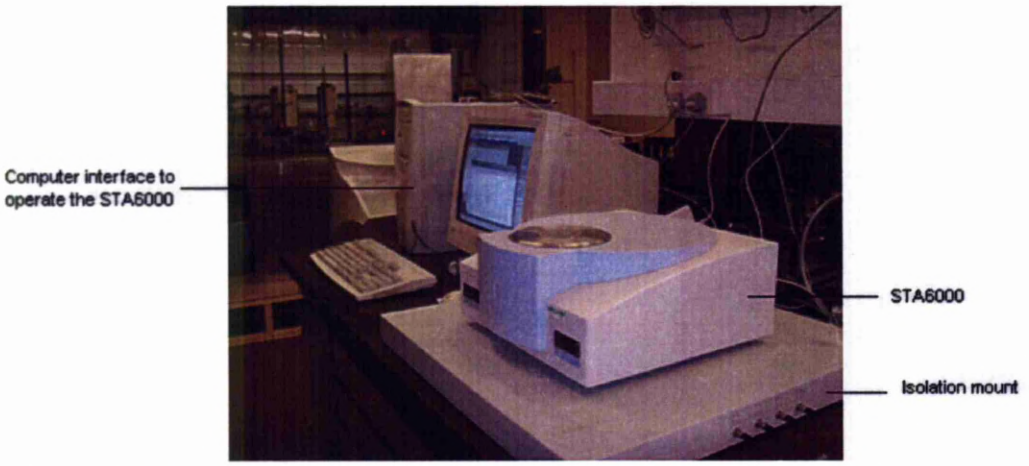

Figure 4.3: A picture of the layout of the STA6000, with the computer interface on the left and the STA6000 on the right mounted upon an isolation table. This reduces the effect of vibrations on the experiments.

To investigate how the inks behaved under controlled temperature conditions, thermal analysis was conducted. A Perkinelmer STA 6000 was used, Figure 4.3. This system simultaneously measured the weight loss (TGA) and the enthalpy change (DSC/DTA) [11] of the sample as it underwent a heat cycle. The DSC system is a heat flux DSC. The Perkin-

Elmer STA 6000 has a corrosion resistant platinum pan holder, Figure 4.4. It uses alumina pans Figure 4.5a with a capacity of 180µl which are loaded with the sample and placed in the pan holder. The pan is placed in to the pan holder vertically, Figure 4.5b, on to the single beam balance. The balance is housed behind stainless steel walls, which act as a heat sink so that the balance is virtually isolated from the furnace. The lid is then placed over the furnace which aids the isothermal heating zone, Figure 4.5c.

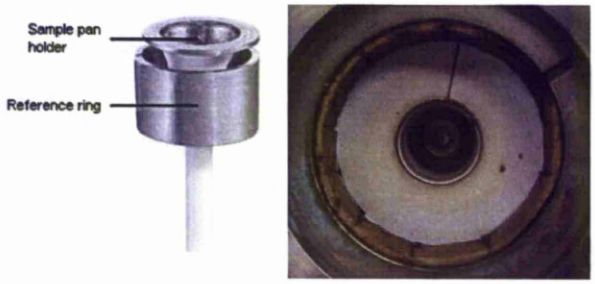

Figure 4.4: Image of the Pt pan holder and reference ring as used in the STA 6000. The left is a side on view [11] whilst the right is a bird`s eye view looking in to the furnace. The pan holder can be seen in the centre of the image.

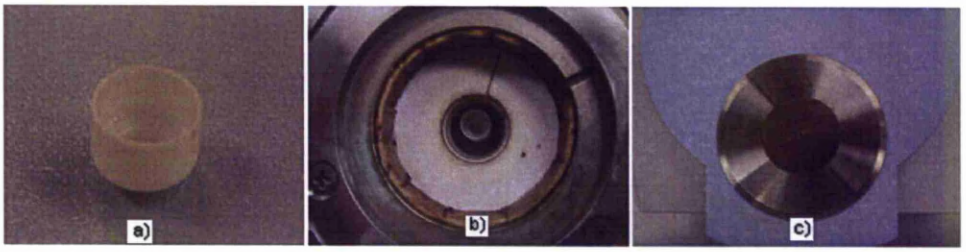

Figure 4.5: a) a close up image of the alumina crucible used for the experiments, b) shows the crucible inside the STA6000 in position, placed within the pan holder, c) shows a bird`s eye view of the lid in place, over the furnace. The small hole in the centre is the vent hole, where the purge gas and any by products of the process escape.

The sample is heated by an alumina furnace which is corrosion resistant and has a large isothermal zone which helps maintain the desired temperature and allows for good temperature reproducibility. A SaTurnA sensor measures both the sample and reference ring directly and the thermocouples are Pt-Pt/Rh type R. There is a built in mass flow controller which monitors and controls purge flow rates and allows for different purge gases to be utilised during the thermal cycle. The system has a temperature range of 15-1000°C with an accuracy and reproducibility of ± 0.5°C and a max sample weight of 1500mg with an accuracy of 1µg.

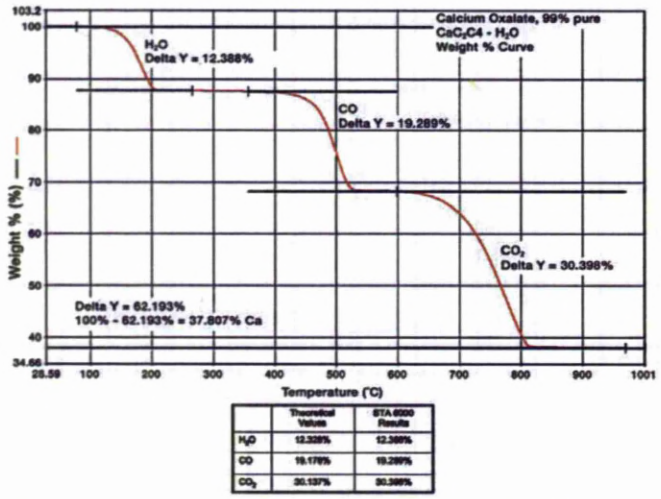

	Theoretical Values	STA 6000 Results
H_2O	12.329%	12.388%
CO	19.179%	19.289%
CO_2	30.137%	30.398%

Figure 4.6: TGA verification using Calcium Oxalate as tested by Perkinelmer [11].

The system is calibrated in the factory against calcium oxalate which has three distinct weight loss regions as it goes through a thermal cycle. The first is the loss of H_2O at around 100°C, the second is the loss of CO at around 400°C and the third is the loss CO_2 at around 600°C. The calibration was conducted using 15mg of calcium oxalate and nitrogen was used as the purge gas with a temperature rise time of 20°C/min. The graph, Figure 4.6, is comparable to that of the theoretical values of calcium oxalate.

4.2.1 Experimental Method

The Perkinelmer STA 6000 was used to investigate how different curing techniques affected the composition of the inks and there thermal properties. As stated previously, the conventional method of curing these inks was to use an oven. The manufacturers quoted curing regimes were 130°C for 20 minutes. For better conductivities, the cure time could be extended and the temperature raised. The cross-linking process would start at 90°C and the resin should be fully cross-linked at 180°C.

Within this investigation, the different inks were investigated, table 4.2, the plain D58 (C2070801D58) ink as sold on the commercial market by the manufacturers. And then the 1% carbon doped ink and the 1% graphite doped ink, D1 (C2061130D1) and D15 (C2070801D15) respectively, as specially created for the laser curing process.

The use of the uncured sample was tested first to be used as a bench mark of how the inks behaved and acted as it went through the various stages of cure, degradation and phase change/melting and how the dopents affected this process.

Stage 1: Removal of solvents
Stage 2: Cross-linking and loss of functional groups
Stage 3: Thermal degradation of polymer
Stage 4: Phase change/Melting of silver particles

The oven and laser cured samples were then tested to compare how the different processing techniques affected the cross-linking process and the end cross-linked product. Using the two DSC and TGA techniques it was possible to determine whether there were any compositional differences between the two cured inks and how the carbon and graphite dopents affected the thermal properties.

Table 4.2: Table of inks tested using the Perkinelmer STA 6000 DTA system.

Ink	Uncured	Oven Cured	Laser Cured
D58	√	√	√
D1	√	X	√
D15	√	X	√

Each sample was taken through the same thermal cycle. The sample was heated from 30°C to 950°C at a rate of 5°C/min and then held at 950°C for 10 minutes. The sample was then cooled at a rate of 10°C/min to 30°C.

4.2.1.1 Calibration runs

In order to assess the accuracy of the Perkin Elmer STA6000 and to get the correct calibration factor, It was required that a couple of calibration runs were conducted. Two distinct runs were necessary. The first was an empty pan run, where the alumina pan was placed inside the pan holder and put through a thermal cycle. The thermal cycle that the pan underwent was a temperature rise of 5°C/min up to 995°C and held there for 10 minutes and then cooled at a rate of 10°C/min down to room temperature. The second run was with a known reference sample. In this case 19.86mg of 99.999% pure zinc foil was

used as this is a recognised standard for DSC calibration [2] and was provided by the manufacturer of the system. It has a well known melting point of 419.53°C , a boiling point of 907°C and a well defined specific heat capacity of 0.39 J/gK at 25°C. It is also relatively cheap and commonly available. The zinc sample was placed in the pan and then placed in the sample pan holder and put through the same thermal cycle as that for the empty pan so that they can be directly correlated. A purge gas of air was used at a flow rate of ~20ml/min.

4.2.1.2 Uncured Inks

The alumina pan is first weighed to find the mass of the pan. Then some ink is taken using a syringe, from the ink pot and placed within the pan. Approximately 100-150mg was used each time to try and keep the experiment consistent between batches. The pan is then placed in the pan holder with tweezers to reduce any contamination, the whole assembly is then covered. The pan is then re-weighed and the mass of the pan subtracted to find the mass of the ink. The purge gas was then turned on at a rate of ~20ml/min to minimise the risk of condensation from evaporated/driven off solvents affecting the weight loss measurement and nitrogen was used as this recreated the oven and laser curing environments and there was no issue with reactive substances. This artificial atmosphere was at standard ambient pressure, but was dynamic over the sample pan.
The thermal cycle parameters were then set, as stated in 3.2.1, and the cycle started.

4.2.1.3 Oven cured inks

Since the samples have very good adhesion when oven cured, it was important to take the samples from a hard substrate so as not to remove any substrate when taking the sample and contaminating the experiment. The samples were oven cured on alumina substrates at 130°C for 20 minutes and then removed from the substrate using a Stanley knife. Approximately 2-3 lines of dimensions ~110x3x0.06 mm were used per test sample.
The samples were then placed in the alumina pan after weighing and then re-weighed. The cycle was then started as stated in 3.2.1.

4.2.1.4 Laser cured inks

The adhesion of the laser cured samples was not as good as the oven cured samples when cured on alumina. Therefore removal of the cured tracks was not as hard, but laser cured samples on alumina were used for consistency and ease of removal.

The different inks were cured using the optimum parameters of the specific ink, to produce the best cured result, regardless of bubbling as long as burning or over cure did not occur.

The D58 ink was cured using a traverse speed of 2mm/s with 2 passes and a power of 20W. The D1 and D15 inks were processed using a traverse speed of 6mm/s with 2 passes and a power of 20W. The samples were then taken in the same manner as that used for the oven cured samples and the process followed as stated in 3.2.1.

4.3 TGA/DSC Results

In this section results from the simultaneous DSC/TGA experiments will be shown, analysed and discussed. This chapter is presented with a brief introduction, followed by the results and analysis along with discussions in the following four sections. A conclusion section and in the final section a brief summary is given.

4.3.1 Introduction

Since the exact composition of the inks used throughout this investigation was not known due to IPR and commercial sensitivity, the thermal and physical properties were not known. It was important to try and investigate the chemistry of the ink systems and how they reacted to the different curing methods employed if laser curing was to be fully investigated and understood. Thermal analysis using TGA/DSC is just one of the techniques employed within this investigation to help understand what is occurring when the inks are being cured by either technique and then to give some idea of the inks thermal properties; in particular the heat capacity and temperatures of first order transitions. This technique alone does not reveal the chemical composition of the inks, but can be inferred when

combined with other techniques such as FTIR (Fourier Transform Infrared) spectroscopy. However it is not within the scope of this investigation or the wish of the author to find out the exact composition, but rather investigate how the inks behave and the differences between oven curing and laser curing when trying to produce a cured conductive area.

The results and analysis presented here are of the thermal analysis techniques as described in section 3.1. The Perkin-Elmer STA6000 was used to analyse the uncured and cured inks used throughout this investigation. The system was first calibrated using an industry standard technique using a pure zinc sample and then tested for any individual characteristics of the machine by conducting an empty pan run. This was necessary to calibrate the machine and also conduct the integration method of DSC analysis as mentioned in 3.1.2.3 and presented in this section. The graphs and results shown are all derived from these experiments and will be shown in a variety of ways to best analyse and ascertain what is occurring during the thermal cycle.

4.3.2 Calibration Results

It is standard when presenting the results of a DSC/TGA measurement to plot percentage mass loss on the left vertical axis and heat flow (mW) on the right vertical axis against temperature on the other vertical axis. The graph in Figure 4.7 is plotted in this way, with endothermic represented as up and exothermic as down. There is no strict convention with regards to the direction of the endothermic or exothermic peaks, but rather a function of the software used or at the author's discretion.

4.3.2.1 Empty Pan

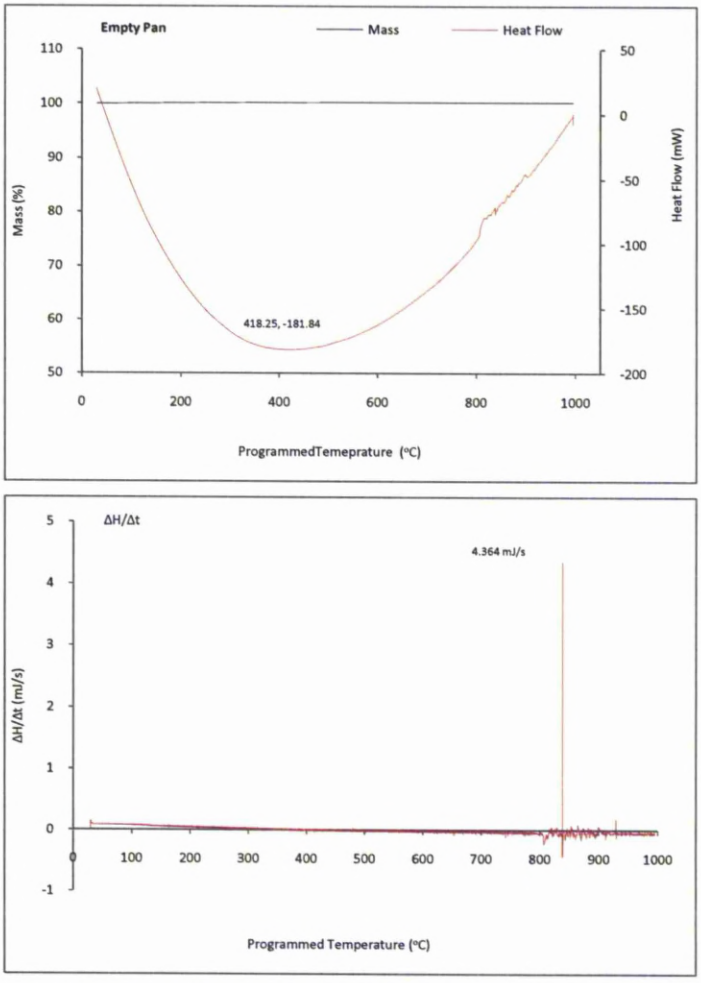

Figure 4.7: Calibration graphs. The left graph is the DSC/TGA cycle with an empty alumina pan, and the right graph is the change in enthalpy (gradient of the left graph) of the system with respect to temperature.

The empty pan calibration graph has an endothermic low of -181.84 mW. This corresponds to a programmed temperature, T_P of 418.25°C and a sample temperature, T_S (the alumina pan) of 412.19°C. The shape of the graph denotes that the sample is constantly giving off heat to the system as the system heats up, until 995°C where it is held for 10 minutes and demonstrates the characteristics of the system; this is the baseline that needs to be subtracted from the results when calculating the enthalpy change of a sample and working out the calibration factor.

There are no major peaks as would be expected when there is no enthalpy change due to a chemical reaction, since alumina is thermally stable up to 2072°C and has a constant heat capacity, though there is some noise above 800°C, but this is not an issue as the area of

interest when investigating the inks is below this temperature regime. The enthalpy change is better illustrated when taking the differential of the heat flow graph as this demonstrates any change in the rate of heat flow to the sample pan and hence the enthalpy, and not the heat flow that occurs directly from the thermal cycle, as shown in Figure 4.7. Looking at Figure 4.7 the baseline of the enthalpy change is linear until around 800°C where some background noise appears. It is uncertain as to why this noise occurs and the resulting peak of 4.364 mJ/s, but as stated before this is not important as the area of interest when analysing the inks is well below this mark. Therefore the noise witnessed here should not affect the results.

4.3.2.2 Programmed Temperature and Sample Temperature

The difference in the programmed temperature and the sample temperature is due to the heat flow resistance that is inherent to the system, Figure 4.8. For cases where a sample is present, the difference could also be due to any chemical reaction that occurs and so the results need to be calibrated accordingly. As the system may act slightly differently when a sample is present, the temperature offset is also checked when running a reference test. In this case zinc is used. This is done through the zinc reference run. With an empty sample pan, the sample temperature is hotter than the programme temperature by 0.62°C. After 11 seconds the programmed temperature is higher than that of the sample temperature as there is thermal inertia within the sample. The sample then lags behind the programmed temperature for the whole thermal cycle due to the heat flow resistance of the system. When the sample is held at a constant programmed temperature of 995°C for ten minutes, the sample temperature goes from 990.73°C to 992.05°C where it levels out after eight minutes.

The initial peak occurs after 6 mins and has a $\Delta T = 4.027°C$, the second peak occurs after 35 mins and has a $\Delta T = 6.423°C$ after this the temperature difference plateaus varying slightly between 5°C and 6°C. This is similar to the reference run with zinc in the sample holder, where the initial peak occurs after 5 mins and has a $\Delta T = 4.027°C$ and a second peak after 35 mins with a $\Delta T = 5.937°C$. The trend with or without a sample is similar in both cases as can be seen from Figure 4.8.

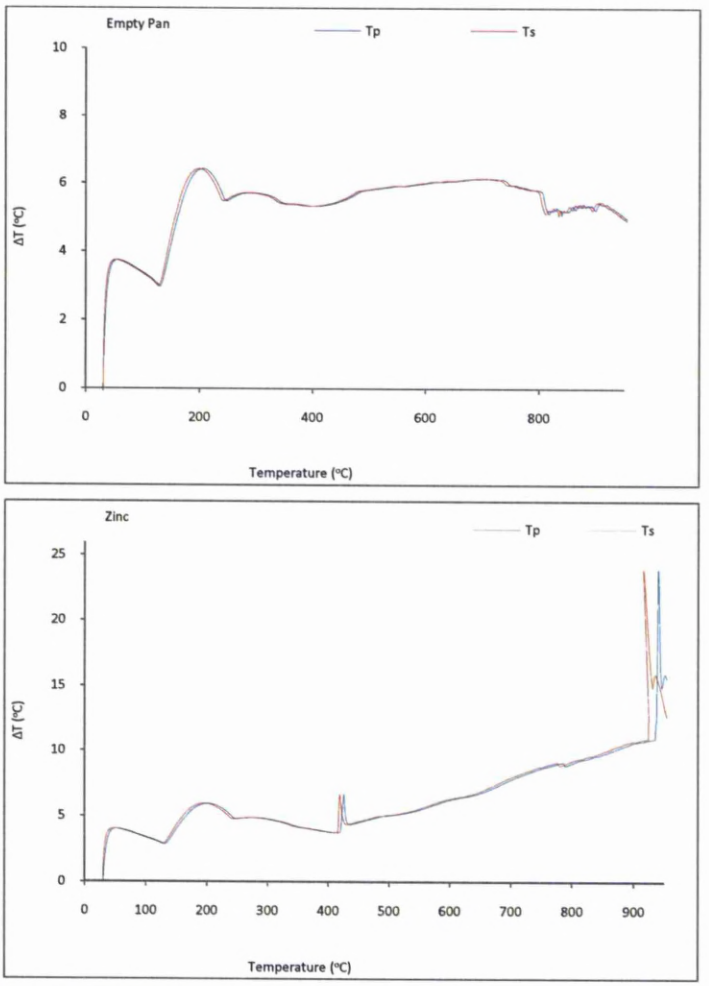

Figure 4.8: The graphs demonstrate the temperature difference between T_P and T_S where $\Delta T = T_P - T_S$.

The zinc sample then has two significant peaks. The first is when the zinc starts to melt at 419.08°C with a ΔT= 6.637°C and this corresponds with literature demonstrating that the sample temperature as recorded is accurate. The difference then steadily increases until a sharp increase in ΔT occurs. This occurs as the zinc is boiled off and a drop in the sample temperature is witnessed as energy is absorbed from the system; latent heat of vaporisation, after 182 mins. ΔT peaks at 23.933°C. In all thermal cycles, the sample temperature lags that of the programmed temperature, but as demonstrated with the reference run, the sample temperature can be confidently taken as the actual temperature of the sample and so no calibration is required. When a sample goes through a first order transition it will have a corresponding change in temperature. If the temperature of the surrounding environment is required during this transition then the temperature can be derived from the programmed temperature recorded using the empty pan run.

4.3.2.3 Zinc Reference Sample

The zinc reference sample used for the calibration of the STA6000 was provided by Perkin-Elmer and was 99.999% pure zinc, was foil form and weighed 19.86 mg. The results of the calibration run are shown in Figure 4.9.

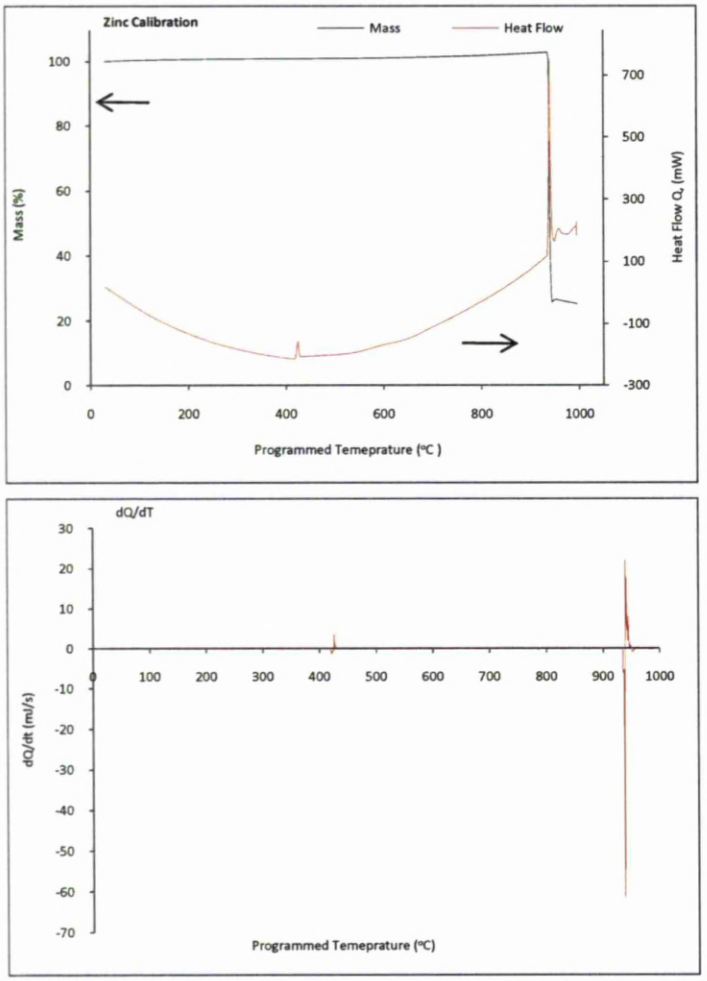

Figure 4.9: Calibration graphs. The left graph is the DSC/TGA cycle with the zinc reference sample, and the right graph is the change in enthalpy (gradient of the left graph) of the system with respect to temperature.

As can be seen from Figure 4.9 the overall trend/shape of the zinc reference run, is similar to that of the empty pan calibration run. The zinc run differs however since it has heat flow peaks when the zinc sample melts and when it boils. These peak correspond to a change in state and hence a change in the heat capacity of the material. This graph and its derivatives will be used to calculate the specific heat capacity of zinc and the calibration coefficient, K (14), that will be required for all subsequent heat capacity calculations of the inks used.

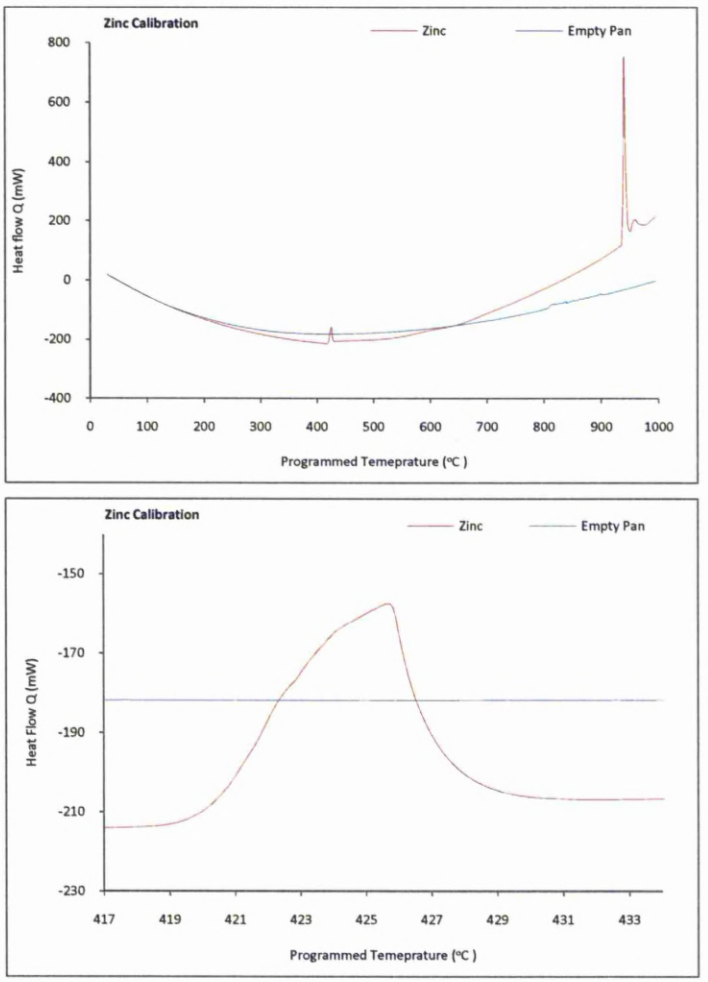

Figure 4.10: The graph on the left shows the zinc calibration (red line) run and the empty pan reference run (blue line) on the same graph. The graph on the right shows the area of interest where the first order transition of the zinc melting occurs and the associated ΔQ of the transition at 419.53°C.

As shown in Figure 4.10, an enthalpy change starts to occur at a programmed temperature of 418.92°C. This corresponds to a sample temperature of 415.14°C. The endothermic first order transition continues to increase as the material absorbs enough energy to change state. This endothermic process peaks at a programmed temperature of 425.67°C which corresponds to a sample temperature of 419.08°C, the melting point of zinc. The zinc melting point is quoted as being 419.53°C and so the measured sample temperature can be said to be 0.45°C out; a negligible amount for the purposes of this research.

To calculate the heat capacity of the zinc and hence get the calibration factor for the system, the differential of the first order transition needs to be obtained so that the total heat flow change can be calculated. The differential of the first order transition is shown in

Figure 4.11. For completeness the second order transition of the zinc boiling is shown in Figure 4.12, however this will not be used to calculate the heat capacity and hence calibration factor as this investigation is not concerned with temperatures of that order.

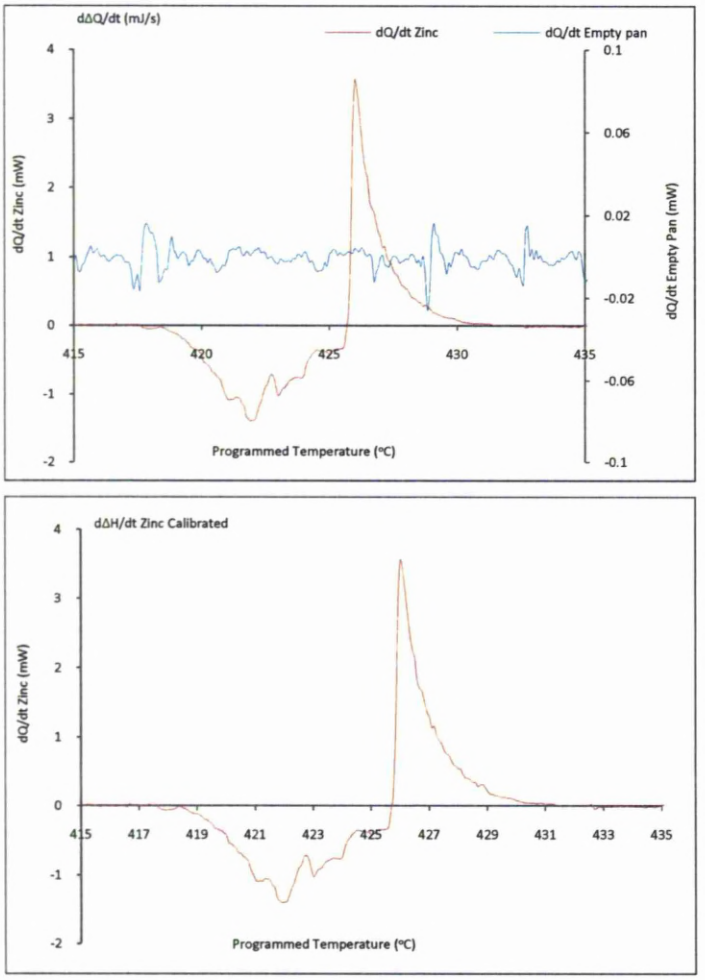

Figure 4.11: Graphs showing the change in enthalpy as the zinc sample starts to melt. The top graph shows the uncalibrated values and the empty pan run, while the right graph shows the calibrated values for the zinc reference run.

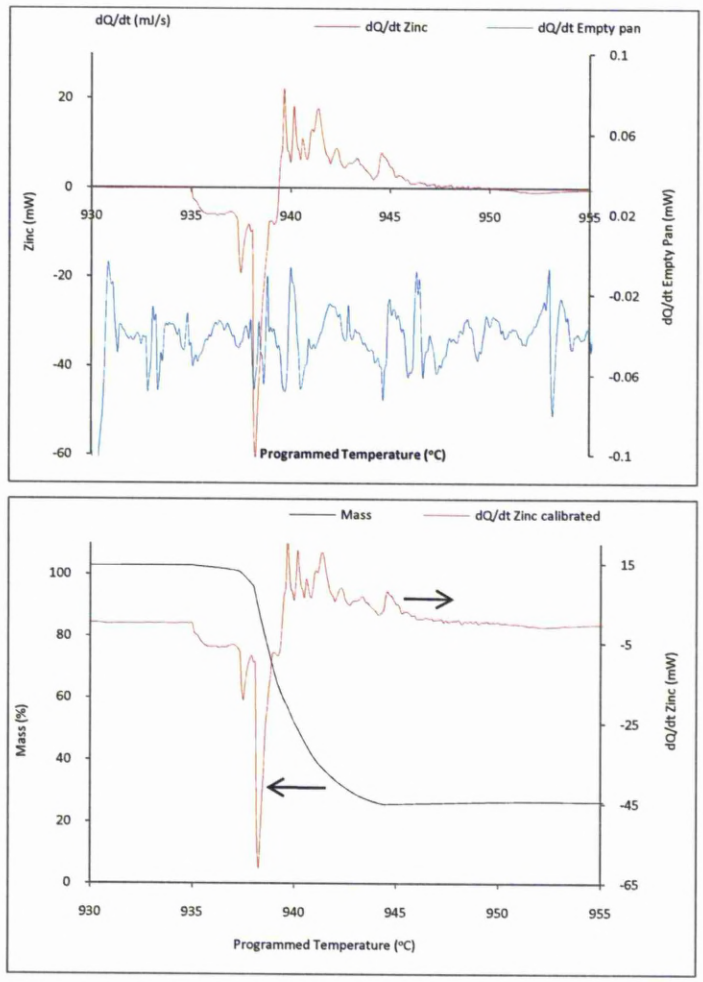

Figure 4.12: Graphs showing the zinc sample as it starts to boil and then evaporates. The left graph shows the uncalibrated values and the empty pan run, while the right graph shows the calibrated values for the zinc reference run and the mass change during the phase transition.

Using equation 12 to calculate the total change in heat flow for the zinc calibration run during the first order transition, with a sample temperature of T_i =415.14°C and T_f = 428.68°C, and $\int\Delta H_Z$=428.68 mJ and $\int\Delta H_{EP}$=415.14 mJ, equation 13 becomes:

$$C_{p,s}(T_i, T_f) = \frac{105.28-1.44}{428.68-415.14} = 7.67\ mJ/K \quad (16)$$

Using equation 15 without the calibration factor, with a mass of 19.86 mg, to find the specific heat capacity, gives

$$C_{P,S} = \frac{103.84x10^{-3}}{19.86x10^{-3}(428.68-415.14)} \quad (17)$$

$$= 0.386\, J/KgK$$

Therefore the calculated specific heat capacity for the zinc calibration run is 386.141 mJ/KgK. The actual value of the specific heat capacity of zinc is 390 J/KgK. The value of the specific heat capacity as calculated using the integration method for the results from the STA 6000 is very close to that of the actual value. This demonstrates that using this technique is an accurate method for calculating the specific heat capacity. Using equation 14 the calibration factor can now be worked out.

$$K = \frac{C_{p(lit)}}{C_{p(meas)}} = \frac{390}{0.386} = 1010.36 \quad (18)$$

Now that the calibration factor has been obtained, it is possible to calculate the specific heat capacity of the inks as they go through their first order transition; cross-linking.

4.3.3 Uncured results

4.3.3.1 Uncured Resin

For the uncured resin run, 92 mg of resin was placed in to the alumina pan holder and put through the thermal cycle as stated in 3.2.1. The results are shown in Figure 4.13.

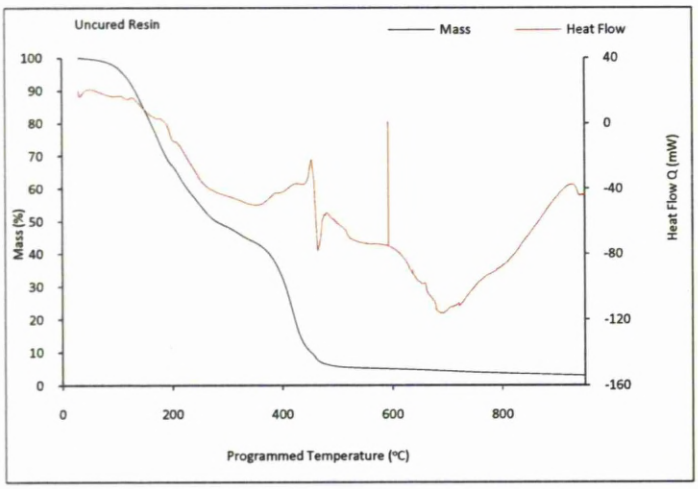

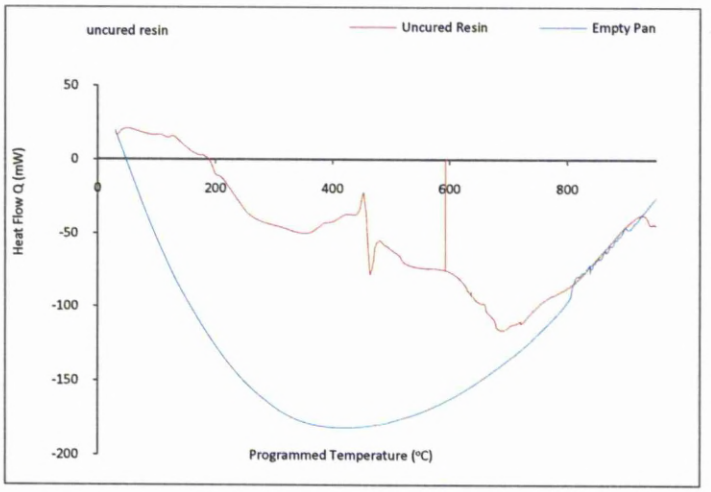

Figure 4.13: The left graph show the TGA graph of the uncured resin and the associated heat flow for the thermal cycle, whilst the right graph shows the heat flow along with the empty pan reference run.

The results of the uncured resin are significantly different from that seen for the zinc calibration run. Looking at the mass loss of the system, there are two clear mass loss regions. This is more clearly shown in Figure 4.16. Solvent evaporation occurs almost immediately, though this is only slight in the first instance but there is an associated thermal change as the solvent evaporates, latent heat of vaporisation. The resin starts to cross-link at about 90°C the associated mass loss along with the solvent evaporation is visible on the graph in Figure 4.13, but the significant mass loss starts to occur at a programmed temperature of 110°C. This corresponds to a sample temperature of about 101°C. Within the cross-linking phase of the resin there is two distinct regions of thermal changes within the resin, as seen in Figure 4.14. The first region occurs between 100°C and 140°C where the cross-linking occurs. This thermal change will be due to the ink going from a liquid to a solid and the associated loss of mass. At 140°C, programmed temperature, the sample has already lost 13% of its mass. The second region is between 175°C and 210°C where the resin, now completely cross-linked goes through what is known as a B-stage curing process. This process changes the properties of the polymer and results in further mass loss and an associated thermal change.

The second mass loss step occurs as the cross-linked resin starts to decompose. The significant mass loss starts to occur at about 375°C, sample temperature of 367°C and ends at about 470°C, sample temp of 468°C. From Figure 4.14 this process can easily been seen as mass loss starts to occur with a reduction in the heat flow out of the sample, exothermic. There is a gradual decrease in the exothermic energy as the mass loss occurs.

This implies that this decrease is directly proportional to the mass of the sample. However when the sample reaches 448°C there is a significant change in the gradient of the reduction of heat flow. As mass loss has occurred prior to this through, presumably vaporisation of the resin, another chemical change appears to occur at this critical temperature, as the sample goes through first a reduction from 448°C to a significant increase in heat flow given out by the sample, peaking at 465°C programmed, 461.59°C sample and with a low of -78.10 mW. Following this there is a significant reduction again. This can only be attributed to a sudden change in the thermal inertia of the system due to the lack of resin present. At this point the mass of the material goes down to about 10% of the original weight, which appears to have a significant effect on the heat flow process. Prior to that, there was a reduction in the exothermic heat flow as the material absorbed energy as the resin was going through a second order phase transition. It appears that as the material mass hits a certain level, there is a rapid redressing of the heat flow. This is shown also in Figure 4.14 where the associated difference between the sample temperature and the programmed temperature for this change of state can be seen. As shown in section 3.3.2.2 it is a good indication of when a change of state is occurring.

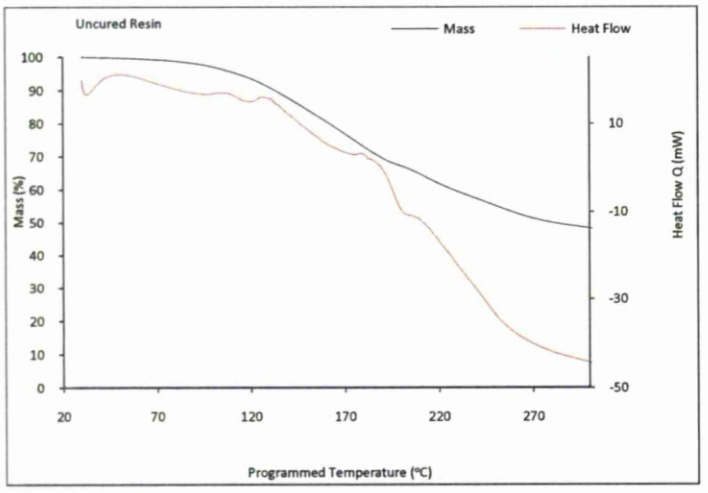

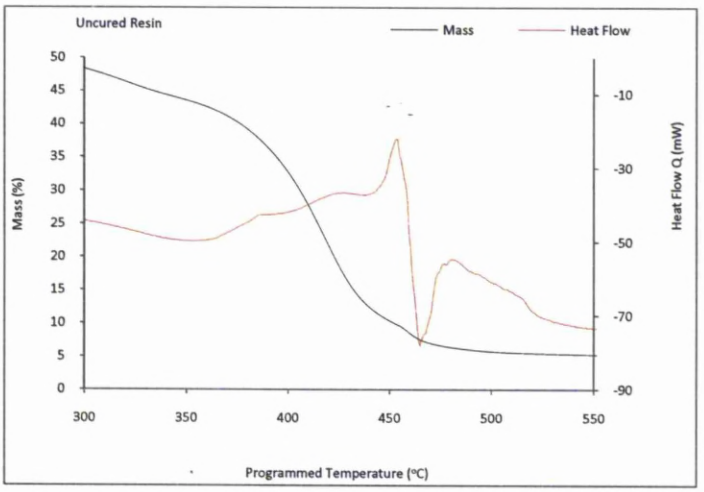

Figure 4.14: Here the graphs have been enlarged within the regions of interest. The left graph showing the cross-linking process that starts at ~90°C, whilst the right graph shows the thermal degradation that starts to occur at ~350°C and results in complete degradation at 465-480°C.

Looking at Figure 4.15 it can be seen that initially the resin heats up at a slower rate than the programmed temperature rate of 5°C/min. This thermal inertia would be expected initially as the system heats up, with a starting temperature of 30°C, the resin would be at room temperature. However it is clear that the temperature difference increases and peaks at 11.15°C with a programmed temperature of 184.58°C. The ink as a liquid will be less thermally conductive then when it is cured. This will be due to the fact that as the ink cures the silver flakes come in to contact creating silver paths through the ink that were not present previously. This fact partially explains the thermal inertia witnessed. There will also be effects due to solvent evaporation and cross-linking of the system as it goes through the cure stage. And this is backed up by the temperature difference reducing rapidly, but not instantaneously, after the ink is cured and the mass loss rate reducing at the same time. This implies that the temperature difference witnessed prior and during cure is not solely down to the thermal inertia of the ink.

Further evidence for this is the plateau seen between 240°C and 435°C. Here there is some mass loss occurring with significant mass loss occurring at 375°C as stated previously, however the difference in temperature is pretty stable as thermal degradation of the resin occurs. There is a significant drop in the difference in temperature of the two at around 460°C and this seems due to the lack of resin left. At this point about 2% of the original mass is present and so the programmed and sample temperatures are very similar, with the difference reducing from that point onwards.

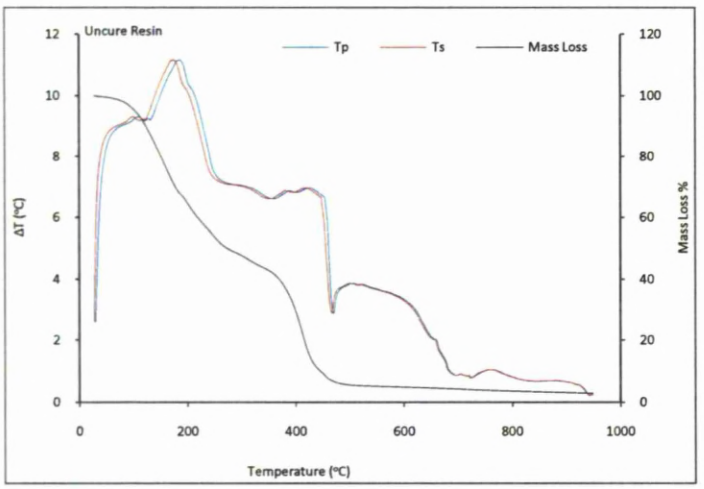

Figure 4.15: The graph shows how the programmed and sample temperatures vary as the ink goes through its various stages as a function of temperature and the change in mass against the sample temperature.

The change in mass is shown in the top graph of Figure 4.16. The mass change starts to increase rapidly at 375°C and peaks at about 410°C with a stated change of mass, of about 0.05 mg/s. From there, the mass change rate decreases until it reaches roughly 0 mg/s for the remainder of the run, where the mass remaining within the sample stays at about 2% of the original resin. Though it would be expected that all the resin would have been degraded and vaporised by the time the heat cycle had reached 950°C and the mass remaining would be effectively 0, upon inspection of the alumina pan after the experiment was completed, an almost wire like skeleton of a charred material was present. This charred material was taken to be carbon remains of the polymeric ink.

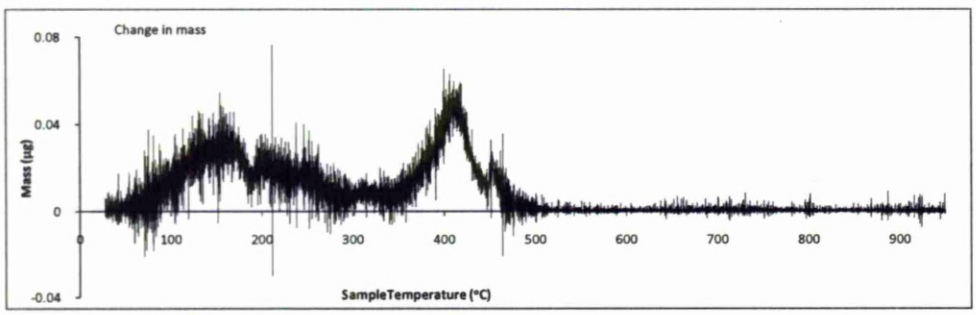

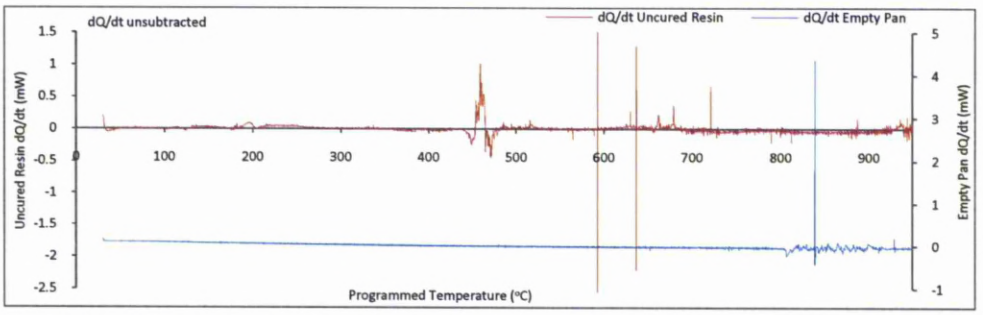

Figure 2.16: The top graph show the change in mass as a function of temperature, illustrating the two areas where significant mass loss occurs. The first being solvent evaporation and cross-linking, whilst the second is the thermal degradation of the resin.

The lower graph shows the rate of change of the heat flow, Q, in to the sample with the results of the empty pan reference run plotted on the right hand vertical axis. From the graph it can be seen that there are a couple points of interest. Firstly the sharp spike seen at around 600°C is probably due to momentary vibrational distortion to the equipment during the heat cycle. It is only one measurement and is an instantaneous change and so can be discounted. Between 600°C and 800°C it is unclear exactly what is exactly occurring within the resin as there is no longer any mass loss. Therefore there must be some slight chemical changes and maybe the carbonising of the polymer as minute amounts of the resin begin to disintegrate and vaporise. Above 800°C noise was present in the empty pan run as can be seen by the blue plot line and so the possible carbonising and the noise is seen in the red plot line.

At lower temperatures we have a very significant change in the rate of heat flow for the sample occurring just after disintegration and vaporisation as mentioned earlier, with a high at a programmed temperature of 459.25°C and a sample temperature of 453.62°C. The main area of interest is the area around cure, ~100°C-200°C. This is the area where the data will be used to calculate the heat capacity of the resin. Within this area are to distinct areas of interest. The first is the change in the rate of heat flow that occurs during cross-linking, where there is an increase in the rate of the heat flow out of the system, hitting a high of -0.03 mJ/s that occurs at a programmed temperature of 124°C and a sample temperature of 114°C. The second area is the endothermic change seen as the ink goes through a B-stage curing process. This process starts at 180°C and peaks at programmed temperature of 195°C and a sample temperature of 185°C with a rate of 0.1 mJ/s.

Due to the nature of the polymeric resin, it is in a constant state of change and therefore the heat capacity and thermal properties are always changing. Initially it will be the loss of the solvent which occurs constantly, then the cross-linking. Unlike the zinc sample which had a clearly defined melting point, and temperature range in which to use data for the calculations, DSC of the resin is not as straight forward. Therefore, a couple of measurements will be taken to create an image of how the heat capacity is changing as the ink goes through these two stated transitions. The first will be the onset of cross-linking, where an oscillation of exothermic and endothermic rate of changes is seen in the heat flow from a programmed temperature of 90°C. The second calculation will use the endothermic rate of change seen during the B-curing process at a temperature of 195°C.

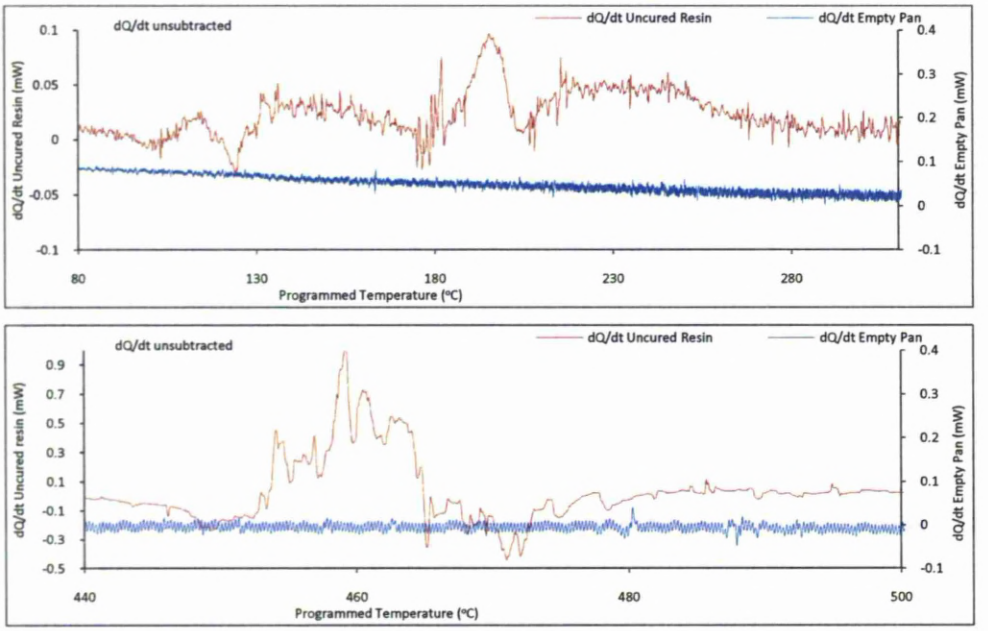

Figure 4.17: The two graphs illustrate the change in heat flow Q, during the thermal cycle in the two significant regions of the process along with the empty pan reference run.

Using equation 12 to calculate the total change in heat flow for the uncured resin run during the first onset stage of cross-linking between the start of cross-linking and the start of the B-curing stage. This correlates to a sample temperature of T_i=81.32°C and T_f = 163.91°C, and $\int\Delta H_{Resin}$=16.7669 mJ $\int\Delta_{EP}$=64.4748 mJ , equation 13 becomes[3]:

[3] Note that in the equation the empty pan run and the resin values are being added and not subtracted as was the case for the zinc sample. This is because the empty pan run had a higher negative value than that of the resin. Therefore to properly reference against the empty pan run. The two values need to be added.

$$C_{p,s}(T_i, T_f) = \frac{16.7669 + 64.4748}{163.91-81.32} \quad (19)$$
$$= 0.9826\, mJ/K$$

Using equation 15 with a calibration factor K=1010.36, and an average mass of 82.00 mg, to find the specific heat capacity, gives

$$C_{P,S} = 1010.36 \text{ x} \frac{81.2417\, x10^{-3}}{82x10^{-3}(163.91-81.32)} \quad (20)$$

$$= 12.12\, J/KgK$$

Therefore the calculated specific heat capacity of the uncured resin during its cross-linking stage is 12.12 J/KgK.

For the B-curing stage, using equation 12 to calculate the total change in heat flow for the uncured resin run during the second onset stage of cross-linking between the end of the first cure stage and the end of the B-curing stage. This correlates to a sample temperature of T_i =163.99°C and T_f =204.44°C, and $\int\Delta H_{Resin}$=17.66 mJ, $\int\Delta_{EP}$=22.81 mJ, equation 13 becomes:

$$C_{p,s}(T_i, T_f) = \frac{17.66 + 22.81}{204.44-163.99} \quad (21)$$
$$= 1.00\, mJ/K$$

Using equation 15 with a calibration factor K=1.01, and an average mass of 68.70 mg, to find the specific heat capacity, gives

$$C_{P,S} = 1.01 \text{ x} \frac{41.2519x10^{-3}}{68.70x10^{-3}(204.44-163.99)} \quad (22)$$

$$= 14.99\, J/KgK$$

From the results, the resin appears to increase in heat capacity as it goes through the B-stage cure. This implies that as it becomes more consolidated and the cross-linking progresses, this has an effect of increasing the heat capacity as it transforms.

4.3.3.2 Uncured D58 Ink

For the uncured D58 ink run, 86.49 mg of ink was placed in to the alumina pan holder and put through the thermal cycle as stated in 3.2.1. The results are shown in Figure 4.18.

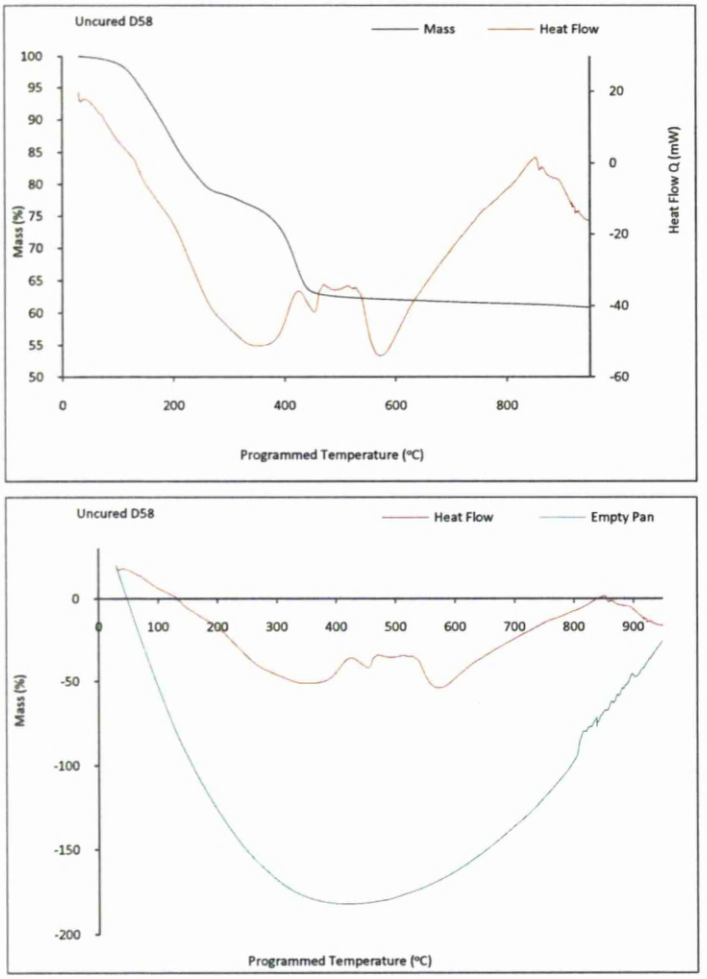

Figure 4.18: The left graph shows the TGA graph of the uncured resin and the associated heat flow for the thermal cycle, whilst the right graph shows the heat flow along with the empty pan reference run.

Whilst the mass reduction profile is very similar to that shown in Figure 4.13 of the uncured resin, allowing for the fact that the mass of the sample does not go below 60% due to the silver being present, the thermal cycle is slightly different. The sample is exothermic in the same way as the uncured resin, but the sharp change that occurs when the resin thermally degrades is not witnessed. The peak structure is a lot broader for the D58 ink which is caused by the presence of the silver. This is because it is not going through any change of state during this thermal cycle. Silver has a melting point of 961°C whilst the thermal cycle only goes up to 950°C. Due to this and the fact that it makes up ~60% of the ink by mass, the heat capacitive change witnessed will be reduced in magnitude when compared to the uncured resin. Since only part of the system is going through a change of state.

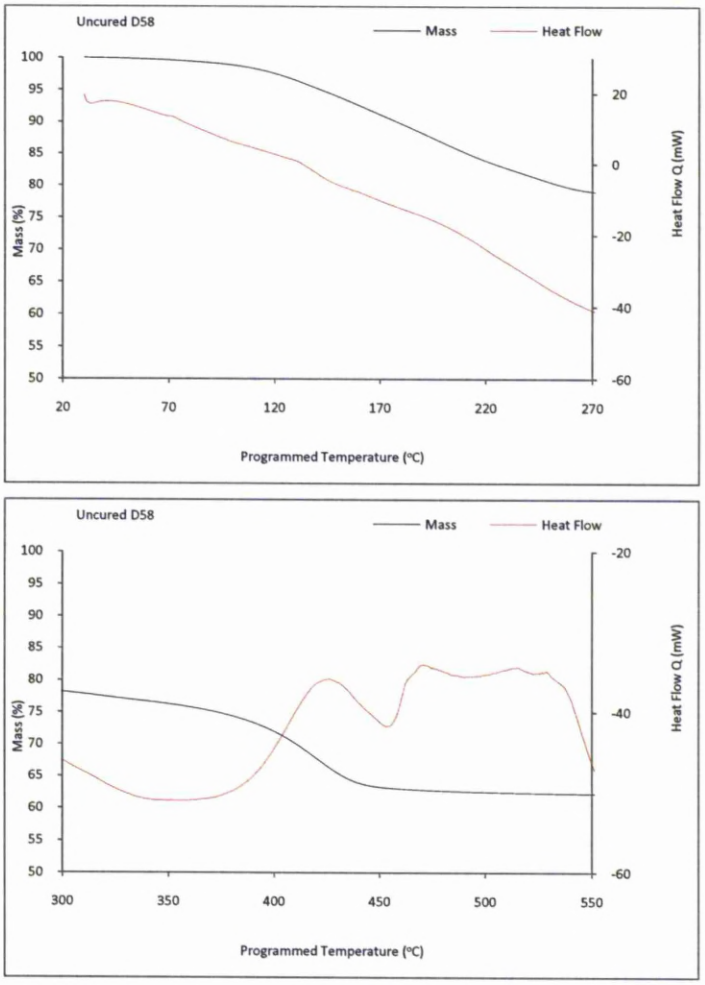

Figure 4.19: Expanded view of the cross-linking stage in the left graph, and the thermal degradation process in the right graph. An endothermic change starts to occur at 350°C with a peak at 426°C and the following exothermic dip at 453°C and then peaks again at 479°C.

From Figure 4.19 it can be seen that during the solvent evaporation and cross-linking phase of the ink, there is little change in the thermal process of the material. The presence of the silver has reduced the effect of the cross-linking phase on the heat capacity change during its first order transition. Using the integration method it is no longer possible to calculate the heat capacity of the ink at this point. The thermal degradation phase occurs in the same place with or without the silver component, however the magnitudes involved are reduced, as would be expected.

If Figure 4.15 is compared to Figure 4.20, it can be seen that the overall profile of the graphs are very similar, but the magnitudes are less with no sharp change in the differences between the programmed temperature and the sample temperature either during cross-

linking, though some change is witnessed, but more noticeably during the thermal degradation stage, where it is very sharp for the uncured resin. The overall shape is the same as that seen for the empty pan reference run and the zinc calibration run, Figure 4.8, and similar in magnitude to the empty pan run. It was hoped that this change could be witnessed and a heat capacity calculated, but looking at the expanded view in Figure 4.21 it is only very slight. As the thermal change is not required for the higher temperatures and during thermal degradation, where there is a significant change, the heat capacity will be derived from the uncured resin and the known heat capacity of the silver and calculated through ratios.

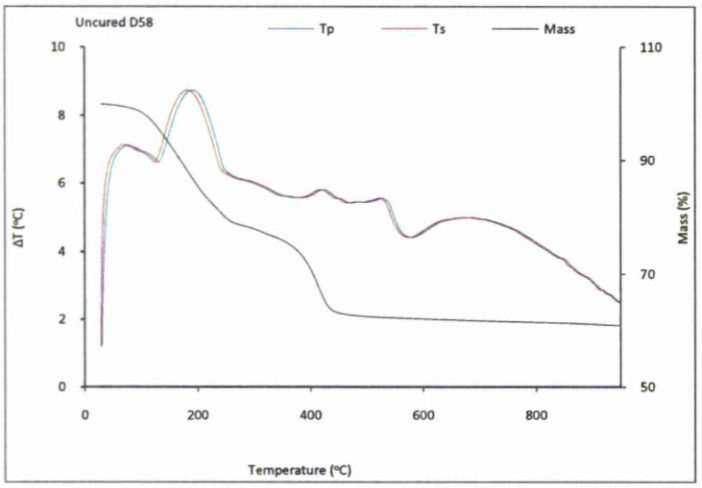

Figure 4.20: The graph shows how the programmed and sample temperatures vary as the ink goes through its various stages as a function of temperature and the change in mass against the sample temperature.

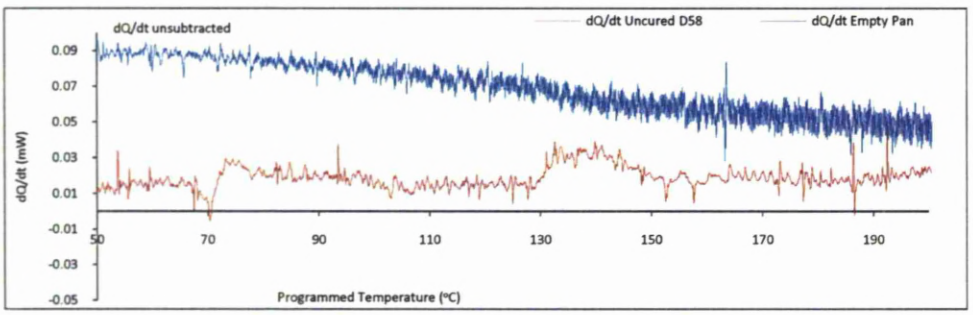

Figure 4.21: An expanded view of the cross-linking phase of the D58 ink. Slight changes in the thermal flow does occur, but the amount is of the order 30μJ.

If the heat capacity of the of the ink was calculated using the values from the cross-linking phase, it would be inaccurate as it would not take in to account the presence of the silver

as it does not go through a first order transition at that point. To calculate the heat capacity of the ink during its cross-linking stage and B-curing stage, the two values for the heat capacity calculated in section 3.3.3.1 will be used with equation 23.

$$C_{D58} = \frac{(m_{silver} \text{x } C_{P\ silver}) + (m_{resin} \text{ x } C_{p\ resin})}{m_{total}} \quad (23)$$

Where C_{D58} is the heat capacity of the D58 ink, m_{D58} is the mass of the silver in the D58 ink, $C_{P\ silver}$ is the calculated heat capacity of the resin, m_{resin} is the mass of the resin, $C_{p\ resin}$ is the calculated heat capacity of the resin and m_{total} is the total mass of the ink.

If we take the following values, m_{silver} = 52.65 mg, $C_{P\ silver}$ = 230 J/KgK, m_{resin} = 33.84mg, and the cross-linking and B-stage cure heat capacities of the resin to be $C_{x\ resin}$ = 12.12 J/KgK and $C_{B\ resin}$ = 14.99 J/KgK respectively with a m_{total} = 86.49mg. We have a heat capacity of the D58 ink which is

$$C_{X\ D58} = 144.75 \text{ J/KgK}$$
$$C_{B\ D58} = 145.88 \text{ J/KgK}$$

Where the x and B suffix denotes the cross-linking stage and B-stage curing regimes respectively.

4.3.3.3 Uncured D1 ink

For the uncured D1 ink run, 140.45 mg of ink was placed in to the alumina pan holder and put through the thermal cycle as stated in 3.2.1. The results are shown in Figure 4.22.

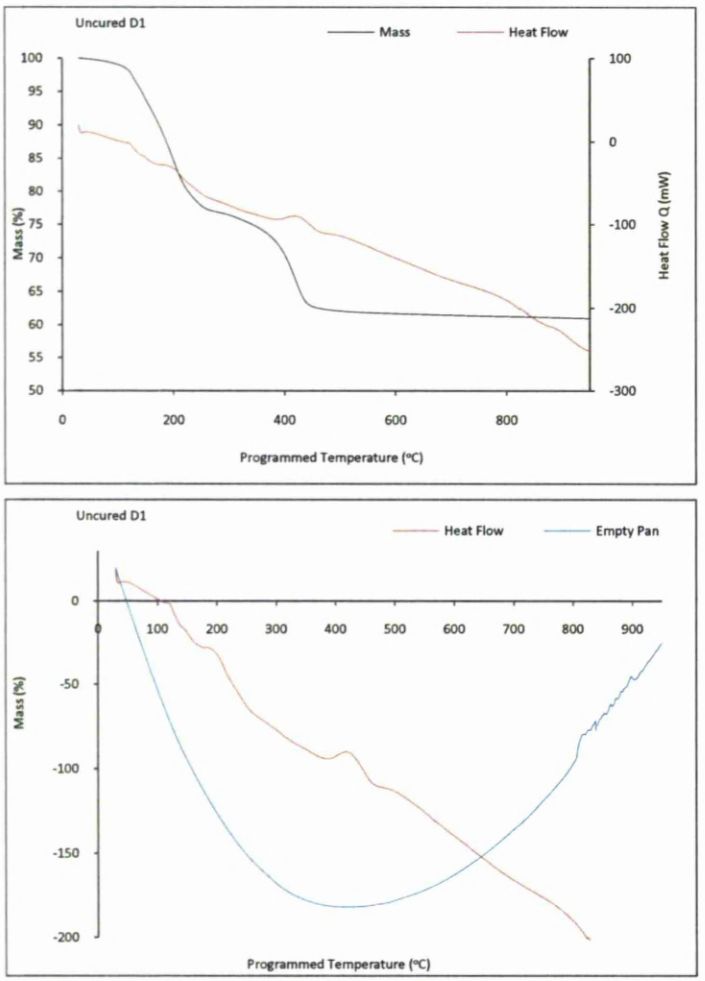

Figure 4.22: The left graph shows the TGA graph of the uncured resin and the associated heat flow for the thermal cycle, whilst the right graph shows the heat flow along with the empty pan reference run.

The addition of 1% carbon doping by mass to the ink has not changed the mass reduction profile of the thermal cycle, with it not going below 60% as seen in the D58 uncured ink run. The heat flow graph however is considerably different from that seen in either the uncured resin or D58 runs. There are slight fluctuations in the cross-linking and B-stage curing regimes as shown in Figures 4.22 and 4.23. Though larger than that of the D58 ink, they are still small in comparison to that of the uncured resin. Therefore the heat capacity will be calculated in the same way as that used for the D58 ink, but also accounting for the carbon dopent. The other noticeable feature of the heat flow graph is the negative gradient of the graph, which unlike the resin or D58 does not have an endothermic change after thermal decomposition.

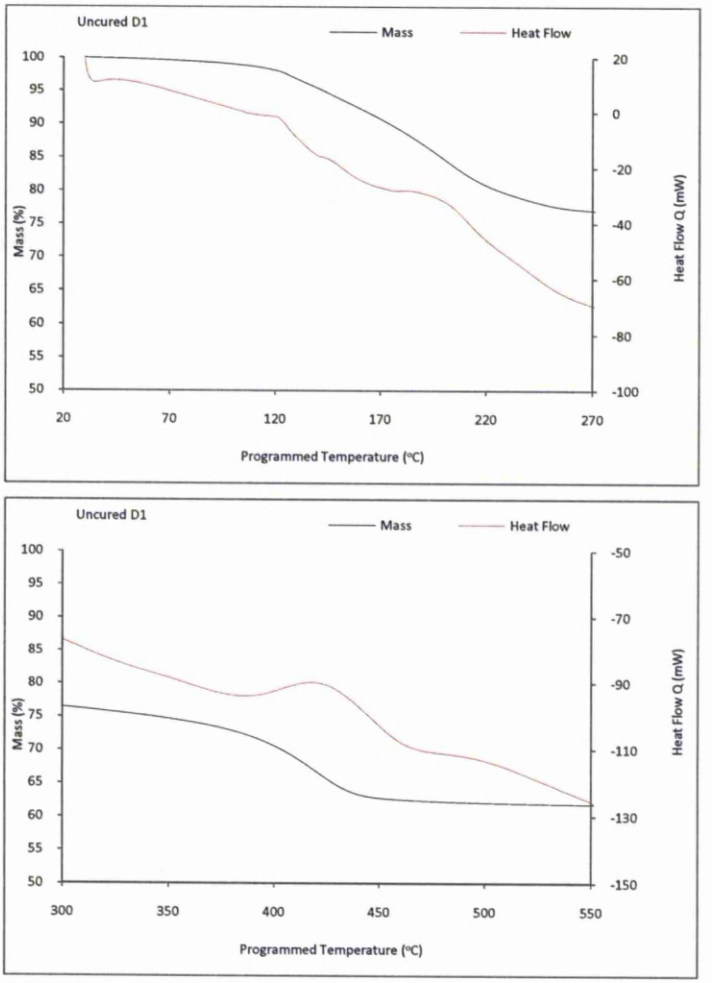

Figure 4.23: Expanded view of the cross-linking stage in the left graph, and the thermal degradation process in the right graph. There is a slight endothermic change at 386°C followed by an exothermic change at about 415°C.

Using equation 23 and with the following values, If we take the following values, m_{silver} = 85.62mg, $C_{P\,silver}$ = 230 J/KgK, m_{resin} = 53.43mg, m_{carbon} =1.40mg, C_{carbon} =519 J/KgK and the cross-linking and B-stage cure heat capacities of the resin to be $C_{x\,resin}$ = 12.12 J/KgK and $C_{B\,resin}$ = 14.99 J/KgK respectively with a m_{total} = 140.45 mg. We have a heat capacity of the D1 ink which is

$$C_{X\,D58} = 149.99 \text{ J/KgK}$$

$$C_{B\,D58} = 151.09 \text{ J/KgK}$$

4.3.3.4 Uncured D15 ink

For the uncured D15 ink run, 122.02 mg of ink was placed in to the alumina pan holder and put through the thermal cycle as stated in 3.2.1. The results are shown in Figure 4.24.

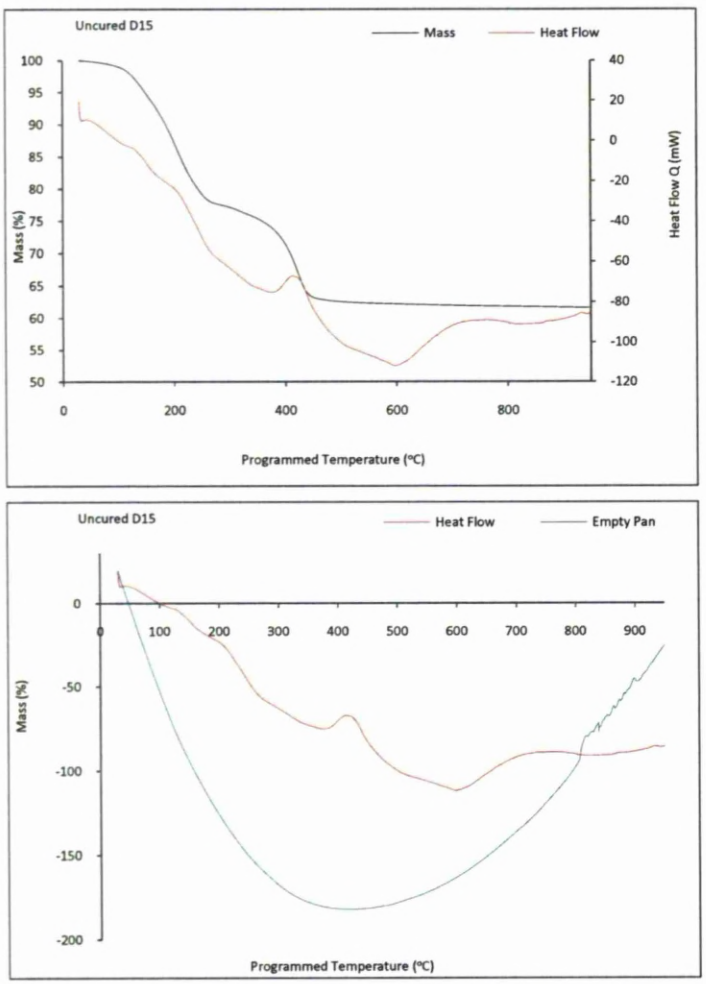

Figure 4.24: The left graph shows the TGA/DSC graph of the uncured resin and the associated heat flow for the thermal cycle, whilst the right graph shows the heat flow along with the empty pan reference run.

The mass loss graph for the D15 ink is similar in nature to that of the other inks, as would be expected. Like the D58 and D1 inks, there is a slight fluctuation of the heat flow around the cross-linking and B-stage cure regimes and the thermal degradation point. The D15 ink thermal flow graph is very similar to that of the D1 ink, but has a slight endothermic change at 600°C which is not seen in the D1 ink, but is seen in the resin and D58 in, however in the D15 ink, the change is not as pronounced. The presents of the graphite seems to have a similar effect on the thermal profile as that of the carbon. That is, there is a slight

fluctuation in the heat flow at the cross-linking and B-stage cure regimes, but a nullifying affect on the thermal degradation regime. The exothermic and endothermic changes also occur in a similar position for the two doped inks, D1 and D15, with the changes occurring at 386°C and 415°C and 377°C and 413°C respectively. Whereas the D58 has a low at 350°C and a high at 426°C. Figure 4.25 illustrates the points of interest in an expanded view of the curing and thermal degradation regimes.

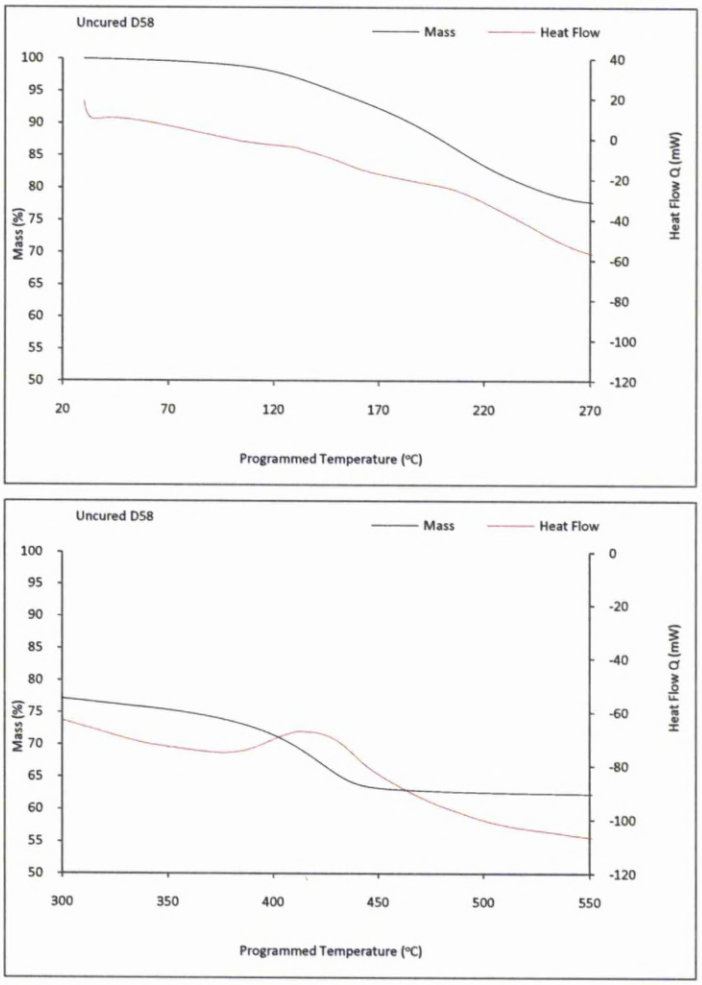

Figure 4.25: Expanded view of the cross-linking stage in the left graph, and the thermal degradation process in the right graph. There is a slight endothermic change at 377°C followed by an exothermic change at about 413°C.

Using equation 23 and with the following values, If we take the following values, m_{silver} = 75.15 mg, $C_{P\,silver}$ = 230 J/KgK, m_{resin} = 55.65 mg, $m_{graphite}$ =1.22 mg, $C_{graphite}$ =711 J/KgK and the cross-linking and B-stage cure heat capacities of the resin to be $C_{x\,resin}$ = 12.12 J/KgK and

$C_{B\,resin}$ = 14.99 J/KgK respectively with a m_{total} = 122.02 mg. We have a heat capacity of the D15 ink which is

$$C_{X\,D58}=153.30\ \text{J/KgK}$$
$$C_{B\,D58}=154.37\ \text{J/KgK}$$

4.3.4 Oven Cured Results

For the oven cured D58 ink run, 10.62 mg of cured ink was placed in to the alumina pan holder and put through the thermal cycle as stated in 3.2.1. The results are shown in Figure 4.26.

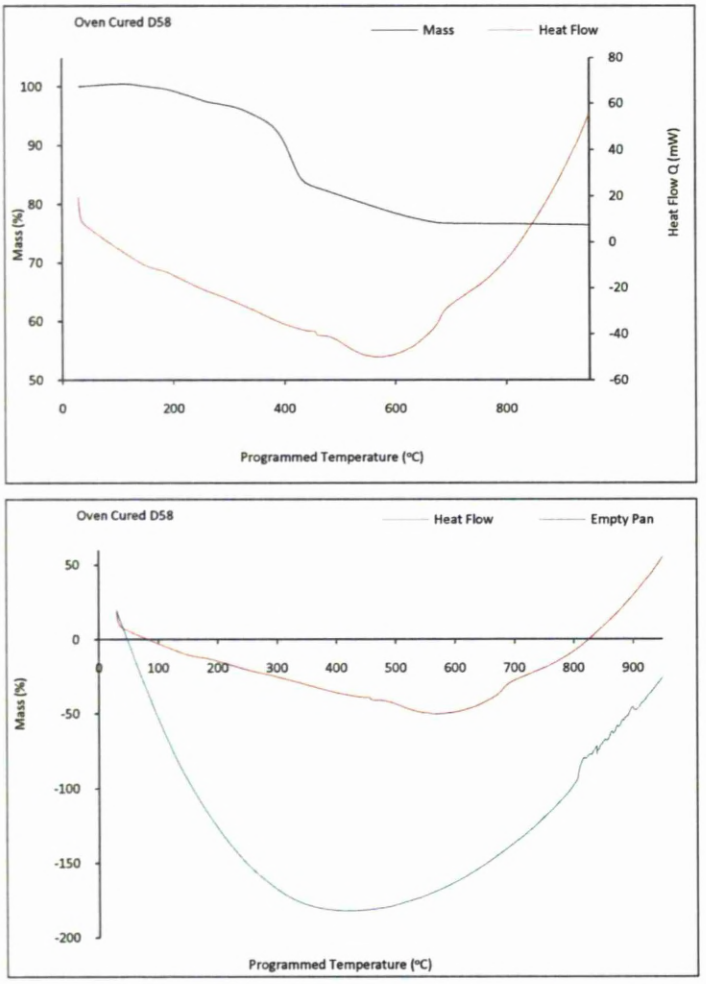

Figure 4.26: The left graph shows the TGA/DSC graph of the oven cured D58 ink and the associated heat flow for the thermal cycle, whilst the right graph shows the heat flow along with the empty pan reference run.

With the oven cured D58 ink, the initial stages of mass loss have gone. Though there is slight loss of mass up until the thermal degradation stage indicating that there is some residual cross-linking and/or solvent evaporation occurring, the majority of mass loss occurs during the thermal degradation stage. The mass loss plateaus at 76 % indicating that 24% of the cured ink is resin.

The shape of the heat flow graph is similar to that of the zinc calibration sample and the empty pan run, Figures 4.7 and 4.9. A slight change in the heat flow can be seen during the B-stage curing which would further imply that the mass loss that occurs is due to cross-linking. There is also a slight exothermic and endothermic change in the heat flow to the sample during the thermal degradation process, in keeping with the uncured inks.

4.3.5 Laser Cured Results

For the laser cured D58, D1 and D15 ink run, 9.72, 14.84 and 12.41 mg, respectively of cured ink was placed in to the alumina pan holder and put through the thermal cycle as stated in 3.2.1. The results are shown in Figure 4.27.

The laser cured mass loss rates are very similar to that of the oven cured D58 ink. With a small loss, shallow gradient, prior to thermal degradation. As thermal degradation occurs, there is a sharp increase in the mass loss rate. At the start of the D1 ink, there appears to be a slight fluctuation in the mass loss of the ink, which appears to be the loss of solvent early on in the heating process. The amount, however, is very small and slight, that the overall shape is still one that resembles that of a cured track. The heat flow graph is also very similar to the oven cured D58 ink, for all the laser cured samples, having a similar parabolic shape to the graph. The D58 and D1 inks more closely resemble that of the D58 oven cured ink, whilst the D15 does not have a complete parabolic shape by the end of the cycle. They do all have a change in heat flow during the thermal degradation stage as would be expected. The D1 ink loses the most mass, with only 67% remaining, whilst the D15 loses the least with 74% remaining at the end of the run. The D58 has 71% of its mass left. This is compared to the mass loss of the oven cured D58 sample which had 76% mass left, implying that though the laser cured samples are electrically cured and what appear to

be physically cured, they have some residual solvent within them and are not fully cross-linked.

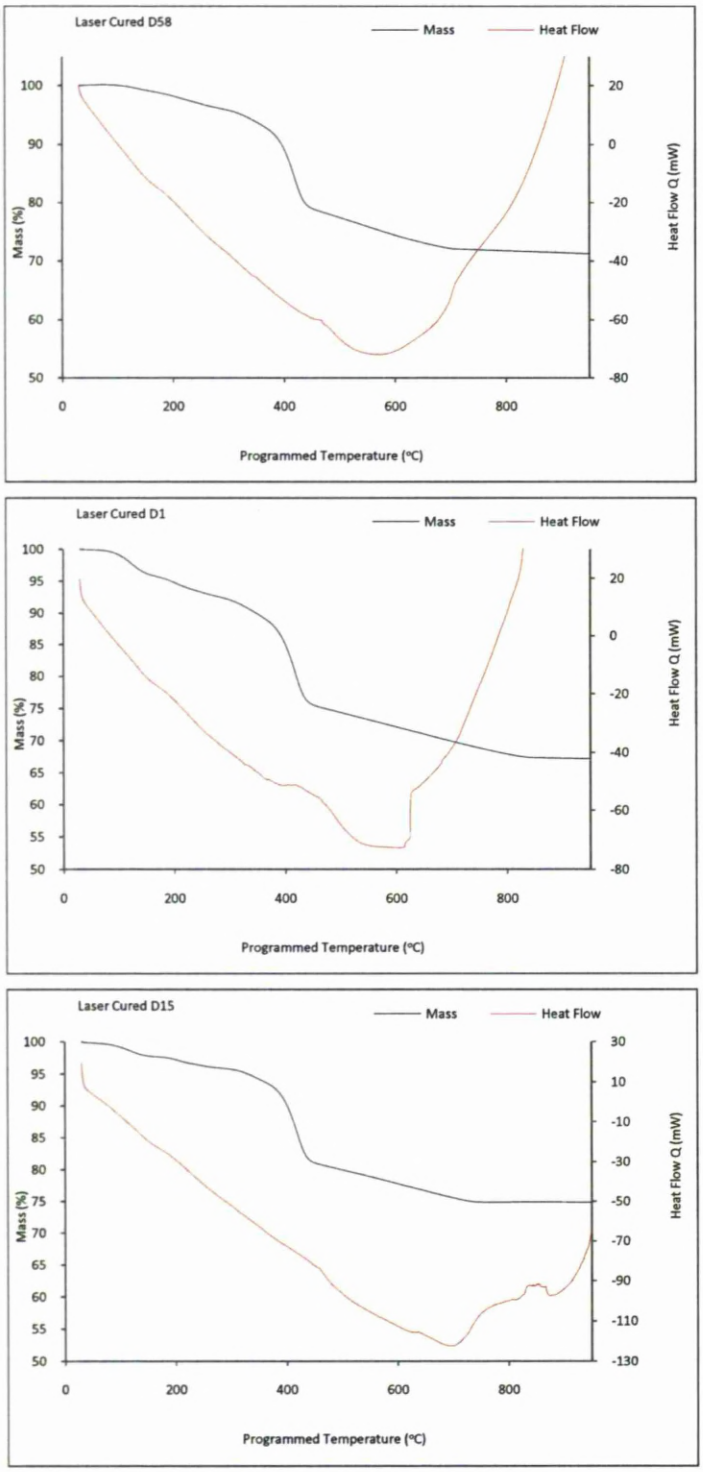

Figure 4.27: TGA/DSC graphs of the laser cured inks. The top left shows the plain D58 ink, the top right shows the carbon doped D1 ink, whilst the middle bottom shows the D15 ink.

References

1 "Characterization and analysis of Polymers" John Wiley & Sons, 2008, ISBN 978 0 470 23300 9.

2 J. O. Hill, *For Better Thermal Analysis Calorimetry*, ICTA, 3rd ed., CPC Reprographics, Portsmouth, U.K., 1991.

3 E. S. Watson, M. J. O`Neill, J. Justin, N. Brenner, *A differential scanning calorimeter for quantitative differential thermal analysis*, Anal. Chem. Vol.36, p.1233, 1964.

4 C. Y. Zahara, A.M. Zahara, *"The Perkin-Elmer 1020 series thermal analysis system"*, Thermochim Acta, vol.276, p. 161 (1996).

5 C. B. P. Finn *"Thermal Physics"*, 2nd ed., Nelson Thornes LTD., 2001, ISBN 0 7487 4379 0

6 J. H. Flynn *Analysis of DSC results by integration*, Thermochimica Acta, 217 (1993), p. 129-149.

7 B Wunderlich, *Thermal analysis,* Academic Press Inc. 1990, ISBN 0 12 765605 7.

8 W. W. M Wendlandt *Thermal Analysis*, 3rd ed. From Chemical Analysis, John Wiley & Sons, 1986, ISBN 0 471 88477 4.

9 H. K. Cammenga, W. Eysel, E. Gmelin, W. Hemminger, G. W. H. Höne, S. M. Sarge *The temperature calibration of scanning calorimeters. Part 2. Calibration substances*, Thermochimica Acta, 219 (1993), p.333.

10 C. M. Guttman, J. H. Flynn, *On the drawing of the baseline for differential scanning calorimetric calculation of heats of transition*, Anal., Chem., Vol. 45, No. 2, 1973, p.408-410

11 Perkin Elmer STA 6000, Simultaneous Thermal Analyser. http://www.perkinelmer.co.uk/search/Search.aspx?Ntt=STA+6000&N=0

5 FTIR Spectroscopy Analysis

The following chapter introduces the concept of using Fourier Transformation Infrared (FTIR) Analysis for the characterisation of polymeric materials and the equipment and methodology employed. The reason for conducting the FTIR analysis was to investigate the differences between the laser and oven curing processes and see if a different curing mechanism was involved along with the chemical constituents of the end products. By conducting these experiments it was possible to deduce whether the two curing processes were initiating the same chemical reaction during the curing process. The chapter is split in to six main sections. The first introduces the idea of FTIR analysis how it works and what it is commonly used for. The second section looks at the equipment used and the experimental method employed, the third section looks at the results of the experiments and analyses them, whilst the fourth is the conclusion of the results, with the fifth introducing a brief summary.

5.1 Introduction

FTIR analysis is a form of spectroscopy that deals with the infra-red region of the electromagnetic spectrum. Like all spectroscopic techniques, it is useful in determining or trying to identify a specific material or compound and its composition. FTIR is specifically useful for identifying functional groups in polymers due to the asymmetric nature of their bonds [1]. It measures the absorption of the material being tested to a range of frequencies in the mid infrared (IR) range. Some IR spectrometers will also look at near infrared wavelengths, however this is more specialist and not so common.

5.1.1 Theory

FTIR analysis relies on the premise that specific bonds have a specific resonant frequency at which they vibrate and hence energy that they absorb, which can be used to characterise their structure. Using a first approach, the frequency can be related to the strength of the bond and the mass of the atoms at either end of the bond, equation 5.1 [1], and hence the frequency of the vibration can be associated with a particular bond type. FTIR spectroscopy

comes under the broader term of vibrational spectroscopy. It is one of the oldest and most widely used forms of analysis for polymer scientists [2].

$$\nu = \frac{1}{2\pi c}\sqrt{\frac{f}{\mu}} \qquad (5.1)$$

Equation 5.1 is essentially Hooke's law for a single harmonic oscillator, and works well for a first approximation. ν is the frequency, c is the speed of light, f is force constant (essentially the bond strength) and μ is the reduced mass, which is found from equation 5.2 [1].

$$\mu = \frac{m_1 m_2}{m_1 + m_2} \qquad (5.2)$$

where m_1 and m_2 are the masses of the two atoms involved in the bond. Stronger bonds vibrate faster as do lighter atoms and hence have a higher energy. There are many different types of bond vibrations, but they can be classed in to three main categories bending, stretching and rotational. FTIR mainly initiates stretching and bending vibrational modes, due to the energies involved. Stretching generally occurs for higher frequency wavelengths or higher energy bonds, whilst bending occurs for lower frequency wavelengths or lower energy bonds.

For any given bond, if either the energy or the resonant frequency at which it absorbs the light is known, the other property can be found through quantum mechanics, equation 5.3 [3].

$$E = h\nu = \frac{hc}{\lambda} \qquad (5.3)$$

Where E is the energy of the photon, h is Planck's constant and λ is the wavelength of the photon. It can also be seen from equation 5.3 that the energy of the photon is directly proportional to the frequency of the photon. Hence as the frequency of the light that is absorbed increases, then so to must the bond energy that absorbed the light.

It is typical for the results of any FTIR analysis to be quoted in terms of transmittance (%) of light at a specific wavenumber, k, where the wavenumber is the inverse of the wavelength

and is shown in equation 5.4 [4]. It is also customary to quote the wavenumber in units of centimetres.

$$k = \frac{1}{\lambda} \ (\text{cm}^{-1}) \qquad (5.4)$$

An FTIR analysis usually takes place in the mid IR range, which corresponds to a wavenumber of 400-4000 cm^{-1} for the mid IR (2.5-30 μm wavelength). The instrument scans over the chosen bandwidth and measures the associated absorption of the spectra at each specific wavelength. Any absorption peak will correspond to a specific bond energy through equation 5.3 and 5.4.

4000	3000	2000	1500	1000
Bonds to Hydrogen	Triple Bonds	Double Bonds	Single Bonds	
O-H	C≡C	C=C	C-O	
N-H	C≡N	C=O	C-F	
C-H			C-Cl	

Table 5.3: Typical bond types for the respective wavenumber regions [1].

The region of a transmission spectrum with a wave number below that of 1500 cm^{-1} pertaining to the single bonds of molecules, is known as the "fingerprint" region. As this is a function of the whole compound rather than a specific bond and is particularly prevalent in polymers. For this reason, this area is not usually investigated in any great depth. From Table 5.1, it can be seen that the H-X bond is a high energy bond, where as all other single bonds are low energy. This is because of the light weight nature of hydrogen compared to other atoms, and hence a smaller reduced mass, μ, (ν is inversely proportional to μ) and as stated previously this means a higher frequency vibrational mode and hence a higher energy bond.

5.1.2 Principles of an FTIR machine

Fourier transform spectroscopy, in practice, is based on the idea of interference occurring between two beams to create an interferogram [2]. The interferogram is a signal that is produced from the interference of the two beams when the path length of the beams is altered with respect to the other beam. Fourier transformation is then used to transpose the distance value of the change in path length to that of frequency.

The most common form of FTIR instrumentation is the use of a Michelson Interferometer [6], as shown schematically in Figure 5.1. A Michelson interferometer consists of a coherent light source (in this case λ changes during the scan) that impinges on a beam splitter. In an idealised scenario, 50% of the beam is transmitted and 50% is deflected. Each split beam then incidents normal on to a mirror. Each of the mirrors are perpendicular to each other. One mirror is moveable while the other is static. The beams reflect off the mirrors and incident upon the beam splitter. Here they recombine. Half of the recombined beam will travel down to the sample, perpendicular to the original beam prior to splitting. This beam is called the transmitted beam, whilst the other half will travel back towards the source, the reflected beam. When the beams are recombined, an interference pattern will emerge dependent on the difference in path length of the two beams after they were first split (function of the linear translation of the moveable mirror). For path differences of $(n + ½)$ λ, the two beams interfere destructively in the case of the transmitted beam and constructively for the reflected beam [7].

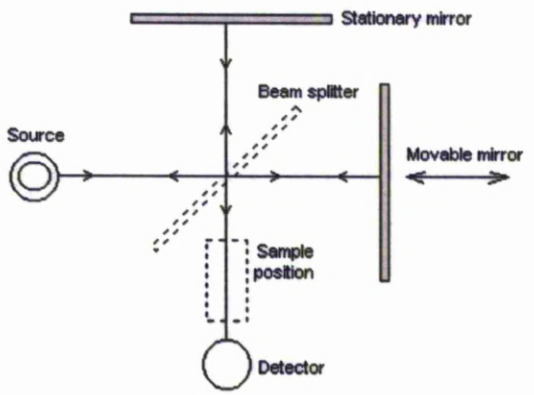

Figure 5.1: A schematic diagram of a Michelson interferometer [6]

The material of the beam splitter has to be chosen according to the IR region being used. Typically, materials such as germanium or iron oxide are coated on to an IR transparent substrate such as potassium bromide or cesium iodide for the near and mid IR range [2].

The equations used to relate the intensity falling on to the detector, $I(\delta)$, to the spectral power density as a function of wavenumber k, is given by $B(k)$ in the following equations.

$$I(\delta) = \int_0^{+\infty} B(k) \cos 2\pi k\delta \, dk \qquad (5.5)$$

Which is one half of a cosine FT pair, the other half being

$$B(k) = \int_{-\infty}^{+\infty} I(\delta) \cos 2\pi k\delta \, d\delta \qquad (5.6)$$

Equations 5.5 and 5.6 are interconvertable and are known as the FT pair. Equation 5.5 shows the variation in intensity as a function of wavenumber, whilst equation 5.6 shows the variation in power density as a function of the difference in path length (this is the interference pattern) [2].
To produce an FTIR spectrum, a reference spectrum is combined with a sample spectrum. That is a spectrum without absorptions and a spectrum with sample absorptions. The ratio of the two is then a double beam dispersive spectrum [2].

A recent development in FTIR analysis has been the transition from transmission analysis as shown in Figure 5.1, where intensity of the resultant spectrograph is dependent upon the sample thickness along with difficulties in sample preparation, to attenuated total reflectance (ATR). ATR has been developed to make the sample preparation easier and to negate the effect of sample thickness. Along with these attributes, it also allows for the sample to be tested directly in its solid, liquid or gas state.

A crystal, typically germanium or zinc selenide [8], is placed in contact with the sample. In the case of a liquid a thin layer is sufficient. For a solid, it is mechanically placed in contact with the sample so as to reduce the possibility of an air gap. However, most modern systems will remove any CO_2 or H_20 "noise" [8]. The IR beam is transmitted through the crystal which has a high refractive index, within which some total internal reflection occurs.

This total internal reflection produces an evanescent wave for which some penetrates in to the sample. For the region of IR where the evanescent wave is absorbed or attenuated by the sample, a change will occur. The beam is then collected as it exits the crystal by a detector, Figure 5.2.

Using this method also means that reflectance is taken as transmission. Highly reflective samples will appear to have a high transmission rate, even though they are opaque to that wavelength. Analysis is then conducted on the detected beam and a spectrograph produced. The ATR method is the processed used during the analysis of the samples.

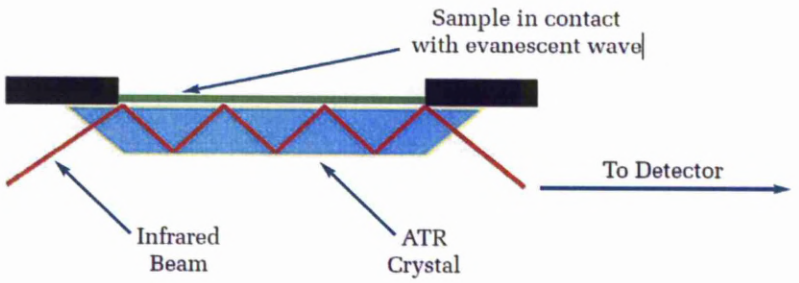

Figure 5.2: Schematic diagram of the principles of the ATR process [8]

5.2 Experimental Setup and Method

The FTIR spectrometer used to conduct the FTIR analysis for these experiments was a Perkin-Elmer Spectrum 100 FTIR Spectrometer. This spectrometer was specifically designed for conducting FTIR analysis in the mid IR range and uses the more modern ATR method, as shown in Figure 5.2. An image of the machine used can be seen in Figure 5.3. For the case of the Spectrum 100, a diamond ATR crystal is used. This is due to its robustness and longevity [8]. The diamond ATR crystal is housed within a top plate mounted on the top of the spectrometer. The sample is placed upon this crystal and a universal ATR accessory (UATR) which is kinematically mounted allowing for precise and repeatable sampling, is used to apply a small force so that the sample is in good contact with the crystal. Figure 5.4 shows the UATR in position. Once the UATR is in position the parameters of the run are set, and then the experiment is started. To acquire a full set of data, it typically takes about 30 seconds. The data is then produced in graph format on the associated computer display (stand alone computer integrated with the Spectrum 100.

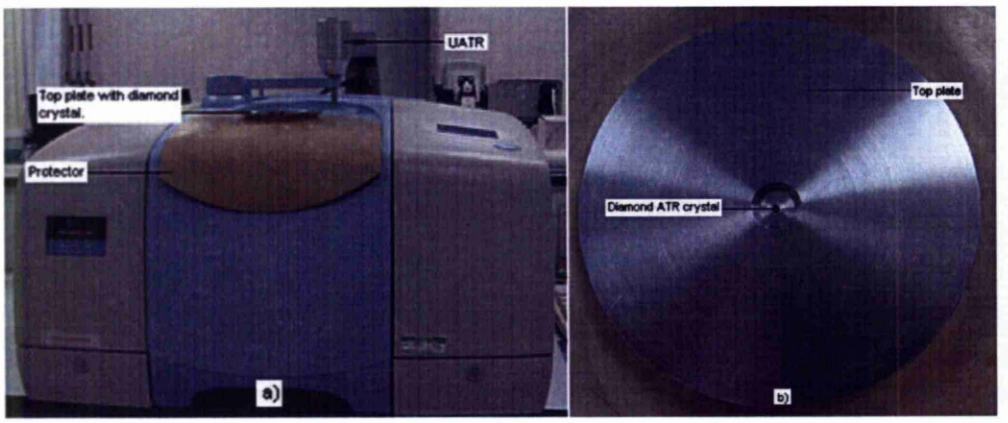

Figure 5.3: a) is a front on view of the Spectrum 100. b) is a close up of the top plate where the sample is placed on the diamond crystal.

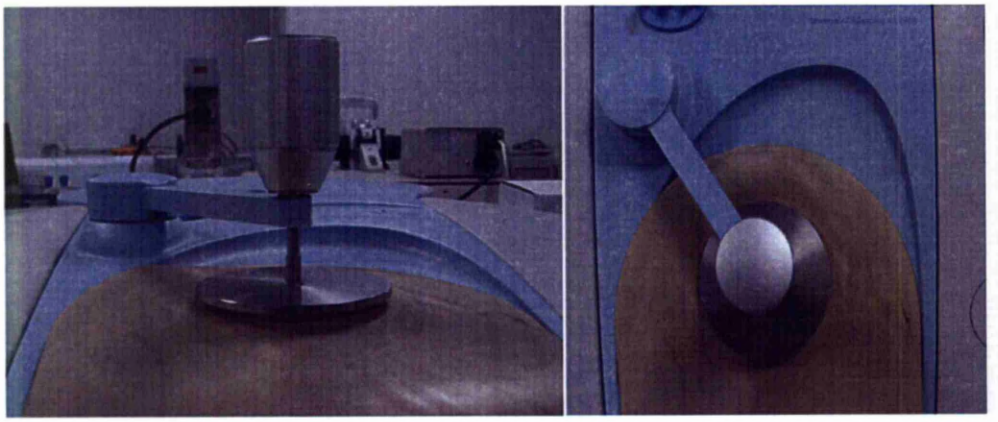

Figure 5.4: Side on and top down image of the UATR over the sample and in position for measurement taking.

FTIR spectroscopy was employed so that information about the inks could be gained and a better understanding of the absorption of the inks at 10.6 μm radiation and the bonds that are present before and after cure. A direct comparison could then be made between the two curing methods; laser and oven cure, between each other and the uncured inks.

Within the FTIR spectroscopy experiments, there were four main groups of tests to be conducted. They were: Constituents, Uncured inks, oven cured inks, laser cured inks. For each group the samples were treated and prepared for analysis in different ways.

5.2.1 Ink Constituents

In this section, the methodology employed for the analysis of the constituent parts of the inks is introduced. The parts are: Silver flakes, Carbon, Graphite and the uncured resin. The solvent used to reduce the viscosity of the resin was not tested individually, as this component was present in the resin and it was not possible to separate it out. Therefore the FTIR spectrograph produced for the uncured resin is an aggregate of the resin binder and the solvent diethylene glycol butyl ether. These constituents were tested for completeness and to see how much absorption of the radiation at 10.6 μm (943.40 cm^{-1}) would occur within the constituents. It is known that silver is highly reflective at this wavelength, so it was important to gauge how much absorption was occurring within the resin, carbon and graphite separately, and to compare the before and after cure bonding.

5.2.1.1 Silver (Ag) Flakes

The silver used for the inks was tested during the FTIR experiments. The Ag flakes used in the D58 series inks and all the subsequently modified inks. Further information and images can be found in **section 2.2.1.10**. The silver flakes have a size distribution as stated in table 5.2, with the thickness of any flake on average only a couple of microns thick. The length of the flake is the varying factor. Though essentially flakes, due to their fineness, the substance appears as a powder. Safety precautions were also taken, where rubber gloves and a mask was worn to prevent any inhalation and contamination of both sample and hands. A clean spatula was used to transfer a small amount of the silver flakes from their container, directly on to the window of the FTIR analyser. The UATR was placed in position and screwed down on to the sample till there was a slight resistance. The parameters were set, where a scan was required from 650-4000 cm^{-1}. The experiment was then started.

Table 5.2: Table of particle size distribution of the flakes tested in the FTIR analyser and used in the D58 series inks [9].

Particle Size Distribution[4]	(μm)
95%	<30.0
90%	<21.0
50%	<9.0
10%	<3.5

5.2.1.2 Carbon and Graphite

The modified D58 ink systems contained either carbon or graphite in varying concentrations. For further information on the carbon and graphite please refer to **chapter 2**. The procedure for testing the carbon and graphite was the same as that for the silver flakes. As with the silver flakes, due to the small particulate nature of the material, protective clothing was worn.

5.2.1.3 Uncured Resin

The uncured resin is a semi viscous polymer liquid which contains the solvent diethylene glycol butyl ether. A container of resin was provided by the manufacturer. The sample to be tested was taken directly from this container so as to reduce the amount of solvent loss as it is a volatile solvent. For further information on the solvent and resin please refer to chapter 2. The resin was taken from the container using a wide gauge syringe. A drop was then placed on the diamond window. Once the drop of resin was in place the UATR, was screwed in to position until a slight resistance was felt. The parameters were set 650-4000 cm^{-1} and the experiment started.

[4] PSD measured by Honeywell X100 particle size analyser [9]

5.2.2 Uncured Inks

The uncured inks; D58 - plain silver, D1- 1% carbon doped, D15 – 1% graphite doped, were tested to see what the absorption of the IR radiation would be like for a complete ink, along with information of the types of bonds and functional groups present prior to curing.

The uncured inks were handled in the same manner as the uncured resin, 5.2.1.3. A new syringe was used for each ink to avoid any cross contamination.

5.2.3 Oven Cured Inks

The oven cured inks were used as a bench mark to compare the laser cured samples against. Therefore it was important to know how the bonds and presence of functional groups changed during cure.

Each ink was deposited on to an alumina substrate using the doctor blade method, as mentioned in **Chapter 3**. The dimensions of the resultant ink track was 110 x 3 x ~0.006 mm. The samples were then cured in an oven at 130^{0}C for 20 mins. Once cured the samples were removed from the oven and the cured track was taken off the substrate with a Stanley knife (same as that conducted in thermal analysis Chapter 4). About three lines of the cured ink was used per FTIR sample. The removed track was then ground up in a pestle and mortar to create a powder which could easily be placed up the testing surface using a spatula. The following procedure was the same as that described in 5.2.1.1.

5.2.4 Laser Cured Inks

The laser cured samples were tested so that a good understanding of what the final cured tracks were like in terms of composition relative to that of the oven cured and uncured samples. It was important to know how the laser cured samples were affected during the curing process and if the end product was the same as that of the oven cured samples.

The laser curing set up for the FTIR trials was the same as that described in chapter 2. The inks were cured on an alumina substrate for consistency and ease of removal. Each ink was deposited using the doctor blade method (chapter 2) then aligned beneath the laser and cured. Each ink was cured using the same set of parameters for consistency. The parameters used for cure were 60 mm/s with 2 passes with a power setting of 24*W*. This produced a good fully cured track for all the inks. The tracks were then removed from the alumina substrate using a Stanley knife, and three tracks were used for each FTIR test. The rest of the method follows that of the oven cured samples (5.2.3.1).

5.3 Experimental Results

In this section, the results of the FTIR spectroscopy experiments are presented. They have been broken up in to 4 sub-sections. The first is the separate constituents of the inks, tested individually. The second shows the results of the uncured inks, whilst the third shows the results of the oven cured inks. The final section introduces the results of the laser cured inks. It should be pointed out that the CO_2 laser used during these experiments had a laser wavelength of 10.6 μm. This correlates to a wavenumber of 943.40 cm^{-1} which is very much in the finger print region.

5.3.1 Constituents

As stated previously. For completeness the separate constituents of the inks were tested for completeness. It was felt that this was necessary to create a good holistic picture of how each individual part looked in terms of its interferogram without any contaminant contributions. Further to this, looking at transmission peaks of any sample, specifically at 943.40 cm^{-1}, will be useful for understanding how the absorption of the materials change with cure to the laser used.

Silver, by mass, is the largest proportion of a single material within the inks. It is known that it is highly reflective to 10.6 μm radiation. The FTIR analysis in Figure 5.5 shows two tests conducted on the silver flakes, both runs demonstrate the same general profile, but with the blue graph slightly offset from the black graph. This is probably due to the amount of the sample used being slightly different in each one. It can also be seen that there is significant absorption, 30-35%, between 4000-3300 cm^{-1} and thereafter it steadily rises to a

peak of 91% transmission at 650 cm^{-1}. There is an increase in absorption to what has been realised when conducting similar tests on silver mirrors with a normal incident of radiation. There appears to be a couple of things going on here.

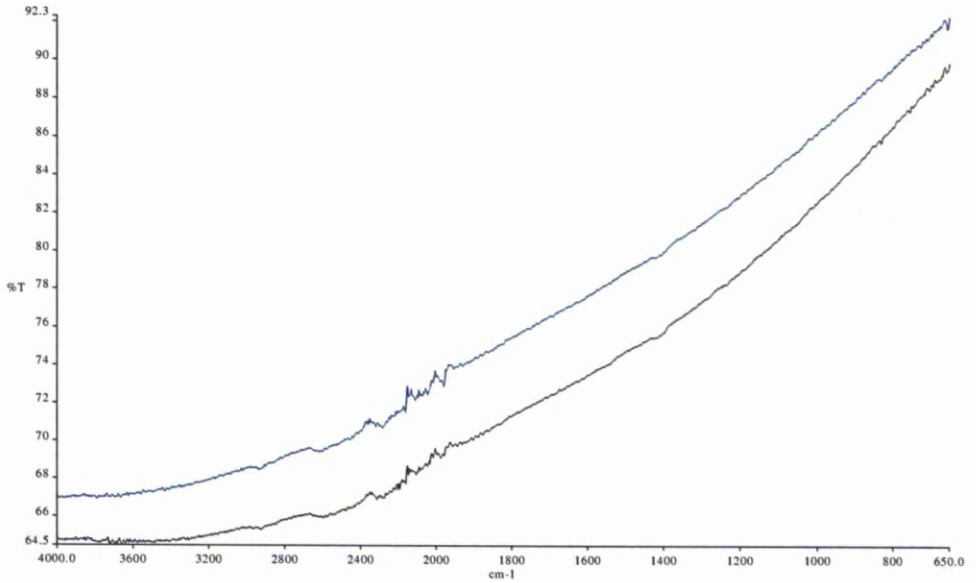

Figure 5.5: D58 silver flakes used in the conductive inks.

The first appears to be the reduced transmission to the material at higher wavenumbers and increased absorption. As the wavelength decreases, it starts to become smaller than the average particle size; a wave number of 650 cm^{-1} has a wavelength of 15.38 µm which is larger than the majority of the particle sizes (Table 5.2), whilst a wavenumber of 4000 cm^{-1} corresponds to a wavelength of 2.5 µm. As the wavelength becomes smaller than that of the particle sizes, it starts to become scattered between the particles. This scattering increases the number of interactions and hence the effective absorption rate as the feature size is similar to or larger than that of the wavelength. The results imply that the silver is still essentially reflective, and that it is the feature size that makes the material appear to be absorptive. This is further backed up by research conducted by Yulan Wang et al [10], in to the absorption of silver coatings on silicon. They witnessed very high absorption rates for radiation of 1.33-10 µm for silver feature sizes of 6-8 µm.

The second is the increased transmission as the wavelength increase. This follows on from the previous argument. As the wavelength increases, it becomes greater in size than that of the majority of the particles. This implies that the scattering that occurs is reduced as a function of wavelength as the radiation cannot resolve the smaller particles and hence be

scattered between flakes as easily, thus the number of interactions is reduced causing a higher percentage of the light to be transmitted (reflected as it is ATR).

As the transmission increases with decreasing wavenumber, there is what appears to be noise, between 2400 and 1900 cm^{-1}. These wavenumbers correspond to a wavelength of 4.16 µm and 5.26 µm respectively. From Table 5.2 in can be seen that the distribution of the silver flakes means that 40% of the silver flakes are between 9 µm and 3.5 µm. Therefore 40% of the material sits within 18% of the size distribution (5.5 µm) and so the noise can be attributed to the dominant feature size of the silver flakes.

The results for carbon and graphite are shown in Figure 5.6 and 5.7 respectively. Though the results of both samples look quite different, they are both demonstrating that there is high absorbance to all IR radiation, though significantly more across the scanning range in carbon. The carbon particle sizes are sub 60 µm [11], with 60% less than 10 µm (~940 cm^{-1}). The peaks between 2400 cm^{-1} and 1800 cm-^{1} cannot be accounted for. However this was consistent for all the test samples of carbon. With the graphite sample there is a more linear distribution of the interferogram. However it was not possible to obtain data from the company on the particle size distribution, so any peaks on the interferogram cannot be correlated to particle size. However there would appear to be some artefacts occurring between 2400 cm^{-1} and 1800 cm^{-1}. These artefacts are similar in shape to that of the carbon interferogram in the same region, and similar in magnitude.

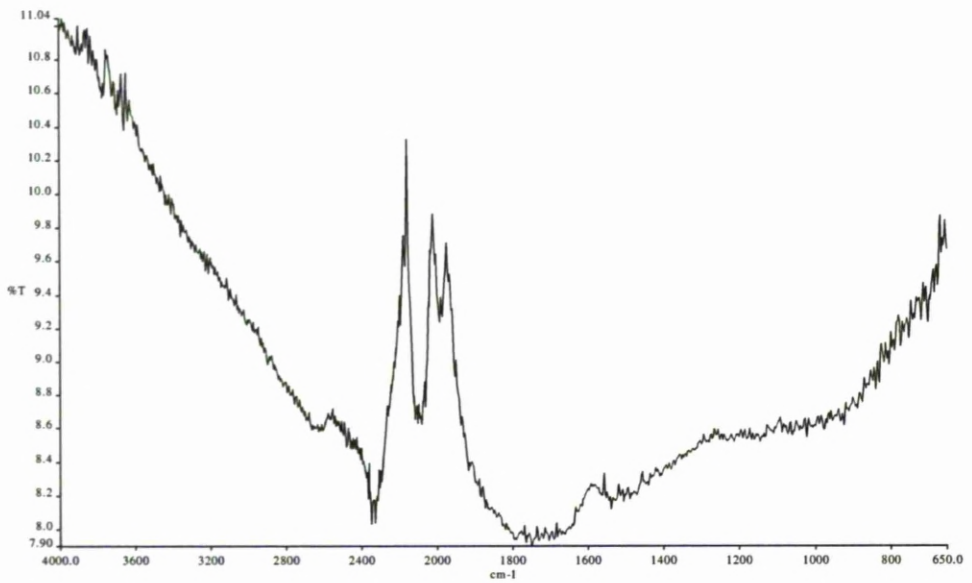

Figure 5.6: Carbon used to dope the silver inks.

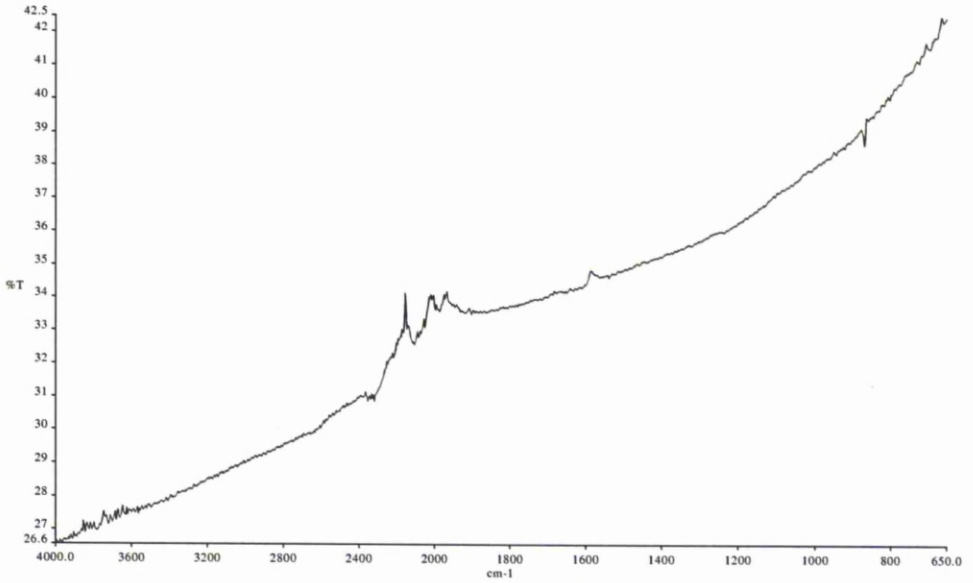

Figure 5.7: Graphite used to dope the silver inks

The interferogram of the uncured resin is shown in Figure 5.8. This interferogram is more typical of what a polymeric FTIR spectrograph should look like compared to Figures 5.5, 5.6 and 5.7. Looking at Figure 5.5 it is immediately clear that there are several absorption peaks across the whole spectrum. The finger print region, < 1500 cm^{-1}, shows that there are a lot of single bonds within the polymer with heavy atoms. The 1039.75 cm^{-1} looks like a C-O bond with the broader absorption peak between 1100 cm^{-1} and 1039 cm^{-1} due to hydrogen bonding within the polymer.

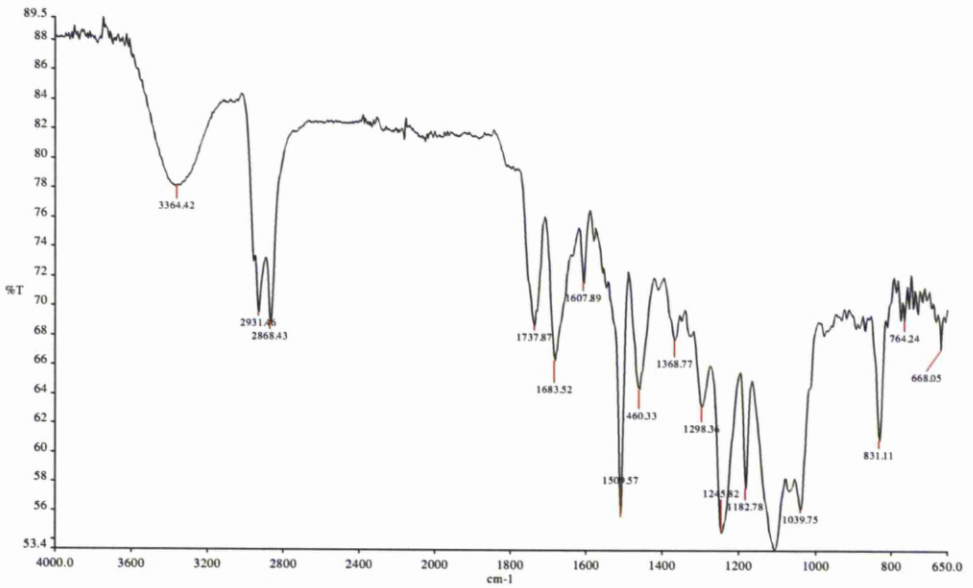

Figure 5.8: Uncured D58 resin

The 1298 cm^{-1} peak is probably due to the presence of as phosphor-oxygen double bond, or similar, within the polymer and is within the finger print region due to the heavier nature of the two atoms compared to carbon.

Going further along to the next set of significant peaks, there is a double absorbance peak at 2868.43 cm^{-1} and 2931.46 cm^{-1}, and this is similar to that seen in the solvent Di(ethylene glycol) butyl ether, Figure 5.10, and also common polymers such as non-aromatic hydrocarbons and non-aromatic ethers, actetals and epoxides. These peaks are attributed to the single C-H bonds present within the polymer and are attributed to there being a methylene group present. 2868.43 cm^{-1} and 2931.46 cm^{-1} are the symmetric and asymmetric stretches of this group respectively [12]. The positions of these peaks, are approximately 11 cm^{-1} off from what is characteristically seen for unsubstituted hydrocarbons and so implies that there is either an anisotropic hydrocarbon or one that has been halogenated. Typical values of unsubstituted hydrocarbons for a methylene group are 2920 cm^{-1} and 2855 cm^{-1} for the asymmetric and symmetric stretches respectively [12].

Just after the double peaks of the C-H bond, there is a slight absorption peak at 3050 cm^{-1}. This very slight peak is characteristic of the methylene terminal group on the epoxide ring. This is characteristic of all the uncured inks as shown in section 5.3.2.

The next peak along, with increasing wavenumber is the 3364.42 cm^{-1} peak. This peak, with its broad shape is a common peak within polymers, and is useful for identifying functional groups. This is because the N-H bond part of an amine group has a wavenumber of 3240 cm^{-1} and 3372 cm^{-1} and the O-H bond part of a hydroxyl group is 3405 cm^{-1} [13]. The broad nature of this peak is due to there being a high presence of both bonds and the close proximity in terms of wavenumbers between them.

There is a hydroxyl group within the solvent which is clearly demonstrated in the FTIR spectra of this solvent, Figure 5.9 [14]. It is known from chapter 2 that the resin is a pendant hydroxyl epoxy urethane of some type. The data of the uncured resin backs this up along with Figure 5.9, where this absorption peak is clearly visible within the solvent. Also at around 943.30 cm^{-1} (10.6 μm), there is high absorption within the resin, ~40%. Table 5.3 shows the major peaks of Figure 5.8 in table form.

Table 5.3: Table of the major peaks marked on Figure 5.6 for the uncured resin.

Wavenumber (cm^{-1})			
3364.42	1683.52	1368.77	1039.75
2931.46	1607.89	1298.36	831.11
2868.43	1509.57	1245.82	764.24
1737.87	1460.33	1182.78	668.05

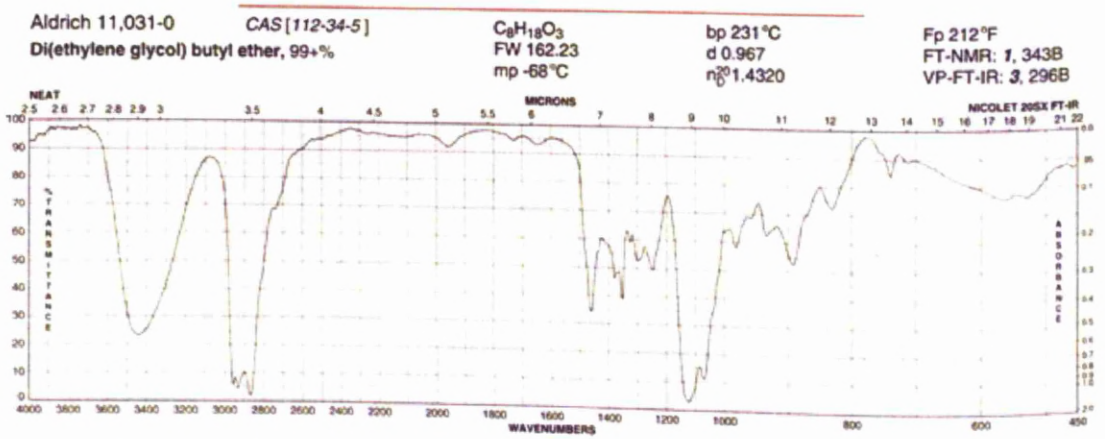

Figure 5.9: FTIR spectra of Di(ethylene glycol) butyl ether. Transmittance is on the left and absorbance on the right axis. The data at the top gives physical data on the solvent and references to the 1st edition of *The Aldrich Library of FT-IR spectra* [14].

From Figure 5.9 there are some common points between the uncured resin and the solvent. The first is the presence of the O-H bond at 3364.42. Like the uncured resin this is a broad deep peak in the solvent spectra. The next two points in the solvent spectra are also seen at 2931.45 and 2868.43. The peak at 1460.33 and 1245.82 are also clearly seen. Since the uncured resin is a mixture of the resin polymer and the solvent, it is right to assume that the spectra of the uncured resin is a combination of the two. For wavenumbers below 3600 cm^{-1} in Figure 5.10 the transmittance of the spectra is significantly reduced. This is attributed to the addition of the resin polymer as Figure 5.9 shows good transmittance for some wavenumbers below 3600 cm^{-1}, and the solvent spectra is contained within this reduced transmittance. The correlated points that are clearly visible between the two graphs are then bonds that are common to the two organic components.

5.3.2 Uncured

The uncured inks are the three inks, D58, D1 and D15, with all their constituent parts within them prior to curing. Therefore the spectrograph will be a combination of the constituents seen in section 5.3.1. Though silver is the largest component by mass, it is also the densest. Therefore the resin which is not as dense, is the largest constituent of the ink by volume. Therefore the resin spectrograph will be the dominant feature of the inks.

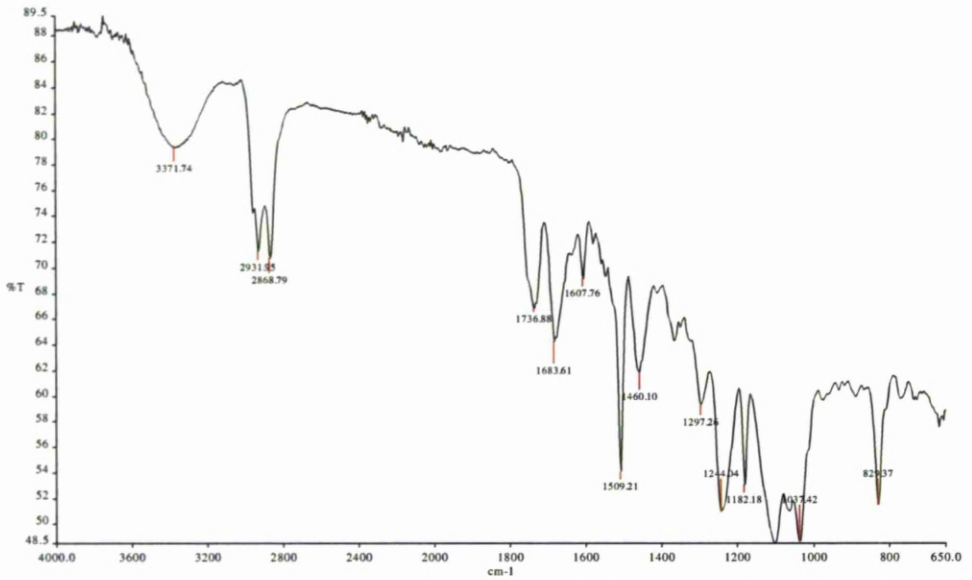

Figure 5.10: Uncured D58 ink

This can be seen in Figure 5.10, where it is immediately clear that the spectrograph of the D58 ink is very similar to that of the uncured resin spectrograph. The absorption peaks occur at the same wavenumbers (allowing for repeatability and the slight shifting affect of the other constituents ± 2 cm^{-1}). Absorption is higher in the fingerprint region for the D58 ink with minimum transmission occurring at 1037.42 cm^{-1} with 48.5% transmission, but less at the C-H peak. This is due to the fact that at the lower wavenumbers, more of the radiation is scattered by the silver particles, as stated in section 5.3.1, as the radiation is scattered multiple interactions occur between the radiation-silver-resin, thus increasing the effective absorption of the radiation in to the resin. The apparent drop in absorption at the C-H peak will be due to the decreased amount of C-H bonds as a percentage within the ink due to the resin making up only ~40% of the ink by mass. There is also a shift in the O-H/N-H peak, from 3364.42 cm^{-1} for the uncured resin, to 3371.74 cm^{-1} for the uncured D58 ink. This implies there is a slight shift towards O-H bonds as nitrogen is lighter then oxygen and

so has a lower frequency of vibration. This shift appears to be an anomaly of the uncured D58 ink, as the uncured D1 and D15 (Figures 5.11 and 5.12 respectively) inks are similar to that of the uncured resin alone with an absorption peak of around 3361 cm^{-1}. This anomaly may arise from a slight increase in the ratio of resin and solvent to silver for the D58 since there are no dopents. The overall shape is very similar and the major peaks of Figure 5.10 are shown in table 5.4.

Figure 5.4: Table of the major peaks marked on Figure 5.10 for the uncured D58 ink.

Wavenumber (cm^{-1})			
3371.74	1683.61	1297.26	829.37
2931.95	1607.76	1244.04	
2868.79	1509.21	1182.18	
1736.88	1460.10	1037.42	

The spectrograph of the carbon doped uncured ink, D1, is shown in Figure 5.11. It is very similar to that of the uncured D58 and resin spectrographs. With absorption peaks and magnitudes similar to that of both inks. The noticeable thing with the D1 ink is that it has more absorption at its C-H peak, 2931.82 cm^{-1} and 2867.17 cm^{-1} than the D58. Similar to that of the resin at about 68% transmission, compared with 70% for the D58. The 3362.02 peak is also closer to that of the resin with about 78% transmission, and this is accounted

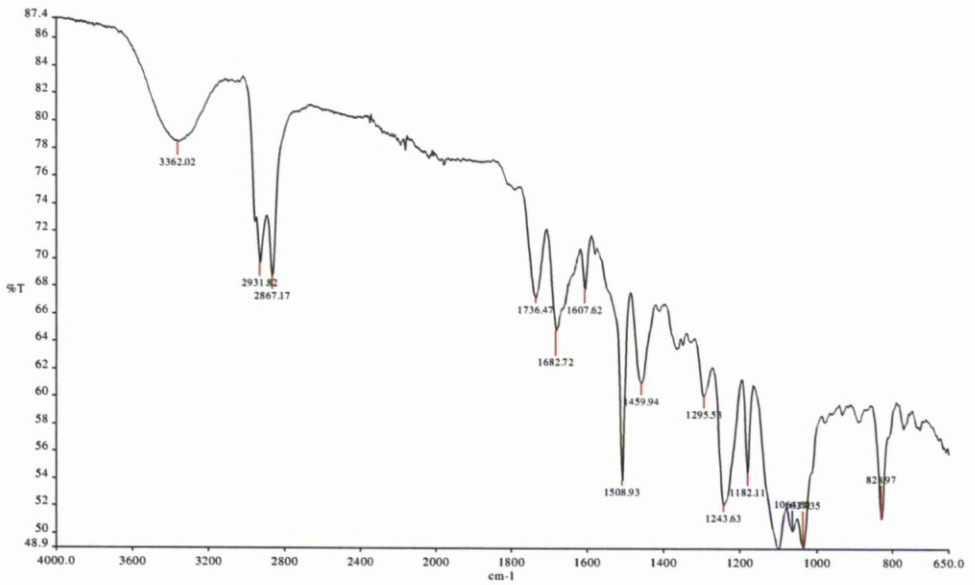

Figure 5.11: Uncured D1 ink

for through the addition of carbon, making the whole system more absorptive. However in the fingerprint region, there is more absorption then that of the resin, with the minimum transmission occurring at 1037.35 cm^{-1} with 48.9% transmission. The carbon component seems to increase the absorption in the fingerprint region over that of the resin alone and with the higher wavenumbers over that of the D58 ink, making the ink overall more absorbent to IR radiation when compared to either the D58 or resin. Table 5.5 lists all the major peaks from Figure 5.11.

Table 5.5: Table of the major peaks marked on Figure 5.11 for the uncured D1 ink.

Wavenumber (cm^{-1})			
3362.02	1682.72	1243.63	828.97
2931.82	1607.62	1182.11	
2867.17	1459.94	1064.60	
1736.47	1295.53	1037.35	

The spectrograph of the D15 uncured ink is similar to that of the uncured resin, uncured D58 and uncured D1 inks. The D15 has a 1% dopent of graphite by mass. The transmission percentages are similar to that of the D1 ink, with 79% transmission in the O-H bond range and 68-70% in the C-H bond range. Also in the fingerprint region, the least transmission occurs at around the peak of 1037.35 cm^{-1} with a transmission of 48.9%. The same as that of the D1 ink. As with the carbon in the D1 ink, the graphite in the D15 ink seems to

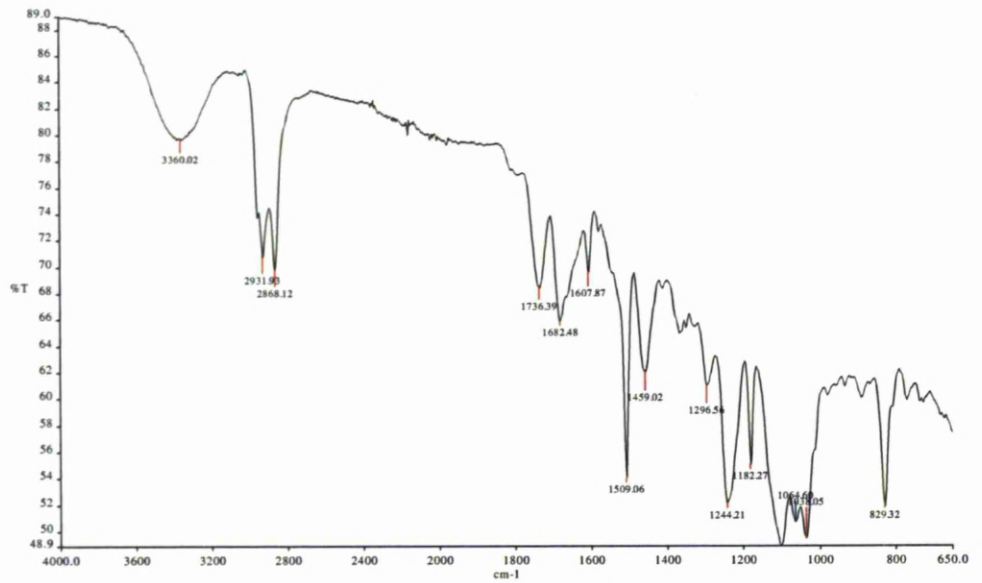

Figure 5.12: Uncured D15 ink

increase the absorption in the fingerprint region over that of the resin alone and with the higher wavenumbers over that of the D58 ink, making the ink overall more absorbent to IR radiation when compared to either the D58 or resin. Table 5.6 lists all the major peaks from Figure 5.12.

Table 5.6: Table of the major peaks marked on Figure 5.12 for the uncured D15 ink.

Wavenumber (cm^{-1})			
3360.02	1682.48	1296.56	1038.05
2931.93	1607.87	1244.21	829.32
2868.12	1509.06	1182.27	
1736.39	1459.02	1064.60	

5.3.3 Oven cured

The results below show what the spectrograph looks like of the oven cured inks. The inks were cured at a temperature of 130^{0}C for 20 minutes and then tested. The results of the oven cured samples were taken as the benchmark or standard as to what the spectrograph of the inks should look like when they are fully cross-linked.

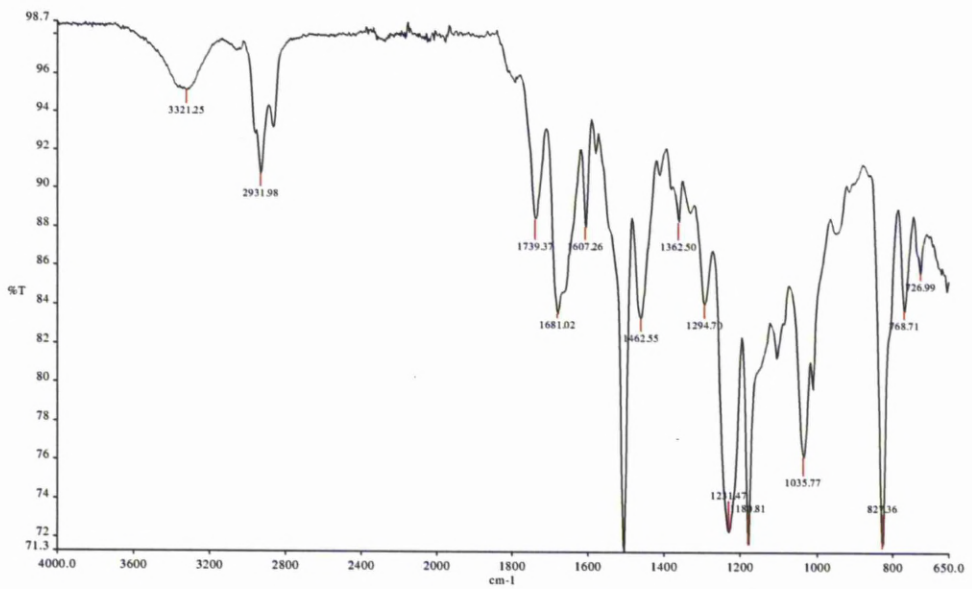

Figure 5.13: Oven cured resin.

Figure 5.13 shows the spectrograph of the oven cured resin of the D58 ink. The sample is fully crosslinked. The O-H/N-H absorption peak at 3321.25 cm^{-1} is reduced to 95% transmission as the functional group reacts with the epoxide ring. As cure takes place, the epoxide reacts with the amine group reducing the absorption at 3370 cm^{-1}. A hydroxyl is produced during this reaction and the epoxide ring also reacts with this functional group. When cross-linking occurs with a hydroxyl, water is given off as a by product, and in this case the associated reduction can be seen from the reduction of the absorption peak at 3405 cm^{-1}. From Figure 5.13 and table 5.7 it can be seen that the hydroxyl and amine peak has been reduced, but also shifted towards lower wavenumbers. This may be accounted for by the reduction of the hydroxyl group through solvent evaporation and reaction with the epoxide ring along with N-H bonds still being present within the cross-linked polymer. Another explanation that may contribute towards this shift that is witnessed in both the oven cured and laser cured samples, is the cross-linking process. As the ink cross-links it reduces in mass, but also increases in density, as shown in chapter 2. It is this densification that helps to make the inks conductive bringing the silver flakes in to contact with each other. By doing this there is an associated increase in pressure within the system along with densification. It has been shown by F. Deon et al that as the pressure upon a sample increases a shift in the FTIR absorption peak of the hydroxyl bond is witnessed [15]. The change occurs linearly with increasing pressure upon the sample. The increase in pressure can be interpreted in terms of the densification of the ink that occurs during curing. The changes in the distances between the neighbouring atoms lead to changes in the anharmonic interatomic potentials, which in turn will affect the frequency of the vibrational bands of the bonds [16]. This along with the other factors may account for the shift witnessed.

There is also a reduction in the C-H bonds at 2931.98 $cm^{-1}$where the transmission is 90%, with a more significant reduction in the symmetric methylene stretch that was present in all the uncured samples (Figures 5.8, 5.10, 5.11 and 5.12). This also implies that water is given off during the cross-linking process as there is a reduction in C-H bonds and a more complex polymer structure is present. This is further witnessed in the fingerprint region. Though the overall absorption becomes less as the ink is cured, the absorption peaks become more discreet in this region with significant peaks at about 1500 cm^{-1} and 827 cm^{-1} whilst keeping the overall distribution very similar to that of the uncured resin. Table 5.7 lists the major peaks for the spectrograph shown in Figure 5.13.

Table 5.7: Table of the major peaks marked on Figure 5.13 for the oven cured resin.

Wavenumber (cm^{-1})			
3321.25	1607.26	1231.47	726.99
2931.98	1462.55	1180.81	
1739.37	1362.50	1035.77	
1681.02	1294.70	827.36	

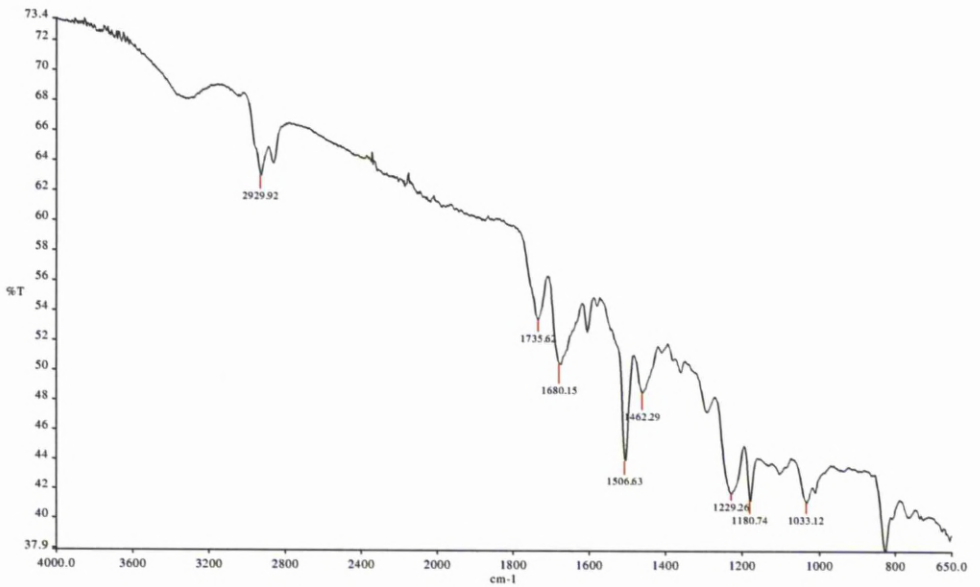

Figure 5.14: Oven cured D58 ink

With the D58 spectrograph shown in Figure 5.14, it is firstly noticeable that there is overall a greater absorption of the radiation across all wavenumbers. The highest absorption point comes at around 829 cm^{-1} with a transmission of 37.9%. This is greater than that of the uncured inks. Whereas the resin had a lower absorption rate after cure, it seems that the D58 ink has a higher rate of absorption. Further to this there is a gradient to the graph where absorption increase as wavenumber decreases. This effect can only be attributable to the addition of the silver when comparing Figures 5.13 and 5.14. There is also a notable reduction in the relative size of the O-H/N-H peak compared with the C-H peak at 2929.92 cm^{-1} (asymmetric stretch), though the absorption is still greater than that of the resin alone when oven cured. The reduction of the symmetric stretch compared to the asymmetric stretch of the methylene group is also not as pronounced when compared to the resin

alone. Therefore, as the wavelength increases the ink becomes more absorptive as it cross-links and cures. A table of the main peaks is shown in table 5.8.

Table 5.8: Table of the major peaks marked on Figure 5.14 for the oven cured D58 ink.

Wavenumber (cm^{-1})	
2929.92	1462.29
1735.62	1229.26
1680.15	1180.74
1506.63	1033.12

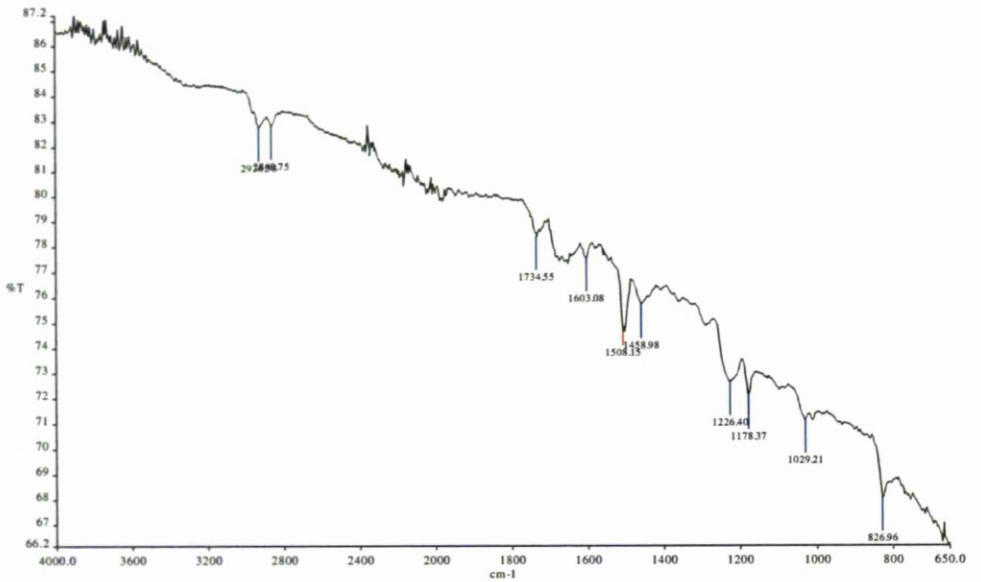

Figure 5.15: D1 oven cured

The spectrograph of the oven cured D1 ink, Figure 5.15, is similar to that of the oven cured D58 ink. However the absorption is less than that of the D58 ink. The D1 ink has a transmission high of about 87% at 4000 cm^{-1} and a low of 66.2% at 650 cm^{-1}. This is compared to the D58 in Figure 5.14 which has a transmission high of 73% at 4000 cm^{-1} and a low of 37% at around 820 cm^{-1}. The peaks however are in a similar position. The O-H/N-H peak has disappeared, and no longer is discernable from the spectrograph along with a significant reduction of the C-H peaks at 2926.58 cm^{-1} and 2860.75 cm^{-1}. The reduction in the two methylene peaks is similar, relative to each other. The addition of the carbon appears to evenly reduce the asymmetric and symmetric peaks along with reducing the wavenumber at which they appear. For the cured D1 ink the asymmetric stretch peak appears at 2926.58 cm^{-1} compared with the same peak for the D58 ink, 2929.92 cm^{-1} and

2931.82 cm^{-1} prior to curing. Whilst the symmetric stretch peak for the D1 ink is at 2860.75 cm^{-1} where prior to cure it was 2867.17 cm^{-1}. This change of wavenumber is not witnessed in the resin or D58 inks before and after cure. The reduction in the peaks, overall are less distinguishable than that of the D58 ink. A table of the significant peaks is shown in table 5.9.

The D15 oven cured ink produces a spectrograph, table 5.10 very similar to that of the D1 spectrograph. It has a transmission high of 81% at 400 cm^{-1} and a low of 56.6% at 650 cm^{-1}. The O-H/N-H absorption peak is gone, similar to that of Figure 5.15 for the D1 ink along with a reduction in the absorption at the C-H bond, 2926.58 cm^{-1} and 2860.75 cm^{-1}. The same reduction in wavenumber of the methylene group is witnessed as seen for the D1 ink, and by a similar amount. Prior to cure the asymmetric and symmetric positions were 2931.93 cm^{-1} and 2868.12 respectively. After cure they were 2926.58 cm^{-1} and 2860.75 cm^{-1}. A table of the significant peaks is shown in table 5.10.

Table 5.9: Table of the major peaks marked on Figure 5.15 for the oven cured D1 ink.

Wavenumber (cm^{-1})		
2926.58	1508.15	1029.21
2860.75	1458.98	826.96
1734.55	1226.40	
1603.08	1178.37	

Table 5.10: Table of the major peaks marked on Figure 5.16 for the oven cured D15 ink.

Wavenumber (cm^{-1})		
2926.58	1605.61	824.43
2860.75	1505.88	
1734.55	1228.93	
1668.82	1178.37	

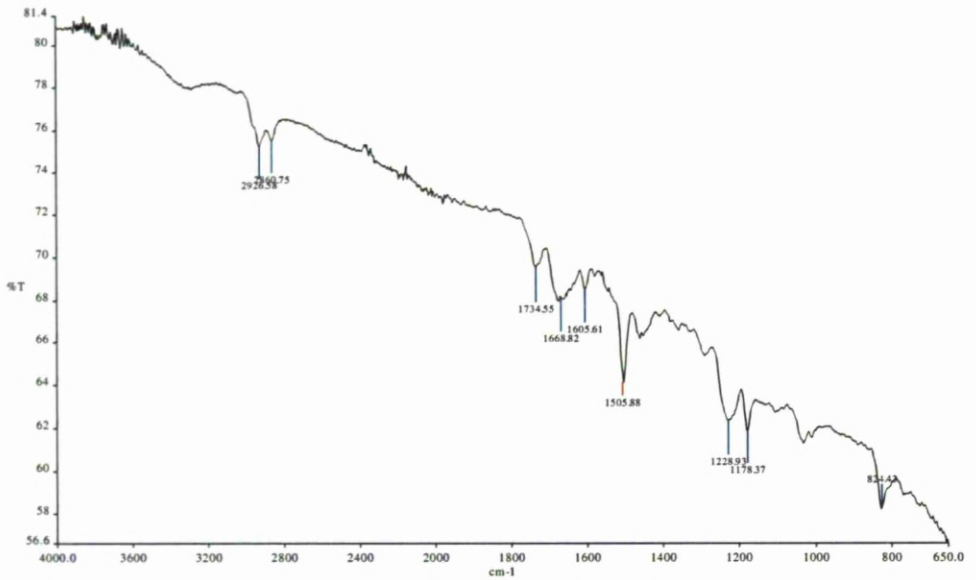

Figure 5.16: D15 oven cured

5.3.4 Laser Cured

In this section the results of the laser cured experiments are shown. The samples were cured with parameters of 24 *W* and a speed of 60 *mm/s* with two passes. This created a solid cured track with low resistance. A resin only sample was not conducted during the laser curing trials due to difficulties in getting a good even cure throughout the sample.

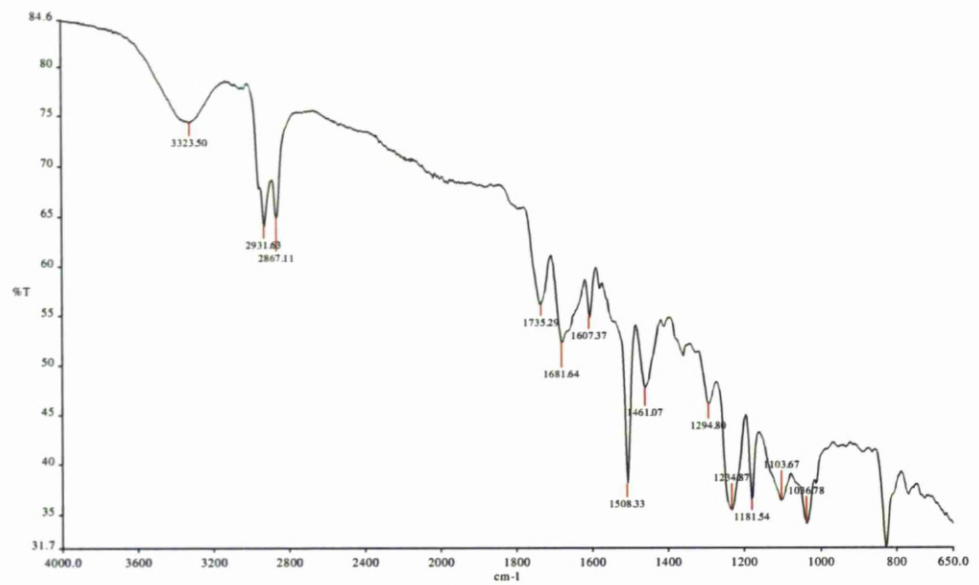

Figure 5.17: D58 Laser cured

As seen from Figure 5.17 the laser cured spectrograph has similarities between the uncured D58 ink, Figure 5.10 and the oven cured D58 ink, Figure 5.14. Like the oven cured sample, it has a high absorption across the whole spectrum compared to the uncured D58 along with a gradient of absorption that is inversely proportional to that of the wavenumber. Transmission is at a high of 84% at a wavenumber of 4000 cm^{-1} and a low of 31% at about 829 cm^{-1}. The slope of the spectrograph is once again attributed to the addition of the silver. Unlike the respective oven cured sample, the O-H/N-H and C-H absorption peaks have only been reduced slightly when compared with the uncured D58 ink. However like the oven cured sample the O-H/N-H absorption peak has been shifted to 3323.50 cm^{-1}. This implies that cross-linking is occurring through the removal of the solvent (loss of the hydroxyl component) along with the reaction of the epoxide with the amine and subsequent hydroxyl group produced (section 5.3.3), however the degree to which this is occurring at the first glance appears not to be as great as that witnessed for the oven cured sample. Like the respective oven cured sample, there is a drop in the symmetric stretch of the methylene group (2867.11 cm^{-1}) with respect to the asymmetric stretch (2931.63cm^{-1}). A table of the significant peaks is show in table .

Table 5.11: Table of the major peaks marked on Figure 5.17 for the laser cured D58 ink.

Wavenumber (cm^{-1})			
3323.50	1681.64	1294.80	1036.78
2931.63	1607.37	1234.87	
2867.11	1508.33	1181.54	
1735.29	1461.07	1103.67	

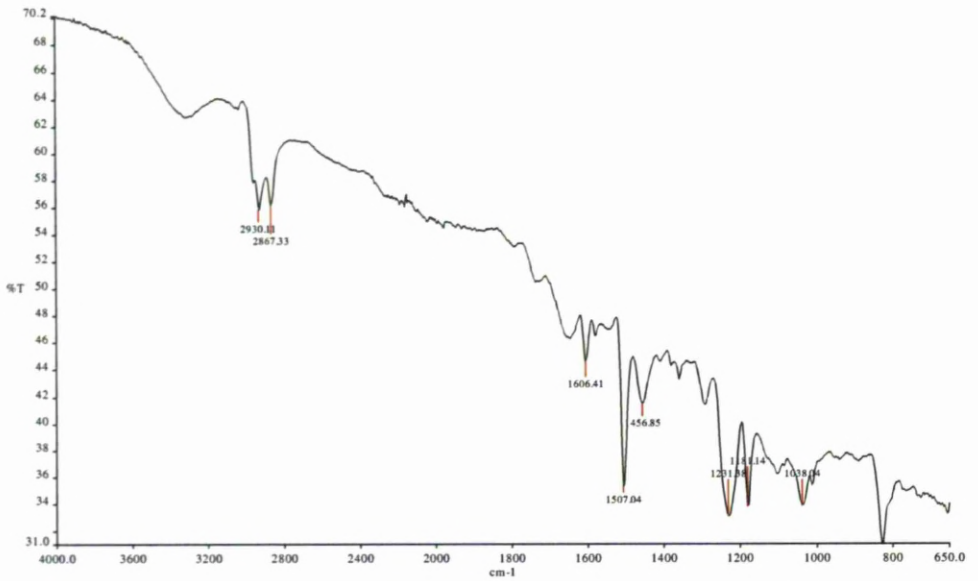

Figure 5.18: D1 Laser cured

Figure 5.18 shows the spectrograph of the D1 laser cured ink. Like the laser cured D58 ink, it has greater absorption across the whole spectrum compared to the respective uncured ink and oven cured ink. The transmission peaks at 70% with a wavenumber of 4000 cm^{-1} and has a low of 31% at about 829 cm^{-1}. The O-H/N-H absorption peak is present, but it is further reduced than that seen in the D58 laser cured spectrograph, Figure 5.17. The same goes for the C-H absorption peak which is still clearly present, but is smaller in magnitude. The absorption of the symmetric stretch of the methylene group is reduced by a greater amount then that of the asymmetric stretch when compared to the uncured D1 spectrograph, Figure 5.11, but the end result is a similar absorption peak for both. Unlike the oven cured D1 and D15 inks, there is no shift in the methylene absorption peaks when laser cured. The absorption peaks appear at the same wavenumbers as for the uncured resin, D58 and D1 inks as well as the oven cured and laser cured D58 inks. Though the relative magnitudes are reduced for the D1 when compared with the D58, the peaks are in a similar position. A table of the significant peaks is shown in table 5.12.

Table 5.12: Table of the major peaks marked on Figure 29 for the laser cured D1 ink.

Wavenumber (cm^{-1})	
2930.11	1456.85
2867.33	1231.38
1606.41	1181.14

1507.04	1038.04

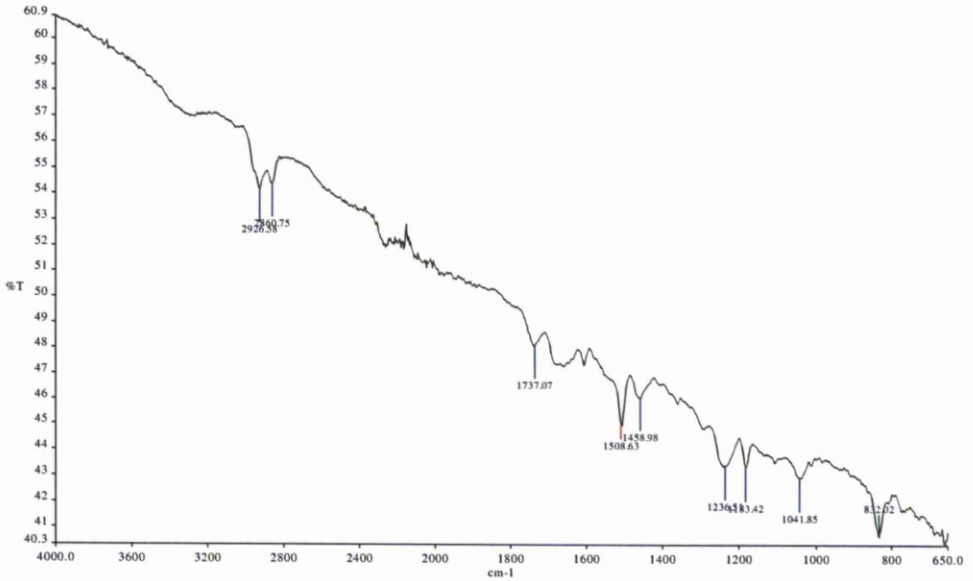

Figure 5.19: D15 Laser Cured.

The D15 laser cured ink spectrograph is shown in Figure 5.19. It has the same characteristics as that of the D58 and D1 laser cured inks, in that it has a straight line gradient of absorption that is inversely proportional to the wavenumber. It peaks at 60.9% transmission for a wavenumber of 4000 cm^{-1} and has a transmission low of 40.3% at 650 cm^{-1}. Like the respective D1 ink, it has reduced absorption at the O-H/N-H and C-H peaks. Closer to that of the oven cured D58. It also has a low at 650 cm^{-1} rather than at 829 cm^{-1} like the D58 and D1 inks. Similar to that of the oven cured D1 and D15 inks. The mehtylene absorption peaks have been shifted to lower wavenumbers in the same way the peaks were shifted for the oven cured samples of the D1 and D15 inks along with a more even absorption of both the asymmetric and symmetric stretches. A table of the significant peaks can be seen in table 5.13.

Table 5.13: Table of the major peaks marked on Figure 5.19 for the laser cured D1 ink.

Wavenumber (cm^{-1})		
2926.58	1458.98	832.02
2860.75	1236.51	
1737.07	1183.42	
1508.63	1041.85	

References

1 J. Clayden, N Greeves, S. Warren, P. Wothers. *"Organic Chemistry"*, Oxford University Press, 2001, ISBN 0 19 850346 6.

2 "Characterization and analysis of Polymers" John Wiley & Sons, 2008, ISBN 978 0 470 23300 9.

3 R. Eisberg, R. Resnick. *"Quantum Mechannics of Atoms, Molecules, Solids, Nuclei, and Particles"*. 2nd edition, John Wiley and Sons, 1985, ISBN 0 471 87373 X.

4 P. Atkins, J De Paula. *"Atkins` Physical Chemistry"*, Oxford University Press, 2006, ISBN 0 19 870072 5.

5 P. R. Griffiths, J. A. De Haseth. *"Fourier Transform Infrared Spectrometry"*, John Wiley & Sons Inc. 1986.

6 http://teaching.shu.ac.uk/hwb/chemistry/tutorials/molspec/irspec3.htm

7 Halliday resnick walker.

8 *FT-IR Spectroscopy-Attenuated Total Reflectance*, Technical note, Perkin-Elmer.

9 Ferro, Electronic Material Systems, Silver Flake #52. www.Ferro.com

10 Y. Wang, S. Liu, Y. Wang, G. Feng, J. Zhu, L. Zhao. *"Infrared light absorption of silver film coated on the surface of femtosecond laser microstructured silicon in SF_6"*, Materials Letters 63 (2009), P. 2718-2720.

11 Timcal data sheet

12 J. E. Sinko, C. A. Schlecht. *"Reflection Fourier transform infrared spectroscopy of polymer targets for CO_2 laser ablation"*. Proc. Of SPIE, Vol. 7005, 70052P-1, 2008.

13 M. A. Drury, P.J. Glatkowski, W. A. Stevenson. *"In situ characterization of resin chemistry with infrared transmitting optical fibres and infrared spectroscopy"*. SPIE Vol. 1437, Applied Spectroscopy in Material Science, P. 66-74. 1991.

14 *The Aldrich Library of FT-IR Spectra*, 2nd Edition, V.1, Sigma-Aldrich Co. 1997. ISBN 0 941 1633 39 X.

15 F. Deon, M Koch-Müller, D. Rhede, M. Gottschalk, R. Wirth, S-M. Thomas. *"Location and quantification of hydroxyl in wadsleyite: New insights"*. American Mineralogist, Vol. 95, P. 312-322, 2010.

16 S.N. Magonov, I.S. Vainilovitch, S. S. Sheiko. *"FTIR spectroscopy of polymer films under uniaxial stretching"*. Springer-Verlag, Polymer Bulletin 25, P.491-498, 1991.

6 Process Applications

This chapter is the culmination of the previous worked presented within this thesis. It brings together the different strands of the research and applies it to the actual fabrication of a functional antenna for aerospace within the Towards a Wireless Aircraft (TaWA) and ASTRAEA projects. The chapter is broken up in to two main sections which represent the different projects. The first being the TaWA project in section 6.1, whilst the work conducted as part of the ASTRAEA project is presented in section 6.2.

6.1 Towards a Wireless Aircraft Working Antenna Demonstrator

6.1.1 Introduction

The Towards a Wireless Aircraft (TaWA) project was a seedcorn project under the auspices of the larger FLAVIIR project sponsored by BAE Systems and EPSRC. It involved three partner universities and BAE Systems. The partner Universities were University of Manchester, University of Nottingham and University of York. Together we collaborated on the remit of looking at possible technologies and the feasibility of removing wires from a UAV, reducing weight, increasing redundancy, and with no performance or cost penalty.

As part of the TaWA, quarterly meetings were held between the collaborators along with reports and presentations detailing the work conducted to date. The work was discussed and ideas for progression were put forward. Within the TaWA project, the work already developed within the FLAVIIR project was developed further and tailored towards the fabrication of antenna using DW on thermally sensitive substrates. The area of antenna fabrication was investigated along with wave propagation within irregular structures such as the airframe. Several platforms were investigated initially, with the Zigbee platform decided upon due to its architecture being designed for a distributed nodal network, with low power consumption and a frequency of 2.4 GHz. As part of the contribution from the University of Liverpool within the project, the replacement of the standard Zigbee antenna was investigated with the remit of creating a low profile, robust, conformal antenna directly on the surface of a wing with no associated thermal damage. The motivation behind the TaWA project was to reduce the overall weight of the aircraft by reducing the requirement for wires, reduce aircraft construction cost along with parts cost, enhance

robustness and reliability though increased redundancy and to enable easier maintenance and modularity of the aircraft so that it can be mission specific enabled. Challenges in creating a wireless aircraft were also investigated early on [1-4] with early emphasis on EM (electromagnetic) propagation within and without an airframe, EM modelling of bulkhead style environments, physical layer communication and the data rates, power consumption and supply, direct manufacturing of the associated components, robustness of manufactured parts and reliability, positioning of parts and materials used along with substrate properties.

The work being conducted could not be done using conventional manufacturing techniques as the remit required conformal antennas directly on to a surface of a wing. Also there had to be no thermal damage to the substrate. This meant that oven curing of a deposited material, chemical etching and lithographic techniques could not be employed. Also the technology needed to be scalable, being able to create a functional component on any substrate, from a demonstrator 0.5 m in length to an actual wing which maybe as long as 3 or 4 m.

Weight in aircraft is an issue and so any means by which it can be reduced, is of interest to the aerospace industry, when looking at wires, typical passenger aircraft (e.g. Boeing 747) contains over 220 000m of wire weighing approximately 1600 kg [7]. To reduce this weight, manufacturers are looking for alternative solutions to conventional copper wiring. The issue is highlighted by the new A380 created by Airbus where over 50 per cent of the 500000m of wiring in the Airbus A380 is aluminium. The wiring of the A380 has been in part, responsible for the delay in the aircraft coming to market along with cost overruns in excess of $2 billion [8]. With so much wiring in an aircraft, weight is not the only issue. Interconnects are also required for the wires, further adding weight and with increased wire numbers, there is an associated increase of interconnects, along with issues in maintenance and post modification of a wired network. There have also been a number of air crashes that are due to wiring failures [9]. Due to these concerns, there is a desire to try and move away from a fly by wire systems towards alternative methods and technologies. Wireless networks being one of them, and one that is still at a relatively early stage of investigation. A way of managing the extensive wired networks within aircraft, has been to employ the use of data buses [9] with less emphasis on point to point connections. Also optical fibre networks have been used in the F35 joint Strike Fighter, however both systems are susceptible to structural failure and require conventional routing methods for

installation and cannot be done as a post process. The benefits are increased reliability and reduction of weight. Redundancy is a major issue within aircraft. However it is limited due to practical reasons such as cost weight, space and installation. They also suffer from the same mode of failure i.e. structural. Wireless communication does not have these difficulties; with a different mode of failure it represents an alternative redundancy path with the added desirables of being modular, light weight and applied as a post process with little or no need to route wires, depending on the applications. As stated previously, wireless interconnects for aerospace are at a relatively early stage, however alongside the work conducted within the TaWA project [9, 10] work has been published on the potential for wireless networks to be used for health monitoring systems [11], whilst Fragoulis et al have looked at the possibility of a distributed sensor network [12]. Coelho et al have investigated using the Bluetooth standard for a simple distributed avionics system [13] and Gulf-Stream have demonstrated wireless flight control to a single actuator [14].

Even with heavy interest in the area of wireless communication for aircraft, there is little literature that examines what is required and how a system would be built from the physical layer upwards. This was addressed somewhat by the publication of a joint paper from the TaWA partners, *"The Opportunities and Challenges Associated with Wireless Interconnects in Aircraft"* [9]. A simplified schematic diagram showing generic subsystem signalling interactions within an aircraft flight control system is shown in Figure 6.1 and gives a basic idea of what is required of a wireless network were it to be employed to replace the entirety of a fly by wire flight control system.

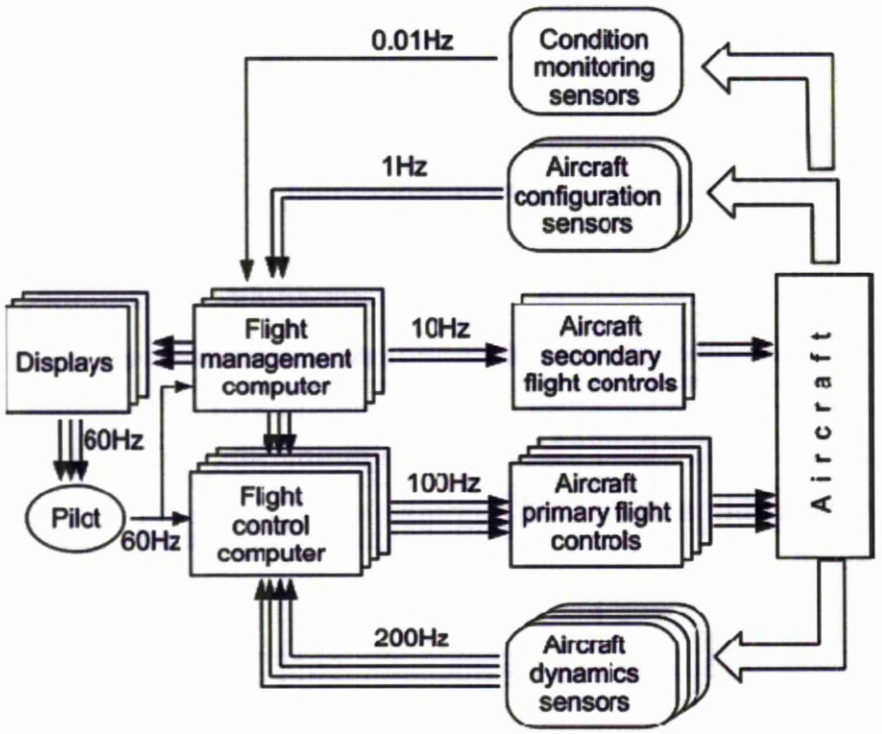

Figure 6.1: Schematic of a flight control system for a generic aircraft. The thin arrows indicate the typical number of communication channels between each subsystem and therefore the associated level of redundancy. Signal sampling frequencies are provided in Hz for different sensing operations and one can expect a minimum of 8 bits per sample. When combining signals into data buses, much higher data rates are reached [9].

6.1.2 Introduction to Antenna

The standard definition of an antenna, is "a usually metallic device (as a rod or wire) for radiating or receiving radio waves" [5]. By this definition it is a medium in which radio waves are either absorbed or emitted from, and is merely the device that converts one form of information in to another, that is radio to electrical and vice versa. Since the antenna is a transitional device, a guiding device is required to receive or transfer the signal from/to the antenna. This guiding device normally takes the form of a coaxial cable or a hollow pipe such as a waveguide which is attached to the appropriate circuitry at the other end. Usually a micro chip or signal generator.

There are several different types of antenna that are used on a daily basis. The simplest is a dipole antenna which is a wire antenna and constitutes two wires that are pointed in opposite directions and arranged either horizontally or vertically, with one end of the wire

attached to the radio or receiver and the other hanging in free space. Since this is the simplest form of an antenna, it is often used as a reference model for other more complicated antennas to compare their gain and efficiency. Another type of antenna, more recently developed is the aperture antenna. This type of antenna is commonly used in the aerospace industry as the can be flush mounted with the surface of an aircraft and covered in a dielectric for weather protection [6]. Aperture antenna are most common at microwave frequencies and have many geometrical configurations from conical horns to rectangular waveguide types. They are normally used in the microwave region of radio transmission and can be broad or narrow band. They are often used as reference antenna as they can be finally tuned. Microstrip antenna are a common type of antenna that were heavily used for space applications in the 1970`s [6]. They generally consist of a metallic patch that is placed upon a grounded substrate with a metallic strip protruding from it that leads to the transmission line. They are low profile in nature and can be placed on conformal surfaces if desired.

A variation of the microstrip antenna is a patch antenna, and mainly consists of a patch of metallic or conductive material that is over a ground plane which is separated by a dielectric. Like the microstrip antenna, a patch antenna is generally low profile robust and can be placed upon conformal surfaces. This work has concentrated upon fabricating a patch Figure 6.2 antenna, as this was the most suitable design for the applications of a UAV. This is due to its low profile nature meaning that it could be placed upon an aerodynamically sensitive surface with little or no drag penalty, and lent itself well to being manufactured using direct write (DW).

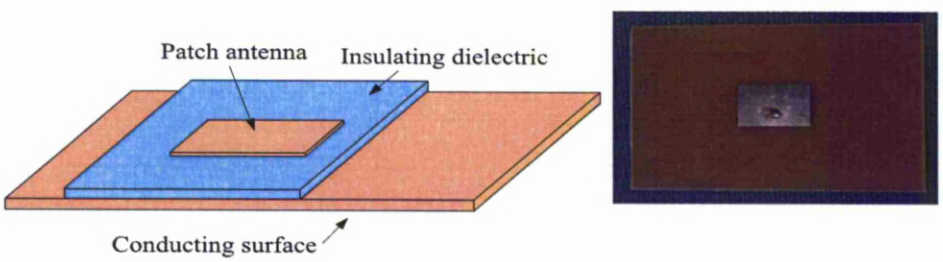

Figure 6.2: The left image is a drawing of a patch antenna design. With the conductive plate on top followed by a dielectric layer, with the ground plane on the underside. The right image is a patch antenna on a PCB FR4 laminate was made using conventional etching techniques [15].

6.1.3 Experimental Investigation

In chapters 2 and 3, the polymeric inks used to create functional components were introduced along with their standard curing regimes and the laser curing process developed as part of this research. This laser curing process was used to investigate the fabrication of directly written antennas on to FR4 board which was 1.6 mm thick and cladded in copper on one side and alumina substrates with a DW ground plane on the other side. This investigation of creating antennas was a prelude to the TaWA demonstrator where a conformal antenna was fabricated on a heat sensitive substrate. A heat sensitive substrate was used, so as to demonstrate the effectiveness of the laser curing process on all materials. There is a tendency, UAV`s in particular to be made out of CFC which cannot withstand temperatures above 120^{0}C once it has been formed. To demonstrate the applicability of such a manufacturing technique a material was chosen that had the same thermal constraints.

Previously the doctor blade technique was used to deposit the inks for the oven and laser cure processes. For the purposes of creating an antenna a syringe deposition system was employed Figure 6.3. The syringe deposition system was chosen for this purpose as it is a filamentary process that is suitable for depositing the specific inks that have been investigated. Further to this it is capable of depositing fine lines down to 200 μm in width and as low as 50 μm in thickness making it an ideal system for fabricating the antennas. The dispensing system used was an I & J Fisner Inc. JBE113 deposition pumping system. Attached to this was a 30cc round bottom syringe with a piston inside. Attached to the syringe was a blunt edge 23 GA half inch syringe tip with an internal diameter of 330 μm. The system was a pneumatic one where pressure was applied to the piston within the syringe which forced the ink through the nozzle. For the preliminary trials, the system was placed on a 3-axis system with linear stages, where the sample moved beneath the syringe. Once the part had been fabricated, the sample was laser cured using the Synrad CO_2 laser as described in chapter 3. The syringe deposition was controlled manually using a foot switch and a standoff of 50 μm was required to achieve a line thickness of <200 μm. The standoff was measured using standard feeler gauges and a pressure of 3 bar was used and a traverse speed of 7mm/s . The stages were controlled using a computer interface and the design of the antennas which were supplied by the University of York [15-17] were converted in to G-Code which in turn drove the stages.

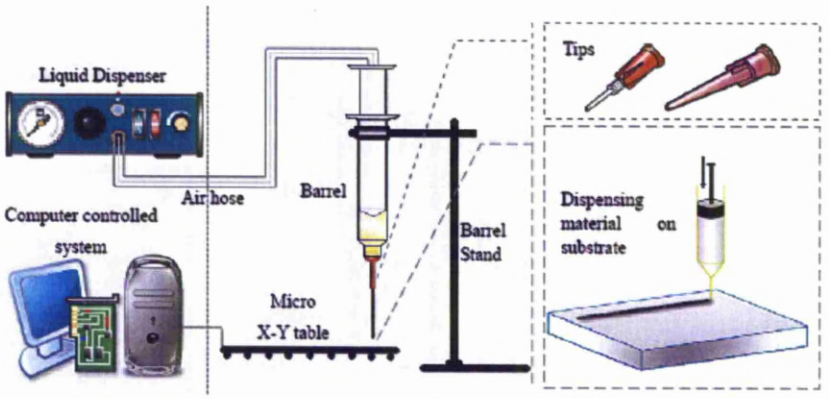

Figure 6.3: Illustration of the syringe deposition system used to carry antenna fabrication trials on FR4.

The design of the antenna followed several permutations with a starting point of a gridded patch antenna. A gridded patch was desirable as it had the benefit of less weight than a full patch. The University of York simulated the effects of removing material from a patch antenna Figure 6.4. By starting off with a full patch and slowly removing material as the spacing between the lines of the grid increases a frequency shift occurs figure 6.5. a significant shift occurs and this needs to be compensated through design iterations of the antenna so that the desired frequency is achieved. If sufficient material is removed, then the antenna no longer works. An optimised medium between the least possible material and best functionality of the antenna was thus investigated.

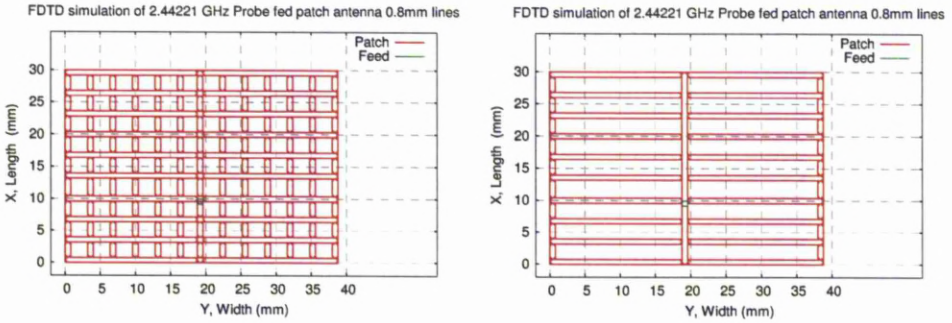

Figure 6.4: FTD simulation of patch antenna with varying amounts of material removal. Here the two designs have 0.8mm line widths with a 2.4mm gap [15].

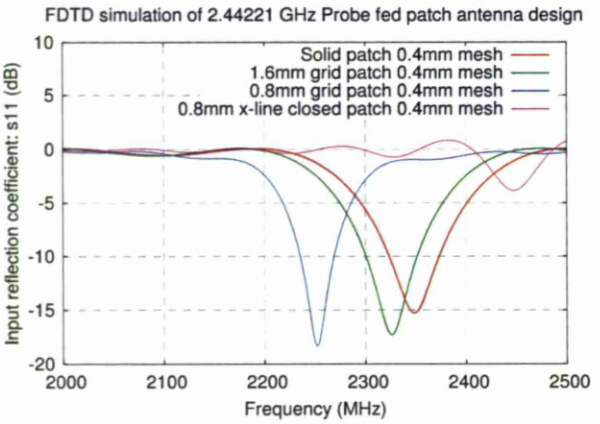

Figure 6.5: Simulated frequency response of different styles of patch antenna in the S11 plane (reflection coefficient). Starting form a solid patch and then increased line spacing to the x-line closed patch which no longer works [15].

The dimensions of the antenna initially used were 38x30mm and is shown in Figure 6.6, with the green spot denoting where the feed line goes.

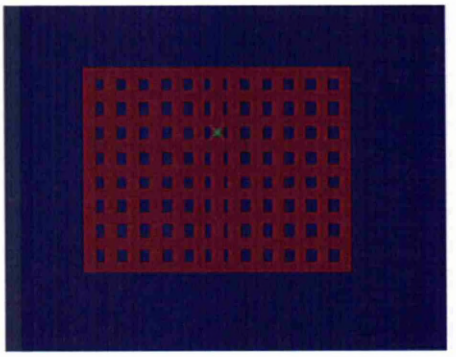

Figure 6.6: Image of the design of the gridded patch antenna to be fabricated on FR4 PCB laminate. The central x-axis green spot is the point where the feed line will be connected to the antenna via an SMA connector.

The gridded antenna were a good starting point for creating DW antenna and were well suited due to their geometry of lines. However from simulations and further testing of the antenna it was realised that the bandwidth of the antenna at ~2% was too narrow for the desired applications. To increase bandwidth, a new type of antenna was designed by the University of York that used genetic algorithms to create a suitable patch antenna with increased bandwidth ~4%. This increased bandwidth could utilise the 85 MHz available using the ZigBee platform. Figure 6.7 shows some genetic algorithm antenna designs. The

size of the antenna would be significantly smaller on an alumina substrate compared with a PCB laminate substrate due to the difference in their relative permeability, ε_r=10 and ε_r=4 respectively, which relates to a reduction factor in size of 1.58.

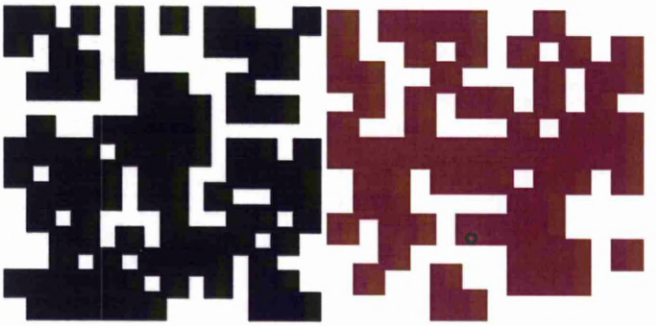

Figure 6.7: Two images of genetic antenna designs. The one on the left is for an FR4 material, whilst the one on the right is for deposition on alumina.

Once the antenna were made, they were tested by the University of York in their anechoic chamber to look at the frequency response, S11 and efficiency, S21. S11 is the reflection coefficient that shows the frequency in which the antenna is working. The S21 is the ratio of received to transmitted power and shows how efficiently the antenna is working.

6.1.4 Antenna Fabrication Results

The results section will be broken in to three sub sections relating to the type of antenna made. The first will be the gridded antenna on PCB laminate, whilst the second will relate to the gridded antenna on alumina and the third will be about the genetic algorithm antenna.

6.1.4.1 Gridded Antenna on PCB Laminate

Several antenna were created and tested using the syringe deposition system setup on FR4. Figure 6.8 shows two antenna that were fabricated and cured, one using conventional oven curing and the other using the laser curing process developed for this project. The results of which can be seen in Figure 6.9.

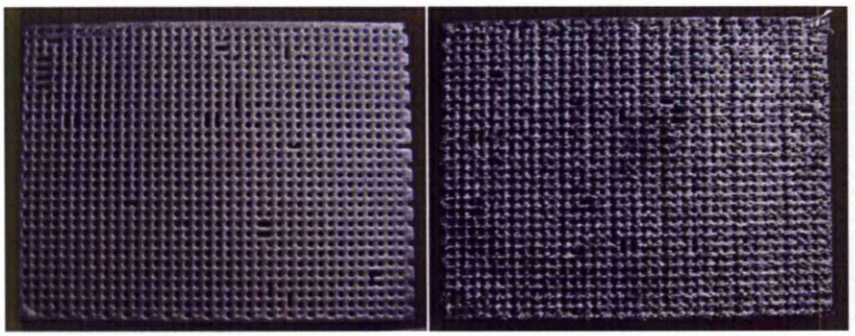

Figure 6.8: Photographs of two antenna fabricated using the syringe deposition system. The picture on the left is of an oven cured sample, whilst the picture on the right is of a laser cured sample.

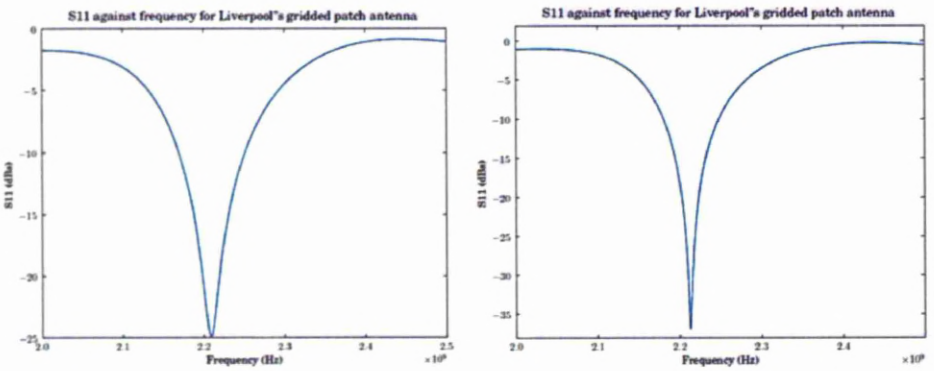

Figure 6.9: Results of S11 measurements using an anechoic chamber. The left graph is the oven cured sample, whilst the right graph is the laser cured sample.

The results show, that the frequency of the antenna is about 200MHz off the desired frequency, and also shows a very narrow bandwidth which was expected. The frequency is about 50 MHz off what would be expected from simulations, Figure 6.5, and this is probably due to the dimensional tolerances within the deposition system. The narrow bandwidth is as expected, but there is a noticeable decrease in bandwidth of the laser cured antenna when compared to the oven cured sample. This was not expected and is probably due to the slight geometrical differences that occur as a result of the different curing process. These results can be compared to the conventionally made antenna on PCB, Figure 6.10.

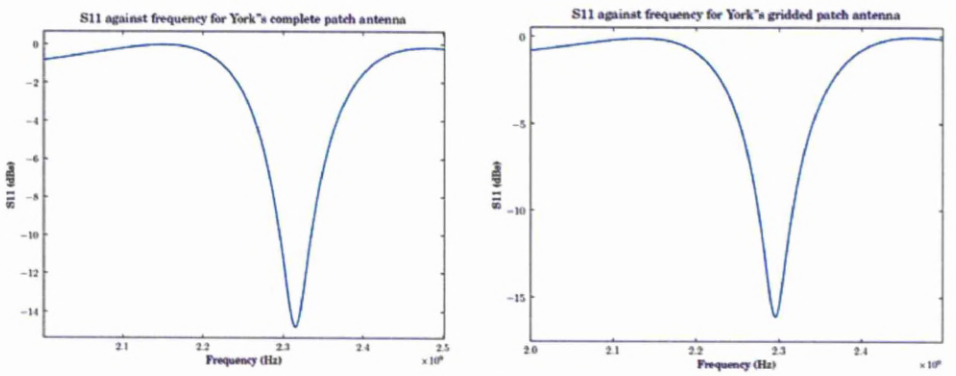

Figure 6.10: Results of the S11 grid antenna as made by the University of York. The left graph is of a full patch and the right is of a gridded patch.

For the conventionally made antenna it can be seen that the S11 frequency response is closer to that of 2.44GHZ, but is still off by about 100MHZ. This is in close agreement for, the full patch with what was modelled. The bandwidth of the antenna is also greater than that seen by the DW fabricated antenna.

Overall it can be seen that there is little difference in performance between the York and the Liverpool antennas. The centre frequencies are shifted relative to the York ones for the Liverpool antennas but this was can be accounted for due to dimensional differences between the two and different PCB laminates and conductors were used. The Liverpool antenna drops to a lower value

of S11 when at its resonant frequency, however neither antenna type is suitable for ZigBee since they have bandwidths that are too small. In all cases the -10dB bandwidth is between 50MHz and 70MHz whereas the band in which the channels can work for ZigBee is 85MHz. When comparing the gridded patch against the complete patch there appears to be little difference with the S11 profiles being very closely matched. The results suggest that provided the spacing of the grid lines is no too large, then performance of the antenna should not be compromised.

In Figure 6.11 shows the S21 coefficient of the different antenna. It can be seen that the DW antenna are less efficient than that of the conventional antenna made by the University of York, but also that the point of highest efficiency is at ~2.2GHz. However the results are pretty consistent and demonstrate that they would be a suitable method of antenna fabrication as long as the correct frequency response could be achieved.

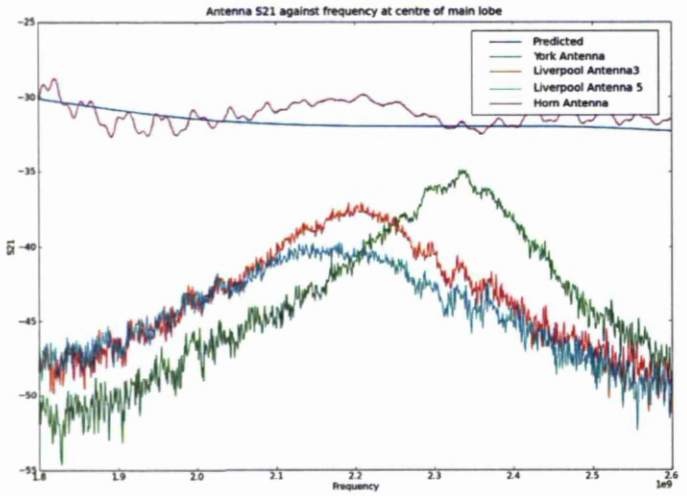

Figure 6.11: Comparison of S21 measurements of the different antenna fabricated. The Liverpool Antenna 3 is the oven cured antenna whilst the Liverpool Antenna 5 is the laser cured antenna.

6.1.4.2 Gridded Antenna on Alumina

Following on from the proof of principle work conducted on PCB laminate, antenna were then fabricated on alumina substrate with a ground plane being directly deposited on to the reverse side using DW. The ground plane was oven cured for ease of testing and consistency. Figure 6.12 shows the fabricated antenna and ground plane.

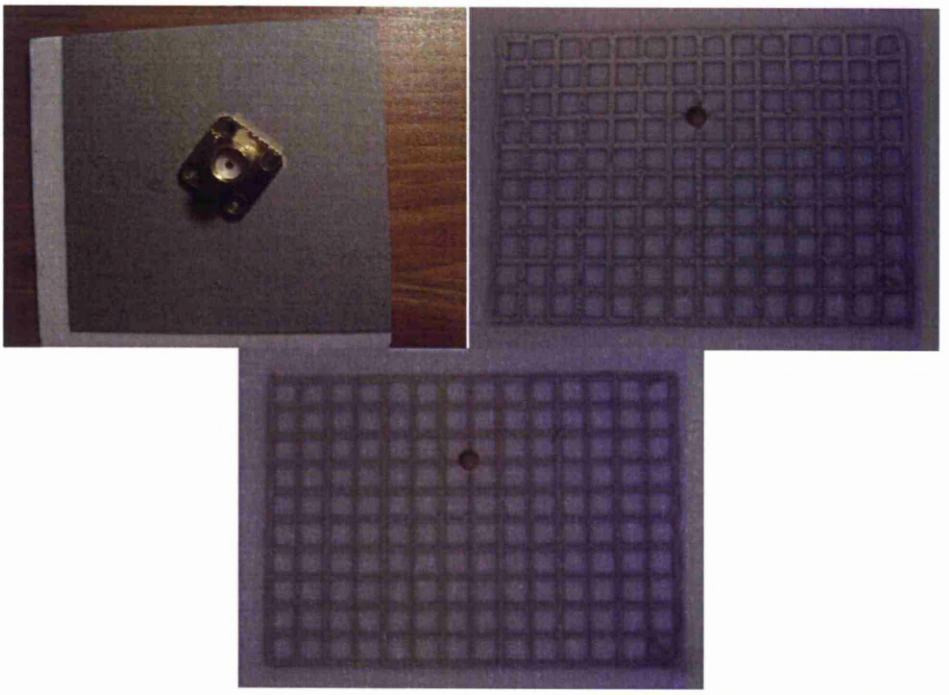

Figure 6.12: Photographs of the gridded antenna on alumina. The top left picture shows the ground plane and an SMA connector attached. The top right is a gridded antenna that was oven cured, whilst the bottom picture is an antenna that was laser cured.

The results of the S11 measurement of the oven cured antenna can be seen in Figure 6.13, whilst there is slight resonance of the antenna at ~2.15 GHz, the results indicate that it is not suitable to be used as a patch antenna. The laser cured sample could not be tested. The reason for this was unclear, but is probably due to connection issues between the ground plane and the SMA connector. The polymeric inks used cannot be soldered and so getting a good electrical connection was probably not achieved and hence produced spurious results if any. This indicated that thought he inks were good for creating the antenna it was not suitable for the ground plane due to electrical connection issues. This area of work was not pursued as it was always intended as a proof of principle and the desire to create a broad band genetic algorithm antenna was the driving force.

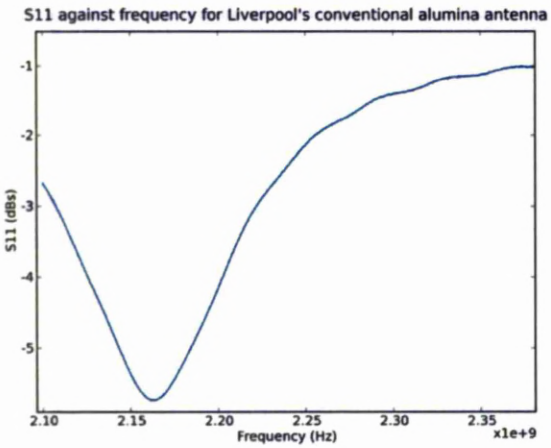

Figure 6.13: S11 results of the oven cured gridded alumina antenna.

6.1.4.3 Genetic Algorithm Antenna on Alumina

Having previously failed to create a successful gridded antenna on alumina, genetic algorithm trials were conducted. The designs were chosen and the antenna fabricated using a screen printer. A screen printer was used due to the intricate nature of the features of the genetic algorithm design. Copper tape was used as a grounding medium with the SMA connector soldered to that to try and achieve a good electrical contact. The antenna fabricated are shown in Figure 6.14 whilst the S11 results are shown in Figure 6.15.

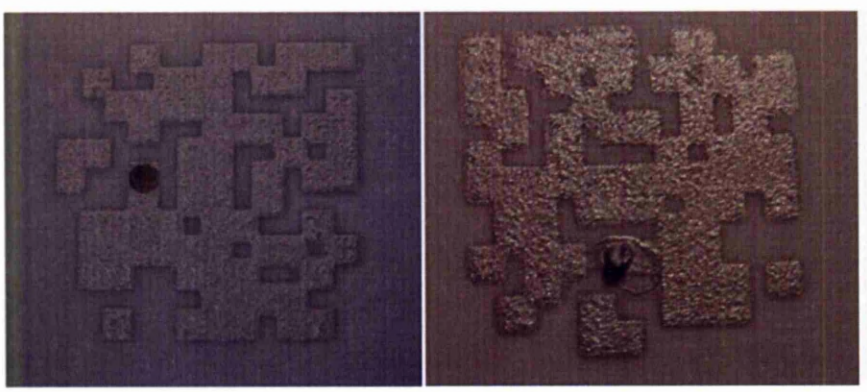

Figure 6.14: Pictures of the genetic algorithm antenna fabricated on alumina. The left image is of an oven cured sample, whilst the right is a laser cured sample.

Form the results of the S11 measurements, the frequency response is good for the laser cured sample whilst the oven cured sample is off by about 200MHz, the bandwidth is better for the oven cured sample however the bandwidth at -10dB is still about 70MHz

which is ~3%. An unexpected consequence of these designs is the lobe that can be seen at lower frequencies. This was not seen for the conventionally made genetic algorithm antenna, and could not be explained. As it was outside the frequency of the ZigBee system, it should not have an effect.

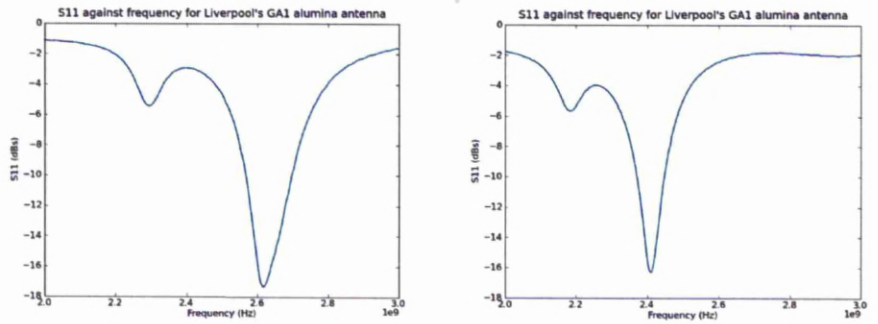

Figure 6.15: results of the S11 reflection coefficient of the two genetic algorithm antenna. The left graph shows the results of the oven cured antenna, whilst the right graph shows the results of the laser cured antenna.

6.1.5 TaWA Demonstrator Fabrication

The DW fabrication process in combination with the laser curing process had been shown to successfully create functional antenna with sufficient bandwidth to utilise the channels with a ZigBee platform. The goal of the TaWA work was to create a demonstrator platform for this technology. The platform was a representative scaled down model of typical aerofoil. The aerofoil would be made out of foam and the surface was coated in glass fibre for strength.

The foam and glass fibre material were commercially available and are commonly used for the fabrication of model plane platforms with a maximum operating temperature of about 100°C. A CAD drawing of the design can be seen in Figure 6.16.

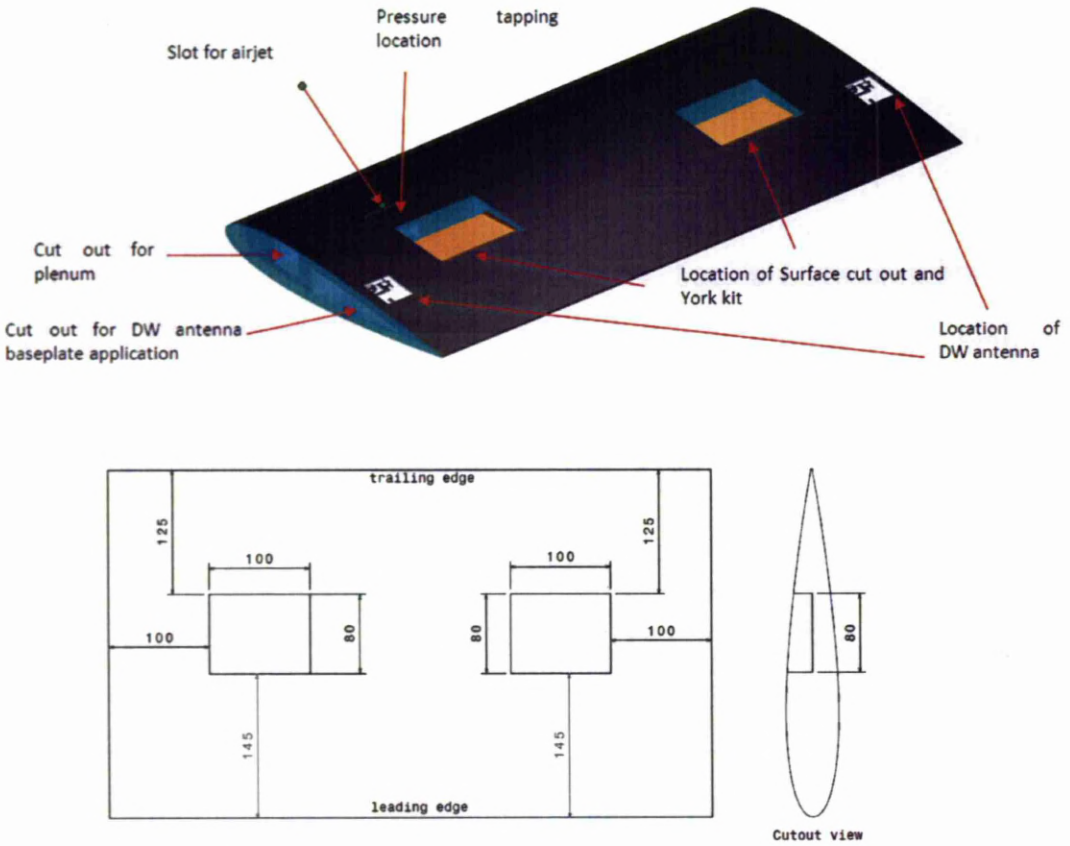

Figure 6.16: CAD drawing of the demonstrator design illustrating the location of the main components to be placed upon the wing. A schematic is also given showing the size of the whole aerofoil the. The measurements are in mm.

To create an antenna directly on the surface of the foam wing, several things needed to be investigated. From a fabrication point of view, laser curing parameters needed to be found that created a sufficiently low resistance track that did not damage the wing during cure along with an appropriate fabrication method for a genetic algorithm antenna and the placement of a grounding plane. From an antenna design point, the properties of the foam needed to be deduced since it was going to act as the dielectric and hence the loss tangent needed to be known. These properties would in turn dictate the design of the antenna to be placed upon the wing.

To understand the dielectric properties and loss tangent of the foam wing, transmission lines were created using samples of foam, Figure 6.17. This consists of a strip of conductive material upon the foam with a grounding plane on the other side. At either end SMA connectors are soldered to the strip. These were then tested in a network analyser to

deduce its impedance, dielectric constant and loss tangent. The transmission lines were fabricated out of copper tape to act as the conductive path and ground plane.

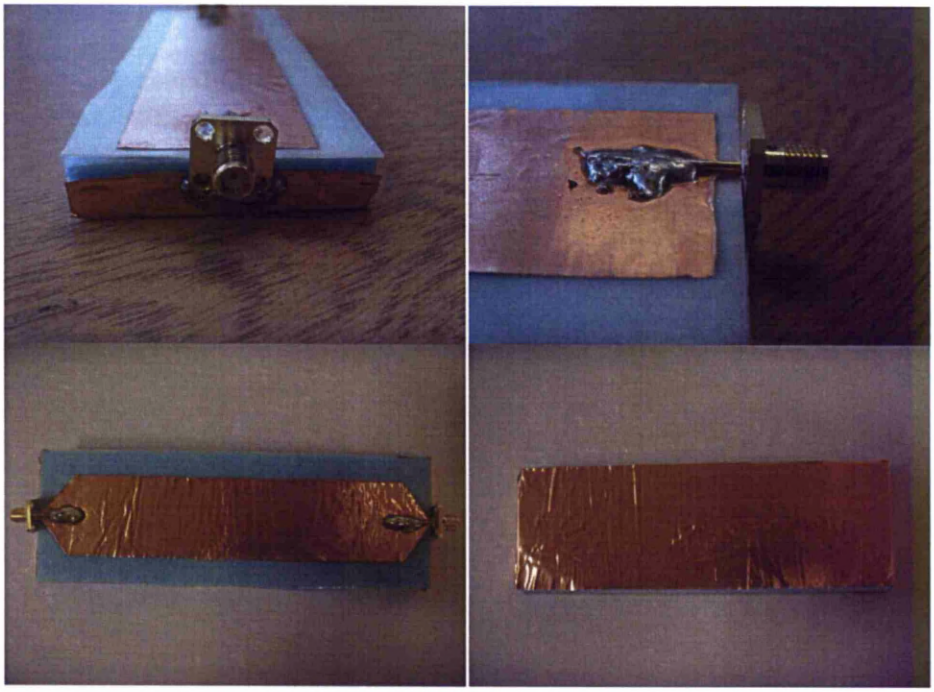

Figure 6.17: Pictures showing the transmission line used to calculate the electromagnetic properties of the foam so that an antenna design could be made.

Due to the nature of the demonstrator, the previous system for deposition and cure was not suitable. The curing trials were transferred to a pulsed Rofin Slab CO_2 laser rated at 300W output, which was attached to a 6-axis gantry system, Figure 6.17. The lowest power setting at which the laser created a stable output was 15W (5%). This setting was still too high for the laser curing process and so a steel aperture was created to fit into the optical setup, which helped to reduce the power output. The aperture had a diameter of 3mm, and the beam output of the laser was 9mm. By transferring to this system, it was capable of depositing on the wing at either end and curing the ink once deposited with no need for re-alignment. Initial trials were conducted on foam samples where the ink tracks were doctor bladed.

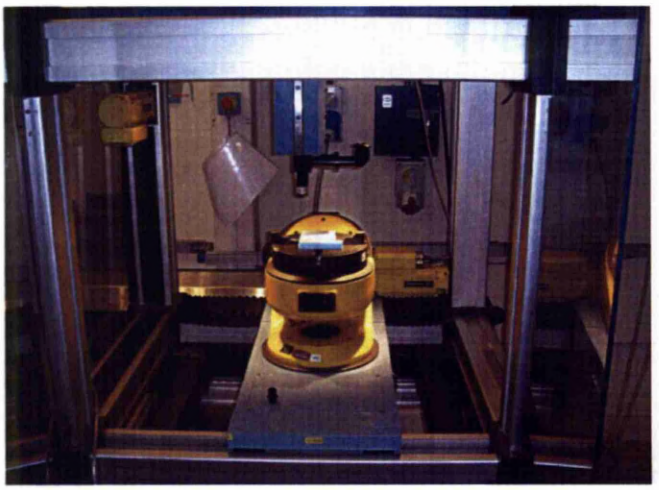

Figure 6.18: Picture of the system upon which the antenna for the TaWA demonstrator was fabricated. The aperture can be seen on the z-axis at the end of the free space optics tubing.

Successful cure was achieved with a spot size of 1.5mm in diameter, a power output of 3.7W and a traverse speed of 30mm/s. Figure 6.19 shows the cured tracks for different curing regimes. The line width is 2mm and has an average height of 62.36µm. the resistivity was calculated to be 7.98×10^{-6} Ωm.

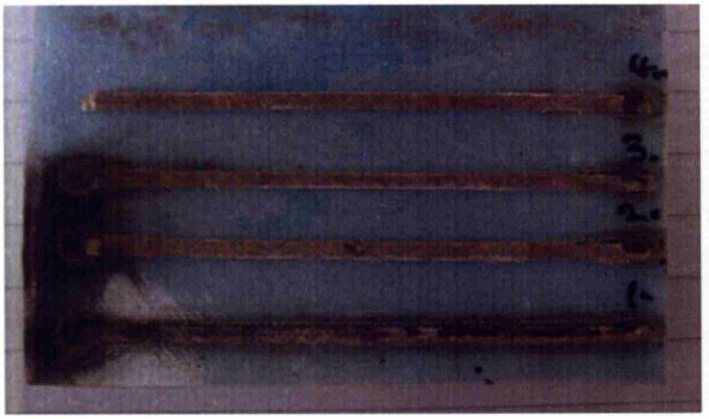

Figure 6.19: Picture of the doctor bladed tracks for the demonstrator curing tests using the Rofin Slab laser. Number 4 was used, with the parameters quoted in the above paragraph. The dwell at the start caused slight burning of the sample.

Due to dimensional issues that were raised when fabricating the antenna previously on alumina and PCB laminate, the genetic algorithm antenna were screen printed. In this case the antenna could not be screen printed and the aim of the demonstrator was to show direct fabrication on to a wing surface. So that an accurate dimensioned antenna could be achieved tape was placed over the wing where the antenna was to be deposited and a

mask cut out using the laser, Figure 6.20, the syringe would then deposit over the mask in a series of straight lines and then the sample cured using the laser. Once the sample had been cured the laser was then used to cut out the shape of the antenna again making it possible for the tape to be peeled off, leaving the cured antenna in place, figure 6.19.

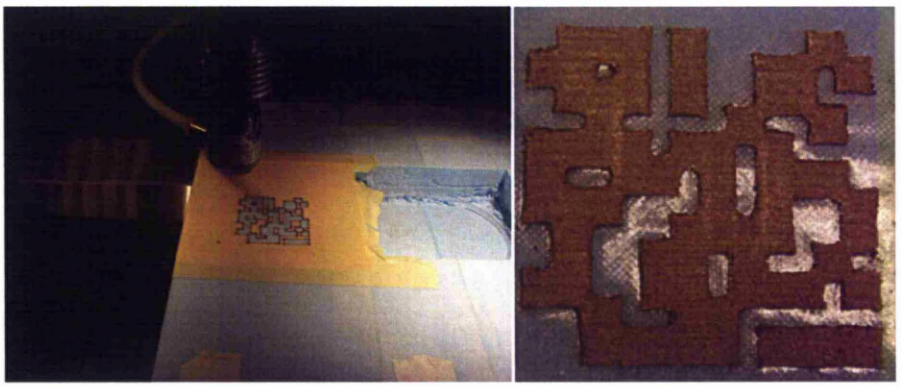

Figure 6.20: Pictures of the laser masking process and the resultant antenna on the foam wing once the tape had been pulled away after deposition and cure.

Once both antenna had been fabricated, the antenna were masked off again and the whole wing painted black, Figure 6.21. Copper tape was used as a ground plane beneath the antenna, and inserted in to the cut out hole for this specific application (refer to Figure 6.16). A whole was manually drilled to allow for the SMA connector which was welded to the copper tape. Once the ZigBee units were in place the antenna could be connected and powered up Figure 6.21.

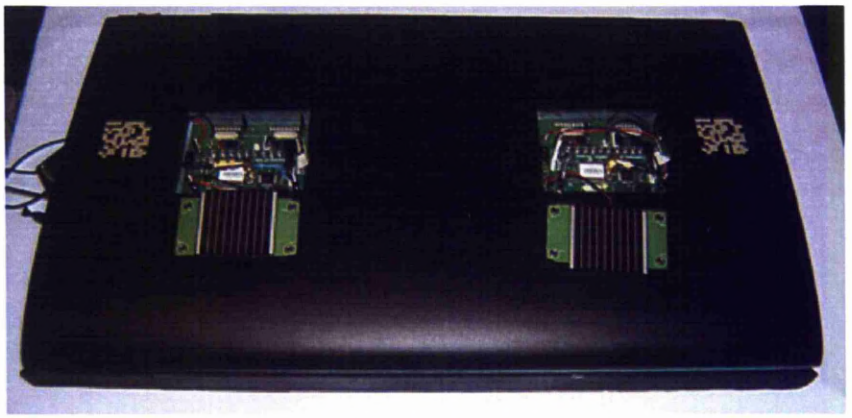

Figure 6.21: Finished TaWA demonstrator with two DW genetic algorithm antenna connected to ZigBee units. Solar panels were added to help recharge the batteries which were powering the modules.

The demonstrator consisted of the two ZigBee modules. One ZigBee module had an accelerometer upon it. When this was moved LED`s would light up on the other unit demonstrating that a signal had been sent. The number of LED`s that lit, out of a possible 10, would indicate the degree of acceleration witnessed by the sensor.

6.1.5.1 TaWA Antenna Test Results

In this sub-section the results of the two antenna are shown. The demonstrator was placed within the anechoic chamber at the University of York and tested in a similar fashion to that of the previous antenna testing. The S11 coefficient was measured and is shown in **Figure 6.22**. They show that there is a significant difference between the two DW genetic algorithm antenna fabricated upon the wing, however they do both have a large bandwidth. The fabricated antenna 2 is very close to what was designed, whilst fabricated antenna 1 was ~200MHz off. It appears that the broad band nature of the antenna design helped to compensate for the disparity in the resonant frequency with overlap occurring at -7dB. This was sufficient enough for creating a working antenna setup for communication channels.

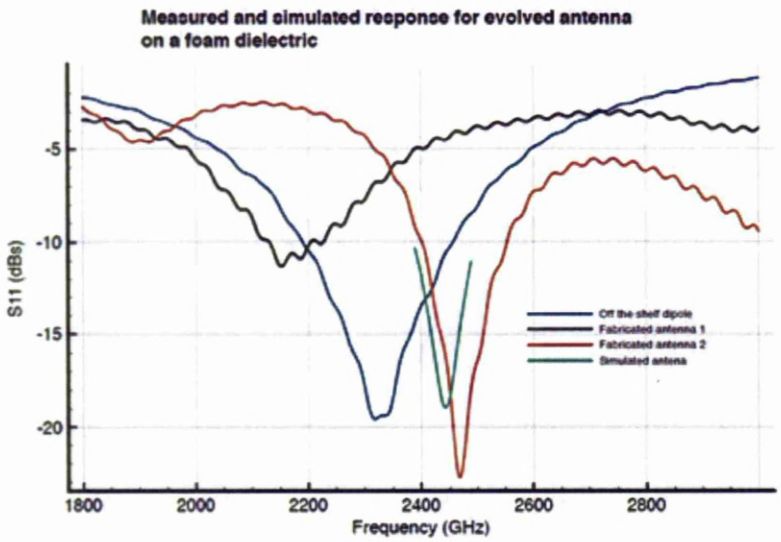

Figure 6.22: The S11 coefficient for the two DW antenna, an off the shelf dipole antenna and the simulated results for the genetic algorithm antenna.

6.2 The ASTRAEA Full Size Demonstrator

ASTRAEA stands for Autonomous Systems Technology Related Airborne Evaluation & Assessment. The programme sought to research and develop the necessary technologies, systems and facilities to promote and enable routine and unrestricted use of UAVs (Unmanned air vehicles). It was a multi-consortium project with over £30 million worth of funding. As part of the ASTRAEA project, the laser group was brought in to work in collaboration with BAE Systems and their laser & Optics division to help develop and integrate the laser curing process of polymeric inks for the DW of antenna on a UAV wing. The goal was to make an antenna array on the leading edge of the HERTI demonstrator UAV.

The goal was similar to that of the TaWA demonstrator and showed a desire within industry for this type of process that had been developed. For this project it was a requirement that a fibre laser would be used for ease of integration of the laser in to BAE Systems 3-axis deposition system. It was also a requirement that the antenna be fabricated upon a carbon fibre wing that was being specially made for the HERTI programme with no associated thermal damage, as the intention was that this would be a flying demonstrator. Also it was of high importance that the resultant track be a smooth as possible due to aerodynamic considerations. The radiating portion would then have to be electrically isolated from the CFC wing with a dielectric. This would also have to be fabricated using DW and the total height of the dielectric and antenna could be no greater than 250μm.

6.2.1 Experimental Procedure for Curing Parameters

The experimental work was conducted in collaboration with BAE Systems. The intention was for the Laser group, University of Liverpool, to investigate the feasibility of laser curing polymeric inks (silver and dielectric) using a fibre laser on primed CFC. Once a process window had been achieved the laser would be integrated into the gantry system they had onsite for the fabrication of the antenna array. All antenna designs were created by BAE Systems.

Due to the constraints of using a fibre laser, a 10.6μm CO_2 laser could not be used as it is highly attenuated by fibre optics. Therefore a 20W 1.5μm Er:YAG SPI fibre laser was procured for the purposes of this investigation. The fibre laser has a collimator head on the

fibre output producing a top hat profile beam with an M^2 ~1.6. The system was setup on a 2-axis system with the collimator head held 13.5cm above the sample which moved beneath it. The raw beam was used for the purposes of this experiment, which was measured to be ~3mm in diameter. A power calibration graph can be seen in Figure 6.23. Since the laser was inherently pulsed, the laser settings were set at 1ms pulse length and 1KHz repetition rate, to create a pseudo continuous wave output.

For consistency of deposition, the samples were fabricated using a doctor blade method as with previous investigations. The experiment concentrated upon varying the power and hence the number of passes till a solid conductive track was achieved, whilst keeping the traverse speed constant, at 1 mm/s. In this way the effects of multiple passes can be seen on the electrical and physical properties of the track and compared to a single pass process, whilst keeping dwell time constant at 3 s for a central portion of the track. The power was varied from 2.6 W to 4.4 W. The samples were checked for their resistance using the four point probe as mentioned in chapters 2 and 3. The design of the antenna array can be seen in Figure 6.24.

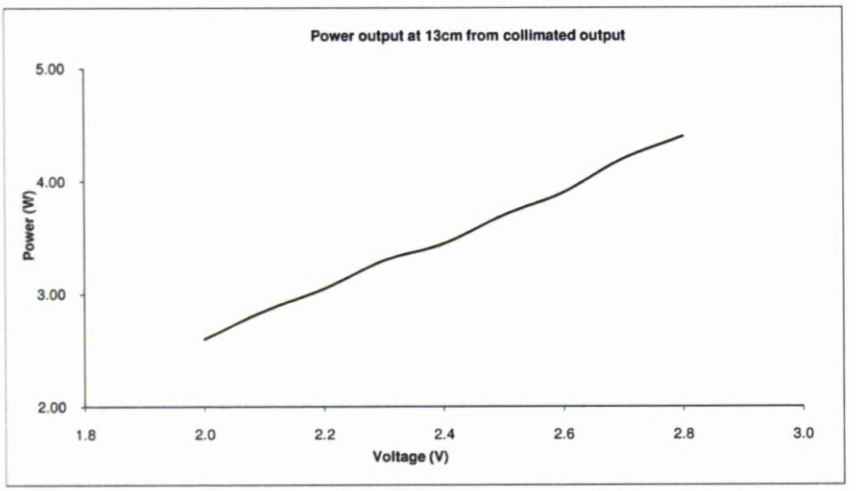

Figure 6.23: Power calibration graph of the SPI laser.

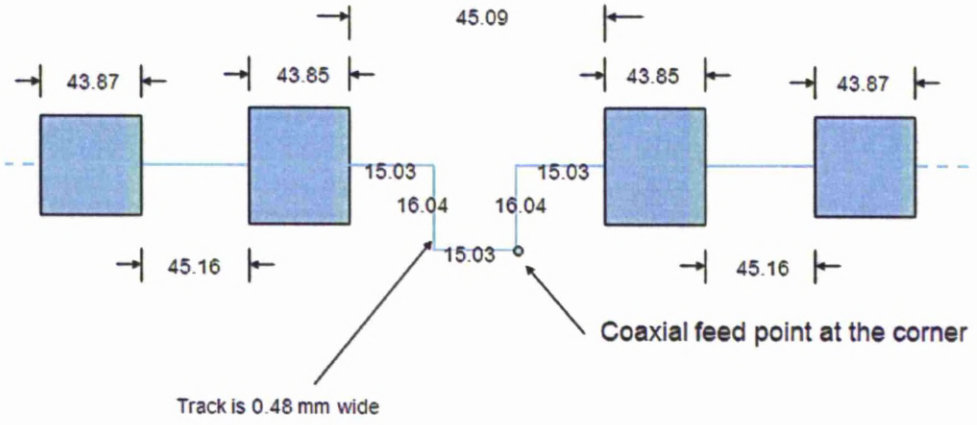

Figure 6.24: Diagram of the design of the antenna array to be fabricated on the leading edge of the wing.

6.2.2 Results of Er:YAG 1.5µm Curing Trials

Curing of the ink tracks was achieved by varying the number of passes and power range. As the power was increased, the number of passes required to cure the ink was reduced, eventually leading to a single pass regime. The resulting resistance values are shown in Table 6.1.

Table 6.1: Sample set showing the effects of varying laser power and number of passes on the cured ink track resistance.

Sample Number	Power (W)	Passes	Resistance (Ω)
1	2.6	6	7.1
2	2.9	6	6.0
3	3.1	5	5.9
4	3.3	4	3.8
5	3.5	4	4.6
6	3.7	3	4.7
7	3.9	2	4.0
8	4.2	2	3.9
9	4.4	1	4.0
Reference Control	n/a	Oven	5.84

From Table 6.1 it is noticeable that the different processing regimes elicit a different resistance from the cured track. Another product of different regimes is the resultant roughness on the surface of the track. As the energy per pass increases, this results in a corresponding increase in roughness of the surface of the track. This can be clearly seen in Figures 6.25-6.28.

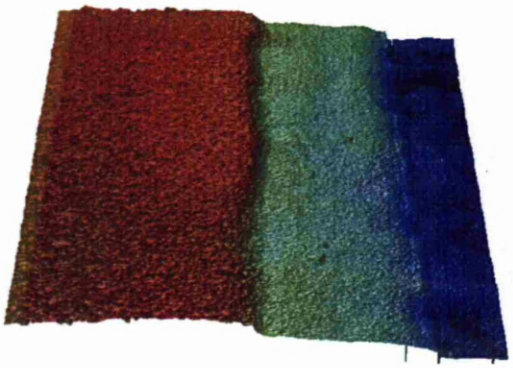

Fig 6.25: White light interferometry image of sample 2 processed using 2.9 W and 6 passes (far left section). The width of the image is 1.9 mm.

Sample 8 processed at 4.2 W and 2 passes has a significant amount of bubbling occurring on the track with an average roughness of 14.31 µm and a peak to trough roughness of 67.94 µm, Figure 6.25. This is to be compared with sample 2 processed using 2.9 W and 6 passes, which has an average roughness of 1.46 µm and a peak to trough roughness of 14.90 µm, Figure 6.24 .

An increase in roughness results from the change in volume of the solvents evaporating per second as the energy input increases, resulting in bubbling of the cured ink track, which can be seen in Figure 6.26 and 6.27. Sample 2 is on the left of Figure 6.26, while sample 8 is on the right. Where the process is particularly rapid, vacant voids are left in the track. This leads to a corresponding increase in volume and hence a decrease in the total density.

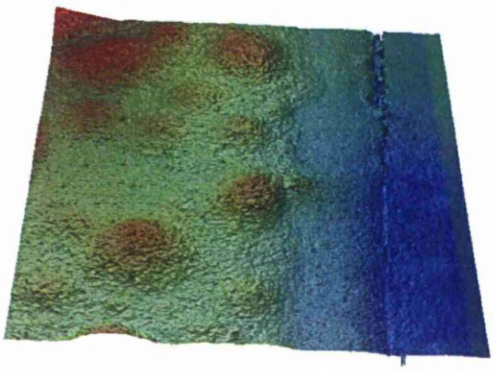

Figure 6.26: An Interferometry image of sample 8 processed at 4.2 W and 2 passes (far left section). The width of the image 1.9 mm.

The increased surface roughness due to bubbling does not seem to adversely affect the resistance of the track, as is shown in table 1 where increase of laser power seems to improve the resistance. Visually, sample 8 seems to have slight degradation, and the voids are easily collapsed by applied pressure. In comparison, for sample 2, shown in Figure 6.25, the measured roughness is approaching that of a reference oven cured sample (where the average roughness is 1.32 μm and the peak to trough roughness is 10.49 μm). The resistance of a reference oven cured track of the same pre-cure dimensions is 5.84 Ω. Hence, the majority of the samples have equalled or surpassed the oven cured sample in terms of resistance alone.

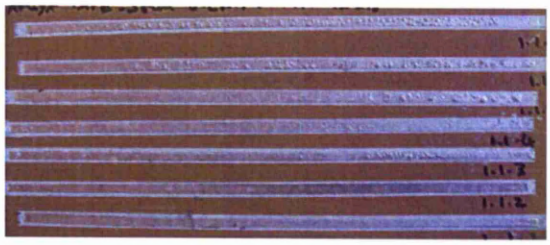

Figure 6.27: Photograph of the solidified lines on CFC substrate with decreasing power from the top down.

An additional consideration is to assess if laser curing can take place without thermally damaging a typical substrate. In this case the substrate used was a primed Carbon Fibre Composite (CFC) of the type used in the aerospace industry. After laser curing, there was no visual damage to the primer at any point during the investigation. However to qualify this and to be certain that no damage occurred beneath the track, the

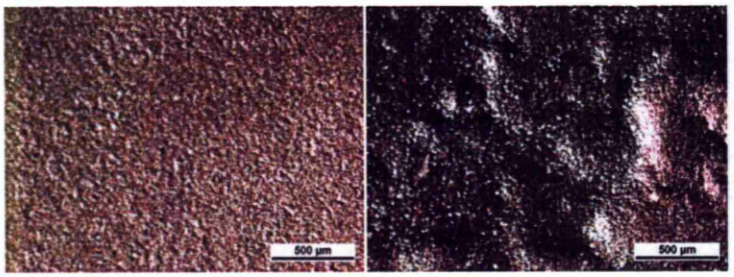

Figure 6.28: Magnification of cured track processed using 2.9 W for the left image, sample 2 and using 3.7 W for the right image, sample 6.

samples were cross-sectioned, mounted and then polished. The finest grade polish paper used was ~ 7 µm. A self imposed limit was placed here, as below this grade the transition on to a cloth based polisher, where the torque is greater, affected the positioning of the silver flakes within the resin and so left an artificial geometry. Above this grade movement of the silver flakes was not seen. Also it can be assumed that the highest temperature achieved on the substrate would be at the highest power setting. An optical image was taken, Figure 6.29. It can be seen from the image that no thermal damage has occurred to the primer and visually it is still intact. Therefore it can be assumed that for lower power settings there would be no damage to the primer or CFC. This turned out to be the case upon further analysis of the other samples.

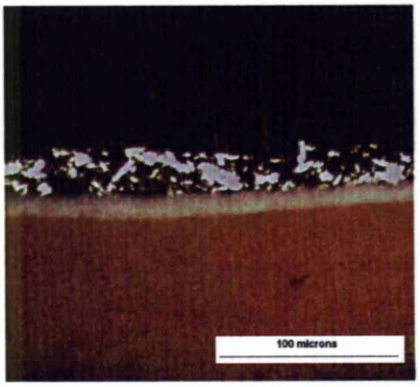

Fig 6.29: Optical image of a sample processed at 4.4W and 1 pass.

In Figure 6.29 the CFC substrate cannot be seen, the yellow/beige layer is the primer upon the CFC and the thin white layer is the dielectric layer that was laser cured, with the silver ink on top. The method for finding a cure regime for the dielectric layer was the same as that for the silver ink and also required a smooth finish as it was the interface for the radiating part of the antenna. The dielectric has a low thermal conductivity compared to

the silver ink and so is harder to evenly cure throughout its depth. Also localised heating occurs due to this causing bubbling. A successful curing regime was found with 2.4W at 0.5mm/s and 9 passes which proved to be very slow and unfeasible when applying to the demonstrator. A smooth finish was achieved Figure 6.30, but due to the slow nature of the process it was decided that a process being developed within BAE as a back be sued, which employed a heat gun.

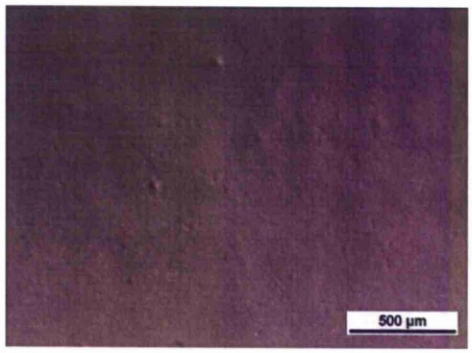

Figure 6.30: Optical image of the surface of the dielectric layer cured using 2.4W at 0.5mm/s and 9 passes.

6.2.3 The ASTRAEA Demonstrator

The demonstrator was initially going to be on a CFC wing which was going to fly on the HERTI platform. However due to certain technical issues unrelated to the antenna fabrication, it was not possible to create the antenna on the CFC wing. A full size section replaced the CFC wing which was made out of GRP (glass re-enforced plastic). Due to the change from CFC to GRP, the antenna was no longer going to be a working antenna as it was not possible to have access to the underside of the surface of the wing to attach a ground plane. This demonstrator then became a logistical and feasibility study of using this technique to create antenna on a wing along with the dielectric component using DW. Since a change in substrate had occurred new curing trials had to be conducted and with the process having a new parameter set. It was possible to reduce the cure speed of the silver ink substantially down to 4 passes using 2.3W of power at 1 mm/s. The setup of deposition and cure for both the dielectric and antenna are shown in Figure 6.31. The airgun was used to cure the dielectric as a series of sections with a temperature of 70°C for 2.5 hours monitored by the use of a type-K thermocouple.

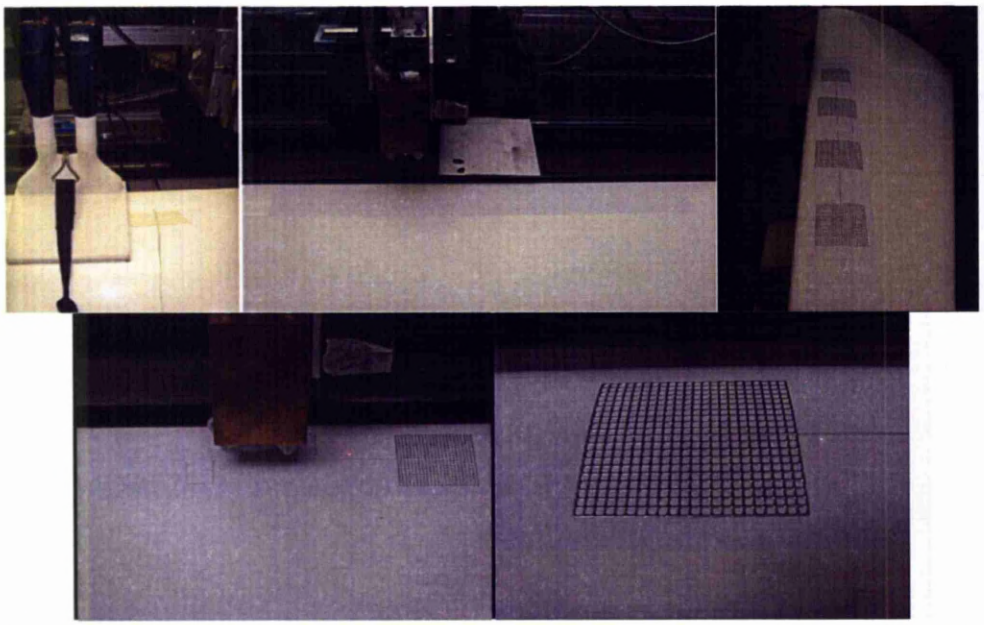

Figure 6.31: Series of images showing the fabrication process of the antenna array on the GRP wing. The manifold for the heat gun was specially designed to give even heat treatment of the dielectric during the curing process.

6.3 Conclusion

Within this chapter two demonstrators have been introduced and discussed. Successful fabrication of a working genetic algorithm antenna on a heat sensitive substrate has been shown, which could not be created using the conventional oven curing technique. Issues were raised in terms of repeatability and dimensional accuracy for the fabrication process, however these areas are being addressed by manufacturers of deposition systems. The laser curing process proved to be very successful. The application of the process to the ASTRAEA project demonstrated the versatility of the process that was developed. It proved problematic when being applied to the curing of dielectrics and although successful was clearly too slow a process to be applied on any large scale. The issues with curing the dielectric could possibly be overcome by going to longer wavelengths such as 10.6μm where a larger thermal association is present due to the wavelength being in the mid-IR region.

References

1 Hope D, Towards a wireless aircraft – January 2007 progress report, York. January 26th 2007.

2 Harley C, University of Manchester Towards a wireless aircraft. January 25th 2007.

3 Panitz M, Towards a wireless aircraft – January 2007 progress report, Nottingham. January 2007.

4 Sato T 1st Quarter progress report, January 2007- Liverpool. 29th January 2007.

5 IEEE, Transactions on Antenna and Propagation, Vol. AP-17, No. 3, 1969.

6 Balanis CA, Antenna Theory- Analysis and Design, 2nd Ed. John Wiley & Sons. (ISBN 0471592684).

7 Furse C, Haupt R, Down to the wire. IEE Spectr., 2001, 38(2), 34-39.

8 Prendergast J, Airbus Industries – Caught between several rocks and a hard place. Eur. J., 2007, 14(3), 14-18.

9 Panitz M, Christopoulos C, Sewell P, Hope DC, Dawson, JF, Marvin AC, Sato T, Fearon E, Watkins KG, Dearden G, Harley CD, Crowther WJ, The Opportunities and challenges associated with wireless interconnects in aircraft, Proc. IMechE vol. 223, Part G: J. Aerospace Engineering, 2009.

10 Sato T, Fearon E, Curran C, Watkins KG, Dearden G, Eckford D, Laser-assisted direct write for aerospace applications, Proc. IMechE, vol.223, Part G: J. Aerospace Engineering, 2009.

11 Daniel JP, Fly by wireless airbus end user viewpoint, technical report, Airbus, March 2007.

12 Fragoulis N, Tsagaris V, Anastassopoulos V, Information fusion in ad hoc wireless sensor networks for aircraft health monitoring. In Engineering against fracture, 2009, Springer.

13 Coelho TE, Fly by wireless UAV platform based on a flexible and distributed architecture, Proc. IEEE Industrial technology, 15-16December 2006, pp. 2359-2364.

14 GulfStream. GulfStream demonstrates fly by wireless aircraft control system, October 2008, available from http://www.gulfstream.com/news/release/2008/101408.htm.

15 Hope D, Towards a wireless aircraft progress report 2, April 2007, Univeristy of York.

16 **Hope D, Towards a wireless aircraft 3rd quarter progress report, July 2007, University of York.**

17 **Hope D, Towards a wireless aircraft 4th quarter progress report, October 2007, University of York.**

7 Conclusions

Use of a novel low thermal laser curing process in combination with a syringe deposition DW technique has been investigated for the fabrication of antenna on low thermal substrates, without the need for an oven curing step. Different variations of ink have been investigated along with in depth analysis to understand how the inks behave under oven and laser curing regimes, along with its suitability for the fabrication of electrical components. From this the following conclusions have been drawn.

7.1 Oven curing of the D58, D1 and D15 inks.

The oven curing experiments have shown how the inks behave under different curing regimes and this has been related to the resistivities that can be achieved, along with the associated mass loss that can be expected. The dynamic response of the inks has also been investigated to see the time dependencies of the inks when oven curing and how this affects the resultant resistivity of the cured tracks.

The best resistivity achieved was with the D58 ink which had a value $\rho=6.7x10^{-7}$ Ωm at 170°C which is x42 bulk silver. The D15 was close to the D58 ink with a low of $\rho=7.35x10^{-7}$ Ωm at 190°C which is x46 of bulk silver. The D1 was somewhat more resistive with a resistivity low of $\rho=9.9x10^{-7}$ Ωm at 210°C which equates to 62 times bulk silver. Overall with increasing temperature a better resistivity can be achieved with a fixed lower limit, with the D58 the ink the resistivity starts to increase above 180°C. The dopants had the expected effect of decreasing the conductivity, but unintended effect of making the inks more tolerant to a wider range of optimum curing regimes. There was no associated rise in resistance above 180°C as seen for the D58 ink. This makes the D1 and D15 inks more suitable for laser curing as it allows greater energy densities to be employed for faster curing times, chapter 3. The increase in resistance above 180°C has been attributed to the onset of the B-cure stage of the inks and has been correlated with the TGA/DSC experiments shown in chapter 5.

Though the mass loss results were not conclusive, they did show a general trend towards increased mass loss as temperature of cure increased. This would be as expected and did correlate to the results of the TGA where similar amounts of mass were lost, though the rate of loss seems to be different for each. This is probably due to the different heating

methods; that is the oven is pre-heated whereas the TGA experiment starts at room temperature and gradually increases. The density of the inks increased when cured, with the D58 becoming more dense than the D1, which was more dense than the D15 ink, before and after cure showing continuity and what would be expected due to the nature of carbon and graphite and their different densities respectively.

The dynamic temperature and resistance results were particularly interesting in that they showed that there is a transition point at which there is a dramatic change in the resistance of the ink track as it goes through cure. It would appear that a certain percentage of cross-linking is required at which point the ink goes from a non-conductor to a conductor. This is backed up by the results seen in section 2.4.1.1 but is more acute when measured in real time. The results also imply that there is a minimum time required for the cross-linking to take place and that even at a given temperature it is not instantaneous and relies on a fixed rate chemical reaction to take place. Also there seems to be an implication of different cure times for different temperatures as seen with the disparity between the 100°C and 200°C results of the dynamic measurements. Though a reason has been put forward involving the thermal properties of the polymer binder in conjunction with the B-Curing stage, it is not fully understood and would be an interesting area of future investigation.

7.2 Laser Curing of D58, D1 and D15 inks

The results of the laser curing trials show that it is possible to cure these polymeric composite inks using a laser and get results comparable to that of oven curing. The resistivities of the inks produced on alumina are much higher than that of oven cured samples. When the volume of the ink track which has been shown to be less dense and highly porous is taken into account by means of calculating the sheet resistance, the values become comparable. The difference between the oven curing and laser curing process is also demonstrated by the fact that the laser cured samples had a different profile to that of the oven cured samples. This is because the laser curing process introduces the energy in an incremental manner across the length of the track. It is also a much more energetic process and solvent evaporation occurs in a more volatile manner increasing the volume and porosity of the track. By contrast the oven curing process is slower and more even across the entire track meaning that solvent evaporation can occur prior to cross-linking. The Gaussian nature of the beam also lends itself to the profile of the track. This is because

the profile of the track is cambered at the edges so a decrease in intensity of the laser beam also correlates to a decrease in material that needs to be cured. The inks, to improve cure had been doped with carbon and graphite for the D1 and D15 inks respectively. This turned out to have an adverse affect on the inks due to the increase in thermal diffusivity that the dopents created. The carbon ink had a smaller range of cure than that of the D15 which in turn had a smaller range of cure compared to the D58 ink. By having a greater thermal diffusivity, more energy was being transferred to the substrate which causes thermal stresses and at higher energies causing the substrate to crack. The volumetric heat capacity was introduced and backed up the findings of the experiments.

The dynamic temperature and resistance measurements also showed that more energy was being transferred to the substrate when curing the D1 and D15 inks. This also resulted in a lower temperature of the inks during cure. There was a significant difference between the D58 inks and the doped inks in terms of temperatures recorded. When laser curing occurs it seems that a surface layer cures and that thermal conduction is required for cure to occur throughout the depth of the track assuming sufficient energy is put in to the ink. As the surface layer cures a noticeable drop, instantaneously, is registered in the measured resistance. If subsequent passes occur the resistance of the track reduces further implying that further consolidation is occurring. This is also seen on tracks that are thought to be fully cured already, as in the case of the D58 being cured with two passes at 1mm/s. As subsequent passes traverse over the track, the resistance is slightly increased for a small duaration of time due to the increased temperature of the track, upon cooling the resistance reduces to a new low. This was seen for several subsequent passes. In the case of the D1 ink, up to 10. Whereas the D15 seemed to plateau after 5 with no discernable change in its resistance after the subsequent two passes.

The absorption coefficient was measured and calculated demonstrating that the resin is fairly absorbent to the radiation with the intensity reducing by just over half for a 40 μm film. It is the vehicle through which the absorption primarily occurs after the carbon and graphite dopents if they are present.

7.3 Thermogravimetric Analysis and Differential Scanning Calorimetry

The thermo analytical techniques of TGA and DSC used in these experiments have given insights into how the polymeric inks behave under a heated environment. They have shown that there are two clear curing stages that the inks go through before they thermally degrade. The first stage of cure is the cross-linking between 90°C and 160°C, which is followed by a B-curing stage that starts at about 180°C. Solvent evaporation occurs almost instantaneously and this is clear from the uncured inks measurements, section 3.3.3.

The zinc calibration run and the empty pan reference run were successful in creating a calibration factor for calculating the specific heat capacities of the inks. The carbon and graphite dopents increased the specific heat capacities of the inks, which would be expected due to the higher specific heat capacities of the two components compared with either silver or the resin. However the resin had a surprisingly low calculated specific heat capacity when compared to other polymers, which are normally much higher than that of the silver, carbon and graphite. Without knowing the composition of the resins it is hard to verify the results.

From Figures 4.26 and 4.27, it is clear that the resultant cured ink tracks are very similar if not the same. They go through the same heat process and mass loss during the thermal cycle, with only slight changes in the D1 ink where some residual solvent seems to be emitted. This also seems to be occurring in the other two inks, but not to the same extent. Further to this it is noticeable that even though the inks are cured they do go through significant mass loss prior to the thermal degradation stage, about 5%, and this is the case even for the oven cured D58 ink, which was surprising. This implies that the curing process is very much a function of temperature and a statement that can be very arbitrary. All the tracks appeared to be cured, and had low resistivities, an indicator of cure.

There was a constant lag between the programmed temperature and the sample temperature as would be expected due to thermal inertia of the system and the sample. However the shape of the lag is not linear as shown in Figure 4.15 for the empty pan reference run, however this shape is common to all the tests and can be seen in the zinc calibration run and the uncured D58 run, Figure 4.20, along with the other samples for which it was not deemed necessary to show the graphs here. From the zinc calibration run

it was shown that the sample temperature was accurate as the melting point of the zinc accorded with literature.

7.4 Fourier Transform Infra Red Analysis of the Inks

The FTIR experiments have been useful in trying to understand what is occurring to the polymeric inks when oven curing and laser curing is occurring, and if there is any difference between the two.

The addition of silver to the resin has the unexpected benefit of increasing absorption in the fingerprint region. This is seen to a greater extent when looking at oven cured and laser cured samples. Also the samples appear to become more absorptive across the whole spectrum at which the FTIR was conducted when cured, especially when laser cured. The addition of the carbon and graphite components appears to increase the overall absorption of the inks, D1 and D15, across the whole spectrum, however unintuitively this appears to be more apparent with the cured products. The addition of the carbon and graphite also had some unexpected consequences. The addition, as seen in the oven and laser cured samples, Figures 5.15, 5.16, 5.18, 5.19, shows that a more even absorption occurs for the symmetric and asymmetric methylene stretches compared to the D58 ink (Figure 5.14), however the same effect is seen with the laser cured D58 ink (Figure 5.17). The starting point for all the uncured inks was a similar absorption spectra. Another consequence of the addition of the carbon and graphite ink is the shift witnessed to lower wavenumbers in the methylene stretches for the oven cured D1 and D15 inks and in the D15 laser cured ink. This shift was not witnessed in the laser cured D1 ink however. The addition of the carbon and graphite maybe aiding the creation of a more isotropic or dehalogenated hydrocarbon upon cure which corresponds to a shift toward what would typically be expected of the wavenumbers for the methylene stretches. This is further backed up by the more symmetrical nature of the methylene absorption peaks. This would imply that a slightly differing polymer is created upon cure when doping the D58 ink with carbon or graphite.

In Figures 7.1-7.3, the spectrographs of the oven and laser cured D58, D1 and D15 inks respectively are shown for ease of comparison. The investigation shows that there is no difference between the oven cured and laser cured spectrographs. There are slight variations in the amount of absorption, but with peaks occurring in the same place for the respective inks for both types of cure. Therefore the laser curing process appears to be

producing the same type of polymer as the one produced during oven curing. This is further backed up by the TGA/DSC analysis shown in chapter 4 where the oven cured and laser cured samples go through the same thermal cycle during the TGA/DTA experiments. By combining the results from the two analytical experiments it can be deduced that the laser and oven curing process are initiating the same curing process within the inks. The thermal cycle, mass loss and FTIR analysis combine to make a conclusive result along with the chemical constituents being the same as shown by the FTIR analysis.

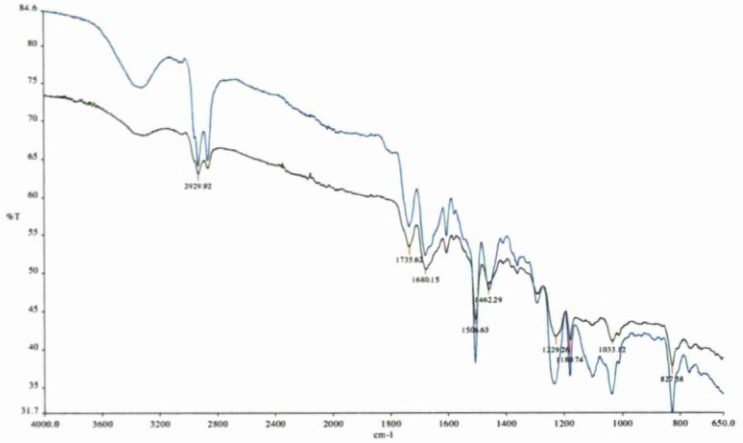

Figure 7.1: D58 oven cure (black) and laser cure (blue)

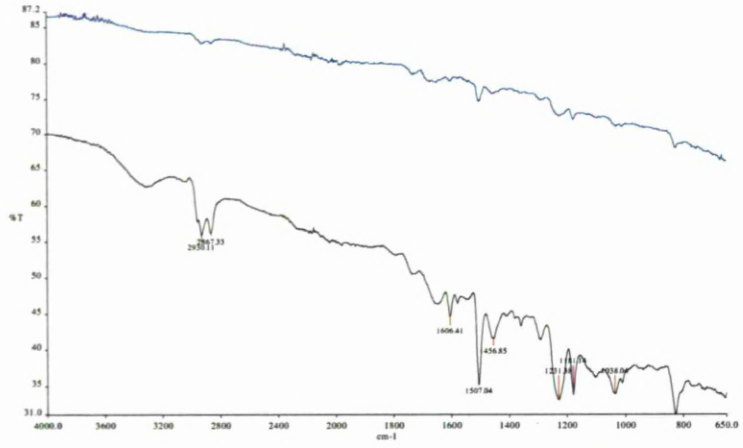

Figure 7.2: D1 oven cure (blue) and laser cure (black)

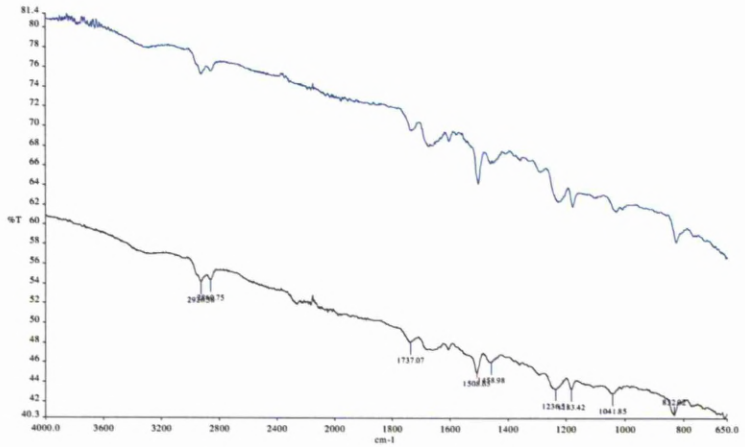

Figure 7.3: D15 oven cure (black) laser cure (blue)

7.5 Process Applications

Within this chapter two demonstrators have been introduced and discussed. Successful fabrication of a working genetic algorithm antenna on a heat sensitive substrate has been shown, which could not be created using the conventional oven curing technique. Issues were raised in terms of repeatability and dimensional accuracy for the fabrication process, however these areas are being addressed by manufacturers of deposition systems. The laser curing process proved to be very successful. The application of the process to the ASTRAEA project demonstrated the versatility of the process that was developed. It proved problematic when being applied to the curing of dielectrics and although successful was clearly too slow a process to be applied on any large scale. The issues with curing the dielectric could possibly be overcome by going to longer wavelengths such as 10.6μm where a larger thermal association is present due to the wavelength being in the mid-IR region.

8 Recommendations for Future Work

- Within this investigation, two laser types have been looked at. Though the CO_2 laser yielded far better performances then that of the Er:YAG laser, the desire for a fibre laser process is strong due to its ease of integration in to any system. Especially when looking at retrospective add on's. There is scope to look at other laser wavelengths to investigate how what sort of curing parameters and results can be achieved.
- In addition to the investigation of different laser types. The final TaWA and ASTRAEA demonstrators and used pulsed lasers. In particular the TaWA where a 5% duty cycle was used. Using a pulsed laser proved to create a good working antenna. Further investigation could be conducted to look at how pulsing affects the results and helps the issue of curing on thermally sensitive substrates.
- This work has solely concentrated on fabricating antenna. A natural extension of this would be to apply the process to the fabrication of other electrical components such as temperature/pressure sensors, strain gauges and inductors.
- The cure of dielectric inks proved to be too slow for industrial purposes. If a suitable dielectric ink could be found or developed, then this increase the flexibility of the process and component architectures which could be deposited.
- The work has thoroughly investigated the process of laser curing polymeric inks. A useful insight could be gained by modelling the work so that in future a parametric regime could be made by knowing the thermal properties of the ink and substrate. Also the model would help to give a further insight in to how the laser curing process works.
- Further investigation in to why there is a difference in the time the ink becomes conductive as a function of temperature could help explain some of the results seen in chapter 2. This could also be extended to include laser curing to see how different power settings and regimes affect the time it takes to get a good cured sample.
- A noticeable difference was witnessed between the conventionally made antenna and the DW made antenna. This difference could not solely be attributed to the dimensional tolerances of the fabrication process, and so this could be further investigated to look at why the polymeric inks act differently to copper tracks when fabricated to make an antenna.

TIME : Mon 12 Sep 2016 09:52AM
TERMINAL : 8
TITLE : Laser assisted ink consolidation for direct write component fabric
CALL NUMBER : THESIS 21060.SAT bls
BARCODE : 014392629
STATUS : IN TRANSIT
Received. Belongs at Brunswick Library Store - Click here to reserve.